Tobias Kraus

Assembly and printing of micro and nano objects

Diss. ETH No. 17334

Cuvillier Verlag Göttingen

Diss. ETH No. 17334

ASSEMBLY AND PRINTING
OF MICRO AND NANO OBJECTS

A dissertation submitted to
ETH ZURICH

for the degree of
Doctor of Sciences

presented by
TOBIAS KRAUS
Dipl.-Ing. Univ., Technische Universität München
born February 2nd, 1979
citizen of Germany

accepted on the recommendation of
Prof. Nicholas D. Spencer, examiner
Prof. Dieter Kern, co-examiner
Prof. Andreas Stemmer, co-examiner
Dr. Heiko Wolf, co-examiner

2007

1. Auflage, 2007
Gedruckt auf säurefreiem Papier
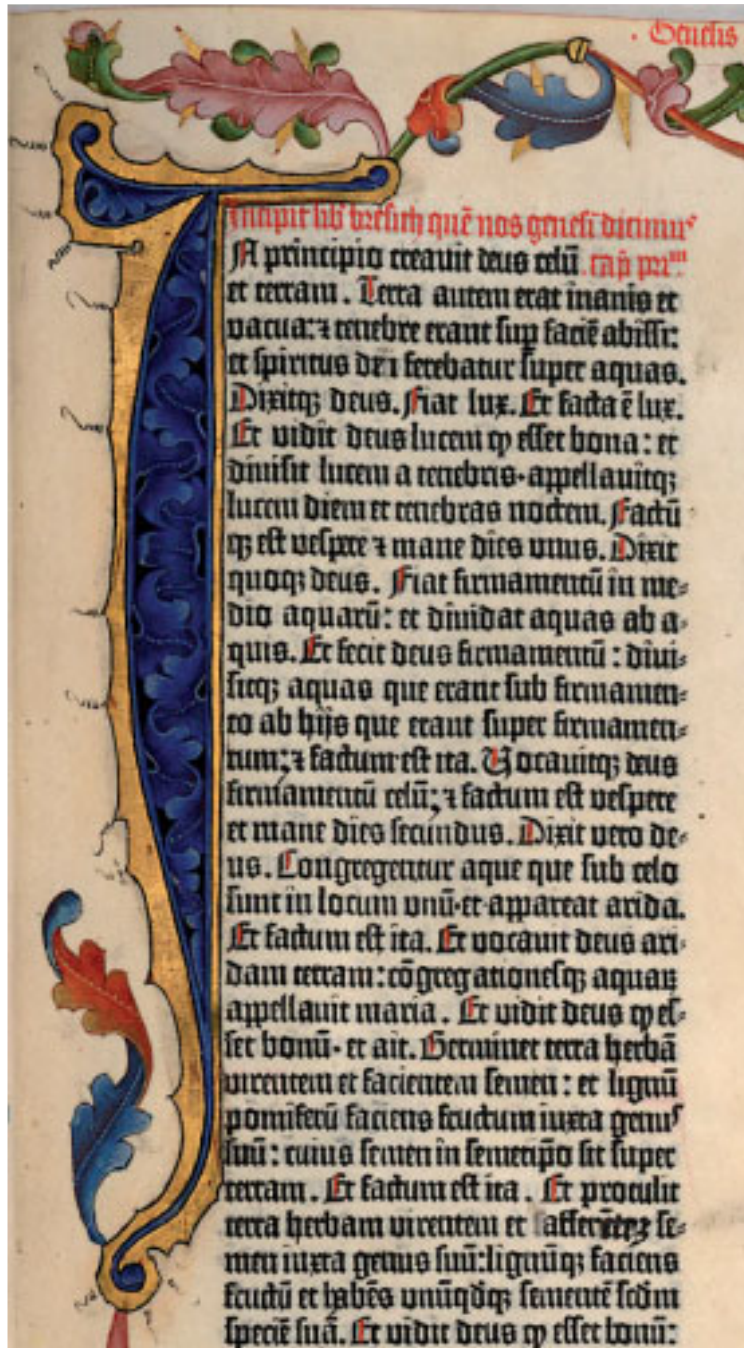
Gutenberg Bible, copy Hubay 2, volume 1, fol. 005r, left column
(Source: SUB Göttingen, 2 BIBL I, 5955 INC.)

Genesis 1

[1]In principo creavit Deus coelum et terram.
[1]Bereshit bara Elohim et hashamayim ve'et ha'arets.
[1]Am anfang schuff Gott Himel und Erden.
[1]In the beginning God created the heaven and the earth.

[2]Terra autem erat inanis et vacua,
      et tenebrae erant super faciem abyssi,
      et spiritus Dei ferebatur super aquas.
      Vulgata, Hieronymus, approx. A.D. 390

[2]Veha'arets hayetah tohu vavohu
      vechoshech al-peney tehom
      veruach Elohim merachefet al-peney hamayim.
      Codex Petropolitanus, A.D. 1008

[2]Und die Erde war wüst und leer /
      und es war finster auff der Tieffe /
      Und der Geist Gottes schwebet auff dem Wasser.
      Lutherbibel, Martin Luther, A.D. 1545

[2]And the earth was without form, and void;
      and darkness was upon the face of the deep.
      And the Spirit of God moved upon the face of the waters.
      King James Version of the Bible, A.D. 1611

Contents

Contents

Contents

x

Kurzfassung

Die Herstellung von Materialien aus Partikeln ist eine effiziente Methode, um Materialien in eine an sich inkompatible Matrix zu integrieren, besondere Eigenschaften sehr kleiner Partikel auszunutzen oder verschiedene Materialeigenschaften durch das Mischen von Partikeln zu kombinieren. Selbst sehr kleine Partikel können heute aus vielen verschiedenen Materialien mit grosser Qualität chemisch synthetisiert werden. Sonst nur sehr schwer erreichbare Strukturgrössen und Materialsysteme sind damit relativ einfach zugänglich.

Im Gegensatz zu anderen Methoden erlaubt der partikelbasierte Ansatz auch, regelmässige Strukturen auf sehr kleinen Skalen herzustellen. Die Anordnung von Partikeln in regelmässige Strukturen kann dabei durch Selbstanordnung geschehen, die je nach Partikelgrösse oft auch die einzig wirtschaftliche Methode ist. In dieser Arbeit wird gezeigt, dass für die praktische Nutzung der Selbstanordnung in technologischen Aufgaben bestimmte Randbedingungen zu erfüllen sind. Aus diesen Überlegungen geht ein Konzept hervor, das von Templaten gelenkte Selbstanordnung mit auf Adhäsion basierender Partikelübertragung kombiniert.

Durch solchen Methoden wurden in dieser Arbeit Partikel mit Durchmessern zwischen 100 µm und 60 nm angeordnet, auf andere Oberflächen übertragen und auf Substrate ohne besondere Strukturierung integriert. Das Resultat sind Materialien, in denen die Partikel ihre spezifische Aktivität behalten. Metallbeschichtete Mikropartikel ergeben elektrische Kontakte zu Halbleitern. Präzise angeordnete Polymerpartikel schützen sub-Mikrometer grosse Bereiche der Oberfläche in Ätzprozessen, so dass sehr kleine Metallscheiben oder Siliziumzylinder entstehen. Nanokristalle aus Gold bleiben katalytisch aktiv, so dass sie in einem Gasphasenprozess das Wachstum von Silizium-Nanodrähten katalysieren. Solche Nanokristalle sind ausserdem optisch aktiv und empfind-

lich auf den Brechungsindex der unmittelbaren Umgebung, was ihre Anwendung für biologische Assays und ähnliche analytische Anwendungen nahelegt.

In dieser Arbeit nutzen wir verschiedene Methoden zur Selbstanordnung von Partikeln, die alle auf topographischen Templaten basieren. Grosse Partikel (100 μm) lassen sich in trockener Form aus einer Wirbelschicht anordnen. Kleinere Partikel liegen im Allgemeinen als Suspension vor und müssen aus der flüssigen Phase auf die Oberfläche gebracht werden. Dazu verwenden wir Kapillarkräfte, wie sie bei Trocknungsprozessen stets auftreten, und die wir gezielt durch eine geeignete Oberflächentopographie beeinflussen. Der Transport der kolloidalen Partikeln muss dabei so eingestellt werden, dass eine Akkumulationszone mit gosser lokaler Konzentration entsteht. Das gelingt einerseits durch die Kontrolle der Substrattemperatur und damit der Verdunstungsrate, andererseits durch Benutzung oberflächenaktiver Substanzen, die den Kontaktwinkel beeinflussen und über die sich die Stabilität der Suspension einstellen lässt. Wir zeigen, dass eine starke lokale Konzentrationserhöhung bei sehr kleinen Partikeln erforderlich ist, weil die Brownsche Molekularbewegung zu stark stochastischem Verhalten führt.

Die passive Handhabung von Partikeln, wie sie hier verwendet wird, basiert auf kontrollierter Partikelhaftung in sogenannten Adhäsionskaskaden und ähnelt der Übertragung von Tinte im traditionellen Buchdruck. Unterschiedliche Oberflächen üben unterschiedlich starke Adhäsionskräfte auf Partikel aus, mit denen sie in Kontakt kommen. Wir modifizieren und kombinieren die Oberflächen so, dass in jedem Schritt die Zieloberfläche eine höhere Adhäsion bietet als die Quelloberfläche. Es stellt sich heraus, dass die Geometrie des Kontaktes zwischen Partikel und Oberfläche einen grossen Einfluss auf die Haftung hat, so dass die mechanischen Eigenschaften der Oberflächen die Adhesion stark be-

einflussen, weil sie sich mehr oder weniger gut der Partikeloberfläche anpassen können. Selbst bei sehr kleinen Partikeln beeinflusst die Geometrie die Adhesion stark, so dass wir Nanokristalle vor allem durch gezielte Beeinflussung der Kontaktflächen übertragen können.

Durch ihre Kombination von Selbstanordnung und Übertragung ist die hier eingeführte Methode modular und kompatibel mit anderen Prozessen. Wir demonstrieren dies durch mehrfache Anwendung unseres Verfahrens, bei der hierarchische Strukturen aus Partikeln verschiedener Grössenordnungen entstehen. Die hier beschriebene Methode sollte auch zu sehr kleinen Objekte skalierbar sein, insbesondere wenn sie mit weiteren Selbstanordnungsprozessen kombiniert wird. In diesem Zusammenhang demonstrieren wir, dass Thiolmoleküle durch gezielte Beeinflussung ihres Transports als Gradienten mit kontrollierter Dichte auf Goldoberflächen abgeschieden werden können.

Summary

Materials can be fabricated using particles as building blocks. Particles from various substances can thus be introduced into normally incompatible matrices, the unique properties of very small particles can be exploited, and different properties of different particles can be combined by mixing them in a material. Even very small particles are readily synthesized with high quality using modern chemical methods. Size ranges and material combinations that are usually difficult to attain can thus be achieved easily.

In contrast to other methods, particle-based approaches allow us to fabricate regular structures at very small scales. The arrangement of particles in such structures is possible via self-assembly, which often is the only economical approach for small particle sizes. This work shows that certain conditions have to be fulfilled for self-assembly to be useful in technological applications. A concept is suggested that meets these requirements by combining templated self-assembly with adhesion-based particle handling.

Using these methods, particles with diameters between 100 μm and 60 nm are assembled, transferred, and integrated on standard substrates without predefined surface structures. This produces materials with particles that retain their specific activities. Metal-coated microbeads provide electrical contact to semiconductors. Precisely arranged polymer beads protect sub-micrometer-scale parts of a surface in etch processes to yield metal nanodiscs or silicon nanorods. Gold nanocrystals remain catalytically active and nucleate the growth of silicon nanowires in a CVD process. Such nanocrystals are also optically active and sensitive to the refractive index of their immediate surroundings, which makes them useful in biological assays and similar analytical problems.

In this work, we use several methods for the self-assembly of particles, all of which are based on topographical templates. Large particles

xvi

(100 μm in diameter) can be assembled in a dry state from a fluidized bed. Smaller particles are generally handled as suspensions and have to be brought from the liquid phase onto a surface. To this end, we exploit capillary forces, which are present in all drying processes, and direct them using specialized surface topographies. The transport of the colloidal particles has to adjusted such as to create an accumulation zone with high local concentrations. This is done by tuning the substrate temperature (and thus, the evaporation rate), but also by using surfactants, which bias contact angle and stability of the suspension. We show that a large increase in local concentration is required when using small particles, which behave in a strongly stochastic manner owing to Brownian Motion.

The passive handling of particles applied here is based on controlled particle adhesion in so-called adhesion cascades and reminds of the ink transfer in traditional printing. Different surfaces exert differently strong adhesion forces on the particles with which they come in contact. We modify and combine surfaces such that in every step the target substrate provides a stronger adhesion than the previous surface did. It becomes clear that the geometry of the particle-surface contact has a large influence on adhesion, so that mechanical properties of the surfaces influence particle adhesion, as their surface can conform to the particle's surface more or less. This dependence of adhesion on the contact geometry is strong enough even in small particles to enable the transfer of nanocrystals solely through contact area differences.

The combination of self-assembly and transfer makes our method modular and compatible with existing techniques. We demonstrate this by its repeated application, which yields hierarchical structures containing different particle sizes. The method should also scale to very small particles, possibly using other self-assembly processes. We demonstrate one

possible route for thiol molecules, which can be patterned in gradients
by controlling their transport.

1 Introduction

This thesis is concerned with the particle-based fabrication of materials. It describes how particles can be arranged and stacked on surfaces to create materials with complex geometries and chemical compositions. This introductory chapter discusses why we want to fabricate such materials, why particles are interesting building blocks to create materials, and how this approach is conceptually different from other routes. It introduces some prior examples of particle-based materials and devices that use particles as functional components. The last section of the chapter describes the structure of the thesis.

1.1 Control of structure in materials fabrication

A paradigm shift is currently taking place in materials science and technology. So far, materials were created by varying well-known materials syntheses (and treatments) with limited control over their microscopic structure. Now, there is widespread optimism about and intense research into the creation of materials with predefined structures that have improved properties.

This shift was initiated by the advent and subsequent spread of two new fields: semiconductor microtechnology and nanoscale metrology. The advances in metrology (which included the invention of scanning probe microscopy and electron microscopy as well as the spatial reconstruction of x-ray diffraction measurements) have made it possible to correlate nanoscale structures of materials with their properties. Semiconductor technology has demonstrated that materials can be patterned with ever-increasing resolution, even at high throughput. The expectation arose that a "nanotechnology" could be developed that can create general materials with well-defined nanostructures, and thus, well-defined properties that might be tailored to solve a given problem.

Such deterministic materials fabrication requires the solution of one central problem: the flow of information from the design to the final material. In semiconductor technology, for example, designs are first created with high-level description languages that define functionality on an abstract level. From these descriptions, an explicit design for the physical structure of the semiconductor is created (automatically or semi-automatically), which can then be translated into a set of masks for photolithography and a sequence of processing steps.

Likewise, to translate a desired materials property into the topographical and chemical structure of a material, high-level information has to somehow be translated into a physical structure. One could imagine, for example, that some future semiconductor technology will define the position and type of each atom in a device according to a design. This is not as outlandish as it might seem: at feature sizes below 10 nm that have been demonstrated in the research laboratories of semiconductor manufacturers [48], fewer than 30 atoms span the gate width. The gate dielectrics in the latest CMOS transistors are only some atomic layers thick.

For materials fabrication, however, such an "explicit" nanotechnology is inefficient in multiple aspects. The generality of the method comes at an extremely high price. After more than 30 years of continuous size reduction in the semiconductor industry, there exists a relatively robust rule for the cost of size reduction: the linewidth can be expected to drop one order of magnitude every 15 years. This decrease of the characteristic dimensions is accompanied by an increase in investments to build the necessary factory by somewhat more than one order of magnitude [37]. A lower bound for the investment required to build one production site capable of achieving atomic resolution would therefore be two trillion US-dollars. This assumes that there are no qualitatively new challenges

involved that further increase the price, but such challenges are very likely to occur. If there are applications for which such investments would be viable, they must be using small amounts of extremely complex materials with very high added value. It is not clear whether even computer CPUs will qualify for this in the future.

Another route proposed for translating the structural information into a physical representation is the "Molecular Assembler" devised by Eric DREXLER [49]. He suggested programming a "finger" (say, the tip of a scanning probe microscope) such that it assembles reactive molecules into a material sequentially, by mechanically removing a carrier part and leaving a single atom at a time. In reply to this proposal (and some of the ideas promised to become feasible with such a fabrication method), Richard SMALLEY published an article in *Scientific American* [161], in which he famously pointed out two problems that such a molecular assembler might have, namely, its *fat fingers* and its *sticky fingers*. He argued that any computer-controlled "finger" would be too large and too imprecise to control motion at an atomic scale, and that it would stick to the molecules involved. He also argued that there was no chemical system that could replace these fingers to place atoms with the required accuracy one by one.

These limitations are still the topic of discussion, but a general problem of an additive, sequential fabrication on a molecular (or other very small) scale is the timescales involved. Even when moving at the speed of light, the finger of an assembler would need at least ten years to assemble 1 mm^3 of silicon from a heap of single silicon atoms that lie at a distance of 1 mm. Even if there were a constant supply of atoms flowing to the tip, the tip would have to travel millions of kilometers.

Several alternative routes have been proposed to avoid such problems. Many of them are based on the idea that during fabrication, the

material itself would act as a machine that arranges its parts so that a defined structure is created. If that machine is sufficiently general, it could produce any structure required. Such concepts are often called "self-assembly", "self-organization" or "emergence". Their archetypes in nature are cells and viruses in which functional parts (or even entire viruses) self-assemble from its parts.

Such materials syntheses could be very efficient. The flow of information, however, is vastly more complex than in semiconductor technology or sequential assemblers. Instead of separating the assembly problem from the material's functionality, both are now one. It is not sufficient to predict the structure required for obtaining certain materials properties, one also has predict the behavior of the disordered system and then choose a system that will arrange into the desired structure. This inverse problem in general is hard, and there is not much hope that we will soon be able to design general systems so that a given structure emerges. Thus, from an engineering standpoint, self-assembly is not yet a general method for materials fabrication.

There might be a compromise, however. Similar to what is done in classical materials fabrication (say, metallurgy or polymer formulation), we can choose systems that produce materials with interesting properties, analyze their nanostructure and bias it by changing the components or changing external parameters. We thus part with the notion of a general materials fabrication in favor of problem-oriented approaches, as they have been traditionally used with great success.

One way to bias materials fabrication in a deterministic manner is to use templates that direct the final structure in a predictable way. Such templates might be created with slower, more direct methods of nanofabrication, for example on a surface. Their order will be replicated by the self-assembling components.

In this thesis, building blocks are arranged at predefined positions of a template. The hope is thus to combine the traditional, engineering-oriented manufacturing technique with the novel, efficient, but complex self-assembly concept. In literature, this often is dubbed the combination of "top-down" with "bottom-up"-fabrication [180].

1.2 Top-down and bottom-up, subtractive and additive fabrication

The main differences between traditional technology and self-assembly are the flow of information (summarized in the "top-down" versus "bottom-up" dichotomy) and the flow of materials. In traditional semiconductor technology and the micro- and nanofabrication technologies that have been derived from it, fabrication is mainly done by subtraction. A wafer of bulk material is etched, thin films are being applied on its entire area only to then be polished, etched or stripped away on most parts, polymer layers are exposed and developed to remove the exposed parts.

Such a subtractive strategy is in marked contrast to macroscopic manufacturing. Machines are generally built from pieces that are fabricated separately. A subtractive route, however, provides cleaner interfaces and bulk materials parts with constant properties (and even continuous crystal structure). These are critical prerequisites for semiconductor integrated devices, which subtractive technology can produce at remarkable yields.

Subtractive methods are inherently costly, however. Each step only patterns one metal or semiconductor layer, and each step involves a pattern transfer — in general, a photolithography step with a top-down flow of information — and an actual material transfer. This becomes

problematic when making large amounts of structured materials, be it in complex thick layers, bulk pieces or large areas. Even when the desired structures are simple, repetitive or sparsely dispersed over the material, many costly fabrication steps are necessary, and many of them cannot be performed in a continuous fashion.

In bottom-up processes, where the process information is stored in the building blocks that will form the material, fabrication usually is additive. These blocks will react, agglomerate or deposit according to the information stored and self-assemble into the desired structures. Some structures are easily fabricated in this way, e.g., dense and ordered molecular "self-assembled monolayers" [175], hexagonal particle crystals (in two or three dimensions) [117], spaced particles on surfaces without particular order [63], or regular dewetting structures of diblock copolymers [72], and some of them are useful in one or the other application. However, numerous other useful structures could so far not be created bottom-up, and there is no general bottom-up process that would easily produce many different structures.

If a self-assembly process is known to create a desired structure, the actual fabrication can be remarkably simple. In contrast to thin-film technology, which commonly requires vacuum equipment, high temperatures and energetic plasmas, many of the known self-assembling systems are closer to dip-coating or spraying. The challenge lies not so much in providing extreme conditions in a relatively simple material system but rather in providing exactly the right, moderate conditions in a complex material system.

It should be possible to find bottom-up processes for many different structures. According to Brownian Dynamics simulations, complex arrangements can emerge from moderately complex building blocks (such as particles with patches on their surfaces) [194]. Such structures of-

ten lack long-range order, as their order will decay at a length that is comparable to particle-particle interaction lengths, unless critical phenomena or kinetic mechanisms provide additional, long-range interactions. Traditional semiconductor devices have very strong long-range correlations, which is a prerequisite required to enable the typical, stepwise fabrication of standard technology. It is possible to introduce longrange order, however, using a template that confines the self-assembling structures, as has been demonstrated for the microphase separation of diblock copolymers [32].

1.3 Particles as building blocks

Instead of using molecules or atoms directly and build materials from scratch, it is easier to move to the mesoscopic level and arrange nanoparticles (or even larger particles) to create structured materials. Such particles are readily synthesized using bottom-up processes. It is a wellknown strategy to introduce surface-active molecules into crystallization and polymerization processes to favor certain geometries during the growth or to seed such processes to create monodispersed crystals, polymer beads, or glassy spheres, and there are recipes available for preparing a large variety of particles from metals, semiconductors, oxides and many other materials. Detailed information on the particle syntheses used to create the particles mentioned in this work will be given in the experimental chapters later on. The reader is also referred to the large number of reviews on the subject of particle synthesis [86,123,135].

Particles can serve two different purposes: they can provide some functionality at a single-particle level, or they can interact to provide some interesting property. The vast literature on particles (in particular, on nanoparticles) contains many examples of functional particles.

The largest interest is currently directed at optically active particles, for example, fluorescing quantum dots, which exhibit very narrow emission bands and do not bleach, even under extremely intense light [136]. Quantum dots are used as alternatives to chemical dyes in the biological sciences [74] and might soon become the light-emitting component in displays [179]. Other applications of individually active particles include catalytic silica and titania particles [12], magnetic particles for high-density storage [166], surface-bound semiconductor particles with quantum confinement properties [140], and many others.

When multiple (perhaps even different) particles are arranged regularly, new properties can emerge. Perhaps the simplest example consists of a monolayer of metal particles (e.g., silver) that can be created and compressed on a LANGMUIR–BLODGETT trough and that changes its color from that of a typical colloid to a silver mirror on the surface as soon as the compression is sufficient to allow coupling of the particles' electron systems [146]. More complex arrangements, possibly involving different particle types, can create more complex electronic structures. Thus, researchers have mixed various types of nanocrystals and let them dry out to find superstructures involving different particles in regular crystals with complex geometries [158].

This approach seems promising because many materials of practical interest have a grainy structure. Novel properties might occur when combining particles from materials that could so far not be combined and introducing an order that has hitherto not been present. One needs to consider, however, that such additive methods create many interfaces, which in traditional technology are regarded as one of the main sources of quality problems. Such interfaces can limit the conductivity (or electronic coupling in general), mechanical strength, optical transparency, and can promote corrosion and aging. Thus, in particle-based materials,

special attention has to be paid to surfaces and interfaces.

1.4 Particle-based materials

A large and important class of particle-based materials consists of thin layers of particles on surfaces, because such layers often suffice to produce the desired effect and because it is still hard to create macroscopic bulk crystals of particles. Ordered arrangements such as thin films are useful both when employing particles with individual functionalities or when using particle superstructures with novel collective properties. Spaced arrays of functional particles allow interfacing with microtechnology and, thus, their macroscopic environment. The particle itself might be smaller than the minimum feature size achievable using a specific technology, but it sits in a well-defined position and can thus be contacted with a larger electrode, or detected optically by means of its emitted or scattered light.

Using this strategy, memory elements have been fabricated from small metal islands that were formed through dewetting [115]. The electrodes used for reading and writing the memory were far larger than the particle dimensions, but the device profited from the small dimensions of the particles that enabled fast writing cycles. Other researchers have created transistors by introducing nanoparticles and contacting them later, or trapping these particles between larger structures (for a review of such devices, see [58]). Efforts are also being made to use self-assembly schemes for the arrangements of particles that form nanophotonic devices [137], but such applications require good positional control, so that most researchers in the field so far rely on top-down-manufactured particles [116].

Regular (often dense) patterns of particles might interact with elec-

tromagnetic radiation and form a metamaterial. Top-down-fabricated structures have shown to focus and guide light [119], and it should be possible to create metamaterials with negative refractive indices [69]. In practical applications, macroscopic amounts of such materials will be needed, which requires efficient fabrication methods. Self-assembled colloidal crystals (or materials derived from them) that act as metamaterials are candidates for on-chip optical computing, where light is guided through the crystal with little loss, even around corners, and interacts with specialized components to provide fast computation [4].

Dense particle arrangements can combine properties of different particles, for example to separate holes and carriers in a solar cell [138], or to combine high electrical with low thermal conductivity in a thermoelectric material [31].

Some of these examples require a level of generality that is not yet available in self-assembly, and researchers therefore wish to combine it with top-down methods. For example, colloidal crystals for guiding and manipulating light should have not only a highly regular crystal structure, but also defects at well-defined positions to allow, e. g. the efficient splitting of an electromagnetic wave traveling through it into two parts.

In these and other cases, additional functionality can be introduced into a system if it is possible to break a regular order at a desired position. Complex functionality often requires complex structure, and one of the most interesting challenges in particle-based materials is the efficient placement of well-controlled, precise structures with arbitrary arrangements efficiently.

1.5 Aim and structure of this thesis

The primary aim of this thesis is the integration of single particles and ordered structures made from particles onto surfaces with high definition. It shows that a combination of self-assembly and adhesion-based particle handling lets us create functional particle arrangements of practical relevance. The approach introduced here is general, and this thesis provides both theoretical arguments and experimental evidence that different types of complex materials can be "printed".

Chapter 2 discusses approaches for a parallel and efficient ordering and surface integration of large numbers of particles. Some general properties and requirements of such processes are used to categorize these processes into broad classes. Existing processes from industry and research are reviewed to obtain estimates of their generality, precision and yield at different length scales. Finally, a novel concept of particle assembly is introduced, and the control of particle transport and adhesion it requires is described.

Chapters 3 and 4 deal with these prerequisites in more detail. Characteristic scales that allow us to compare the different forces acting on particles during processing are introduced. More specifically, in Chapter 3, the transport of particles is discussed on different scales, ranging from the bulk motion of the colloid to the microscopic particle motion during assembly, and a generalizing framework on particle mobility and interaction is presented. This framework will be used later on to discuss properties of the different experimental systems. Chapter 4 is concerned with the state of particles that are no longer mobile, but adhere to surfaces. Again, we start with a survey of effects that cause adhesion and compare their potential strengths. Three major aspects are discussed at some length: contact mechanics, surface chemistry, and attractive bulk

interactions.

Chapter 5 presents the experimental implementation of the models and considerations presented in the preceding chapters. Four different "objects" are arranged on surfaces: thiol molecules (with control of their density only), glass microspheres (macroscopic objects with a diameter of 100 μm), polymer beads (popular carriers in the biological sciences, but largely used in disordered form), and gold nanocrystals. For each particle, the corresponding section in the chapter discusses its properties and applications, the assembly technique used, transfer mechanisms, and finally applications of the assembled particles.

To conclude, Chapter 6 discusses the results of this thesis and provides an assessment of the feasibility of the assembly of smaller particles, more complex structures and, finally, printed bulk materials.

The appendices contain technical details on particle synthesis, tools built for this work, and the microfabrication techniques used.

1 Introduction

2 Parallelized assembly and fabrication

2 Parallelized assembly and fabrication

Arranging objects with parallelized assembly is an old and widespread strategy, and templated particle self-assembly is merely a generalization of this concept. In this thesis, we use self-assembly methods to create structured materials from small particles. Section 2.1 therefore introduces self-assembly and provides a definition to differentiate the various methods often summarized under this single term. Self-assembly is regarded a key to manufacturing at small scales, and Section 2.2 discusses why fabrication and assembly on a nanoscale are more challenging than on a macroscopic scale, and in which cases self-assembly can provide an economical route to nanostructures. Section 2.3 reviews some of the methods that have been published to arrange particles on surfaces. These include both approaches from academic research and industrially applied methods.

Many parallelized assembly processes include a transfer step, in which the arranged objects are picked up in parallel and brought to the target substrate. This is partially due to their evolution from pick-and-place approaches, in which a single object is picked up actively and placed at its target position. A transfer step also is desirable, however, to separate assembly from integration and thus lift the requirements of the assembly process from the target substrate. The complex geometries or unusual materials that are required for many assembly processes are thus only required on the template and not the target substrate. This thesis describes how controlled adhesion can be used to transfer particles, a concept that Section 2.4 introduces, alongside with related examples from the literature.

The use of parallelized assembly methods in industry suggests that they are more economical than the traditional pick-and-place. We have seen in the last chapter that materials synthesis (or micro- and nanostructuring of materials) is another field that can benefit from using tem-

plated self-assembly. Some of the reasons given apply for both fields, some take on extreme extents in the case of materials fabrication: not only is it inefficient to place very large numbers of small objects using pick-and-place, it oftentimes is impossible to do so.

Still, not all assembly in industry is carried out using parallelized assembly, and not all materials-related problems will be addressable using templated self-assembly. In this chapter we will therefore discuss the merits and problems of different self-assembly approaches and identify fields of applications. The focus will be on the assembly of particles on surfaces, as introduced in the preceding chapter.

2.1 Self-assembly, self-organization, and directed assembly

Self-assembly is a catchy term, but it is defined rather poorly. One of its main proponents, George WHITESIDES, asked rhetorically in a review [181], "Is anything not self-assembly?". He then went on to define,

> Here, we limit the term to processes that involve pre-existing components (separate or distinct parts of a disordered structure), are reversible, and can be controlled by proper design of the components. "Self-assembly" is thus not synonymous with "formation."

This is a pragmatic, heuristic definition, although it seems slightly arbitrary (why does the process have to be reversible, for example, and in which sense?). An alternative approach is to analyze the flow of information, as we have suggested in the previous chapter, and to see where the information regarding the target position is stored. WHITESIDES

seems to imply that it should be the components that store the information, or at least part of it, for their design should control the outcome of the assembly. This is indeed the case for many well-known systems in which self-assembly occurs. We might therefore define self-assembly as

> A process that arranges previously disordered objects in a predictable way according to information that is stored in the objects.

The new definition goes along well with another popular categorization of self-assembly, which distinguishes self-assembly from self-organization by requiring that self-assembly is due to the descent to a lower energy state (although it might be a local one), while self-organization proceeds far from equilibrium and is not driven by an energy gradient. In self-assembly, the information is stored in the particles, namely the parameters that describe their interactions. In self-organization, the information is more spread, stored more indirectly, and can include properties of the matrix (say, the diffusivity in the continuous medium), making self-organization even harder to engineer than self-assembly. Perhaps the first system to self-organize was that proposed by Allen TUR-ING as a model of biological systems [173], based on a reaction-diffusion network. In this system, all diffusion constants, the reaction kinetics constants and the geometry are relevant for the developing patterns, and it will be very hard in practice to tune those in a wide range to enforce a certain outcome.

If information that is spread over many different properties of a system is problematic, then inefficiently stored information is even more so. It has been shown, for example, that large DNA strands can be arranged into various shapes by taking advantage of unique sequences

on them that are then "tacked" together with shorter strands [151]. The actual information in these sequences is irrelevant, but the sequences need to be sufficiently different to provide clear binding energy differences. For this assembly, one therefore has to produce many different DNA fragments, although the information that they actually carry for the assembly is small and could be encoded in a short oligonucleotide.

The minimum information that has to be stored in the self-assembling components is the KOLMOGOROV complexity of the resultant structure[1]. This complexity can be much smaller than that of a program needed to control, say, a hypothetical molecular assembler that would put together the structure, in particular if the structure in question is repetitive. In fact, a high-level description of an integrated circuit (as is used today in the design process) together with the description of the elementary devices would be sufficient to self-assemble an integrated circuit. Many relevant materials and devices are highly repetitive and could be described with little information. To find a system, however, that can be programmed with this "compressed" information and then assemble into the respective device, is very hard.

Systems that store information inefficiently are far easier to design than those that do so efficiently. For example, even before the DNA "Origami" described above was published, researchers had shown that one can construct cellular automata from DNA, which operate after a rule set encoded in the involved DNA fragments. Such automata can produce complex structures, and since several of them have proven to be TURING-complete (including at least one made from DNA [152,183]), every conceivable pattern could be created with them. *Finding* one automaton and initial conditions to produces a certain pattern, however, is

---

[1]The KOLMOGOROV complexity does not tell us anything about the usefulness of a certain structure, as has been pointed out by Adami [1], but it does allow statements to be made about their fabrication.

challenging.

To be useful as an assembly technique, the effort required for design cannot be excessive. If the goal of the assembly is arranging objects on certain positions of a surface (which could in principle be stored very efficiently as coordinates), this might mean that it is much easier to have a real-space template than particles that contain the positional information. Such a real-space template has binding sites at the right spatial positions, in which the particles will come to sit during the self-assembly process. Self-assembly processes where the information is stored in such a single object are often called templated self-assembly. They barely fit into WHITESIDE's definition of self-assembly, but they are amongst the most popular targets of research today, as they seem to be closest to real applications.

Introducing a template causes a number of practical problems, however, in particular with real-space templates. The binding sites will often interfere with the functionality of the assembled device or material, they are costly to make on every single target, and they might not even be compatible with relevant materials, depending on the assembly process that is to be used. Thus, for templated assembly to be useful, we likely have to introduce a transfer step similar to that used industrially in parallel assembly processes.

Systems with explicit (and inefficient) information storage often are also more robust. This can be a simple consequence of redundancy in its representation. However, a system that is general enough to form very different (perhaps all possible) structures and still store information efficiently tends to be delicate in general, and its error rate can be prohibitive. There is no theory available today to describe such trade-offs quantitatively for realistic physical systems, but we will try to give some qualitative insights in the next section.

2.2 Generality, usefulness and economics

When a material or structure is to be created using a self-assembly or templated assembly process, one has to decide how general, precise and accurate the chosen process has to be and how complex, slow, delicate and (therefore) costly it may be. Precision and low error rate is a very challenging goal when creating nanoscale structures. Statistical effects and the constant thermal excitation necessitate large energy differences to confine a certain state with high precision, as we shall see later more quantitatively. As an alternative (used in biological systems), proofreading systems can be used to constantly correct the error-prone mechanisms, but this introduces large complexity.

Table 2.1 shows the negentropy of different processes that create nanoscale structures. The negentropy is a measure for the number of errors made by a given process, roughly defined as the negative logarithm of the error rate, $S = -\ln(\text{errorrates})$. The table illustrates one of the arguments made in the last chapter: silicon single crystals, which are the starting material in the top-down fabrication of semiconductor integrated circuitry, are orders of magnitude better in quality than the best available "monodispersed" nanocrystals. Those are considerably worse in quality than macroscopic precision-machined parts. It is also clear that naturally occurring systems (included here is the DNA transcription machinery) are roughly as good in quality as integrated circuit components, but they reach this quality by entirely different routes. While IC production is based on freedom of error in every single fabrication step, DNA replication relies on elaborate error-correcting mechanisms.

There exists a general trade-off between the complexity of a self-assembling system (that is, the effort required to design it), the range of structures it can create (that is, its generality), the accuracy and yield

Table 2.1: Measures for the "quality" of various processes, most of them structure-creating, in terms of negentropy, a measure of order. The values were communicated by Steven BLOCK.

Process	$S = -\ln(\text{errorrate})$
Digital computing	> 50
Crystal purity (silicon)	28
Replication (DNA polymerase)	$18 - 23$
IC components	21
Telescope mirror (large)	20
Book typesetting	15
Transcription (RNA polymerase)	$12 - 13$
PCR (Taq polymerase)	12
Precision machining	$9 - 11$
Translation (ribosomes)	$6 - 8$
Human typing (no spell check)	$4 - 7$
Nanoparticle size distribution	≈ 2
Polymer dispersion (typical)	$1 - 2$

that it can produce and the energy differences that it requires. Many of the self-assembly techniques used in this thesis rely on very large energy differences, often based on topography, to provide large accuracy for sub-100 nm particles. Such geometries are formed on templates that control the assembly process in real space. While the templates are reusable, their production requires a high-resolution lithography step. On the other hand, the nanoparticles used here are formed in a controlled crystallization method, where the control of shape and size happens very indirectly through transport limitations and timing, and their quality is consequently worse than the quality of assembly.

Another route to high yield and accuracy in an assembly system that is not too complex is to forgo generality. Many schemes that have been published through the last years form structures at relatively high yield with some accuracy, but they cannot be generalized to other materials or structures. In nature, the "assembly" has evolved simultaneously with the functionality, so that a possible lack of generality is irrelevant. In man-made systems, however, the fabrication is traditionally separated from the actual functionality to make engineering possible. Many of the published schemes therefore suffer from a lack of applicability, i.e., there is no problem that is directly solved by them, and they cannot be adapted to relevant problems, because they are not general enough.

This is the reason for us to go from general, "elegant", perhaps intriguing, self-assembly schemes to more pragmatic ones that use templates. The resulting processes may only solve part of a fabrication problem, but are amendable to relevant problems, say, to fabrication challenges in semiconductor fabrication or the creation of metamaterials. It is also the reason for combining such assembly processes with transfer methods that resemble classical "pick-and-place", precisely because it allows separating assembly from function, as is common for all standard tech-

nologies.

The next section will review some published assembly methods that use such pragmatic approaches, to then discuss which methods we have chosen in this thesis.

2.3 Implementations of parallel assembly

Forces are required for particles to assemble into regular structures. These forces can originate from a template with functional binding sites, from other particles or from a continuous medium they are immersed in. We will review parallelized assembly methods that use different forces in the following and discuss the implications of the respective choices. This review will necessarily be incomplete: the number of publications in the field exploded over the last years. For a more complete overview, the reader should also refer to several reviews published in the field. SHIPWAY et al. provide a general overview over nanoparticle arrays (including their applications) [159]. A general review with an even broader view and more theoretical background is provided by ROLDUGHIN [149]. Many of the templated methods on which we focus below are also covered by [180] and [52]. Finally, surface-tension driven assembly techniques (not only including particle assembly) were reviewed by SYMS et al. [169].

Of the various colloidal interactions, electrostatic charges often cause the longest-ranged forces, but they are not specific to one particle type, and even with complex patterns is it hard to define a certain particle arrangement at high accuracy using charge. Covalent interactions, on the other hand, are very short-ranged, and while they can provide very precise particle arrangement (essentially limited by the surface patterning resolution), their weak particle guiding ability can limit the yield,

as discussed in Chapter 3. Surface-particle linkers that bind covalently on both sides include dithiols, and it has been shown that different particle materials can be adsorbed on different parts of the same surface, depending on the respective functionalization.

In between electrostatic and covalent interactions lies the great variety of supramolecular interactions, and among them interactions between biological molecules, including that of DNA. Not only are such interactions very diverse, so that different types of particles can be functionalized specifically to bind on a specific surface site; their strength also can be tuned to optimize assembly. Here, the problem lies in the synthesis of the linker molecules, which often is challenging and of limited yield, and in the proper tuning of the interactions to actually profit from this investment.

Hydrodynamic forces occur in colloidal suspensions in every assembly and are often a problem, because they tend to destroy the carefully established particle order. They are, however, also very good candidates for establishing order, in particular when combined with proper templates, as we will see.

In the following, we will review how the different colloidal forces mentioned above have been used for the assembly of particles in literature, with a focus on templated assembly methods.

Electrostatic forces. Electrostatic forces can originate from charged self-assembled monolayers, as were used by Tien et al. to arrange charged, top-down fabricated 10-µm gold particles that also were functionalized with charged monolayers [172]. The accuracy of the assembly was limited to a random distribution inside the charged area, and percolation was not reached between the particles.

Charge can be directly injected into some surfaces with scanning pro-

be tips, an effect that has been exploited for assembly as well. Particles with diameters of 290 nm and 50 nm assemble from their suspensions on SPM-written charge patterns in a fluorocarbon electret [129,130]. The arrangement quality is comparable to that obtained with chemically patterned, charged substrates, although the resolution that can be reached is much higher thanks to the SPM tip used for patterning.

When compared to chemical patterning through microcontact printing, a parallel approach, the SPM patterning of charge appears to be a very slow process. BARRY et al. address this issue by patterning silicon surfaces topographically that can then be charged in a single step to "print" a charge on an electret surface. These printed patterns provide the same assembly capability as the SPM-written ones [10].

Electrostatic interactions can be combined with capillary forces to increase the assembly accuracy [2]. Particles are assembled from suspension and then allowed to dry out, and the capillary forces that occur in the wetting film further compact the assembly, beyond the accuracy reached in the above examples.

Electrical fields can, of course, also be created by electrodes with applied potentials. If the particles are then made mobile, for example through vibration, they will follow the gradient and assemble into predefined positions [16]. In the dry phase, such methods are applicable to particles above 1 μm in size, which are not governed by adhesion in their motion.

Actively applied fields can make the assembly process programmable, as O'RIORDAN et al. have demonstrated [139]. Their template attracts 50 μm large LEDs to positions depending on the active electrodes in a process named "Field Configured Assembly". The LEDs are suspended in an organic solvent to avoid electrochemical effects.

A particularly elegant way of creating spatially differing electrical

fields was presented by CHIOU et al., who projected an optical image on a photosensitive surface to modulate the field above it [34]. This field could then arrange particles (or cells) according to a pattern created with a commercially available digital micromirror array.

Electrophoretic forces. Electrophoretic forces occur when particles become polarized in non-uniform electric fields, for example, AC fields. These forces are more complex and tunable than electrostatic forces, because changes in the field characteristics translate into changes in the forces and their direction. A method based on such forces has been patented for the assembly of microfabricated devices already in 1994 [36]. Dielectrophoretic forces are particularly useful for the assembly of wires and other elongated objects which are easily polarized and which have very different polarization frequencies for their different space axes. Assembly is then not only capable of positioning these particles, but can also align them, for example normal to electrodes to connect them.

Along these lines, LEE and BASHIR demonstrated the arrangement of silicon resistors having a diameter of approximately 3.6 µm with both positional and configurational control [108]. The resistors were functionally integrated between two electrodes.

Very much thinner but longer nanowires (8 µm long, but only 350 nm wide) were also arranged between electrodes and then contacted successfully [162]. In all these cases (and later publications on the same subjects) it proved necessary to optimize both electrode designs (which requires new microfabricated templates) and the field parameters (frequency and amplitude, which are easily changed).

Magnetic forces. Closely related to electrical fields are magnetic fields, which have been less frequently used for the assembly of particles, mainly because magnetic fields are harder to create with surface coatings and harder to tune in strength. YELLEN and FRIEDMAN used magnetic biases to assemble and move different magnetic beads in wells. The fields were created by micromagnets (patterned cobalt films) combined with a strong external magnetic field.

Magnetic nanoparticles themselves assemble into superlattices due to their magnetic interactions, and it has been suggested that the structured layers that result might be useable as magnetic recording media [166]. These structures still lack a long-range order, however.

Molecular interactions. Electrostatic forces are the longest-ranged forces that occur in colloidal systems (at moderate ionic strengths), which makes them an obvious and useful choice for particle assembly, but they are not specific beyond the simple positive and negative charge difference. Molecular interactions, from the rather weak hydrogen bonds and supramolecular interactions to very strong covalent bonds, are more specific.

At the lower end of binding energy, David REINHOUDT's group in Twente has introduced β-cyclodextrin functionalities on particles that bind adamantyl groups which can be linked to surface-bound cyclodextrines. When the cyclodextrines are patterned on a surface, e.g. through microcontact printing, particles can be selectively deposited on the desired regions [118]. The interaction strength of these "Molecular Printboards" can be tuned by changing the specifics of the supramolecular interactions.

At the higher end of binding energy, thiol linkers bind strongly to gold surfaces. Monolayers exposing thiol groups can therefore be patterned

to bind gold and other coinage metal particles in specific areas, for example by photolithography, where the areas exposed to UV radiations are oxidized and therefore become non-binding [113]. The patterns thus created are much larger than the particle dimensions, which again leads to random distributions of particles that are limited to well-defined parts of the surface.

Very much smaller assembly patterns can be created using an AFM tip and the local oxidation method developed by Jacob SAGIV's group. Using lines written with this method, LIU et al. were able to arrange very small Au$_{55}$-clusters in linear assemblies, which they contacted electrically [114]. This required sequential writing and was time consuming, but represents one of the highest-resolution particle assemblies demonstrated so far.

Biological molecules and organisms.　Biological systems self-assemble, some of them with very high quality, and both the full organisms and their elements have been used for particle assembly. The simplest approaches use binding proteins, notably the biotin-streptavidin system with its extraordinarily high binding energy, for example to immobilize quantum dots in microcontact printed features [25]. Other systems provide more flexibility, and particularly tempting are DNA oligonucleotides with their ability to very specifically bind oligonucleotides with the complementary sequence. GOTHELF and LABEAN review the diverse work performed in this field [68]. In many cases, researchers use the binding ability of DNA to form repetitive nanostructures that then provide scaffolds to bind DNA-functionalized particles, and some can do so even with control over the position in the scaffold for every particle with a unique DNA sequence [3]. These scaffolds are not very sturdy and have weak long-range order, but they can produce relative arrange-

ments in a unique fashion without a surface-bound template.

Using the DNA binding event for assembly often is an inefficient way of storing assembly information. More efficient is it to use the entire expression mechanism of a cell that produces regular protein structures, and to tailor these structures so that they assemble particles in a desired order. Chaperonins have thus been used to arrange quantum dot arrays that were bound in the protein center [126]. Particles can also be synthesized on proteins, for example in viruses, that have certain structural motives. Others have created particle wires from genetically modified bacteriophages [122].

One of the main problems in using proteins or even full organisms to assemble particles is the large amount of organic material around the final assembly. In some applications, this shell might not be detrimental, but it will generally have to be removed without damaging the particles, which can be challenging.

Hydrodynamic forces. The continuous phase of particle suspensions — often water, sometimes organic solvents — inevitably exert several forces on the suspended particles. Hydrodynamic drag occurs whenever the fluid moves relative to the particles, and the fluid mediates interactions between the particles when they are in close proximity. If gas-liquid interfaces are present, very large capillary forces can occur. Drying processes usually involve such interfaces (with critical point drying methods being the exception), and they very often lead to changes in previously established particle arrangements or destroy created patterns. Many researchers have therefore decided to voluntarily use the capillary forces in dewetting processes for particle assembly.

It has long been known that capillary forces can arrange monodispersed spheres into regular, "colloidal" crystals. Only much later, when

microfabricated structures became available, did researchers use templates to impose an order different from the natural (often hexagonal) one. One of the first approaches was "Micromolding in Capillaries" (MIMIC), where a suspension is placed at the entry of channels in a silicone rubber piece that sits on a substrate. The suspension fills these channels through capillary action, and the suspended (micron or submicron) particles can arrange inside the channels. The stamp is then removed (possibly after additional surface reactions have been performed) and the patterned particles remain on the substrate [92].

Instead of closed channels, the templates can also be surface structures. XIA's group has shown in several articles that the meniscus of a colloidal suspension will deposit particles in certain structures and that the particles will generally form regular shapes inside these structures due to capillary action [186, 192]. Similar effects had been observed in the bulk for emulsions with particles, but XIA and his coworkers were the first to use surface-templated structures arranged through capillary forces.

An at least experimentally similar approach can also arrange very small particles, down to 8 nm, as CUI et al. have demonstrated [40]. They used topographically e-beam patterned polymethylmethacrylate (PMMA) directly as a template, which they immersed into a colloidal suspension, sometimes with, sometimes without wetting contrasts between holes in the template and its surface. GORDON and PEYRADE performed similar experiments with wetting contrasts and showed that 100 nm gold particles arrange inside (larger) holes of a template in a way that suggests capillary effects occur during drying [67].

Instead of topographical features on the surface, pure wetting differences on a flat surface can define particle structures as well. FAN and STEBE show that, during the evaporation of the solvent, microparticles

are almost only deposited on hydrophilic parts [56]. The quality of these assemblies is lower than with topographical templates, however: the energy barriers from the wetting differences are not as large as those due to geometrical constraints.

An extension of this technique is the use of two liquid phases, one of which only wets certain parts of the assembled microparts and substrates [164]. This can be exploited to construct switchable assembly sites, as BÖHRINGER's group has demonstrated [187]. The acting force here is the capillary force of the liquid bridge between object and substrate.

Even in the absence of gas-liquid interfaces, hydrodynamic forces are capable of assembling suitably shaped objects in the micrometer size regime. One of the first self-assembly processes devised for the arrangement of microobjects for electronics was "Fluidic Assembly", based on trapezoidal blocks (fabricated top-down with an anisotropic etch method) that would assemble into oppositely-shaped holes from a slurry deposited on the template [170]. This concept has been adopted by a company, the ALIEN TECHNOLOGY CORPORATION, which extended it to an entire parallelized fabrication concept ("web fabrication") and originally applied it to LED displays. With the advent of LC displays and the subsequent loss of interest for LED displays, ALIEN changed its focus and now fabricates RFID tags. Fluidic Assembly has been extended by multiple researchers, for example through the introduction of ultrasound to allow for smaller particles [89].

Hydrodynamic forces are very versatile for the assembly of particles and objects, they scale well with particle sizes, they are often unavoidable and they are sufficiently complex to provide diverse arrangements, but not too complex to be handled. In this thesis, we use capillarity-based assembly methods extensively together with topographical tem-

plates to create well-defined particle arrangements.

Vibrational sorting and gravitational assembly.   Even before the concept of fluidic assembly was devised, small objects had been sorted, aligned and integrated in industrial processes. One standard process to do so without having to pick and place individual objects is *vibrational sorting*, where the dry objects are placed on a vibrating surface that can rotate and transport them into a defined position [15]. Closely related is *gravitational assembly*, where the same vibrations lend particles sufficient mobility to reach holes in the substrate, where they then are trapped due to their weight. Both methods work only for relatively large particles, and we will use gravitational assembly in this thesis for particles above 10 µm in diameter.

2.4 Particle transfer and SATI

The first approaches to particle integration on surfaces were based on pick-and-place, a method that is still the first choice in industry, because it is simple and general. We have discussed its limitations above, but if small assemblies are sufficient, it is possible to arrange even small particles piece by piece. In a striking example, GARCIA–SANTAMARIA et al. have used robotic manipulation to stack silica particles into photonic crystals [65]. Such heroic deeds notwithstanding, pick-and-place techniques scale badly with critical size even for small numbers of particles. As the particles become smaller, their adhesion to surfaces increases, so that it finally becomes impossible to remove them from the vacuum nozzle, microgripper or tip used for transfer. Researchers working on microgrippers acknowledge this fact [133].

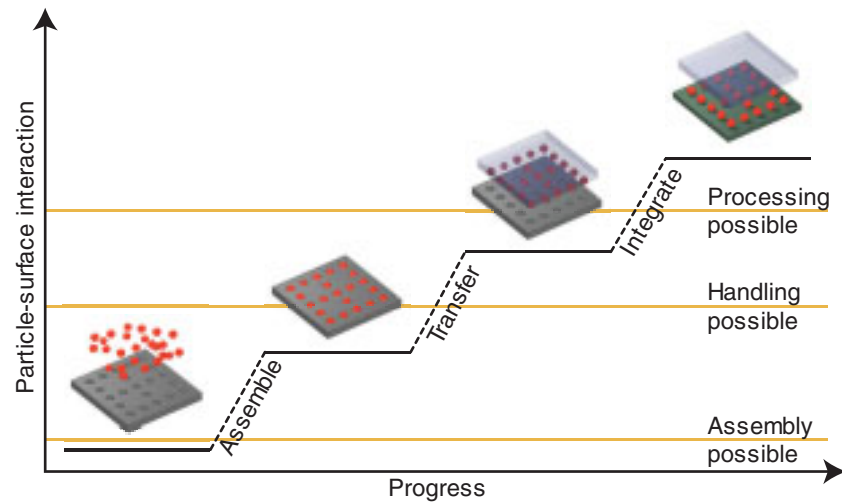A viable alternative is to directly utilize adhesion itself for particle

Figure 2.1: The adhesion cascade that transfers particles in parallel, for example from a self-assembly template to a target substrate. The overall process is termed SATI, for "Self-assembly, transfer, and integration", and will be used throughout this thesis.

handling. If the adhesion of a particle to its original substrate is smaller than to a carrier, it can be picked up passively when both surfaces are in contact with the particle. The carrier with the particles can then be removed and brought into contact with a target substrate. If the adhesion to the target substrate is larger than to the carrier, the particle will be deposited on the target. Overall, an *adhesion cascade* is formed as depicted in Fig. 2.1.

Adhesion-based approaches provide multiple advantages. They make it unnecessary to pick up the particle at a particular position of a gripper or nozzle, because the carrier can hold it anywhere on its surface. The carrier can hold many particles in parallel, only limited by the

carrier area. The handling is passive, so that particle transfer becomes purely a matter of material properties and the process can be very simple. If combined with self-assembly, we obtain a process that arranges the particles in parallel on a specialized substrate to then transfer them in parallel to a target substrate that does not have to sustain assembly. In the following, we will refer such processes as SATI, for "Self-assembly, transfer, and integration".

The challenge now lies in tuning the adhesion. As we will see in Chapter 4, particle adhesion is a complex effect that depends both on geometry and material properties. An adhesion cascade has to provide sufficient adhesion differences to provide large yields, even if particle geometries vary, as they often do in reality. Likewise, contamination layers can dramatically change the very short-ranged VAN DER WAALS forces that usually dominate particle adhesion and have to be avoided.

Despite these difficulties there are multiple industrial processes that rely on adhesive transfer in fields such as chip bumping, placement of small electronic components (surface mounted device, SMD), and generally the integration of objects in incompatible matrices, for example, polymers. The ALIEN TECHNOLOGY CORPORATION holds a portfolio of patents that include the basic "Methods for transferring elements from a template to a substrate" [81], the handling of functional objects ("blocks") with vacuum nozzles, adhesion or other methods [39] and a number of related patents on methods for continuous production [80].

The industrial interest so far is limited to objects well above the one-micrometer size. However, academic research has demonstrated adhesion-based transfer for very small objects. John ROGER's group showed in several articles that top-down fabricated objects, including wires [167] and silicon ribbons [128], can be removed from wafers after fabrication and printed, for example on polymer targets. Their adhesion cascade

is usually formed from differences in contact area and the presence of shear forces, but they have also demonstrated [127] that kinetic effects can be used to control the strength of adhesion and thus create a cascade solely through timing differences.

When particles from a suspension are transferred with a patterned carrier, the overall process is reminiscent of micro contact printing with a colloid as the ink. Some groups have thus printed disordered particle films of colloidal particles [185]. The printing step itself often incurs capillary effects that can be used to introduce some order into the particles which are preferentially deposited at the edges of the stamp's features [33]. If the patterned carrier — the stamp — is not directly inked with a colloid, but from a particle monolayer on a LANGMUIR–BLODGETT trough, the particles inside the printed features will be densely packed, as SANTHANAM and ANDRES show [155]. If the printed particles are gold colloids, such structures are useful matrices for molecular electronics: dithiol molecules will link the particles and create a conductive composite [110].

The inking monolayer does not have to be formed on the gas-liquid interface of a LANGMUIR–BLODGETT trough, it can also be the topmost layer of a colloidal crystal deposited on a hard surface. A carrier can then pick up the uppermost layer and print it onto a target [189]. If the carrier is stretched in the process, the particle spacing can be changed to create other geometries of printed layers [188].

All of the above techniques create large patterns of nanostructured, but uniform particle layers. The next step is now to arrange particles with single-particle resolution and transfer them. This thesis demonstrates how this can be achieved.

3 Particle transport

In this chapter, we will develop a theory of transport phenomena as they occur in directed particle assembly on a surface. This theory will draw heavily on well-established models of colloidal dynamics, and the reader is referred to the excellent monographs that exist on the subject [46, 125, 154]. Some of the questions that arise here relate to engineering problems such as membrane filtration or chemical kinetics, where models similar to those in Section 3.3 are used extensively. Other aspects of the assembly processes, in particular its microscopic details, are reminiscent of problems pertinent to solid-state physics, such as the trapping of charges in lattice defects, or of astrophysics, where the distribution of stellar objects in space is due to gravitational attraction [29]. A complete theory is certainly out of reach, but it might be possible to increase our understanding of the assembly methods used in this work and make predictions on their scalability towards smaller particle sizes.

Treatments of particle dynamics typically start out by assuming very low particle concentrations, so that the effects of particle interactions become negligible. On the other hand, the numbers of particles involved are assumed to be very large, so that Gaussian statistics apply and thermodynamic quantities (e.g. osmotic pressures) can be used to describe their behavior. This is the situation we encounter in molecular self-assembly, where very low concentrations are sufficient to create the extremely thin monolayers, whereas the lateral dimensions of the patterns created are much larger than the particles' (molecular) dimensions. It is then sufficient to work with constant diffusivities and boundary conditions. In Section 3.2, we investigate the diffusion of molecules through a solid matrix, where the transport problem reduces to a pure geometry-dependent diffusion model.

Thermodynamic models describe the behavior of large particle ensembles very well. However, directed particle assembly eventually aims

at the placement of *single particles* or a small number of particles. Thermodynamic models cannot provide detailed insight into the final stage of the process, which involves single-particle trajectories. From a technological standpoint, the single-particle point of view has become interesting only recently, because only very recently did it become possible to fabricate structures on the length scale of the particle diameters. As we start imposing boundary conditions at these scales, we become interested in the particle dynamics at very small scales.

What we are ultimately interested in is the *yield* and the *accuracy* that can be reached in a directed assembly process, depending on particle size and the energy landscape provided in the assembly process. The problem of yield is related to the probability of finding a particle in a specific volume of space at a certain time, and can be discussed in terms of probability densities that translate to concentration distributions. The problem of accuracy is related to the shape of the potential well the particle sits in when trapped at the assembly site.

In Section 3.1.1, we use the bulk values obtained from thermodynamic models in microscopic models to derive statistical expressions for assembly yield and rate. It turns out that in addition to the transport and kinetic limitations that are well known from molecular adsorption, directed surface assembly processes are often affected by statistical effects. As shown in Section 3.1.2, such assembly processes can be limited by the stochastic fluctuations caused by Brownian Motion.

To quantitatively predict yield and accuracy, we have to analyze the magnitude of the forces that direct the particle motion towards a binding site. This drift is opposed by the diffusive motion of the particles, which does not have a preferred direction. The question is now whether the drift can overcome diffusion, that is, whether entropy is overcome by the directing forces. A general formalism for such situations is pro-

vided by the FOKKER–PLANCK equation that describes the probability distribution of particle positions and will be introduced in Section 3.1.3. It will be simplified for dilute particle suspensions and for longer time and length scales to obtain analytical expressions that capture some general properties of particle assembly presented in Section 3.1.4.

One force field commonly used to bias particle motion in directed surface self-assembly is hydrodynamic drag. Predicting the force requires predicting the flow field. In most practical cases involving colloids, it is sufficient to solve the problem of laminar flow, as we do in Section 3.3.1. The flow field then yields a macroscopic particle flux that enters the thermodynamic expressions on a macroscopic scale, and it provides a confining force that will direct single particles to the binding site on a microscopic scale.

Because particles are transported towards some region where assembly takes place, their concentration increases, and so does the chemical potential owing to particle interactions. High concentrations are required in many types of directed assembly if high yield and accuracy are required, and it appears necessary to handle them properly in our model. High concentrations also commonly occur in ultrafiltration, and models which employ a thermodynamic approach exist in the literature: particle interaction potentials are expressed in terms of osmotic pressures, which can be combined with the hydrodynamic flow to produce concentration profiles. Section 3.3.2 uses such a model to derive a convection-diffusion model of particle assembly.

Colloidal stability becomes an issue at higher particle concentrations as well, because kinetic hinderance might be overcome. In this case, the system needs to be thermodynamically stable to prevent agglomeration. The results derived for the concentration-dependent diffusion behavior allow the prediction of ranges of colloidal stability, which we discuss in

a brief excursion in Section 3.3.2.

Returning to the microscopic length scale, we will apply some of the models developed before to the experimental parameters actually used for particle assembly in this thesis in Section 3.3.3. This yields values that can finally be compared with experimental observations in Section 3.3.4.

3.1 Directed particle transport

In directed self-assembly, the final order of particles is defined by the "binding sites" of a template. These binding sites can either actively attract the particles or bind them when they come into contact with the site accidentally. In practice, particle-surface interactions are always of finite length, and for nanoparticles their range is often on the order of the particle diameter. The shape of the potential well formed by these forces depends on the type of force — most commonly, VAN DER WAALS type, hydrophobic, electrostatic or hydrodynamic interactions — and on the process parameters.

Directed surface self-assembly can be seen as an adsorption process in which only parts of the surface are adsorbing and where the adsorbates can be as large as the adsorbing areas. Its kinetics should be similar to conventional adsorption. It is interesting to know how the properties of the binding sites are related to yield, accuracy, and assembly rate for different colloid systems. We will develop general expressions to describe kinetics and accuracy in the following sections.

3.1.1 Assembly isotherms

Particle concentration, assembly yield and assembly speed can be connected through an expression analogous to an adsorption isotherm in molecular adsorption. We follow LANGMUIR's familiar approach for adsorption [106] and model such an "assembly isotherm" assuming that

1. All binding sites on the template are equivalent,

2. Assembled particles do not affect other sites or adsorbed particles,

3. The assembly mechanism is identical for all sites,

4. Only one particle can be adsorbed per assembly site.

In addition, we assume that the binding sites are perfect traps, that is, assembled particles never leave their sites. The probability for capturing is then proportional to the fraction of unoccupied binding sites, $(1 - \theta)$, and so is the rate of assembly:

$$\frac{\mathrm{d}\theta}{\mathrm{d}t} = C(1 - \theta). \tag{3.1}$$

The constant C is proportional to the concentration if we neglect any particle interactions, and it includes a term that characterizes the number of collisions per unit time which occur between particles and the surface. One way to estimate the collision frequency would be to use the flux J_s from FICK's first law of diffusion for a gradient in the concentration c,

$$J_s = -D\nabla c, \tag{3.2}$$

where the diffusion coefficient D can be the STOKES–EINSTEIN diffusion coefficient [53],

$$D_0 = \frac{k_B T}{6\pi\eta a}. \tag{3.3}$$

The diffusion constant (and thus, the flux) is then proportional to the temperature T, BOLTZMANN's constant k_B, the reciprocal viscosity η and the reciprocal particle radius a. This estimate assumes, however, that the surface is a sink (and not a reflecting boundary, as it is in most cases); it also assumes that the fixed-step random walk in three dimensions is a good model for the surface collisions, which is unlikely. A better expression for the collision frequency can be derived from an expression by SCHURR [157], which assumes a MAXWELL–BOLTZMANN velocity distribution for the particles and can be simplified to yield the flux onto the surface

$$J_s = c_s \sqrt{\frac{k_B T}{2\pi M}} \qquad (3.4)$$

for particles having a concentration close to the surface c_s and a mass M. It is possible to derive this flux in a way that also takes into account particles that enter a certain volume around the binding sites, which we will do in the next section.

We can now insert the proportionality constant into Eq. (3.2), which then becomes

$$\frac{\mathrm{d}\theta}{\mathrm{d}t} = A_{bs} J_s (1 - \theta), \qquad (3.5)$$

where A_{bs} is the total area of the binding sites. This differential equation is easily solved by separation of variables to give

$$\theta(t) = 1 - \mathrm{e}^{-A_{bs} J_s t}. \qquad (3.6)$$

Diffusion limitations. This isotherm is a very crude representation of the actual situation, although it has the advantage of being well known from the field of surface adsorption. It does not consider the transport of particles from the liquid to the surface, which will change the local concentration (and, thus, the surface flux). In directed assembly, the

targeted particle density might vary, so that the transport situation is heterogeneous. If the density of binding sites on the surface is high, the colloid might be depleted of particles during the assembly. Particles then have to diffuse from the bulk suspension with a concentration c_c towards the surface with a concentration c_s directly above the surface. It might be that the assembly process is not the limiting step because the process is diffusion controlled. We shall develop a criterion for this limitation in the following.

The standard way of checking for a diffusion limitation is to compare the characteristic time scales of the particle flux to the surface caused by the assembly process to the diffusion time scale [18]. We have to be aware, however, that such comparisons rely on bulk diffusion constants, while we often have small numbers of particles here, in particular when assembling from low concentrations onto templates with dense binding sites. A rigorous treatment would require the FOKKER–PLANCK equation to be solved with proper boundary conditions. We will come back to this point later.

The time scale for the diffusion across a given length l_{diff} is

$$\tau_{\text{diff}} = \frac{l_{\text{diff}}^2}{D}. \tag{3.7}$$

This characteristic length δ can be a hypothetical depletion layer thickness. It is common to use the surface concentration after half the binding sites are saturated, $c_a/2$, to calculate it as

$$\delta_{1/2} = \frac{c_a/2}{c_c} \tag{3.8}$$

with the bulk colloid concentration c_c. A characteristic time for the dif-

fusion is then

$$\tau_{\text{diff}} = \frac{c_{\text{a}}^2}{4c_{\text{c}}^2 D} \tag{3.9}$$

which should be compared to the time that it takes (according to the kinetic expressions of above) to assemble in half the sites.

Confined transport. Equation (3.2) also does not take into account geometrical confinement that might keep particles close to the surface, rendering the notion of a surface flux inapplicable. The confinement might be geometrical or due to additional, long-ranging forces. It is difficult to describe such situations with bulk equilibrium concepts. Instead, we introduce here a concept that also becomes useful later to describe small-number statistics: the random walk.

Random walks are a popular model for Brownian Motion and the basis for a family of numerical methods widely used today for the simulation of fluctuating systems [125]. It is often hard to predict averages of variances for a random walk with certain parameters, in particular if boundary conditions are imposed. However, it is often possible to give limits for important properties. A particularly useful model for directed surface assembly is the random walk with traps that has been used first by ROSENSTOCK to model optical adsorption phenomena [150].

If we consider a single particle on a plane that is performing a random walk (due to Brownian Motion, but observed at a coarse scale), and if there are randomly distributed binding sites of a density c present on this plane, we can calculate the average number of steps in the random walk which it takes the particle to "find" one of these sites, i.e., to be bound. If we take the diameter of the binding site, d_{b}, as the average length of one step, we may find an absolute lower bound for the time this takes.

The mean lifetime of a particle, $\overline{\langle N^\dagger \rangle}$, is the number of steps it makes before being absorbed, averaged both over different walks it might take and over different distributions of binding sites. The probability ϕ_n of surviving at least n steps is related to the probability W of a specific lifetime of n steps as

$$W(N^\dagger = n) = \phi_{n-1} - \phi_n \tag{3.10}$$

which leads to a relationship for the mean lifetime

$$\overline{\langle N^\dagger \rangle} = \sum_{n=1}^{\infty} n(\phi_{n-1} - \phi_n) = \sum_{n=0}^{\infty} \phi_n. \tag{3.11}$$

We can produce a lower bound for the mean lifetime [44] if we take into account that the number of distinct sites visited after n steps, R_n, is always smaller than the total length of the walk,

$$R_n \leq n + 1. \tag{3.12}$$

Because the probability of surviving must always be larger than the fraction $(1 - q)$ of non-binding sites visited, it is

$$\phi_n = \langle (1 - q)^{R_n} \rangle \geq (1 - q)^{n+1} \tag{3.13}$$

and we can state very generally that

$$\overline{\langle N^\dagger \rangle} \geq \sum_{n=0}^{\infty} (1 - q)^{n+1} = \frac{1 - q}{q}. \tag{3.14}$$

This is a simple result and quite general, but the random walk has its own problems for the modeling of surface adsorption. First of all, if multiple particles are involved, the number of binding sites decreases while

other particles still are searching. This leaves intact the upper limit of 3.14, but makes it even more crude an estimation. There is also no obvious choice for the step length. However, the limit used here is probably robust enough to hold for a wide choice of step lengths.

We can convert the lifetime of the particles to real time using the EINSTEIN expression in a plane for the diffusion of particles along a length s in a time t with a friction coefficient χ averaged across many particles [53],

$$\overline{s^2} = 4Dt = \frac{4kT}{\chi}t. \tag{3.15}$$

The step site of the random walk above might be taken as the particle diameter, d_p, so that the binding sites are assumed to be just as large as the particles. If we have enough particles to fill every site (but not more), a lower bound for the single-particle assembly time is

$$t_a \geq \overline{\langle N^\dagger \rangle} \frac{d_p^2}{4D} \geq \frac{\theta}{1-\theta}\frac{d_p^2}{4D}, \tag{3.16}$$

with the limit of Eq. (3.14).

Let us transfer this result to large particle assemblies. If all particles in the ensemble are captured after a time t_a, the assembly rate r_a will be inversely proportional to this time and proportional to the number of particles N, $r_a = N/t_a$, and we can use it in Eq. (3.1) to define the rate of change in the number of occupied sites:

$$\frac{d\theta}{dt} = \frac{N}{t_a} \tag{3.17}$$

The average lifetime t_a depends on the concentration of binding sites on the template which changes with time according to

$$q(t) = q_0(1 - \theta), \tag{3.18}$$

and if we combine this with Equations (3.17) and (3.16), we obtain a kinetic expression

$$\frac{d\theta}{dt} \leq \frac{q_0(1-\theta)}{1 - q_0(1-\theta)} \frac{4D}{d_P^2} N. \tag{3.19}$$

This is hard to solve in closed form, but can be expressed in terms of LAMBERT's Ω function, which is defined by[1]

$$z = \Omega(z)e^{\Omega(z)}. \tag{3.20}$$

The solution then reads

$$\theta \leq \Omega\left(q_0 e^{-\tilde{t}q_0 - q_0 - C_1 q_0}\right)/q_0 + 1, \tag{3.21}$$

where $\tilde{t} = t \times 4DN/d_P^2$ is the dimensionless time and C_1 a constant which has to be chosen such that $\theta(\tilde{t} = 0) = 0$. It is often not realistic to assume that N remains constant. In general, the assembly will deplete the particles on top of the template. In the extreme case, no new particles are transported towards the surface, which changes Eq. (3.19) to

$$\frac{d\theta}{dt} \leq \frac{q_0(1-\theta)}{1 - q_0(1-\theta)} \frac{4D}{d_P^2} N_0(1-\theta), \tag{3.22}$$

which is solved by

$$\theta \leq e^{\Omega\left(e^{-\tilde{t}'-C_2/q_0}\right)+q_0}/q_0, \tag{3.23}$$

where the dimensionless time now is $\tilde{t}' = t \times 4DN_0/d_P^2$ and the constant C_2 has to be chosen such that $\theta(\tilde{t}' = 0) = 0$.

---

[1] Numerical values for this function are now included in most computer algebra systems, e.g., in MAPLE.

Imperfect binding sites. So far we have assumed the binding sites to be perfect traps. Particles are captured exactly when they hit the site anywhere inside its area. In reality, there is a finite time required for the particle to adhere on the site, and if it moves away from the site too quickly (perhaps due to Brownian Motion), it will not be assembled. Such a behavior can be introduced in the above models through a stiction coefficient that gives the probability for a particle to be adsorbed at a given site [88]. Likewise, the random walk can be analyzed under the assumption of imperfect traps [76].

An unusual limiting effect occurs with assembly methods that have short sampling times, where only those particles are assembled that are present in a certain volume at a specific point in time. This is due to fluctuations that generally occur in strongly stochastic systems. Such fluctuations are a general and important feature of microscopic small-number systems. The next section will discuss them in detail.

3.1.2 Fluctuations in the small-number limit

Statistical fluctuations occur when the number of particles that determines a quantity becomes small. A common example in electronics and photonics is shot noise, a type of noise that occurs when the number of electrons or photons becomes small. The signal-to-noise ratio for shot noise is the square root of the number of particles [145].

A similar effect occurs in particle assembly when the number of particles to be assembled per site is small, so that the sampling volume from which the particles are captured contains only small numbers of particles. The assembly yield is then related to the magnitude and the frequency of concentration fluctuations in a given colloid volume, first treated by SMOLUCHOWSKI in 1916 [176].

For large numbers of particles, Gaussian distributions are a good approximation of the particle statistics. Their exact behavior, however, is according to POISSON statistics, which have to be used when small numbers of particles are to be considered (an elegant derivation of this fact is given by CHANRADSEKHAR [29]). For example, the probability W of finding n particles in a given volume V_c (part of a much larger volume of the same colloid)is given by

$$W(n) = \mathbf{e}^{-\nu} \frac{\nu^n}{n!},\qquad(3.24)$$

where ν is the average number of particles in this volume that simply depends on the bulk concentration c_c,

$$\nu = \langle n \rangle = c_c V_c.\qquad(3.25)$$

Notice that the probability is a function only of the average number of particles and independent of all other properties of the colloid. This allows a very general statement on the maximum yield that can be reached in an ensemble of assembly sites. The immobilization of a single particle in a capture site of the template can be modeled by assuming that any particle from a certain volume V_c above this site will be captured (Figure 3.1). We can sum up the probabilities of finding an arbitrary number of particles from Eq. (3.24),

$$W(n \geq 1) \approx \sum_{n=1}^{\infty} W(n) = 1 - \mathbf{e}^{-\nu}.\qquad(3.26)$$

This is the probability of finding at least one particle in a given assembly site at a certain point in time. When we now consider a large ensemble of binding sites, this directly translates into the yield. Thus, we can state
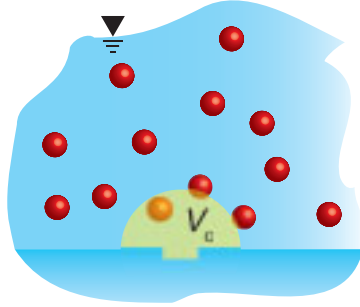
Figure 3.1: The capture volume V_c of the assembly process. All particles in this volume (and only those) will be assembled in the process.

that the minimum concentration required to achieve a certain assembly yield γ is

$$c_c \geq -\ln(1-\gamma)/V_c. \tag{3.27}$$

For example, the minimum concentration that guarantees a 90% yield across many capture sites is $c_c \geq 2.3/V_c$, which is large when compared with common colloidal concentrations. This expression always underestimates the number of particles actually required, because the assembly volume is of finite size, and the sum in Eq. (3.26) should only extend to the maximum number of particles that fit into it. Particles are also often stabilized, which introduces a repulsive charge that reduces the probability of having additional particles in the volume. The error made in this summation is not very large, however, because of the exponential decay of the contributions.

In many assembly processes, particles interact with the binding sites for a longer period of time. This affects the yield only when the interaction time exceeds the time scale of fluctuations in the system. If so, a

binding site might capture a particle that only enters V_c after some time, and the yield will increase with time and finally reach unity.

It is possible to calculate the time scale of fluctuations in the number of particles inside V_c. We start again with the POISSON distribution in Eq. (3.24), but now we search the probability for a certain number of particles entering (or leaving) this volume in a given time τ. Let us assume that there is a probability P for a given particle to leave the volume V_c during this time τ. Along the lines of the derivation at the beginning of Section 3.1.1 and following SMOLUCHOWSKI [176], we also assume that

1. Particles do not interact,

2. The distribution of particles is uniform over the entire volume.

The probability for i of the original n particles leaving this volume is then[2]

$$A_i^{(n)} = \binom{n}{i} P^i (1-P)^{n-i} = \frac{n!}{i!(n-i)!} P^i (1-P)^{n-i}. \qquad (3.28)$$

The probability of particles entering this volume has to be identical to that for leaving the volume in order to create a stable equilibrium state. Because the number of particles entering the volume is independent of the number already contained in V_c, we need to average over all n:

$$E_i = \langle A_i^{(n)} \rangle = \sum_{n=i}^{\infty} W(n) A_i^{(n)} = \frac{e^{-\nu P}(\nu P)^i}{i!}. \qquad (3.29)$$

It is now a matter of algebra to calculate the average change in particle

---

[2]The original paper of SMOLUCHOWSKI [176] contains a typographical error in this equation.

numbers during a time τ when starting from $n(t)$ particles[3]:

$$\langle n(t) - n(t+\tau) \rangle = (\nu - n)P, \tag{3.30}$$

or, averaged over all possible $n(t)$, a mean square difference of

$$\langle (n(t) - n(t+\tau))^2 \rangle = 2\nu P. \tag{3.31}$$

The probability P, introduced to encapsulate all system-dependent effects, can be calculated either using methods introduced in the next section (which would also allow considering the effect of biasing fields) or, much more easily, when assuming that the diffusion equation described the particle's behavior. We can then use EINSTEIN's result [53] for the probability of a particle to move from $\vec{r}_1$ to $\vec{r}_2$,

$$(4\pi Dt)^{-3/2} e^{-|\vec{r}_2 - \vec{r}_1|^2/(4Dt)}. \tag{3.32}$$

The probability for a certain particle to move out of the volume V_c during the time τ then follows from integrating

$$P = \frac{1}{(4\pi D\tau)^{3/2} V_c} \int \int e^{-|\vec{r}_2 - \vec{r}_1|^2/(4D\tau)} d\vec{r}_1 d\vec{r}_2. \tag{3.33}$$

The first integration, that over $\vec{r}_1$, includes all points inside the volume V_c, while the second integration, that over $\vec{r}_2$, includes all points outside V_c. This can be rewritten (following [29]) so that both integrations only

---

[3]Or, as SMOLUCHOWSKI put it: "Aus diesen komplizierten Formeln lassen sich mittels verwickelter Summationen merkwürdigerweise recht einfache Resultate für die durchschnittliche Änderung der Teilchenzahl ableiten..."

include points inside V_c,

$$1 - P = \frac{1}{(4\pi D\tau)^{3/2} V_c} \int_{\vec{r}_1 \in V_c} \int_{\vec{r}_2 \in V_c} \mathbf{e}^{-|\vec{r}_2 - \vec{r}_1|^2/(4D\tau)} \mathrm{d}\vec{r}_1 \mathrm{d}\vec{r}_2. \qquad (3.34)$$

For a general assembly site it seems appropriate to assume a hemispherical capture volume V_c. We transform Eq. (3.33) to spherical coordinates and perform both integrations over a full sphere, which provides double the sought probability,

$$2P = \frac{1}{(4\pi D\tau)^{3/2} V_c} \int_\varphi \int_\psi \int_{r_2} \int_\varphi \int_\psi \int_{r_1} \mathbf{e}^{-\frac{(r_2 - r_1)^2}{4D\tau}} r_1^2 \sin\psi \mathrm{d}r_1 \mathrm{d}\psi \mathrm{d}\varphi \, r_2^2 \sin\varphi \mathrm{d}r_2 \mathrm{d}\psi \mathrm{d}\varphi, \qquad (3.35)$$

where the inner integration is done over the volume of the sphere and the outer over the entire space without the sphere. A change in coordinates,

$$r \longrightarrow \xi \cdot 2\sqrt{2D\tau}, \qquad (3.36)$$

and performing the integrations over the angles somewhat simplifies the integral, finally to

$$2P = \frac{12}{\sqrt{\pi}\xi^3} \int_\xi^\infty \int_0^\xi \mathbf{e}^{-(\xi_2 - \xi_1)^2} \xi_1^2 \xi_2^2 \mathrm{d}\xi_1 \mathrm{d}\xi_2, \qquad (3.37)$$

but I was still unable to find a closed expression for the second volume integration (the first one yields a lengthy expression including error functions). It is relatively simple, however, to integrate the resulting expression numerically, in particular if the integration boundaries are changed such that

$$2(1 - P) = \frac{12}{\sqrt{\pi}\xi^3} \int_0^\xi \int_0^\xi \mathbf{e}^{-(\xi_2 - \xi_1)^2} \xi_1^2 \xi_2^2 \mathrm{d}\xi_1 \mathrm{d}\xi_2. \qquad (3.38)$$
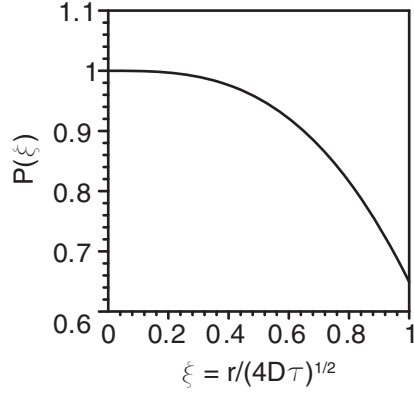
Figure 3.2: Numerically evaluated probability after-effect factor as defined by Eq. (3.38). The integration was performed using MAPLE's finite difference implementation.

This expression is numerically evaluated in Fig. 3.2.

From the above follows a characteristic time scale of the fluctuations. If the interaction time of the binding site exceeds this time scale, the assembly probability increases. It is not easy to extend the above model to predict this increase, because its central arguments are based on stable long-term averages. However, we can use a standard approach from signal theory [145] and interpret the particle flux through the surface of the capture volume V_c statistically. Assuming that SCHURR's Equation (3.4) for the flux through a surface,

$$J_s = c_c \sqrt{\frac{k_B T}{2\pi M}},$$

(3.39)

holds for this case, there will be a time-averaged flux through the surface

$$\Theta = J_s A_c,$$

(3.40)

where A_c denotes the surface of the capture volume. This flux will be small in general. In analogy to rare events in a signal, the probability of *n* particles crossing the boundary of the binding volume during a time τ will therefore follow the expression

$$P_\tau(n) = \mathbf{e}^{-\Theta\tau} \frac{(\Theta\tau)^n}{n!}, \tag{3.41}$$

a POISSON distribution. As before, we can sum here over all *n*, slightly overestimating the yield, to arrive at an assembly probability for a time τ:

$$P_\tau(n \geq 1) \approx \sum_{n=1}^{\infty} \mathbf{e}^{-\Theta\tau} \frac{(\Theta\tau)^n}{n!} = 1 - \mathbf{e}^{-\Theta\tau}. \tag{3.42}$$

This corresponds to the time-dependent increase in assembly probability, and can be added to the original (equilibrium) probability from above.

Neither the diffusive flux nor the integral that we use to compute *P* here hold if external force fields are present. The entire treatment from above also does not provide the variations of particle positions. For such questions it is useful to obtain probability density functions of the particle positions. The required formalism will be introduced in the next chapter.

3.1.3 Particles diffusing in force fields

Let us first consider a single particle moving in a fluid under the influence of a force field formed by a single binding site. The particle suffers a force caused by the motion of the fluid molecules, which is unknown, but assumed to be entirely stochastic with a Gaussian distribution. This force alone would lead to entirely undirected, *diffusive* motion of the particle, and we assume here that after a long time this particle will visit

every point of the fluid volume (that is, we assume the particle to be ergodic, as is commonly done). In addition, there exists a force field $K(x)$ which is constant in time and superimposes a *drift* on the particle. The presence of the stochastic component precludes a prediction of the actual trajectory of the particle's motion, but it is possible to predict the probability density function (pdf) of the particle's coordinates in phase space. The evolution of this function $p(x,t|y,0)$ from a certain original state is described by the FOKKER–PLANCK equation

$$\frac{\partial p(x,t|y,0)}{\partial t} = -\frac{\partial}{\partial x}\left(\mathcal{A}(x)p\right) + \frac{\partial^2}{\partial x^2}\left(\mathcal{B}(x)p\right), \qquad (3.43)$$

where $\mathcal{A}(x)$ is the drift vector, describing the effect of the force on (for example) particle position x and velocity u, while $\mathcal{B}(x)$ is the diffusion tensor, describing the stochastic part of (say) particle position and velocity [125]. Both can be expressed by correlation functions of the respective parameters for short times:

$$\mathcal{A}(x) = \begin{pmatrix} \mathcal{A}_x \\ \mathcal{A}_u \end{pmatrix} = \lim_{\Delta t \to 0} \frac{1}{\Delta t}\int (x-z)p(x,\Delta t|y,0)\mathrm{d}z, \qquad (3.44)$$

$$\mathcal{B}(x) = \begin{pmatrix} \mathcal{B}_{xx} & \mathcal{B}_{xu} \\ \mathcal{B}_{uu} & \mathcal{B}_{ux} \end{pmatrix} = \lim_{\Delta t \to 0} \frac{1}{\Delta t}\int (x-z)^2 p(x,\Delta t|y,0)\mathrm{d}z. \qquad (3.45)$$

These parameters capture the physical properties of the system; for moving particles, they are described by the respective equations of motion. An equation of motion that includes stochastic forces is the LANGEVIN equation, which has the general form (for any stochastic variable ξ)

$$\frac{\mathrm{d}\xi}{\mathrm{d}t} = h(\xi,t) + g(\xi,t)\Gamma(t) \qquad (3.46)$$

where h and g are arbitrary functions, while $\Gamma(t)$ is a (Gaussian) random variable with vanishing mean and a delta correlation function. For a moving particle, a typical LANGEVIN equation would be

$$M\frac{\mathrm{d}u}{\mathrm{d}t} = -\chi u + K(x) + F(t) \tag{3.47}$$

$$\frac{\mathrm{d}x}{\mathrm{d}t} = u, \tag{3.48}$$

which explicitly include the friction constant χ and the particle mass M, the external force $K(x)$, and the stochastic force $F(t)$. This ordinary stochastic differential equation is solved to a first order by

$$x(t + \Delta t) = x(t) + u(t)\Delta t \tag{3.49}$$

$$u(t + \Delta t) = u(t) - \frac{\chi}{M}u(t)\Delta t + \frac{K(x(t))}{M}\Delta t + \frac{1}{M}\int_t^{t+\Delta t} F(s)\mathrm{d}s. \tag{3.50}$$

The LANGEVIN equation in principle defines the diffusion and drift coefficients, although there are some subtle questions involved (technically speaking, the difference between ITÔ and STRATONOVIC integration) which we will not address here (see e.g. [148]). When using the STRATONOVIC definition and only regarding the particle position, diffusion and drift depend on the factors in the LANGEVIN equation according to

$$\mathcal{A}(x,t) = h(x,t) + \frac{\partial g(x,t)}{\partial x}g(x,t) \tag{3.51}$$

$$\mathcal{B}(x,t) = g^2(x,t). \tag{3.52}$$

We can either use these expressions or directly use the first-order solution (which also describes the particle velocity) to find the FOKKER–

PLANCK coefficients, yielding

$$\mathcal{A}_x = u \tag{3.53}$$

$$\mathcal{A}_u = -\beta u + \frac{K(x)}{M} \tag{3.54}$$

$$\mathcal{B}_{uu} = \frac{2k_B T \beta}{M}, \tag{3.55}$$

with a parameter $\beta = \chi/M$, while all other components of $\mathcal{B}$ vanish. Together with Eq. (3.43) we arrive at

$$\frac{\partial p}{\partial t} + \vec{u} \nabla_{\vec{x}} p = \beta \nabla_u \left(\vec{u} - \frac{K}{\chi} + \frac{k_B T}{M} \nabla_{\vec{u}} \right) p \tag{3.56}$$

which was found, independently, by KLEIN and KRAMERS [99]. This result is in vector notation, but the scalar derivation given above is identical to that for the vector form. While the equation is already useful, it cannot be solved in closed form. It describes the particle motion for the case that not only the particle positions, but also the particle velocities are far from their equilibrium distributions. In many cases of interest — including directed particle assembly — the distribution of the velocity is very close to equilibrium, and we are in any case mainly interested in the particle positions. It can be shown [125] that if the particle motion can be separated into a fast and a slow component, and if we are only interested in the slow one, the LANGEVIN equation can be taken to be

$$0 = -\beta u + K(x) + F(t) \tag{3.57}$$

$$\frac{dx}{dt} = u, \tag{3.58}$$

with the simpler first-order solutions

$$\mathcal{A} = K(x) \tag{3.59}$$

$$\mathcal{B} = \frac{k_B T}{\chi} \tag{3.60}$$

so that Eq. (3.56) reduces to

$$\frac{\partial p'}{\partial t} + \frac{1}{\chi}\frac{\partial K p'}{\partial x} = \frac{k_B T}{\chi}\frac{\partial^2 p'}{\partial x^2}, \tag{3.61}$$

the SMOLUCHOWSKI equation. Notice that the velocity probability density function is not described by the above — we have assumed it to follow an equilibrium distribution.

Particle in a constant force field. Directing forces increase the concentration locally and bias the particle motion towards the binding sites. The simplest force field is constant, as is the gravitational force field,

$$K(x) = Mg, \tag{3.62}$$

so that the LANGEVIN equations become

$$M\frac{\mathrm{d}u}{\mathrm{d}t} = -\chi u + Mg + F(t) \tag{3.63}$$

$$\frac{\mathrm{d}x}{\mathrm{d}t} = u \tag{3.64}$$

and the short-term correlations of the variables yield

$$\langle x \rangle = x_0 + \frac{Kt}{M\beta} - \frac{1}{\beta}\left(u_0 - \frac{K}{M\beta}\right)\mathbf{e}^{-\beta t} \tag{3.65}$$

$$\langle (x - \langle x \rangle)^2 \rangle = \frac{KT}{M\beta^2}(2\beta t - 3 + 4\mathbf{e}^{-\beta t} + \mathbf{e}^{-2\beta t}). \tag{3.66}$$

The distribution of the velocities follow a similar analytic expression. It is possible to solve the FOKKER–PLANCK equation (3.43) for this system,

$$\frac{\partial p}{\partial t} = -\frac{\partial}{\partial x}(up) + \frac{\partial}{\partial u}(\beta u - K)p + D\frac{\partial^2 p}{\partial u^2}, \tag{3.67}$$

by Gaussian distributions for all variables, with the means and variances given above.

Notice how the particle mobility influences its reaction to the external force: β can be interpreted as a measure of the particle reaction to an external force, and it appears both in the time-linear term in $\langle x \rangle$ and is the time constant in its memory term, where it describes the rate of exponential decay of the particle's "memory". The average particle position does not converge with time, because we have not imposed any boundary conditions. The drift will move the particle further indefinitely. It is not easy to obtain a solution of this KRAMERS–KLEIN-type equation with a reflecting boundary condition at $x = 0$, and I am not aware of a closed expression for the resulting distribution. For the stationary case, however, WANG and UHLENBECK suggest [132] that the unique result is the barometric distribution[4] (for both velocity and position) with a constant C,

$$P(x, u, t = \infty) = C\mathbf{e}^{-\frac{\beta}{2D}u^2 - \frac{g\beta}{D}x}, \tag{3.68}$$

---

[4]The monograph of RISKEN [148] includes a general formalism to derive such stationary solutions for a large class of FOKKER–PLANCK equations.

in a gravitational force field.

The standard deviation of the particle position is directly connected to the assembly accuracy; however, the case of unbounded diffusion with a force field is not a reasonable situation for particle assembly. The time-independent prefactor shows that the standard deviation is proportional to temperature and to the force field (which is not intuitive), but the situation will of course change for particles that are bound to a certain position, as we will see next.

The bound particle. A binding site that is to confine the particle to a certain position will often exert a force on the particle that is directed towards the desired position. This might, for example, be a linear restoring force

$$K = -\omega^2 x \tag{3.69}$$

with a frequency ω. The LANGEVIN equations are then

$$\frac{\mathrm{d}u}{\mathrm{d}t} = -\beta u - \omega^2 x + \frac{1}{M} F(t), \tag{3.70}$$

$$\frac{\mathrm{d}x}{\mathrm{d}t} = u, \tag{3.71}$$

and the FOKKER–PLANCK equation

$$\frac{\partial p}{\partial t} = -\frac{\partial}{\partial x}(up) + \frac{\partial}{\partial u}((\beta u + \omega^2 x)p) + D\frac{\partial^2 p}{\partial u^2}. \tag{3.72}$$

The latter equation can be solved using a change of variables, FOURIER transformation and a set of auxiliary ordinary differential equations [125]. It turns out that the solutions are Gaussian distributions. With this knowledge we can avoid the cumbersome derivation of the solution and compute the means and moments of the distribution directly from the LAN-

GEVIN equations. This is possible both for the particle velocities and their positions, but we will limit ourselves to the positions here.

Following MAZO [125], we introduce the frequency

$$\omega_1^2 = \omega^2 - \frac{\beta^2}{4} \tag{3.73}$$

which indicates whether the particle motion is overdamped (for real values of ω_1), periodic (for imaginary values of ω_1) or aperiodic (if ω_1 vanishes). The moments of the Gaussian distributions depend on the present case. If we allow for trigonometric functions with complex arguments[5], they are described for all cases by

$$\langle x \rangle = \mathbf{e}^{-\beta t/2} \left(x_0 \left(\cos \omega_1 t + \frac{\beta}{2\omega_2} \sin \omega_1 t \right) + u_0 \frac{\sin \omega_1 t}{\omega_1} \right) \tag{3.74}$$

$$\langle (x - \langle x \rangle)^2 \rangle = \frac{\mathcal{D}}{\beta \omega_0^2} \left(1 - \frac{\mathbf{e}^{-\beta t}}{\omega_1^2} \left(\omega_1^2 + \frac{1}{2} \beta^2 \sin^2 \omega_2 t + \beta \omega_1 \sin \omega_1 t \cos \omega_1 t \right) \right) \tag{3.75}$$

with a constant $\mathcal{D}$ similar to the diffusion constant but not identical to it,

$$\mathcal{D} = \frac{kT\beta}{M}. \tag{3.76}$$

The average particle position converges to the origin, as expected, and the convergence is oscillatory unless the motion is overdamped. Meanwhile the standard deviation of the position converges to $\lim_{t \to \infty} \langle (x - \langle x \rangle)^2 \rangle = k_B T / \omega^2$ (in concordance with the equipartition theorem), and it does so in a time that is again set by β.

---

[5]CHANDRASEKHAR [29] introduces all three cases separately, but it is common today to define the trigonometric functions such that they yield their hyperbolic equivalent for imaginary arguments, which simplifies notation.

3.1.4 Limits of yield and accuracy

With the results obtained so far, we can make some statements on the yield and accuracy of directed surface-assembly processes. Very generally, if an assembly process only makes a "snapshot" of the situation at a time t, so that only particles are assembled that are present in a certain volume V_c at that point in time, its yield γ cannot exceed

$$\gamma \leq 1 - e^{-cV_c}. \tag{3.77}$$

If the number of binding sites is small, the actual yield will also fluctuate with a standard deviation that is dependent on the number of sites. There are only two parameters that can increase the yield: the capture volume V_c (which generally will be hard to increase, for it depends on the assembly mechanism itself) and on the local concentration c. Increasing this concentration requires a force field and time. From Eq. (3.68) we know that the increase in probability density for a particle in a gravitational field is proportional to

$$p \sim e^{-\frac{g\beta}{D}x}. \tag{3.78}$$

To convert this probability into a concentration increase, we have to assume a certain limiting concentration (dense packing, for example) and multiply it by this probability. One could derive such expressions for different force fields and integrate to get an average concentration increase. This would lead us too far here, however. We will perform a related calculation for a hydrodynamic field in Section 3.3.2.

If we have binding sites that do not only capture the particles that are inside V_c at one point in time, but capture any particle that enter V_c during a certain period of time (of the duration τ) that is longer than the

fluctuations in the colloid, the assembly yield increases by

$$\gamma \leq 1 - \mathbf{e}^{-\Theta\tau}. \tag{3.79}$$

When τ is very long $\tau \to \infty$, the assembly approaches perfect yield. This increase is system-dependent, it depends on the geometry of the binding site and the diffusion constant D.

Once a particle is trapped successfully, the question arises as to how accurately it is held at a certain position. Again, two different situations occur, the first for assembly mechanisms that freeze the particle to its position in V_c at a certain point in time, the second for assembly mechanisms that exert a force on the particle for a certain time which drags them to its desired position. The first situation is rather unusual, and it leads to a standard deviation in the particle position that depends on the geometry of V_c. If the binding site exerts a force, the assembly accuracy depends on the distance-dependence of this force.

By the equipartition theorem, the thermal energy of the particle due to Brownian Motion for each degree of freedom[6] will be $k_B T/2$. For a particle that is bound by a site to form a harmonic oscillator with an kinetic energy $E_o = \Delta x^2 \omega_0^2 / 2$, the time-averaged deviation from a desired position x_a will be

$$\langle (x - x_a)^2 \rangle = \frac{k_B T}{M \omega_0^2}. \tag{3.80}$$

The time required for the average position to have reached its target value is on the order of $2M/\chi$.

The harmonic oscillator is often a good model for a relatively strongly bound particle. If more precision is required, or if the particle is bound

---

[6]This only holds if the coordinate enters the Hamiltonian of the system as a square, which is true for harmonic oscillators, but not for arbitrary force fields, where additional care has to be taken.

rather loosely, it might be necessary to numerically incorporate all the involved force fields, as we will do later in this chapter for particles at high concentration. It is much harder to solve the FOKKER–PLANCK equations for such cases, and one generally has to resort to numeric methods. The accuracy can then still be estimated by numerical integration and comparison with the thermal energy.

3.2 Diffusion and reaction of molecules[7]

It is not yet possible to arrange single, small molecules on templates of the kind described above, because we do not have a technology that would form molecular-size binding sites. (Scanning Tunneling Microscopes could be used for this purpose, but the technique is not suitable for any but small numbers of sites). There are some applications, however, where it is not necessary to control the individual position, but only the local density of molecules. Surface chemistry gradients are a good example: if the density of an adsorbed molecule changes with position on a substrate, some property of this surface might change as well. What is needed to create a gradient is a method to guide a certain amount of molecules to a certain position, where they adsorb to form sub-monolayers.

We can use some of the principles described above to this purpose. If we can control the transport of the monomers towards the surface, we might influence the composition of the resulting layers. When working with solutions of the monomers, this can be done by varying the immersion time depending on the position on a substrate [134]. When working with stamps that can print monolayers, it can be done by adjusting the stamp's geometry to provide different amounts of molecules to different

---

[7]This work has been published in [102].

Figure 3.3: Principle of diffusion-controlled depletion printing. The stamp thickness $h(x,y)$ directly governs the amount of substance $n_s(x,y)$ transferred to each part of the surface.

positions on the surface. We will follow the latter route here.

To a first approximation, the amount of a thiol n_s that is transferred from a stamp to a gold surface, where it forms a (partial or full) self-assembled monolayer, is controlled by the initial concentration c_0 inside the stamp and the thickness of the stamp:

$$n_s(x,y) = \int_0^{h(x,y)} c_0(x,y,z)dz. \tag{3.81}$$

Both of these quantities can, in principle, be varied in order to control the final surface composition. However, it is difficult to ink a stamp with a defined concentration pattern. The basic idea of our method is therefore to prepare a stamp with variable thickness h over its area of contact, $h = h(x,y)$. Ideally, the printed amount at a specific point of the surface produced then only depends on the height of the stamp above this point (Fig. 3.3):

$$n_s(x,y) = h(x,y)c_0. \tag{3.82}$$

The above equation is applicable if during the printing process most of the molecules travel towards the surface vertically. This is only possible if diffusion (and not reaction) limits the monolayer formation. Sev-

eral groups have found the process of monolayer formation from ethanol solution to be diffusion-limited [26,87]. As the diffusion constant of hexadecanethiol (HDT) in PDMS is one order of magnitude lower than in ethanol [9], one might expect that the formation of monolayers from PDMS stamps is diffusion-limited as well. However, further inspection shows that the situation is somewhat more complex in our case: even if the initial rate of monolayer formation is high, it will drop considerably while achieving full coverage. At the same time, the concentration inside the stamp decreases. We will provide a more quantitative treatment in the following that takes the thickness of the stamp into account.

3.2.1 Diffusion limit of monolayer formation

The transport of thiol inside the stamp is described by FICK's second law of diffusion [9],

$$\frac{\partial c}{\partial t} = D\nabla^2 c, \tag{3.83}$$

which deals with the temporal evolution of the solute concentration c in a material where the solute has a constant diffusion coefficient D.

We use dimensionless variables in the following. A characteristic diffusion time t^* for a stamp of thickness h is $t^* = h^2/D$, so that we express time as $\tilde{t} \equiv tD/h^2$. The surface-normal coordinate becomes $\tilde{z} \equiv z/h$ and the lateral coordinate $\tilde{x} \equiv x/h$. Concentrations are normalized to the initial concentration, $\tilde{c} \equiv c/c_0$. For the two-dimensional case, Eq. (3.83) becomes

$$\frac{\partial \tilde{c}}{\partial \tilde{t}} = \frac{\partial^2 \tilde{c}}{\partial \tilde{x}^2} + \frac{\partial^2 \tilde{c}}{\partial \tilde{z}^2}. \tag{3.84}$$

Let us assume that the rate of monolayer formation is governed by diffusion and that the reaction is rapid enough to model the gold surface as a perfect thiol sink. A stamp of constant thickness is then adequately

represented by the one-dimensional version of Eq. (3.84) with a zero-concentration boundary condition on its printing side and a zero-flux boundary condition on its other side.

An analytical solution for diffusion in a slab between $\tilde{z} = -1$ and $\tilde{z} = 1$ with constant-concentration boundary conditions of $\tilde{c}(\tilde{z}' = \pm 1) = 0$ and a uniform initial concentration c_0 is given by Crank [38] as an infinite series:

$$\tilde{c} = \frac{4}{\pi} \sum_{i=0}^{\infty} \frac{(-1)^i}{2i+1} e^{\left(-\frac{(2i+1)^2 \pi^2 \tilde{t}}{4} \right)} \cos\left(\frac{(2i+1)\pi}{2} \tilde{z} \right). \qquad (3.85)$$

Owing to symmetry, there is no flux across $\tilde{z} = 0$. One half of the solution where $1 > \tilde{z} > 0$ can thus be used as model for the thick part of the actual stamp. The dimensionless diffusive flux $\psi_{\text{diffusion}}$ through the surface towards the substrate is then

$$\psi_{\text{diffusion}} = -\left. \frac{\partial \tilde{c}}{\partial \tilde{z}} \right|_{\tilde{z}=1} = -2 \sum_{n=0}^{\infty} e^{\left(-\frac{(2n+1)^2 \pi^2 \tilde{t}}{4} \right)}. \qquad (3.86)$$

According to our assumption, the full diffusive flux is adsorbed onto the substrate. Numerical evaluation shows that the fraction of surface covered ϵ then changes according to Fig. 3.4.

3.2.2 Reaction limit of monolayer formation

The above result indicates the maximum amount of thiol that can be transported towards the interface. Another possible limit for the overall speed is the adsorption reaction with its finite reaction rate that depends on the surface thiol concentration.

We follow JUNG and CAMPBELL [88] and state the surface reaction rate R_{ads} in terms of a sticking probability S that decreases from S_0
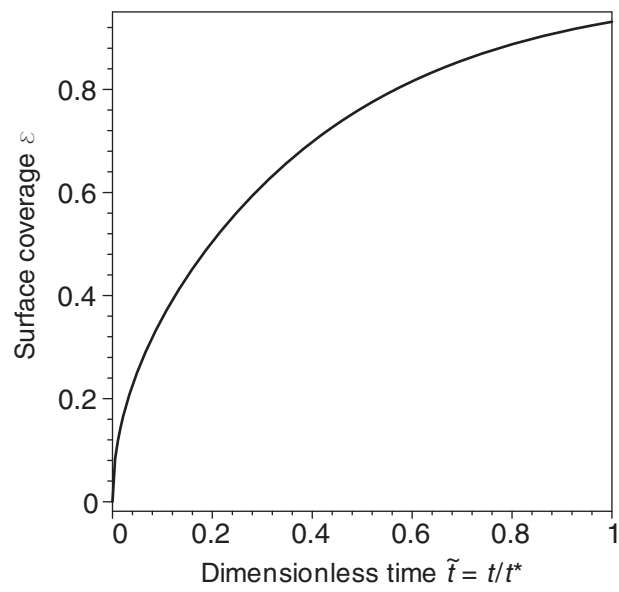
Figure 3.4: Change of surface coverage in an entirely diffusion-controlled printing process.

whereas the fraction of surface covered, ϵ, increases from zero (to a maximum of unity for a full monolayer):

$$R_{\text{ads}} = S_0\,(1-\epsilon)\,c_{\text{thiol}}\sqrt{\frac{k_B T}{2\pi M}}, \tag{3.87}$$

where c_{thiol} is the concentration of free thiol at the surface, k_B the Boltzmann constant and M, the mass of a molecule[8]. The reactive flux to the surface J_{reaction} reaches the surface at most until a full monolayer with a concentration at the surface c_{ML} has been reached so that we can state

$$\epsilon(x,t) = \frac{\int_0^t J_{\text{reaction}}(x,t')dt'}{c_{\text{ML}}}. \tag{3.88}$$

For an entirely reaction-limited system where the thiol can diffuse in the stamp infinitely rapidly, the surface concentration $\tilde{c}_s$ of free thiol decreases at the same rate as the surface coverage ϵ of the monolayer increases: $\tilde{c}_s = 1 - \epsilon$. The reaction-limited flux towards the surface in dimensionless form ψ_{reaction} is then:

$$\psi_{\text{reaction}} = S_0(1-\epsilon)^2\frac{h}{D}\sqrt{\frac{k_B T}{2\pi m}}. \tag{3.89}$$

Thermodynamic data suggest that very little thiol will be left in the stamp when the chemical equilibrium is finally reached. From literature values [7] of the desorption enthalpy we can calculate the equilibrium constant to be on the order of $\mathcal{K} \approx 3 \times 10^{22}$. The concentration of free thiol at an initial concentration of 1 mmol/L then becomes negligible ($c \leq 10^{-23}$ mmol/L).

---

[8]These adsorption kinetics have been established for the formation of monolayers from ethanol. The conformal contact between PDMS and gold and the high mobility of HDT in the silicone lead to a comparable adsorption situation. Printed monolayers are identical in structure to those obtained from solution [107].

3.2.3 Comparison of diffusive and reactive limits

The surface reaction might not be fast enough to consume all substance that diffuses to the surface immediately. By comparing the kinetics of monolayer formation to the diffusive flux, we identify the actual rate-limiting step that controls the monolayer formation in the printing process.

Figure 3.5 shows the maximum reactive flux as well as the maximum flux that can be reached with an actual PDMS stamp, as obtained from Eq. (3.86). The reaction can take up considerably more thiol than diffusion can provide during most of the process. Only in the very beginning (where the "fresh stamp" comes in contact with the gold) and towards the very end (where the concentrations become very low and the reaction slows down) might the reaction briefly limit monolayer formation. For the largest part, printing is diffusion-limited. Although we have shown this for the thickest part of the stamp, the conclusion also holds for the thin parts.

3.2.4 Applicability of the perfect-sink model

There remains the question of how close the actual situation is to the diffusion limit. The concentration of free thiol at the stamp-gold interface does not drop to zero as we had assumed for the calculation of the upper mass transfer limit. It is also smaller than it would be for a stamp with an infinite diffusion coefficient of thiol. We can estimate the deviation from the assumed concentration profile by numerical evaluation of the concentration terms in both the diffusion and the kinetic equations. The comparison of these concentrations then leads to the plot in Fig. 3.6. During most of the printing time, i.e. until a coverage of about 80% is reached according to Fig. 3.4, the concentration very close to the
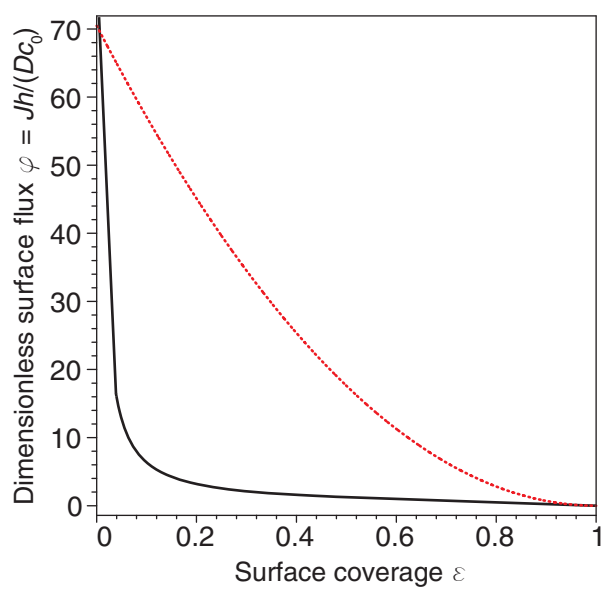
Figure 3.5: Flux of thiol towards the gold surface for a hypothetical reaction-limited (dashed line) and the diffusion-limited (solid line) process
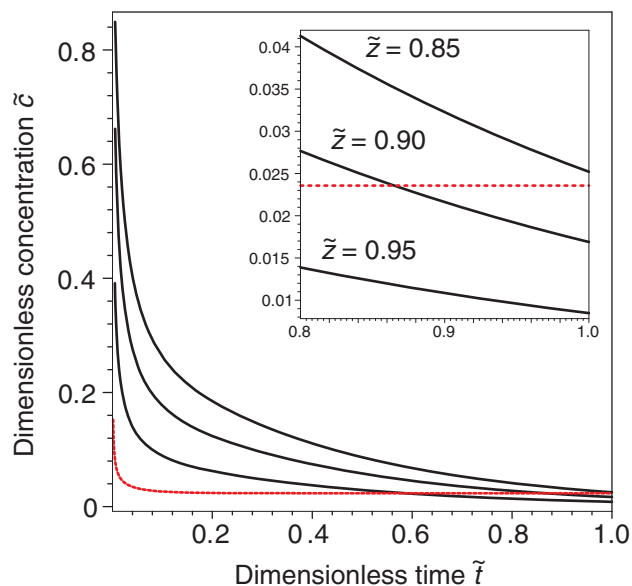
Figure 3.6: Comparison of solute concentrations inside the stamp for an infinitely rapid surface reaction at different locations close to the surface (solid line) to the "kinetic" concentration required to take up all substance (dashed line).

surface of our above-mentioned model is higher than that required for the reaction to take up all the thiol diffusing towards the surface. This is equivalent to saying that the depletion layer that is commonly used in liquid systems as a measure for the diffusion limitation of the total process [18] *is as thick as the entire stamp* during most of the printing process. The actual situation is therefore close to the diffusion model described above.

Towards the end of printing, the kinetics of monolayer formation change: Eq. (3.87) is probably not valid for surface coverage above 80% where

a slower formation process has been reported [7]. At the same time, concentrations inside the stamp reach levels that are so low that diffusion control is not necessarily maintained. Comparing the amounts transferred, we can expect that the influence of this last phase is much smaller than that of lateral diffusion during the main part of printing. We will therefore model the entire printing process purely based on diffusion with a zero-concentration boundary condition at the interface.

3.2.5 Stamp design

Several constraints have to be taken into account in the design of the stamp. We will provide some design rules in the following.

Maximum gradient steepness.   During the depletion of the stamp, diffusion will not only transfer ink towards the surface, but also distribute it laterally, effectively smoothing the gradients to be printed. This limits the steepness of the surface composition gradient that can be printed. The effect is most easily seen for a linear gradient obtained from a wedge-shaped stamp: The aspect ratio of such a stamp (length to thickness) has to be larger than unity to obtain a linear gradient.

To be more quantitative, we analyze the interplay of lateral and normal diffusion. A two-dimensional finite element method (FEM) discretization of Eq. (3.84) for a stamp with triangular cross section reveals the limitations of our method. As the process proceeds at the upper diffusion limit according to the above results, a simple sink condition at the gold surface is sufficient for modelling[9].

All calculations to find a finite element solution of diffusive transport inside the wedge were performed using MatLab (The MathWorks, Nat-

---

[9]The combination of diffusion and reaction processes using FEM has been demonstrated [111], but introduces a high level of complexity to the model.

ick, MA, USA). The diffusive flux through the contact area arises from the concentration gradient in the elements close to the edge. We calculated it for every time step and balanced it with the content of the stamp to check for consistency. Integration over all time steps for every element at the boundary at the edge then yielded the amount of substance absorbed at this point.

Figure 3.7 shows the printed amount in dependence of the normalized coordinate along the gradient for wedge-shaped stamps with different aspect ratios. All of them contained enough ink to establish a full monolayer at their thick end (corresponding to a dimensionless surface concentration of unity). Small aspect ratios lead to considerable lateral diffusion inside the stamp and thus nonlinear gradients. At an aspect ratio of 10, the gradients become fairly linear. Only in the thick part of the stamp remains a slight "bulging", even in long gradients (aspect ratio of 100). The thin ends of the high-aspect-ratio stamps exhibit artefacts of the FEM mesh and have been removed in the plot.

Thiol concentration. The amount of thiol required to form a monolayer has to be soluble in the stamp. If one molecule in the self-assembled monolayer covers an area of 0.21 nm^2 (as reported by DUBOIS and NUZZO [51]), we require an amount of 7.9 µmol/m^2. The solubility of HDT in polydimethylsiloxane (PDMS) was measured by BALMER et al. [9] to be 486 mmol/m^3, so that the minimum thickness is on the order of tens of nanometers. All stamps used in practice are considerably thicker.

Printing time. The maximum thickness of the stamp has to be small enough to allow all of the substance to diffuse onto the surface in a reasonable time. In addition, it has to be possible to prepare an ink pad of reasonable thickness with the same concentration.
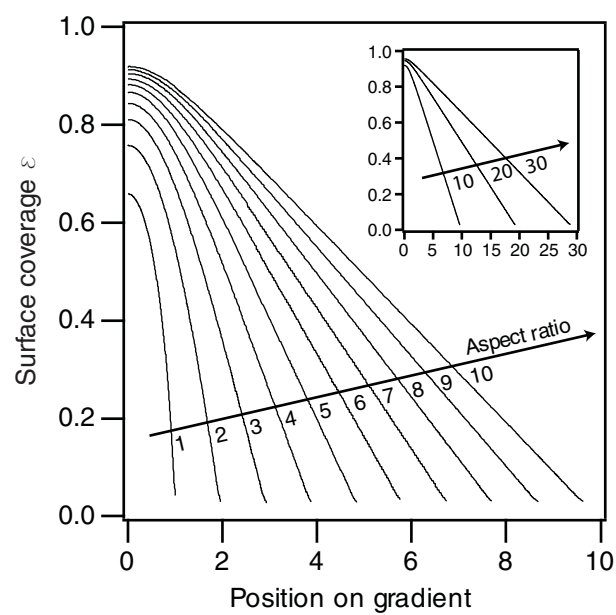
Figure 3.7: Calculated amounts of thiol adsorbed from the stamp at different positions along the gradient, for stamps with aspect ratios from one to ten (higher ratios are shown in the inset). A full monolayer is reached at a dimensionless concentration of unity.

The characteristic diffusion time $t^* = h^2/D$ provides a rough estimate of the printing time required. In the case of HDT in PDMS with a diffusion coefficient of [9] $D = 5.9 \times 10^{-11}$ m²/s, a reasonable stamp thickness is 50 μm, corresponding to a characteristic time of 42 s. Note that this time is independent of the initial concentration. It indicates when a considerable part of the thiol (roughly 90%) has left the stamp.

3.3 Diffusion and convection of colloids[10]

In the previous chapter, we have seen how the density of molecules adsorbed at certain parts of a surface can be influenced by curtailing their transport to the surface. The position of *individual* molecules has not been controlled directly, however. In this section, we address the transport problems that arise when single objects or small numbers of objects are to be transported to specific positions using directed self-assembly.

In this work, assembly of small colloidal particles was performed either using capillary assembly, convective assembly, or similar methods (refer to Chapter 5 for the experimental details). The meniscus of the colloidal suspension moves over a patterned template, while evaporation from the meniscus creates a convective flux of liquid that is directed at the meniscus. This flux drives particles into the vicinity of the three-phase boundary line. The particles are then either assembled in binding sites, most likely through the joint action of confinement and capillary forces, or deposited (if the contact angle is low) inside the thin wetting layer that is left behind by the meniscus (see Fig. 3.8).

The transport problem thus posed is least a two-phase problem, involving the continuous phase of the solvent and the dispersed phase of the particles. In techniques that use the liquid-gas interface in the place-

---

[10]Part of this work has been published in [121].

Figure 3.8: Meniscus-based particle assembly methods.

ment of colloidal particles, such as capillary assembly, we have a dynamic three-phase system. These are complex and cannot at present be dealt with in a single model. Instead, I will set out to describe one part of the system (the bulk colloid) using a diffusion-convection system, which can be simulated numerically with a high degree of precision. Close to the region where the actual assembly takes place, the concentration of particles increases, and particle-particle-interactions become decisive. This situation can be handled using a thermodynamical model, where the involved forces are taken to be additive.

The macroscopic model is useful as long as the particles can be seen as a continuum, but this approximation breaks down as we come close to the three-phase boundary line, where particles are actually trapped in the template. For this last step we will instead employ some of the models developed in Section 3.1 and calculate their numerical values for the experimental parameters in Section 3.3.3.

The final goal of this section is to compare our models to the observable situation at particle diameters of 500 nm and (with some limitations) 60 nm, so that we can make predictions on the behavior of smaller particles that are harder to observe.

3.3.1 Macroscopic convection

Particles are transported in the bulk volume through the convective flux of liquid towards the meniscus caused by water evaporating from the meniscus. For small gold particles (diameter $d_\mathrm{p} = 60$ nm, density $\rho_\mathrm{Au} = 19300$ kg/m^3), the time scale of inertial response

$$\tau_p = \frac{(2\rho_\mathrm{Au} + \rho_\mathrm{f}) \cdot d_\mathrm{P}^2}{36\eta} \approx 4 \cdot 10^{-9} \text{ s} \tag{3.90}$$

in water under standard conditions with a density $\rho_f = 1000$ kg/m^3 and a viscosity $\eta = 10^{-4}$ Pa s is on the order of nanoseconds.

The Brownian time scale for a typical length $l = 1$ mm,

$$\tau_b = \frac{d_\mathrm{p} l^2 \mu}{k_\mathrm{B} T} \approx 1.5 \cdot 10^4 \text{ s} \tag{3.91}$$

is very long compared to convective time scales. Particles do move across streamlines through the action of Brownian Motion, but the time it would take them to appreciably deviate from the path set by the liquid flow is very long, so that these movements can be neglected as long as we are not interested in microscopic distances.

Thus, in the bulk part of the fluid volume, particles can be regarded as solutes that travel along the streamlines. The streamlines depend on experimental parameters, notably temperature, humidity and substrate velocity, and their knowledge is sufficient to predict the particle trans-

port in the bulk region.

The liquid flow inside the colloid volume can be safely regarded as laminar, with REYNOLD's numbers

$$Re = \frac{ul\rho}{\eta} \approx 2 \cdot 10^{-5} \dots 1 \cdot 10^{-3} \qquad (3.92)$$

using the temperature-dependent density ρ and dynamic viscosity η of water and estimates for the evaporation of liquid from the meniscus. The laminar flow field can be simulated easily with a standard FEM discretization of the NAVIER–STOKES equation if the boundary conditions are known. Here, we use a commercial code (COMSOL, FEMLAB GmbH, Zürich, Switzerland) that allows arbitrary geometries and automatically creates a mesh with smaller grid spacings in critical regions. The mesh of the full, two-dimensional simulation, comprising both the liquid volume and the surrounding air, is shown in Fig. 3.9. It consists of 2336 triangular elements that make up the liquid part and 9232 triangular elements for the gas phase. The geometry used here assumes a contact angle of 50° and a meniscus profile taken from microscopic observation of the actual profile occurring in experiments.

The colloid was modeled using the temperature-dependent viscosity and density of water, which is a very good approximation in the bulk region with its low particle load. The boundaries of the liquid were represented by no-slip conditions at the walls and by a flux condition at the meniscus. For the bottom wall, a constant horizontal velocity was imposed to simulate the moving substrate during assembly. The boundary opposite of the meniscus was taken to be "neutral", with a vanishing normal component of the stress tensor. Finally, evaporation of water from the meniscus sets the liquid flow rate from this boundary, and we coupled the fluid dynamics simulation to a diffusion simulation to find
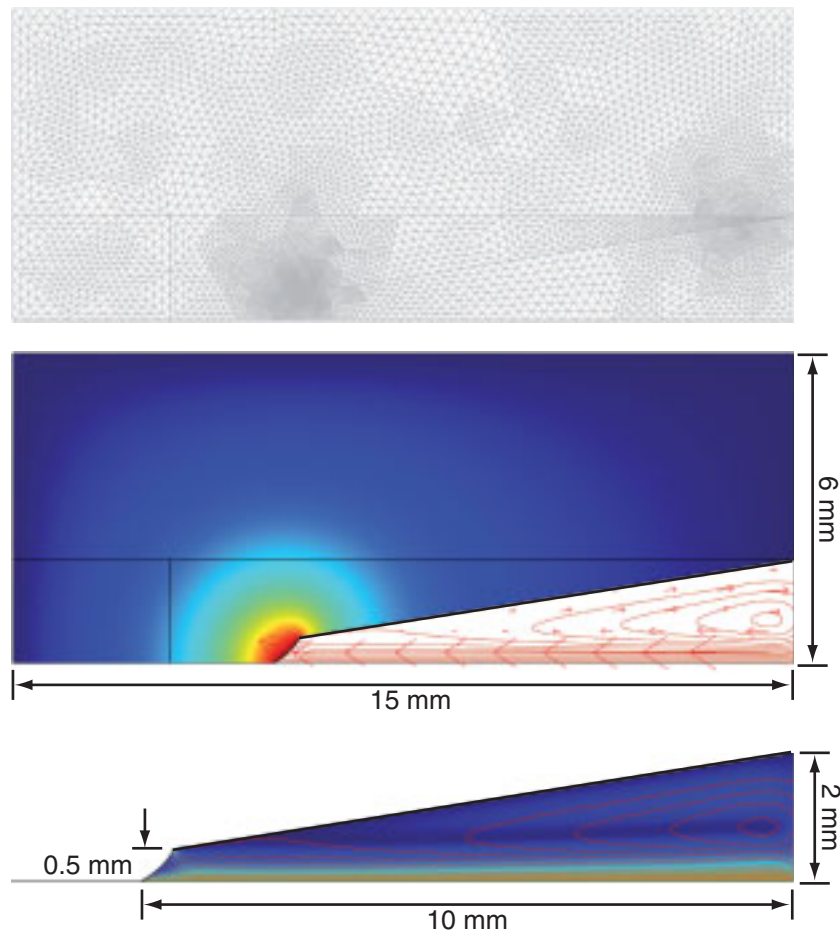
Figure 3.9: Grid details and geometry used in the CFD simulations. Results shown are for a temperature of 12 °C and at a relative humidity of 50%.

this rate.

Evaporation is commonly modeled by assuming a boundary layer of water-saturated air above the gas-liquid boundary, where diffusion and convection deplete from this region. The actual concentration of water in this boundary layer is then calculated according to one of the many equations for the saturation vapor pressure of water, for example the ARDEN–BUCK equation

$$p_W = 6.1121 \text{ hPa } \mathbf{e}^{\frac{(18.678 - T/(234.5\,^\circ\text{C}))T}{257.14\,^\circ\text{C}+T}},\tag{3.93}$$

which is used here. To provide a lower boundary, we assume static air (i.e., no convection) and take into account only water diffusion through the air, which is simulated using the discretized form of FICK's law with a diffusion constant of $D_{\text{water}-\text{air}} = 6.27 \cdot 10^{-5} \text{ m}^2/\text{s}$. The surrounding air had a relative humidity of 50% at a temperature of $T_{\text{air}} = 293$ K, imposing a constant concentration boundary condition at all but the bottom limits of the simulation area.

Evaporation implies enthalpy reduction in the liquid and thus decreasing temperature. We neglect the temperature gradients that might be caused here, as we keep the bulk temperature constant (through the heated substrate) and have relative short thermal paths from the heated substrate to the upper wall. This includes neglecting natural convection of liquid.

Results of the simulation are shown in Figs. 3.10 and 3.11, using different liquid temperatures and humidities. For clarity, we only show the water concentration in the surrounding air (color-coded) and the streamlines in the liquid volume (indicated by red lines), which are all directed towards the three-phase contact line, or recirculate. (One solution is shown in more details in the lower part of Fig. 3.9). Two main

features appear in the laminar flow of the colloid: A flow component that is directed towards the meniscus and a recirculation in the upper part of the liquid. As the evaporation rate increases, the recirculation zone moves away from the meniscus. Higher liquid temperature or lower outside humidity increase the flux toward the contact line. The transition is not abrupt, as it is in some convection flow patterns; the recirculation eddy rather moves steadily away from the meniscus. The exact details depend also on the geometry, and thus the angle of the upper wall, but the overall behavior is consistent.

In our model, where only diffusion transports water from the meniscus, there should be an almost linear relationship between the environmental humidity and the liquid flux towards the meniscus, and another one between the vapor pressure above the meniscus and the liquid flux towards the meniscus, which leads to a power law (from the equation of state that describes the water pressure above water) that connects temperature and liquid flux. Both relationships are indeed recovered when integrating the flux across the meniscus, as becomes obvious in Fig. 3.12. Instead of plotting absolute liquid fluxes, the results were normalized here to the liquid flux required to create a single monolayer, which follows from the particle flux necessary to establish a single monolayer

$$J_{ML} = l_m \cdot \rho_{ML} \cdot v_s, \tag{3.94}$$

with the density of a particle monolayer ρ_{ML}, the meniscus length l_m, and the substrate velocity v_s. For a hexagonal monolayer, the density is

$$\rho_{ML} = \frac{N}{A} = \frac{A - A_{void}}{A_{particle}A} = \frac{A\pi/(3\sqrt{2})}{a^2\pi A} \approx 6.547 \cdot 10^{13} \text{ m}^{-2} \tag{3.95}$$

with particles of a radius $a = 30$ nm that occupy an area $A_{particle}$ in the

T$_p$ = 10°C

RH = 50%

T$_p$ = 12°C

RH = 50%

T$_p$ = 15°C

RH = 50%

T$_p$ = 17°C

RH = 50%

T$_p$ = 20°C

RH = 50%
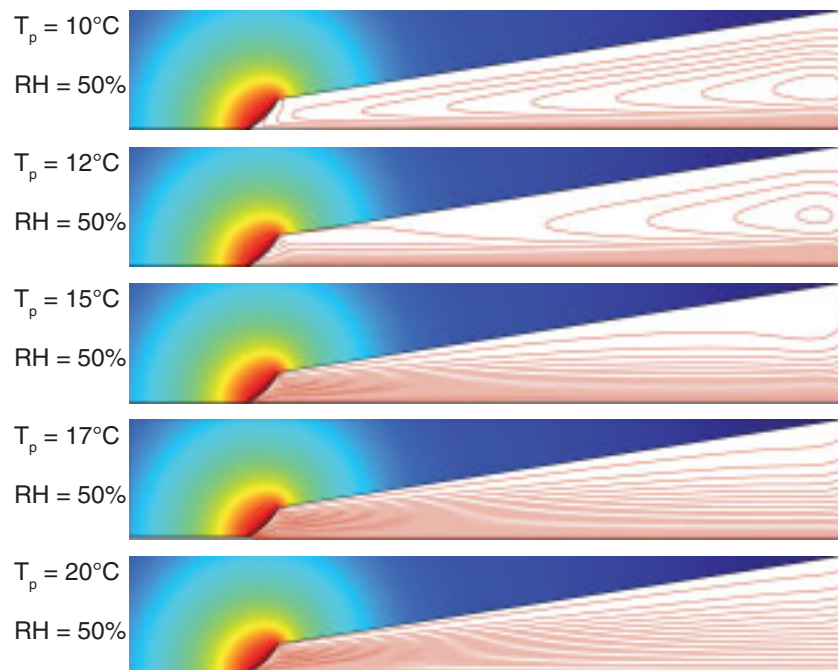
Figure 3.10: Simulation results for a constant relative humidity of 50% at varying colloid temperatures. The red lines are streamlines in the liquid volume, the color coding refers to the water concentration in the surrounding air.
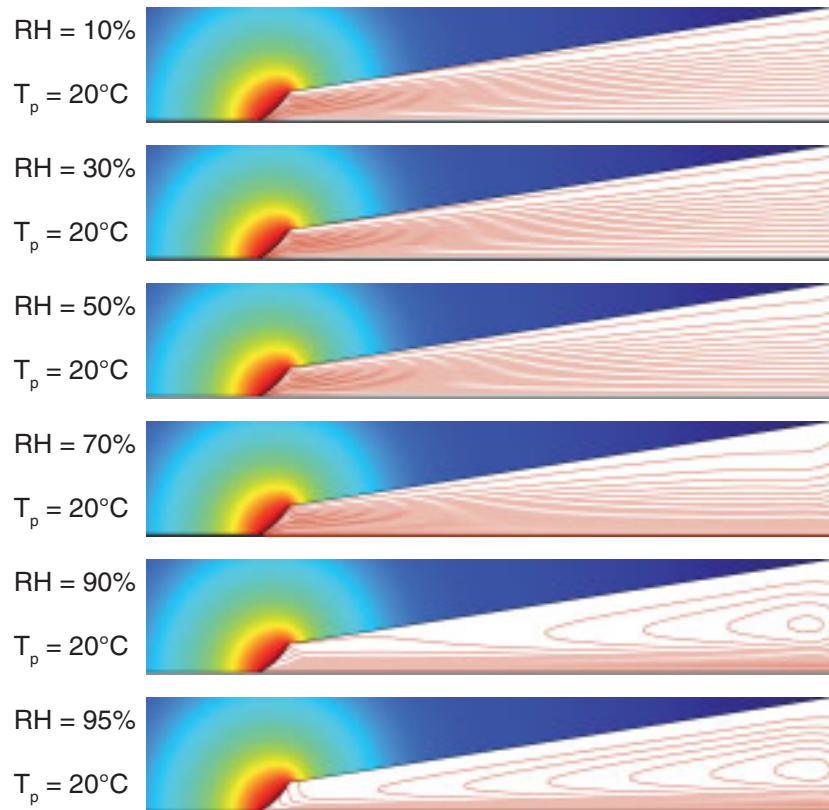
Figure 3.11: Simulation results for a constant colloid temperature of 20 °C at varying relative humidities of the environment. The red lines are streamlines in the liquid volume, the color coding refers to the water concentration in the surrounding air.

monolayer. The volumetric flow of a colloid with a particle concentration $c_c = 2 \cdot 10^{14} \text{ L}^{-1}$ required to provide exactly this particle flux is then

$$\dot{V} = \frac{J_{\text{ML}}}{c_c} = \frac{l\rho v_s}{c_c} \approx 7.55 \cdot 10^{-7} \text{ L}/(\text{m s}). \qquad (3.96)$$

As the fluxes are also directly proportional to the original particle concentration, values for other starting concentrations c_c' can be simply obtained by multiplication with c_c'/c_c.

The above model assumes that all particles contained in the evaporating colloid will be transported to the meniscus, and be available there for assembly in an "accumulation zone". In reality, there are two mechanisms that remove particles from this region which can act together: diffusion of particles out of the zone and recirculation flow that drags particles that are too far from the meniscus immediately back to the bulk. While diffusion always occurs and will generally be stronger at increased temperatures, the recirculation eddies already move away from the meniscus at moderate temperature according to above simulations, so that their influence on the particle transport is likely to be limited to low temperatures.

This recirculation can therefore not be the explanation for the experimentally observed stability of the accumulation zone. Under stable assembly conditions, the zone does not grow beyond a certain point, even if the depletion due to assembly is small. It rather appears that there exists a steady-state equilibrium, in which convection and diffusion balance each other. The next chapter will establish a model for this situation by introducing concentration-dependent diffusion constants for the colloidal particles.
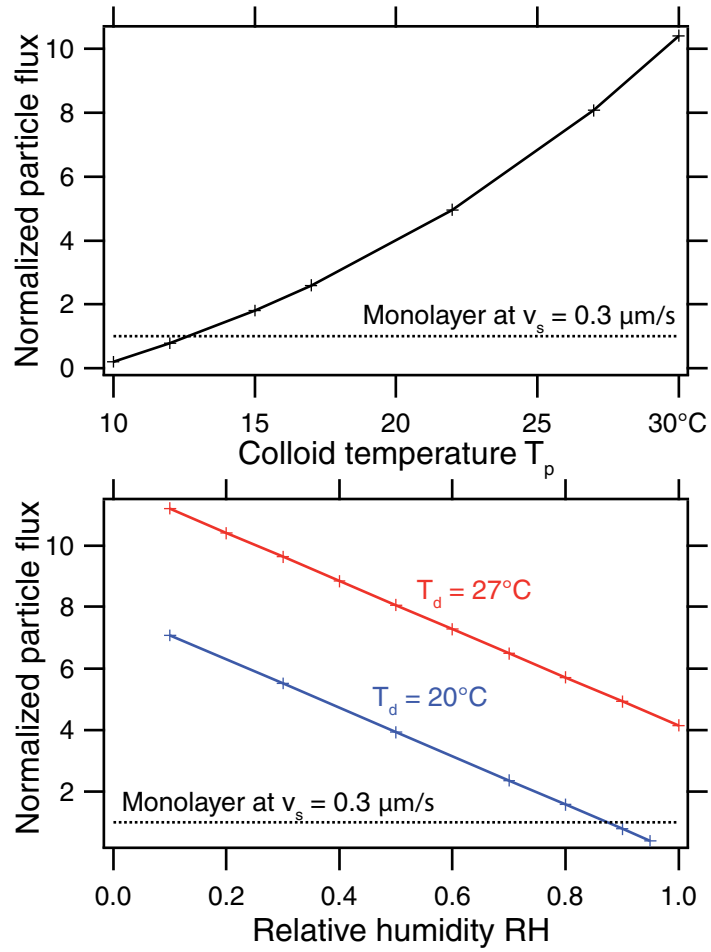
Figure 3.12: Particle flux as calculated from the evaporative flux of colloid, expressed as the number of layers that could be deposited at the respective flux when the substrate moves at 0.3 µm/s. Lines between data points serve as guide to the eye.

3.3.2 Macroscopic convection and diffusion

Let us now analyze the colloid volume in the vicinity of the three-phase contact line, at a length scale that is still much larger than the particle diameter, on the order of the capillary decay length. Experimentally, we often find the concentration of particles to be increased in this "accumulation" zone, and this locally increased concentration appears to be a prerequisite of successful particle assembly.

A comparable system where particles (or macromolecules) are transported towards an interface where they accumulate is ultrafiltration. The barrier there usually consists of a semipermeable membrane which retains all (or most) of the solute while letting the permeate pass. The gas-liquid interface of our meniscus is a perfect barrier for particles, so that we can use some of the results obtained in ultrafiltration in the analysis of the accumulation zone. This zone also appears in ultrafiltration, where it is usually named "concentration polarization layer".

In membrane ultrafiltration, it is usually not possible to directly observe the structure of the polarization layer, as we can do with the accumulation zone. What can be observed is the permeate flux as a function of pressure. Researchers often find that this flux decreases strongly after some time and attribute this to the formation of a "gel layer" [131]. In this layer, the colloid behaves like a solid, exhibiting increased structural ordering. The thickness of this layer can be small — perhaps only a monolayer directly at the membrane — but for larger colloidal particles, it can be sufficiently large to be optically observable.

We will try in the following to produce a model for the concentration polarization layer that can be adapted to the situation in particle assembly. This should give us expressions for the thickness of the polarization layer, which can be compared to the observed sizes of the accumulation zone, to find whether the systems do indeed behave similarly.

Let us first assume that in the proximity of the interface, only the flow towards the interface is relevant for the formation of the accumulation zone. The only important hydrodynamic parameter is then the liquid velocity of the convective flow, which we assume to be independent of the position in the region close to the meniscus, $\vec{v}_b \neq f(x, y)$. This flow exerts a STOKES drag on the particle, which move towards the gas-colloid boundary. As their concentration increases, however, the particle interaction increases, and both the entropic and energetic cost of further concentration increase have to be balanced by the flow. If the pressure and temperature in this zone are constant, FICK's law holds for the diffusive transport of particles. Likewise, if the particles are small enough, their convective mass flux can be simply expressed as

$$\vec{n}_p = c_c \vec{u} \tag{3.97}$$

where $\vec{u}$ is the particle velocity and c_c their number concentration. If the particles now can be assumed to be massless, they will (in the absence of particle-particle interactions) always follow the liquid streamlines, so that the particle velocity is identical with the liquid velocity, $\vec{u} = \vec{v}_b$.

From the general transport equation it follows for a steady-state system with the above properties in one dimension that

$$-v_b \phi - D(\phi) \frac{\partial \phi}{\partial x} = 0, \tag{3.98}$$

a result often called the diffusion-convection equation. Instead of using mass concentrations, the volume fraction of the colloidal particles ϕ is used here, which is equivalent in an incompressible system[11]. Analyt-

---

[11] Volume fractions are a more natural choice in thermodynamic models of particle behavior that are based on interparticle forces and excluded volumes, as will be used later to derive particle diffusivities.

ical solutions for this equation exist if the diffusivity D is not a function of the concentration. Here, however, we are interested in a system of charge-stabilized colloidal particles that already interact at relatively large distances, and we are interested in relatively large local concentrations of these particles. With the caveats mentioned above, we can incorporate the interactions using a concentration-dependent diffusivity derived from thermodynamic arguments. The STOKES–EINSTEIN equation,

$$D_0 = \frac{k_B T}{6\pi\eta a}, \tag{3.99}$$

which only takes into account simple STOKES drag on the particles, can be generalized [11] to

$$D(\phi) = D_0 L(\phi) \frac{d(\phi Z(\phi))}{d\phi}. \tag{3.100}$$

The particles' behavior is characterized here by the sedimentation coefficient $L(\phi) = u/u_0$ which compares their sedimentation velocity to that of non-interacting particles, and the compressibility factor

$$Z(\phi) = \frac{\Pi}{c_c k_B T}, \tag{3.101}$$

which considers the change of osmotic pressure Π as the particle number concentration c_c increases.

Interparticle forces are often described using the DLVO theory, which is based on the assumption that the different contributions are simply additive [79]. The same assumption allows calculating the osmotic pressure in Eq. (3.101) as the sum of multiple osmotic pressures:

$$\Pi = \Pi_{\text{entropic}} + \Pi_{\text{VdW}} + \Pi_{\text{electrostatic}}. \tag{3.102}$$

Expressions exist in literature for different contributions to the osmotic pressure, others can be derived from expressions for interparticle potentials. Two limitations must be kept in mind, however. First, it is excessively complex to incorporate anything beyond nearest-neighbor interactions in the case of dispersion interactions. At low to moderately high concentrations, this does not cause large errors, as these forces rapidly decay with distance. At very high concentrations with very small particles in the low nanometer range, the errors might become substantial, however. Second, to calculate the particle interactions both in the case of dispersive and electrostatic interactions, it is necessary to assume a certain particle arrangement [55]. The classical WIGNER–SEITZ approach for electrostatic interaction for example is based on the idea that only the spacing, but not the particle arrangement, changes from dense packing to sparse distributions. Again, this assumption does not cause large errors for low-concentration colloids, and it also describes accurately dense packings, but it makes only for a crude model of the order-disorder transitions that occur at high concentrations and will be discussed later.

Entropic pressure. Finite concentrations limit the possible configurations of particles, thus decreasing entropy. This effect is familiar from gas phase, and many molecular dynamics simulations have been conducted to produce equations of state for systems of non-interacting spheres moving about freely, extending the VAN'T HOFF equation to higher concentrations. From the numerical results of such studies, several authors have derived expressions, and one commonly used is that of Hall [75] for hard spheres, stated in terms of compressibility as

$$Z = \frac{1 + \tilde{\rho} + \tilde{\rho}^2 - 0.67825\tilde{\rho}^3 - \tilde{\rho}^4 - 0.5\tilde{\rho}^5 - 6.028\mathbf{e}^{\xi(7.9-3.9\xi)}\tilde{\rho}^6}{1 - 3\tilde{\rho} + 3\tilde{\rho}^2 - 1.04305\tilde{\rho}^3} \quad (3.103)$$

where $\tilde{\rho} = b/(4V_M)$ is the reduced density from covolume $b = \frac{2}{3}\pi Na^3$ and molar volume V_M and where ξ is defined as

$$\xi = \frac{\pi\sqrt{2}}{6} - \tilde{\rho} \tag{3.104}$$

from the closest hexagonal packing density, $\phi_{hcp} = \pi\sqrt{2}/6$. The definition of the compressibility factor implies that

$$\Pi_{\text{entropic}} = c_c k_B T Z \tag{3.105}$$

$$= \frac{3}{4a^3\pi}\phi k_B T Z(\phi) \tag{3.106}$$

$$= \frac{3}{4a^3\pi}\phi k_B T \frac{1 + \phi + \phi^2 - 0.67825\phi^3 - \phi^4 - 0.5\phi^5 - 6.028e^{\xi(7.9-3.9\xi)}\phi^6}{1 - 3\phi + 3\phi^2 - 1.04305\phi^3}. \tag{3.107}$$

Dispersion interactions. Exact calculations of dispersion interactions are challenging for plate-plate geometries and become very demanding in particle-particle systems. For colloidal systems, a pragmatic approach has become widely accepted. It is based on HAMAKER's concept of additivity and treats retardation effects only in a basic manner (for a detailed criticism of this approach, refer to [141]). The VAN DER WAALS interaction potential of two spheres at a distance d is taken to be [19]

$$\Phi_{\text{VdW}}(d) = -\frac{H}{6}\left(\frac{2a^2}{d^2 + 4ad} + \frac{2a^2}{(d + 2a)^2} + \ln\left(1 - \frac{4a^2}{d + 2a^2}\right)\right). \tag{3.108}$$

The HAMAKER constant H includes the material properties, screening and, to an extent, retardation. Differentiation yields the interparticle force as

$$F_{\text{VdW}}(d) = \frac{d\Phi_{\text{VdW}}(d)}{dd}. \tag{3.109}$$

It is then necessary to assume that only nearest neighbors interact, and that a specific particle arrangement exists, to arrive at an expression for the overall interactions in terms of the osmotic pressure. Assuming hexagonal packing [55] leads to

$$\Pi_{\text{VdW}}(d) = \frac{\sqrt{6}}{S_{\text{h}}} F_{\text{VdW}}(d), \tag{3.110}$$

where the area S_{h} denotes the effective area occupied per particle in the crystal lattice [20]:

$$S_{\text{h}} = 2\sqrt{3}(a + 0.5d)^2. \tag{3.111}$$

Electrostatic interactions.   Electrostatic interactions provide the stabilizing repulsive forces in colloids. They are comparatively long-ranged, which makes the nearest-neighbor-only approach from above rather inaccurate. Cell-based approaches, inspired by solid-state mean-field approaches such as the WIGNER–SEITZ free electron energy approximation, have therefore replaced the pairwise DLVO models. The electrostatic potential in a cell with a dimensionless radius $\tilde{r}_{\text{cell}} = \kappa r_{\text{cell}}$ and an outer surface area S_{cell} is calculated, again assuming a certain (here, hexagonal) packing. At a certain number concentration of ions in the surrounding electrolyte c_{ion}^0, the interparticle force results from this potential Ψ as

$$F_{\text{electrostatic}}(d) = \frac{1}{3} S_{\text{cell}} c_{\text{ion}}^0 kT \left(\cosh \left(\frac{z e \Psi(\tilde{r}_{\text{cell}})}{k_B T} \right) - 1 \right), \tag{3.112}$$

which requires knowledge of the potential at the cell boundary. The potential distribution is described by the POISSON–BOLTZMANN equation (PBE)

$$\frac{d^2 \Psi}{d\tilde{r}^2} + \frac{2}{\tilde{r}} \frac{d\Psi}{d\tilde{r}} = \sinh \Psi, \tag{3.113}$$

made dimensionless using $\Psi = \psi e / (k_B T)$ for ions with a single charge, where e is the elementary charge, at some dimensionless radius $\tilde{r} = \kappa r$ around the cell center. The first boundary condition stems from the symmetry of the problem which implies that the charge density at the cell surface is zero, and thus, with GAUSS' theorem,

$$\left. \frac{d\Psi}{d\tilde{r}} \right|_{\tilde{r} = \tilde{r}_{\text{cell}}} = 0. \tag{3.114}$$

Besides, the potential at the shear plane of the particle (here dimensionless as $\alpha = \kappa(a + d)$) is a material-specific value often called zeta potential ζ and sets the second boundary condition as

$$\left. \frac{d\Psi}{d\tilde{r}} \right|_{\tilde{r} = \alpha} = \frac{\zeta ez}{kT}. \tag{3.115}$$

The PBE can only be solved numerically, as has been done e.g. by BOWEN and JENNER [19]. For approximation, we can linearize the equation by assuming

$$\frac{d^2\Psi}{d\tilde{r}^2} + \frac{2}{\tilde{r}} \frac{d\Psi}{d\tilde{r}} = \Psi, \tag{3.116}$$

which is applicable at small potentials. This DEBYE–HÜCKEL equation has an analytic solution of the form

$$\Psi = \frac{A}{\tilde{r}} e^{\tilde{r} - \alpha} + \frac{B}{\tilde{r}} e^{-(\tilde{r} - \alpha)}, \tag{3.117}$$

with the integration constants set by the boundary conditions. This provides an initial guess for the numerical solution, which we have performed using the MAPLE software package (Maplesoft, Waterloo, Canada), using a finite difference method. With the numerical values we can now calculate a configurational force between the particles us-

ing Eq. (3.112) and finally express them as a pressure

$$\Pi_{\text{electrostatic}}(d) = \frac{\sqrt{6}}{S_h} F(d), \tag{3.118}$$

exactly as above.

Generalized diffusion coefficients of some relevant colloids. Following the general idea of additivity that was laid out at the beginning of this section, all of the above pressures are now assumed to be additive. The total osmotic pressure is then

$$\Pi = \Pi_{\text{entropic}} + \Pi_{\text{VdW}} + \Pi_{\text{electrostatic}}. \tag{3.119}$$

We can simply add the expressions derived above for all osmotic pressure components, with the exception of that for the electrostatic interaction, $\Pi_{\text{electrostatic}}$, for which there exists no analytical expression. Instead, we fit splines to the results of Eq. (3.118) and use it in this sum. From the result, we can calculate the concentration-dependent mutual diffusion coefficient for the colloidal particles from

$$D(\phi) = D_0 L(\phi) \frac{\mathrm{d}(\phi Z(\phi))}{\mathrm{d}\phi}. \tag{3.120}$$

Results are shown in Figures 3.13 and 3.14 for 500 nm polystyrene particles and the 60 nm gold crystals used in this work. In both cases, the total osmotic pressure increases first with increasing particle volume fraction, to then decrease, finally reaching negative values. While the decrease does not describe the actual evolution of the osmotic pressure in the system, its onset is usually interpreted as the point of spinodal decomposition, where a solid phase can form in the colloid [154]. This
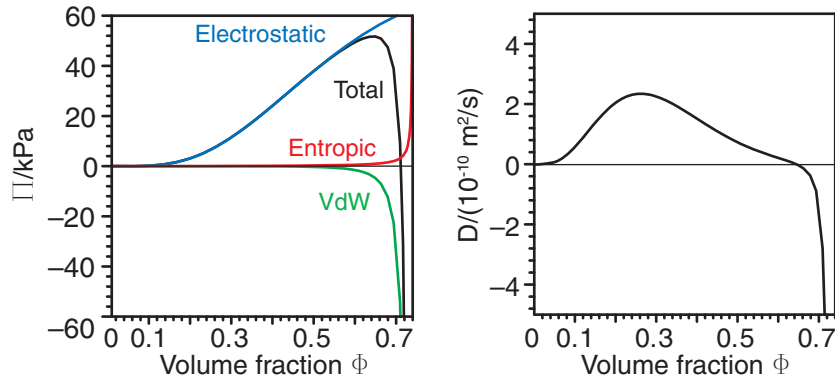
Figure 3.13: Osmotic pressures (left) and diffusion constant (right) in dependence of particle volume fractions for polystyrene beads with 500 nm diameter at an ionic strength of 10 μmol/L. Negative pressures and diffusion constants indicate aggregation, the decline of the osmotic pressure indicates a phase transition (see text).

transition is reversible, and the zone should decompose as soon as the convective flow is stopped. At even higher particle volume fractions, however, the total osmotic pressure becomes negative. The attractive VAN DER WAALS forces are not outweighed by the stabilizing electrostatic interactions any more. Particles start attracting each other and try to minimize the occupied volume. This might be kinetically hindered, but as soon as the particles have reached sufficient proximity, irreversible agglomeration ensues. Thus, while some aggregation can already occur at finite total osmotic pressures, the zero-crossing of the curve should be interpreted as the maximum particle content in a stable colloid.

Both transitions are also present in the diffusion constant that we can derive from the total osmotic pressure. Negative "diffusion coefficients"
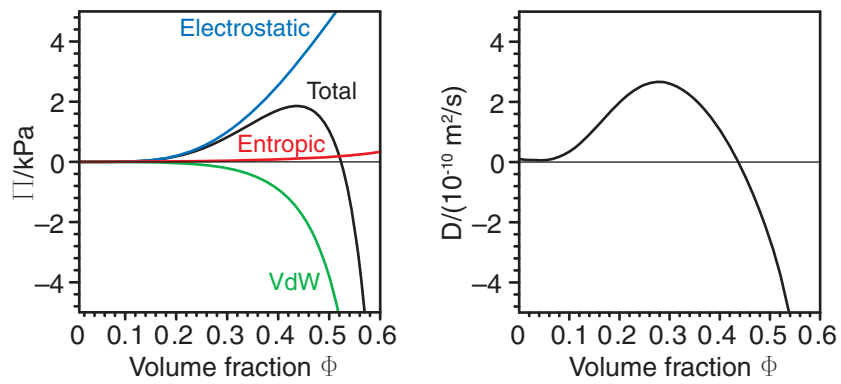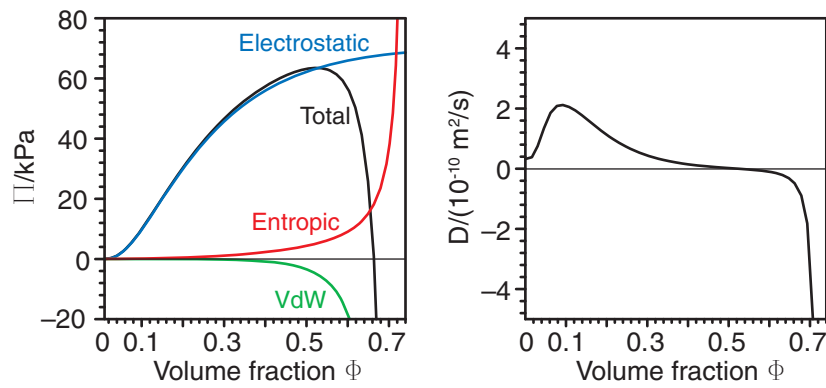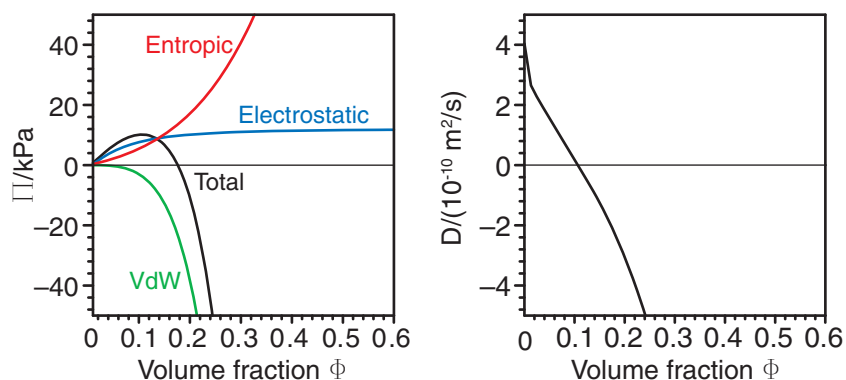
Figure 3.14: Osmotic pressures (left) and diffusion constant (right) in de-
pendence of particle volume fractions for gold nanocrys-
tals with 60 nm diameter at an ionic strength of 1 mmol/L.
Negative pressures and diffusion constants indicate aggre-
gation, the decline of the osmotic pressure indicates a phase
transition (see text).

as they occur at higher volume fractions indicate thermodynamically instable colloids, the decrease of the diffusion constant at slightly lower particle content indicates the liquid-solid transition. In both cases, the calculated diffusion constant is of limited use: for the solid phase, we may well have other transport mechanisms, and there are likely to be both crystalline and liquid regions, dynamically exchanging particles. For the instable colloid, transport properties will change as more and more particles form aggregates, and the system will finally not be able to assemble single particles.

To verify these results, we have calculated the osmotic pressures for a well-known model system from ultrafiltration: silica particles with 100 nm diameter in a low-ionic strength colloid. Results are shown in Fig. 3.15, and they are almost identical to those of BACCHIN et al. [6], although they used different approximations, in particular of the electrostatic interactions. The parameters used in all of the above calculations are summarized in Table 3.1.

Colloidal stability For both the gold and the polystyrene particles shown here, electrostatic interactions are the main stabilizing effect. Gold particles, with their large dispersive interactions, are destabilized comparably early by VAN DER WAALS forces, while polystyrene particles only aggregate late. Entropic stabilization does not play a large role for any of them. This changes when going to smaller particle diameters, as becomes visible in Fig. 3.16, where gold particles with 6 nm diameter have been modeled. VAN DER WAALS attraction finally becomes governing for them, too, and at considerably lower volume fractions around 0.2, but the main stabilization at lower concentrations is due to entropic effects. Entropic stabilization is independent of the ionic strength in the solution, but it cannot stabilize small particles at high

Table 3.1: Numerical values of variables used for the numerical evaluations in this section. "PS Beads" denotes 500 nm-diameter polystyrene beads, "Au crystals" stands for 60 nm-diameter gold nanocrystals, "Silica spheres" has variables taken from [6].

Au nanocrystals			
Particle diameter	d_p	60	nm
Hamaker's constant	H	30×10^{-20}	J
Number concentration of ions	c_{ion}^0	1	mol/m^3
Distance outer Helmholtz plane	d_H	0.55×10^{-9}	m
Zeta potential	ζ	37.81×10^{-3}	V
Solvent dielectric constant	ϵ_m	80	
Inverse Debye length	κ	1.0385×10^8	m^{-1}
PS beads			
Particle diameter	d_p	500	nm
Hamaker's constant	H	13×10^{-21}	J
Number concentration of ions	c_{ion}^0	0.01	mol/m^3
Distance outer Helmholtz plane	d_H	0.55×10^{-9}	m
Zeta potential	ζ	30×10^{-3}	V
Solvent dielectric constant	ϵ_m	80	
Inverse Debye length	κ	1.04×10^7	m^{-1}
Silica spheres			
Particle diameter	d_p	200	nm
Hamaker's constant	H	1×10^{-20}	J
Number concentration of ions	c_{ion}^0	0.01	mol/m^3
Distance outer Helmholtz plane	d_H	0.55×10^{-9}	m
Zeta potential	ζ	30×10^{-3}	V
Solvent dielectric constant	ϵ_m	80	
Inverse Debye length	κ	1.04×10^7	m^{-1}
General constants			
Boltzmann's constant	k_B	1.38066×10^{-23}	J/K
Temperature	T	293.15	K
Avogadro's number	N_A	6.022×10^{23}	
Solvent viscosity	η	10^{-3}	Pa s
Elementary charge	e	1.602177×10^{-19}	C
Permittivity of vacuum	ϵ_0	8.854×10^{-12}	CV^{-1}m^{-1}

Figure 3.15: Osmotic pressures (left) and diffusion constant (right) in dependence of particle volume fractions for silica spheres with 200 nm diameter at an ionic strength of 10 μmol/L. Negative pressures and diffusion constants indicate aggregation, the decline of the osmotic pressure indicates a phase transition (see text).

Figure 3.16: Osmotic pressures (left) and diffusion constant (right) in dependence of particle volume fractions for gold nanocrystals with 6 nm diameter at an ionic strength of 1 mmol/L. Entropic stabilization becomes relevant at these particle sizes. Negative pressures and diffusion constants indicate aggregation, the decline of the osmotic pressure indicates a phase transition (see text).

concentrations. When working with particles around or below 10 nm in diameter it might therefore become necessary to introduce additional stabilization (e.g., through polymers), and to tune this stabilization such that an assembly is still possible.

A common additive to stabilize colloids at higher concentration are polymers, which increase stability through entropic effects [154]. For example, the water-soluble polyvinylpyrrolidone (PVP) adsorbs on negatively charged colloids, including gold nanocrystals, to form a low-density layer that does not easily overlap with others. The colloidal suspension of gold nanocrystals used in Chapter 5.4 contains surfactants, which do not only change the wetting behavior of the colloid, but also increase their stability at higher concentrations. It is not easy to quantify

the polymer concentration in the accumulation zone during assembly —
the polymer is likely to form a region of increased concentration as well
— but we can compare the situation both in the absence and presence
of the surfactants, namely, sodium dodecyl sulfonate (SDS) and Triton,
a class of commercial octylphenol ethoxylates from UNION CARBIDE.

While we clearly do not want particles to agglomerate in the accumu-
lation zone, the assembly of monolayers or multi-particle structures is
akin to agglomeration, albeit in a directed fashion. A very well-stabilized
colloid might therefore be harder to assemble into certain structures. For
example, if particles are flowing into a channel where they should ar-
range to form lines, the driving force has to overcome the repulsive in-
teractions such as to arrange the particles in close proximity. Again it
is hard to analyze the situation at the assembly front directly, but it is
conceivable that the concentration of counterions increases sufficiently
inside a channel to lower electrostatic repulsion. We shall discuss this
aspect in some more depth later.

Concentration profiles. At the gas-liquid-interface, similar to the mem-
brane-colloid-interface in ultrafiltration, it is reasonable to assume at
least one densely packed monolayer of particles. In ultrafiltration, it
is customary to assume the volume fraction of this layer to be at the
critical volume fraction ϕ_c, where the transition between fluid and solid
phase in the colloid occurs. Here, we do the same to obtain a boundary
condition of the diffusion-convection equation (Eq. (3.98)). We can then
integrate the equation to calculate the polarization layer thickness λ:

$$\int_{z=0}^{z=\lambda} \mathrm{d}z = \frac{1}{v_\mathrm{w}} \int_{\phi_\mathrm{wall}}^{\phi_\mathrm{bulk}} \frac{D(\phi)}{\phi} \mathrm{d}\phi. \tag{3.121}$$

The value of the integral,

$$I = \int_{\phi_{\text{wall}}}^{\phi_{\text{bulk}}} \frac{D(\phi)}{\phi} \, \mathrm{d}\phi, \qquad (3.122)$$

can be evaluated numerically.

For gold crystals (60 nm diameter), assuming a volume fraction at the boundary of $\phi_{\text{wall}} = 0.3$ and a bulk volume fraction of $\phi_{\text{bulk}} = 2 \cdot 10^{-5}$, the integral equals $-2.4 \cdot 10^{-10}$ m^2/s. From the hydrodynamic model in Section 3.3.1, we take the liquid velocity close to the boundary at a temperature of 27 °C and at 50% relative humidity, which is around $2.5 \cdot 10^{-7}$ m/s. The polarization layer thickness (Eq. (3.121)) then becomes $\lambda \approx 963$ µm. This is in the range of accumulation zone lengths that we observe experimentally after long assemblies.

For polystyrene beads (500 nm diameter) we assume a relatively large volume fraction at the boundary of $\phi_{\text{wall}} = 0.6$, as they are much harder to destabilize, and a bulk volume fraction of $\phi_{\text{bulk}} = 0.01$. The integral then evaluates as $-2.9 \cdot 10^{-10}$ m^2/s, leading to a polarization layer thickness of $\lambda \approx 1144$ µm, in good qualitative agreement with experimental data.

The volume fractions at the boundary have so far been assumed *a priori*, with the solid-liquid transition of the concentrated colloid as a guide. In principle, it is possible to use the length of the accumulation zone (corresponding to the polarization layer thickness) that we can measure experimentally to estimate the boundary volume fraction. This estimate will not be very precise, for our model disregards both surface effects at the gas-liquid interface and the hydrodynamic effects of the accumulation zone on the bulk flow. It is useful, however, to provide upper and lower bounds, as they are compiled in Table 3.2. Experimentally, we find that very short accumulation zones inhibit particle assembly en-

Table 3.2: The thickness of the polarization layer depending on boundary conditions at a liquid velocity of $v_b = -2.4 \cdot 10^{-10}$ m^2/s.

Particle	Bulk ϕ_{bulk}	Boundary ϕ_{wall}	Integral Eq. (3.122) $I/(10^{-11}$m^2/s)	Pol. layer $\lambda/(\mu$m)
PS	0.01	0.1	−1.56	62
PS	0.01	0.2	−10.4	416
PS	0.01	0.3	−19.6	784
PS	0.01	0.4	−25.2	1007
PS	0.01	0.5	−28.0	1121
PS	0.01	0.6	−28.6	1144
Au	3.2×10^{-5}	0.01	−4.89	196
Au	3.2×10^{-5}	0.1	−7.05	282
Au	3.2×10^{-5}	0.2	−13.9	555
Au	3.2×10^{-5}	0.3	−24.1	963

tirely, and we can use the values given here to test possible explanations of this behavior, as they are given in the next section.

3.3.3 Microscopic transport

When we calculated the rates of monolayer formation for thiols in Section 3.2, the thiol concentration at the gold surface provided a boundary condition for the kinetic equations that describe the rates of surface reaction. Now that we have obtained the concentration ranges that can occur in the colloidal suspension, it would be desirable to have such a kinetic expression for the assembly of colloidal particles to calculate the rate of assembly and the yield for different assembly conditions.

Such an expression is much harder to find for colloidal systems, however. In thiol adsorption, the scales are well-separated: thiols are much smaller than the smallest printed feature, and molecular interactions happen much faster than the diffusive transport of molecules. In colloid

assembly, the particle diameters are often comparable to feature sizes of binding sites, and the directed transport that brings the particles close to the surface often is identical to the mechanism that finally assembles them on the surface.

In the following, we will calculate numerical values for some of the expressions obtained in Section 3.1. Two particle systems will be considered: the 500 nm-diameter polystyrene beads (named "PS beads" in the following) and the 60 nm-diameter gold nanocrystals (named "Au crystals" in the following). The "standard arrangement" of particles that we use has 20000 particles arranged in an image on a square with a 90 μm side length (for the exact geometry, see Figure 5.66). The binding sites are circular, with a diameter identical to, or slightly larger than, the particle diameter.

The results can be compared with experimental observations, to check the used models and to assess the applicability of alternative assembly methods. Unless otherwise noted, the values used in this section are given in Table 3.3.

The assembly from a bulk colloid which covers the entire surface and where all binding sites are active simultaneously is the simplest case. Assuming a final assembly yield of 99%, the basic assembly isotherm of Eq. (3.6) (which assumes perfect binding sites without any statistical limitations) predicts an extremely short assembly time on the order of 0.5 μs for Au crystals and 0.04 μs for PS beads. At high concentrations, this assembly method can therefore be extremely rapid. At lower concentrations, however, depletion will occur which even for the (rather sparse) standard arrangement. After half the sites have been occupied, $\delta_{1/2} \approx 50$ μm of both colloids would have been depleted, and it would take a time on the order of $\tau_{\text{diff}} \approx 347$ s for Au crystals and $\tau_{\text{diff}} \approx 2907$ s for PS beads to replenish particles through diffusion. Thus, such an as-

Table 3.3: Numerical values of variables used for the evaluation of kinetic expressions in this section. Diffusion constants were calculated using the STOKES–EINSTEIN equation (Eq. (3.99)).

Property		Value	Unit
Au crystal diameter	d_P	60	nm
Au crystal bulk concentration	c_c	2×10^{13}	L^{-1}
Density of Au crystals	ρ_{Au}	19300	kg/m^3
Diffusion constant of Au crystals	D_0	7.2×10^{-12}	m^2/s
PS bead diameter	d_P	500	nm
PS bead bulk concentration	c_c	1.9×10^{13}	L^{-1}
Density of PS beads	ρ_{PS}	1050	kg/m^3
Diffusion constant of PS beads	D_0	8.6×10^{-13}	m^2/s
BOLTZMANN's constant	k_B	1.38066×10^{-23}	J/K
Temperature	T	293.15	K
Solvent viscosity	η	10^{-3}	Pa s
Target particle surface density	c_a	2×10^{12}	m^{-2}

sembly clearly is diffusion-controlled, and the characteristic diffusion times given are good indications of the expected assembly times (until half the assembly sites are occupied), unless there are directing force fields acting.

If the particles are confined in a thin layer, fewer particles are involved in the assembly process (increasing the assembly time), but those do not have to travel as far as in an unbound system. Using Eq. (3.22) we obtain a lower limit for the standard assembly, with just sufficient particles in the confined volume to fill all assembly sites of the standard assembly. The time to fill 99% of the sites is then larger than approximately $18000 d_P^2 / (4DN_0)$, or more than 113 µs for gold crystals and more than 65 ms for PS beads. This seems very fast and might well be a crude limit, and it assumes (perhaps unrealistically) that the diffusion constant for

the diffusion in the confined system is that of the bulk. Notice also that the last gold crystal to be assembled will (on average) diffuse for more than about 7 min until it finds its assembly site, while the last PS bead even requires more than 62 min on average to find the last binding site.

These figures suggest that a high concentration is often required for a high-yield assembly to be accomplished within a reasonable time. In addition, there are statistical effects which have not been considered so far. According to Eq. (3.77), the concentration required for a 99% yield with an instantaneous assembly process is $4.6/V_c$, and if we assume a hemispherical assembly volume with ten times the radius of the assembled particles (a very optimistic assumption), we need particle concentrations on the order of 10^{18} L^{-1} for Au crystals and 10^{15} L^{-1} for PS beads. At their original concentration, the average yield is only $\gamma \leq 0.113\%$ for gold crystals and $\gamma \leq 46.3\%$ for PS beads.

If we assume the assembly process to have capture particles not only at one moment in time, but during a certain "integration time" τ, the yield will increase depending on the particle flux into V_c. According to Eq. (3.39), this flux is (for a hemispherical assembly volume with radius a) 1.94 Hz for Au crystals and 22.8 Hz for PS beads. Thus, to increase the assembly yield from 0 to 99%, τ would have to be 2.4 s for Au crystals and 0.2 s for PS beads.

3.3.4 Experimentally observed mechanisms

We can now compare the theoretical values to check their assumptions against experimental observations. For this work, particles below 1 μm were assembled using convective and capillary assembly. I will use results from these assemblies (discussed in more detail in Section 5.3 and 5.4 here together with more detailed kinetic studies from [121]).

Convective assembly.   As a first step, we investigated the influence of the temperature on the formation of monolayers from suspensions of PS beads on an oxidized PDMS surface. We recorded the evolution of the assembly rate for temperatures between the dew point and 30 °C. The velocity of the surface v_s was adjusted such that it coincided with the growth velocity v_c of the monolayer, $v_c \approx v_s$, providing a measure of the growth rate. In accordance with previous studies [47,144], the assembly rate depended on the original particle concentration c. It also increased (nonlinearly) with the assembly temperature. When using a suspension with a solid content of $\phi = 0.5\%$, the assembly velocity increased from stagnation at the dew point to 10 μm/s at 28 °C. At a lower volume fraction of $\phi = 0.1\%$, it only increased to 1.5 μm/s. An experimental challenge here is that the small suspension volumes used change their concentration rather rapidly during the assembly.

The PS beads moving from the bulk suspension to the wetting layer are visible under the microscope. Particle tracking allows us to estimate their velocity, which was found to be around 19.8 ± 0.8 μm/s at a temperature of 20 °C and a substrate velocity of 0.5 μm/s. At temperatures close to the dew point, where the evaporation from the solvent is negligible, no directed particle motion remained. The Brownian Motion of the particles was, however, clearly visible.

Such observations prove that the driving force for the particle assembly really is evaporation, as we had assumed so far in this chapter. They also show that for PS beads with 500 nm diameter, Brownian Motion is weak even at low-to-moderate liquid flow rates, so that the particles' motion is governed by the hydrodynamic flow field situation. For Au crystals it is hard to discern single-particle trajectories, and the stability of the convective assembly is lower, but we have no indications from experiments that would suggest that particle motion deviates from liquid

motion.

The nonlinearity that we observe in assembly velocity versus temperature is probably an outcome of the changing hydrodynamic situation due to larger zones of evaporation at higher substrate velocities. The flux calculations above did not take such effects into account, because they focused on capillary assembly. This is also true for the values obtained from the CFD simulation in Section 3.3.1: the thin wetting film and the presence of the assembled monolayer efficiently increase the evaporation rate and thus increase the assembly velocity as compared to the CFD model.

Capillary assembly.   The most prominent feature of capillary assembly is the formation of an accumulation zone during the assembly if the contact angle is between about 30° and 60°. This accumulation zone occurs for all particles we have investigated, which include the PS Beads and Au crystals, but also silver nanocubes, silica beads and even rod-shapes metal crystals. It occurs for particles stabilized both with positive and negative charges.

The accumulation zone appears to be a prerequisite for the assembly of particles. In the absence of such a local concentration increase, it is hard to capture any particles in the binding sites. Because the extent (and even existence) of the accumulation zone depends on the substrate temperature, we could investigate the relationship between accumulation and yield by investigating the relationship between substrate temperature and assembly yield. Thus, the temperature was changed during an assembly of PS beads (0.1% solid content) on a hydrophobic PDMS template. The substrate velocity was kept constant at 1 µm/s, while we varied the temperature between 27 °C and 32 °C. Figure 3.17 shows the evolution of the temperature and assembly yield versus time
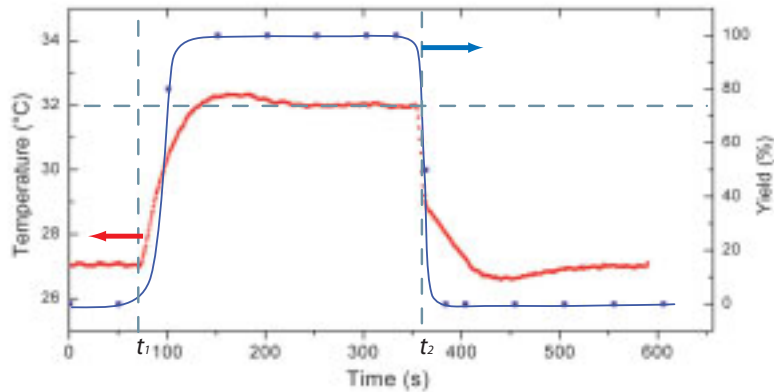
Figure 3.17: Experimentally determined yield of the assembly depending on the colloid temperature.

during one cycle.

Almost no particle accumulation was visible at 27 °C, and no assembled particles could be found. Upon increasing the temperature to 32 °C, an accumulation zone formed close to the three-phase boundary line. During this transitional period, the yield rapidly increased to 80% for a substrate temperature of 30 °C, to then reach about 99% at the target temperature of 32 °C. This temperature was maintained for the following 200 s. The accumulation zone continued to grow until it reached a stable length, but we did not investigate these dynamics in any detail. After 360 s, the temperature was reduced to the original 27 °C, which led to a drop from high yield to no assembled particles in 20 s. Simulta-

neously, we observed rapid depletion of the accumulation zone, which finally disappeared to leave a situation very similar to the original one.

We can explain this strong dependence of the yield on accumulation solely with the statistical arguments from Section 3.1.2. If the capture volume of the particle binding sites are on the order of the particle size, and if the assembly mechanism can be seen as instantaneous, the expected yields at the original particle concentrations are below 10% for PS beads (and even below 0.1% for the smaller Au crystals). Because the experimentally determined yields without accumulation are very low indeed, we conclude that the effects of the hydrodynamic drag, topographical confinement and particle interactions do not increase the yield, or only do so at high concentrations, where it cannot be distinguished from the purely statistical effect of a higher particle concentration. On the other hand, if the local particle concentrations reach the values predicted using the polarization layer model from Section 3.3.2, and if we again assume capture volumes on the order of the particle size, we can expect assembly yields exceeding 99%, as we observe them. Thus, while it is difficult to prove the sole responsibility of statistical effects for the yield, it is clear that capillary assembly is always limited by statistical effects. They have to be overcome first to enable assembly, which can be done by local concentration increase due to the accumulation zone.

The length of the accumulation zone varies depending on the used particles, the contact angle, temperature, humidity, substrate velocity and sometimes even the surface properties of the template. It also changes with time, sometimes without reaching a constant values even after tens of minutes. The observed lengths of the accumulation zones are generally much shorter than the equilibrium lengths given in Table 3.2. The equilibrium situation seems not to be reached in most cases. However, the strong effect of the concentration increase on the assem-

bly yield implies that the local concentration is changed markedly, as was predicted by the concentration polarization models of above.

Another feature of the accumulation zone that supports its interpretation as a product of a diffusion-convection balance is the existence of a small temperature interval in which the yield increases very rapidly. Such a rapid change could be explained with a radical change in the hydrodynamics inside the liquid volume, but the CFD simulations show that these changes are gradual and that there is no qualitative difference between temperatures several degrees above and below the observed transition temperature. The concentration polarization, in contrast, often features a strong dependence on the liquid velocity, in particular at short polarization lengths (refer to Table 3.2).

One way to investigate the influence of other parameters on the accumulation zone and the assembly yield is to look for the critical temperature range in which the yield changes rapidly and find its dependence on other parameters. For different bulk particle concentrations and different substrate velocities, we increased the assembly temperature until the yield increased above 98%. The resulting critical temperatures are plotted in Fig. 3.18. It is particularly interesting to see that the increase in necessary substrate temperature (and, thus, the required liquid velocity) decreases with increasing volume fractions, and that the proportionality constant between required temperature and substrate velocity generally is below unity. Both facts cannot be explained with simple minimum flux requirements, but are in agreement with the diffusion-convection model.

Influence of surfactant concentration. So far we have not discussed the details of the two-phase microflow that finally is responsible for the particle immobilization. It is hard to observe its dynamics in detail, and
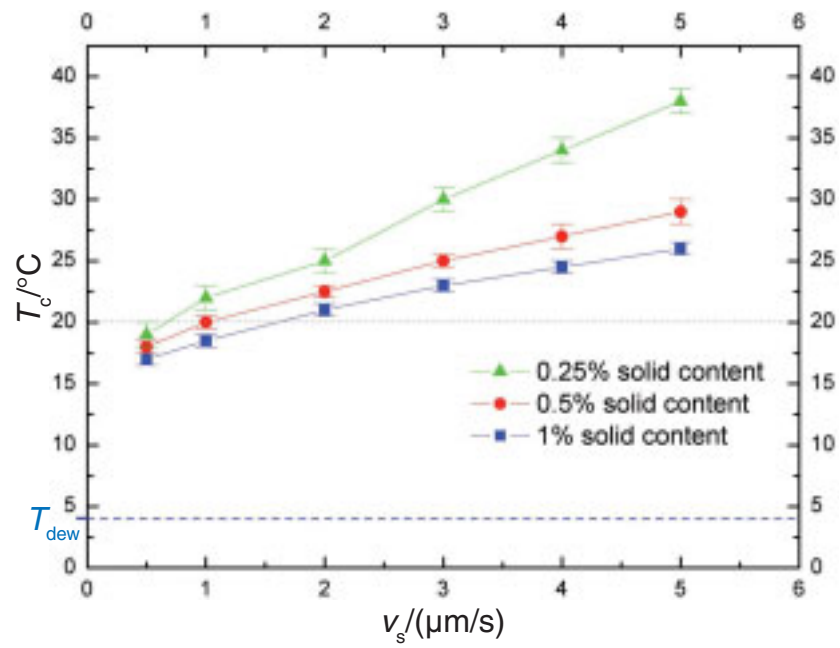
Figure 3.18: Experimental dependence of the critical assembly tempera-
ture (see text) on the substrate velocity and the particle con-
centration.

it is very hard to simulate such flows. One experimental probe is the surfactant concentration which is easily changed and influences the contact angle of the liquid. It might also change properties of the suspension, however.

The main experimental result from systematically changing surfactant concentrations is that there exists an optimum contact angle for particle assembly. For PS beads this contact angle is $60 \pm 4°$, and no assembly is possible with higher contact angles, even if an accumulation zone is visibly established. For lower contact angles, assembly is often possible, but pinning becomes large and the selectivity of the assembly process degrades. For gold particles, the optimal angle is around $50°$, although assembly is possible at higher angles (at least until $60°$), where it is often harder to create a stable accumulation zone. At much smaller contact angles the assembly mode changes from capillary to convective assembly with its deposition of mono- and multilayers of particles.

All models developed above are independent of the actual capturing mechanism, and even the size and geometry of the capture volume V_c does probably depend less on the final moment of the assembly and more on the short time interval before and the confinement involved. The contact angle is likely to change both the confinement and the final arrangement of particles inside the binding sites by influencing the amount of pinning that occurs.

Influence of pattern geometry. Pinning is caused by geometrical features on the template, be they convex or concave, and is visible when observing the assembly process microscopically. The pinning finally leads to a small liquid volume to be trapped behind an obstacle together with a particle, or the meniscus to break up over a feature, so that the confined particles cannot escape from a capture site. This pinning is
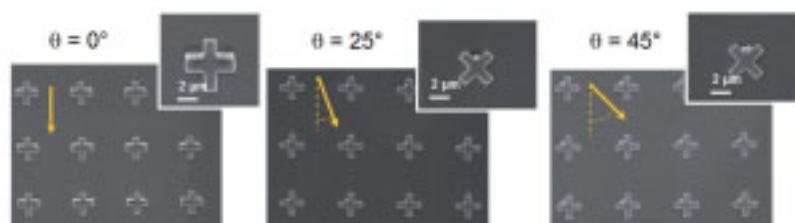
Figure 3.19: Results of PS bead assembly using the same template geometry under different assembly angles (the yellow arrows indicate the motion, normal to the contact line).

strongly geometry-dependent.

The contact angle during the assembly therefore has a large influence on the assembly results. Figure 3.19 shows three SEM images of PS beads (0.5% solid content, substrate velocity 1 μm/s, substrate temperature 25 °C). Depending on the amount of pinning created, the number of particles captured varies. These results also indicate that the capillary assembly process is "instantaneous" in the sense discussed above: only in the very latest moment of breakup do particles actually get immobilized, thus, there is only one particle deposited when assembling into the open corner of one cross.

One interesting question that is still not entirely resolved is the role of confinement versus capillary bridges in the immobilization. Some results from the assembly of Au crystals suggest that it is mainly confinement that finally traps them in binding sites. For example, relatively shallow holes are sufficient to trap the nanocrystals even at high density, while it is hard to capture them in convex features. We did not succeed in capturing single crystals in structures similar to the corners shown above. On the other hand, there are cases where PS beads are

captured in groups when using larger concave structures, while their position varies over many of these capture sites and is not confined to the corners. Thus, both mechanisms seem to appear for different particle sizes, although confinement might be governing smaller particles more frequently.

If the binding sites are approximately as large as the particles, the assembly accuracy is set by the geometrical confinement and is only limited by the lithographic resolution. If larger sites are used (for example to increase the yield), we observe differences between PS beads and Au crystals. In Fig. 3.20, the larger PS beads are deposited at identical positions in all holes. In contrast, the position of Au crystals in holes varies across different binding sites, although a bias towards one side of the site (in the direction of the meniscus motion) is clearly visible in Fig. 3.20. This might be due to the different geometries, which change both the pinning of the colloid's meniscus on the binding site and the remaining liquid volume after meniscus has passed. It might also be due to a decrease in the "binding strength" of the smaller sites due to the different hydrodynamic situations, an aspect that has to be considered when going to far smaller particles. In general, positional variations are expected to drop for smaller, lighter particles if the system can be described by a harmonic oscillator (Eq. (3.80)).
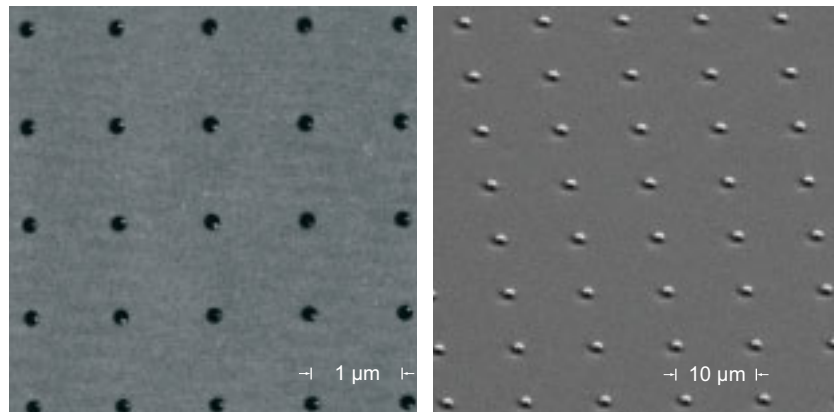
Figure 3.20: Assembly accuracy in large binding sites depending on the particle diameter. Gold nanocrystals (left plot, AFM topography) exhibit considerably stronger deviations in assembly position than PS beads (left image, electron micrograph).

3.4 List of symbols

Symbol	Description	Unit
$\mathcal{A}$	Drift vector	m/s
A_{bs}	Overall area of binding sites	m^2
$A_{particle}$	Area occupied by single particle	m^2
A_{void}	Unoccupied area	m^2
A_i	Probability of i particles leaving V_c	1
a	Particle radius	m
$\mathcal{B}$	Diffusion tensor	m^2/s
b	Covolume	m^3
c	Concentration	m^{-3}
c_a	Saturation surface particle coverage	m^{-2}
c_c	Colloid bulk concentration	m^{-3}
c_{ion}	Ion concentration	mol/m^3
c_{ML}	Thiol concentration in monolayer	mol/m^2
c_s	Particle concentration close to surface	m^{-3}
c_{thiol}	Surface concentration of free thiol	mol/m^2
c_0	Initial concentration	mol/m^3
$\tilde{c}$	Dimensionless concentration	1
D	Diffusion coefficient	m^2/s
$D_{water-air}$	Diffusivity of water vapor in air	m^2/s
D_0	STOKES–EINSTEIN diffusion coefficient	m^2/s
d	Particle-particle distance	m
d_b	Diameter of binding site	m
d_h	Distance to outer HELMHOLTZ plane	m
d_p	Particle diameter	m
E_i	Probability of i particles entering V_c	1
E_o	Energy of the harmonic oscillator	J

Symbol	Description	Unit
e	Elementary charge	C
$F(t)$	Force	N
$F_{\text{electrostatic}}$	Electrostatic force between particles	N
F_{VdW}	VAN DER WAALS force between particles	N
g	Gravitational field strength	N/kg
H	HAMAKER's constant	m^2/s
$h(x,y)$	Height	m
J	Particle flux through surface	$m^{-2}s^{-1}$
J_{ML}	Particle flux required for monolayer formation	s^{-1}
J_{reaction}	Reactive flux to surface	$mol/(m^2 s)$
J_{s}	Flux of particles to surface	$mol/(m^2 s)$
$\mathcal{K}$	Equilibrium constant of adsorption	1
$K(x)$	Force field	N
k_{B}	BOLTZMANN's constant	J/K
$L(\phi)$	Sedimentation coefficient	1
l	Characteristic length	m
l_{diff}	Diffusion length	m
l_{M}	Meniscus length	m
M	Particle mass	kg
N	Number of particles	1
N_{a}	AVOGADRO's number	1
$N^{\dagger}$	Lifetime (in steps) of particle	1
$\dot{\vec{n}}_{\text{P}}$	Particle number flux	$m^{-2}s^{-1}$
$n_{\text{s}}(x,y)$	Amount of substance transferred onto surface	mol/m^2
P	Probability for a particle to leave V_{c} during τ	1
$p(x,t|y,0)$	Probability density function of particle position	1
p_{W}	Saturation vapor pressure of water	Pa
q	Dimensionless concentration of binding sites	1

Symbol	Description	Unit
R_{ads}	Rate of surface reaction	mol/(m^{2}s)
R_{n}	Number of distinct sites visited after n steps	1
$\tilde{r}$	Dimensionless radius	1
$\tilde{r}_{\text{cell}}$	Dimensionless electrostatic cell radius	1
r_{a}	Rate of particle assembly	s^{-1}
$\vec{r}$	Particle position	m
r_{cell}	WIGNER–SEITZ cell radius	m
Re	REYNOLD's number	1
S	Stiction probability	1
S_{cell}	Surface area of WIGNER–SEITZ cell	m^2
S_{h}	Area occupied by a particle in a hcp lattice	m^2
s	Diffusion length of single particle	m
T	Absolute temperature	K
T_{air}	Air temperature	K
t	Time	s
t^*	Characteristic diffusion time	s
t_{a}	Assembly time	s
u	Particle velocity	m/s
u_0	Sedimentation velocity at infinite dilution	m/s
$\dot{V}$	Volumetric flow	m^3/s
V_{c}	Capture volume of binding site	m^{-3}
V_{M}	Molar volume	m^3/mol
$\vec{v}_b$	Bulk colloid velocity	m/s
v_{c}	Monolayer growth velocity	m/s
v_{s}	Substrate velocity	m/s
W	Probability	1
W_{assy}	Probability of assembling a particle at a given site	1
x, y, z	Cartesian coordinates	m

Symbol	Description	Unit
$\tilde{x}$	Dimensionless lateral coordinate	1
$Z(\phi)$	Compressibility factor	1
$\tilde{z}$	Dimensionless surface-normal coordinate	1
α	Dimensionless shear plane radius	1
β	Dimensionless friction coefficient	1
χ	Friction coefficient	kg
Γ	GAUSS-distributed random variable	1
γ	Assembly yield	1
δ	Depletion layer thickness	m
λ	Polarization layer thickness	m
ϵ	Fraction of surface covered	1
ϵ_{m}	Dielectric constant of medium	1
ζ	Zeta potential	V
η	Viscosity	Pa s
Θ	Time-averaged flux through given surface	s^{-1}
θ	Fraction of occupied sites	1
κ	Reciprocal DEBYE length	m^{-1}
ν	Average number of particles in ν	1
Π	Osmotic pressure	Pa
$\Pi_{\mathrm{electrostatic}}$	Electrostatic part of osmotic pressure	Pa
Π_{entropic}	Entropic part of osmotic pressure	Pa
Π_{VdW}	VAN DER WAALS part of osmotic pressure	Pa
$\tilde{\rho}$	Reduced density	1
ρ_f	Density of continuous phase	$\mathrm{kg/m^3}$
ρ_{Au}	Density of gold particles	$\mathrm{kg/m^3}$
ρ_{ML}	Particle density of monolayer	m^{-2}
ρ_{PS}	Density of polystyrene particles	$\mathrm{kg/m^3}$
τ_{b}	Characteristic time of Brownian Motion	s

Symbol	Description	Unit
τ_{diff}	Characteristic diffusion time	s
τ_{p}	Characteristic time of inertial response	s
Φ_{VdW}	VAN DER WAALS interaction potential	J
ϕ	Volume fraction	1
ϕ_{bulk}	Bulk volume fraction	1
ϕ_{c}	Critical volume fraction of phase transition	1
ϕ_{hcp}	Density of hexagonal dense packing	1
ϕ_n	Probability of surviving n steps	1
ϕ_{wall}	Boundary volume fraction	1
Ψ	Dimensionless electrostatic potential	1
ψ	Electrostatic potential	V
$\psi_{\text{diffusion}}$	Dimensionless diffusive flux	1
ω	Frequency of harmonic oscillator	Hz

4 Particle adhesion

Conventional printing often involves the transfer of a liquid ink from one surface to another, and it is a key question in the printing industry which surfaces are printable using which inks. When using an adhesion-based handling scheme for particles, the situation is similar. Particles need to be transferred from one surface to another only by the difference in adhesive forces using an *adhesion cascade*.

Adhesion is a complex problem: the breakage of an adhesive bond is a dynamic process, so that equilibrium arguments can mislead, and adhesion is caused by a number of different forces that can depend on minute details of the geometry and chemistry of the surfaces involved. Because of its practical importance, the engineering community has developed a number of heuristic principles and phenomenological expressions for adhesion, but these are often less than helpful when introducing new systems, as we do it here.

The central question of adhesion may be summarized as follows: "Why does anything not stick?" In principle, dry bodies that are in close proximity always attract each other rather strongly [91]. In reality, however, very rarely are there clean, smooth surfaces that come into contact over their entire area. Microscale asperities and surface contamination reduce the adhesive forces until they are easily overcome by other forces.

As we go to smaller dimensions, however, the particle size reaches the size range of the asperities mentioned. Small objects also have large surface-to-volume areas and well-defined surfaces. It appears feasible to provide sufficient adhesion at such length scales, and to create adhesion cascades to handle these objects completely passively.

In this chapter, particle adhesion is discussed as it occurs during particle assembly and in particular during particle transfer. We first analyze the origin of these adhesion forces in Section 4.1, to decide which forces dominate the particle-surface system. The geometry turns out to

be vital for a proper model, and Section 4.2 presents both theoretical and experimental results showing that differences in contact area need to be considered and can be utilized in particle transfer. Finally, we draw conclusions from these results in Section 4.3 for the adhesion cascades used in particle transfer.

4.1 Forces in particle adhesion

All forces that contribute to bulk cohesion in materials can also occur in adhesion. This includes strong covalent, ionic (i.e. electrostatic) and metallic bonds and the weaker VAN DER WAALS interactions. In a classical review [104], KRUPP classified the different interactions in *class I*, which includes the long-range attractive interactions as they originate from electrostatic and VAN DER WAALS forces, *class II*, which includes those short-range interactions that result from strong covalent bonds and weaker (say, hydrogen) bonds, and a *class III*, which covers the interfacial reactions, including interdiffusion and mixing, alloying, and similar effects. KRUPP then argued that forces from classes I and III were those of primary importance, while class III generally was less important at room temperature.

To verify this assumption, the early researchers used actual particles, which they sprinkled on surfaces and analyzed for adhesion in centrifuges and similar setups [14]. With the invention of the atomic force microscope, it became possible to measure adhesion forces more directly, and there is a large body of literature devoted to the adhesive interactions between AFM tips (or particles mounted on these tips) and the substrate that the tip is moved on. Force-distance curves could now be measured with high precision, which enabled the identification of different contributing forces. AFM experiments led to the recognition of

liquid menisci as an important contributor to adhesion, and it is likely that such forces play a role in dry particle systems as well [28].

The contact mechanics of an AFM tip with a substrate are far better defined (if the tip is new and of high quality) than those between the often rough particles and the surfaces, which greatly simplifies the data interpretation. Another well-defined contact is provided in the Surface Forces Apparatus, in which two flat surfaces come into contact which can be observed using interferometry. This geometry is even further from particle adhesion, and we shall not discuss it any further, although very important results on surface interactions have been obtained using it [79]. Later in this chapter, we will see how the complex geometry of particles can affect the adhesion forces occurring.

In this chapter we will assume that VAN DER WAALS forces are the main origin of adhesion. This does not exclude capillary forces, for they are a consequence of wetting layers that depend on the wettability of a surface, which in turn is connected to the VAN DER WAALS forces it exerts on the liquid film. We explicitly neglect all forces from KRUPP's classes II and III, unless in special cases where we will explicitly mention them. Some aspects of class-III-interactions will still be covered insofar as they change the interfacial areas between particle and surface and thus effect all short-ranging forces, such as VAN DER WAALS attraction.

VAN DER WAALS forces originate from interactions between the electrons in the attracting bodies. It was HAMAKER who first showed (by pairwise summation of these interactions over all volume elements of two macroscopic bodies) that these forces do not decay with distance d according to a d^{-6} power law, which would make them irrelevant for any but extremely small objects, but will frequently follow d^{-2}-type laws in relevant systems [141]. He went on to introduce a constant to characterize the effective VAN DER WAALS (vdW) force independent of

the geometry, the HAMAKER constant H. This constant has become extremely popular for the calculation of attractive vdW forces, because it produces simple expressions for many important geometries. It does not take into account several aspects, however, and it suggests a weak geometry-dependence, where the actual adhesion is extremely dependent on the precise geometry. We shall come back to this point later.

Some of the simple expressions that occur for the vdW potentials when using HAMAKER constants are worth being repeated here. A very small sphere with radius a at a large distance d from a surface has a potential energy

$$E_{\text{vdW}} = -\frac{2H}{9} \left(\frac{a}{d}\right)^3,$$
(4.1)

which leads to a d^{-4}-dependence of the corresponding force. It is a common mistake, however, to apply this form for particle adhesion. In the limiting case of a perfect sphere in very close proximity of a large, thick slab, the potential becomes

$$E_{\text{vdW}} = -\frac{H}{6}\frac{a}{d},$$
(4.2)

so that the force only depends on the square reciprocal of the distance.

Even this expression can be misleading. Consider the corresponding expression of a cubic particle with a side length L:

$$E_{\text{vdW}} = -\frac{H}{12\pi} \left(\frac{L}{d}\right)^2.$$
(4.3)

Now the distance-dependence of the adhesion force is proportional to d^{-3} and to the area of interaction, while the particle radius a was only directly proportional to this force for spheres. Geometry therefore should play an important role if vdW forces are governing particle adhesion.

It is worth mentioning here that the prevalence of vdW forces in adhesion has a long history of heated scientific debate. At the core of these debates lies the question for the actual (and not only the maximal) force necessary to separate two bodies, which requires knowledge of the energy dissipation mechanisms that play a role during this separation. At a conference in 1981 in Paris, DERJAGUIN therefore complained, after a review talk by MAUGIS,

> . . . it is difficult to understand at first the mechanical onesided approach to explain the adherence forces. For example, the pure mechanical approach can not give any explanation of the dependence of the peeling force versus rate function on pressure and content of the ambient gaz *(sic)* (. . .) (our results) aided to discover and investigate the role of donor-acceptor interactions in adhesion (. . .) It is mysterious that all is ignored in west-countries! [124]

Not only did the "Russian school" maintain that mechanically stored energy was the main reason of energy dissipation during the break of an adhesive bond, it also claimed that charge separation was ubiquitous even in equilibrium, and stronger than vdW forces.

What we are most interested in here is the maximum adhesion force depending on the geometry and material at the contact. During transfer, the particle will be in contact with two surfaces, and it will adhere to one of them after the surfaces have been separated. To a first approximation, both particle-surface junctions will be stressed until one of them breaks during the separation of the surfaces. The work of adhesion is therefore not decisive, it is the maximum force that the respective adhesive joint can withstand that determines on which surface the particle ends up.

Relevant are all effects that increase or decrease the maximum adhe-

sive force that occurs. Amongst them are the deformation and stresses
of the interface due to adhesion and the surface roughness on both sides
that change the contact areas, adlayers (due to contamination) in be-
tween the particle and the surface, and dynamic effects. The best-inves-
tigated items on this list are the deformation and stresses upon contact,
which we will discuss in the next section.

Adhesion is in general time-dependent, and if at least one involved
material is soft, the time-dependence can be discernible at moderate ve-
locities. For example, MEITL et al. show that the viscoelastic behavior
of an elastomer carrier allows one to tune particle adhesion via peel-
ing velocity. If the carrier is removed from the original substrate at a
high velocity (≥ 10 cm/s in their system), particles adhere to the carrier
and can be removed. On the target substrate the peeling is done at low
speed, so that the particles adhere to the substrate [127]. Such effects
are likely to play a smaller role for smaller particles, but they have to be
taken into account.

A very common occurrence in colloidal suspensions are adlayers that
occur during drying. Colloidal suspensions commonly contain stabiliz-
ing agents, be it the surfactants that are adsorbed on the particle sur-
faces during synthesis or additional polymers, or small amounts of ex-
cess precursors. As the colloid dries (e.g., during an assembly process),
these solution contents are deposited on the surface. They can create a
layer of material that behaves differently from both particle and surface,
thereby increasing the particle-surface distance and changing the vdW
situation as well as the contact area [178]. If they are hydrophilic (which
commonly is the case when coming from aqueous colloidal suspensions)
they might contain water that can form capillary bridges, further com-
plicating the situation. Figure 4.1 shows a micrograph of crystalline ad-
layers, obtained after a small amount of a commercial gold colloid (as

131
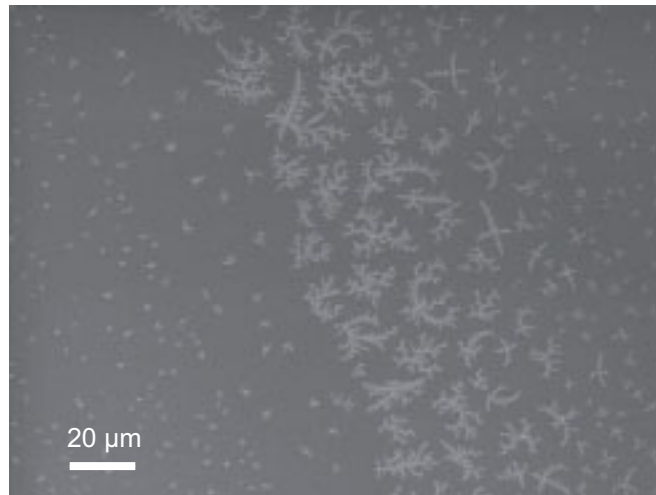
Figure 4.1: Electron micrograph recorded using the surface-sensitive in-lens detector showing adlayers deposited during the drying of a gold colloidal suspension.

used later in this work) had dried on a silicon surface. VdW forces are influenced even by very thin adlayers, and when the adlayer thickness exceeds the particle thickness, the actual substrate has little effect on the adhesion force anymore.

4.2 The area of contact in hard and soft systems

Adhesion forces strongly depend on the area of contact. For flat geometries, it is a good estimate to assume the area of contact to be proportional to the adhesion force. In reality, most contacts are tip-like, be-

cause most surfaces are not perfectly smooth and too hard to provide conformal contact. The actual area of contact therefore is established on contact through deformation of the involved surfaces. The final area has been described, with increasing precision and completeness, by models named after HERTZ, JOHNSON–KENDALL–ROBERTS, DERJAGUIN–MÜLLER–TOPOROV and finally MAUGIS, whose refined model is regarded valid for the adhesion of AFM tips and small particles [28]. These theories take the work of adhesion, W_A, and convert it into the maximum adhesion force F_A. For example, according to JOHNSON–KENDALL–ROBERTS-theory [84], the adhesive force is

$$F_A = \frac{3}{2}\pi a W_A, \tag{4.4}$$

which we can use as a reasonable estimate. With more complex geometries, the situation rapidly becomes intractable, and we are again left with upper limits, for example by assuming conformal contact.

When surfaces with complex geometries (e.g., surface roughness) come into contact with soft materials, conformal contact can arise. The soft material may deform sufficiently to come into molecular contact with the surface of the particle, depending on its elastic modulus [17]. If the yield strength of the soft material is sufficient, this creates a reversible adhesive joint with high strength. One material that has this combination of properties is polydimethylsiloxane (PDMS), a silicone rubber with an elastic modulus between 2.5 and 10 MPa. Its ability to establish conformal contact with surfaces is widely exploited in microcontact printing, where ink molecules diffuse through the intimate contact between a PDMS stamp and a target surface.

Likewise, the area of contact between a soft surface and a particle can be very different from that between a hard surface and a particle, de-

viating substantially from the predictions of the idealized theories mentioned above. For a microparticle having a rough surface, the actual area of contact is not a circular spot as predicted for a perfect sphere, it rather is a number of small circular contacts at positions where asperities of the particle come into contact with the substrate. It is very hard or impossible to calculate the resultant adhesion force, but it will often be lower than predicted from idealized pictures. The failure of the adhesive joints does not occur at once as soon as a critical contact area is reached, it proceeds stepwise while multiple contact points are split. A soft material can establish a much larger area of contact, even if its work of adhesion is nominally lower, and can thus create a greater adhesive force.

This also explains why the elastic modulus of the carrier material strongly influences adhesive strength, although classical theory predicts adhesion to be independent of any material properties of particle and substrate besides their work of adhesion per area. As we will see, it is possible to exploit this additional effect for the creation of adhesion cascades.

For nanoparticles, the situation is somewhat different. While most experimental studies available are concerned with larger gold particles [14], it is known that small particles can undergo structural conformations when deposited on hard surfaces [191]. The atomic-scale "roughness" of the interface creates extremely large stresses that cause very rapid deformation if the interface is clean. YEADON et al. have shown such "contact epitaxy" experimentally, GRYAZNOV et al. provide an extensive review on such effects [71]. If the substrate is from a soft material (as in the case of particle carriers), it will not induce particle deformations but can substantially deform itself, possibly even engulfing the particle [147].

One might also expect that the very short-ranged vdW forces will not
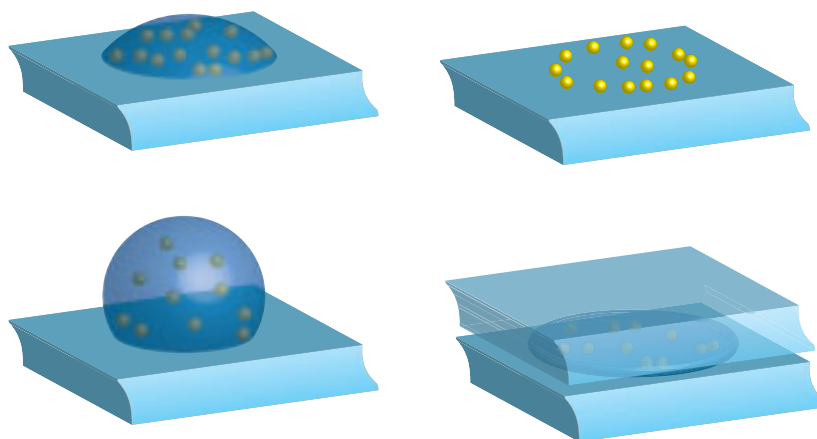
Figure 4.2: Simple particle distribution methods for adhesion studies. The unmodified colloid is deposited on an oxidized (and thus hydrophilic) PDMS carrier and left to dry (top row), or it is squeezed in between two hydrophobic PDMS surfaces, which prevent the formation of coffee stain rings.

strongly depend on geometry for very small particles, because the average particle-surface distance for a flat particle is similar (in absolute numbers) to that of a round particle. Experimental results contradict this assumption, however [97]. We have distributed particles with different geometries on flat surfaces, either by depositing a droplet of liquid on oxidized (hydrophilic) PDMS surfaces or by squeezing colloids in between two hydrophobic PDMS surfaces (Figure 4.2). This creates either the familiar "coffee stain rings" or randomly dispersed particles on the surface. The dried particles on their PDMS carriers were then brought into contact with oxidized, polished silicon surfaces, separated, and the transfer analyzed via scanning electron microscopy of the target substrate.
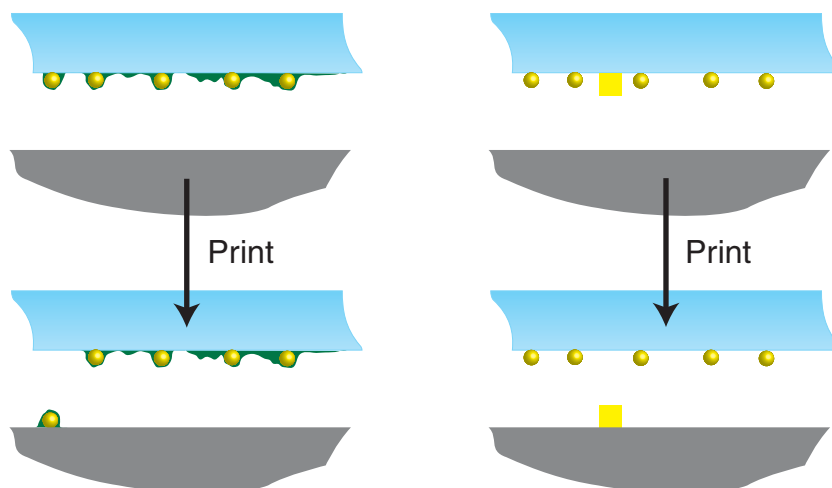
Figure 4.3: The effect of adlayers (left panel) and particle shape varia-
tions (right panel) on particle printing. Both can introduce
adhesion variations that severely limit the yield.

Particles deposited by such methods always feature adlayers from
other solution contents of the continuous phase. It is still meaningful
to compare the transfer results: adlayers are such a common occurrence
that their effect has to be taken into account for particle assembly as well.
The differences in transfer yield that occur are quite striking (Figure 4.3).
It is almost impossible to print single, spherical 60-nm gold particles, but
it is possible to print cubic particles of similar size at the same time: gold
colloids commonly contain such (100 nm to 300 nm side length) cubes,
and we find on the target substrate only them, and no spherical crystals.

Similar results occur when using silver nanocubes (which can be syn-
thesized selectively using surfactant systems, as discussed later in this
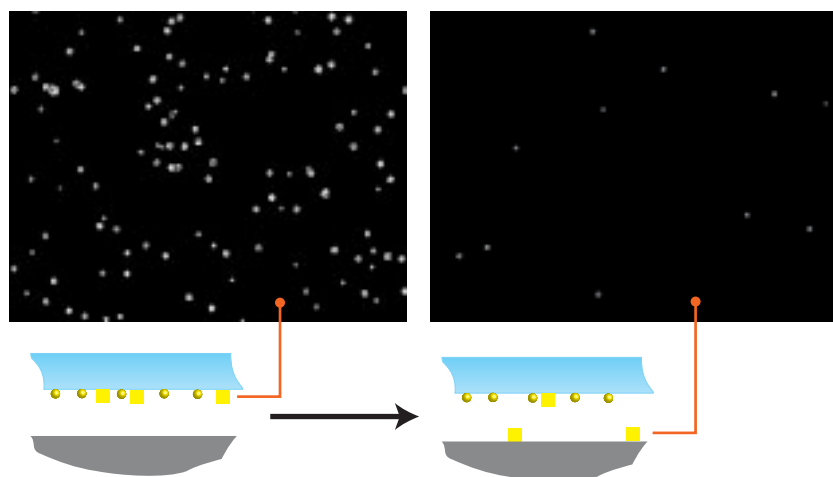
Figure 4.4: A mixture of 60-nm-diameter gold spheres and 100-nm-wide silver cubes (both from colloids) was deposited on a plasma-oxidized PDMS carrier to create sparse, mixed particle layers as shown in the left electron micrograph. The stamps were then brought into contact with an oxidized silicon surface. No gold spheres, but many silver cubes were transferred from the PDMS to the silicon oxide (right electron micrograph).

thesis) that were mixed with gold nanoparticles. Again, the spheres were not transferred, while a large fraction of the cubes left the carrier surface for the target silicon (see Fig. 4.4).

Another geometrical effect occurs when printing particle monolayers. It is generally much easier to print multiple nanoparticles in a dense layer than single nanoparticles, independent of the exact geometry. When printed, such multi-particle features tend to keep their structural integrity even after vigorous washing, and when they fail they remind of metals, by forming grains that keep their crystal structure and dislo-

cations that allow deformation. This behavior is likely due to the strong adhesion amongst nanoparticles and the contact-splitting effect of a particle layer in contact with a flat surface which increases the overall work needed to overcome adhesion, an effect well-known from other complex adhesion geometries (such as in biological systems [5]).

These results have led us to engineer the strength of adhesion in particle transfer mainly through engineering the area of contact. The next section discusses how this has been done for different particle size regimes.

4.3 Adhesion cascades

Traditional printing processes do not use an adhesion cascade, although printability is a major concern in gravure printing, offset printing and many other high volume techniques. Traditionally, the ink layer is split while being transferred to a surface, so that a part remain on the printing plate and another part is left on the target [93]. In particle printing, but also in microcontact printing of proteins and related techniques, we are interested in transferring the complete layer from the stamp to the substrate. Thus, tuning of adhesion is less a problem of tuning the ink properties and more a problem of tuning the particle-surface interactions.

One effect that we can exploit for this cascade is conformal contact. With larger particles, it allows us to provide sufficient adhesion to a soft carrier without having to resort to very large adhesion forces that could compromise the structural integrity of either particle or carrier. For small particles it is vital to provide a very intimate contact, and to provide a sufficient force that presses the nanoparticle against the substrate. This is the prerequisite for any adhesion tuning.

An example of large molecules that can be printed through an adhe-

sion cascade are proteins. Proteins form a dense layer on hydrophobic PDMS from solution, for example, which is easily transferred from the PDMS surface after drying. This is usually attributed to the surface energy difference between the (hydrophobic) PDMS and the (hydrophilic) target (usually silicon oxide or glass) [13]. The proteins are small and mobile enough to explore the energy landscape during contact and find a conformation on the hydrophilic substrate that is lower in energy than on the carrier.

Similar surface energy differences can be constructed for particle handling. We coat the templates for 100-µm-particles which are arranged by gravitational assembly with perfluorinated silane monolayers to create a surface energy that is even lower than that of PDMS, and we find that this coating reduces the strength of vibration needed to fluidize these particles. For smaller particles we use PDMS templates. This alone is not sufficient, however, to provide good yields.

Particle adhesion is characterized by wide distributions, mainly due to the strong distance dependence of the vdW forces detailed above. Nanoparticles are generally not mobile enough (unless printed wet) to find the minimum energy configuration, even if it would provide sufficient adhesion. An adhesion cascade that is to produce a high yield therefore needs to provide large energy differences. This is best done by using conformal *adhesion* layers that form a conformal contact with the particle that is larger than its interface with the carrier. For gold nanocrystals, for example, it is sufficient to have a 10 nm to 30 nm thick PMMA layer at elevated temperatures to increase the interfacial area such that the nanoparticles leave their carrier, although the surface energy of PMMA (around $30 - 40 \, \mathrm{mJ/cm^2}$) is similar to that of PDMS (around $40 \, \mathrm{mJ/cm^2}$). For glass microspheres, spin-on glass layers, which consist of a gel containing reactive silanol groups and a polymer com-

ponent, provide both conformal contact and chemical reactivity. It is remarkable that the transfer still is only possible at elevated temperatures, where the layer becomes soft, underlining the prevalence of geometrical effects when compared to chemical effects.

5 Particle integration

We have seen in the preceding chapters how directed transport and controlled adhesion can be used to arrange molecules, nanoparticles and macroscopic objects on surfaces. In this chapter, we shall see how this can be applied in practice.

In Section 5.1, thiol molecules are brought onto a surface while the transport of the molecules in a polymer matrix is constrained such that they are distributed unevenly on a macroscopic scale. The molecules spontaneously form covalent bonds when they reach the surface, and their adhesion is extremely strong. This simple behavior allows us to create well-defined gradient surfaces where the density of molecules on the surface changes from one point to the other. While the molecules that form these gradients are the smallest "objects" used in this work, the gradients formed from them have a length of tens of millimeters. The molecular transport is only influenced via geometry at a very coarse level.

One order of magnitude smaller are the arrangements of microbeads in Section 5.2. The beads assemble according to topographical templates fabricated by standard surface micromachining in a fluidized bed, where their mobility is increased. Once the beads are mobile, they arrange themselves in predefined positions via a simple trapping mechanism, and they stay there when the fluidization ends and their mobility drops again. The beads used here have a diameter of 100 μm, i. e. are at the lower end of object sizes that are positioned with pick-and-place-methods in the industry. In this work, instead of actively holding the particles, an adhesion cascade brings them from the template to the substrate.

At length scales below one micrometer, adhesive forces are so strong that individual particles cannot be stabilized in a dry form. The polystyrene latex beads in Section 5.3 are therefore kept as liquid suspensions.

For assembly, the beads must first travel from the bulk suspension to the surface and then be trapped on the surface in the desired positions. This requires providing the directing forces and geometry discussed in Chapter 3, and we will see how temperature-controlled evaporation together with well-adjusted angles of contact produce high-yield assemblies. Once a dry arrangement has formed on the surface, the beads adhere strongly. Removing them to place them on another substrate once again requires an adhesion cascade, in this case provided by deforming the particles towards an increased interfacial area.

The smallest features created in this work are formed from 60-nm-diameter colloidal gold crystals. Gold nanocrystals strongly interact with each other, making their stability a primary concern during assembly. Thus, transporting them to the surface for assembly not only requires a directing force, but also sufficient stabilization to prevent agglomeration. The nanocrystals exhibit strong Brownian Motion, which has to be overcome to arrange them in a template. Finally, such crystals have complex shapes, which produce small and varying interfaces, requiring large adhesion differences for a reliable transfer. Section 5.4 shows how reliable integration and transfer are possible when using surfactant systems, optimal parameters for the assembly process, and engineered adhesion depending on the printed geometry.

5.1 Thiol molecules[1]

---

[1]Part of this work has been published in [102].

5.1.1 Particles

Thiol molecules represent a well-studied system for modifying the surface properties of coinage metals. They adsorb readily and form very thin and well-ordered layers, so-called "self-assembled monolayers". In these monolayers, the thiol molecules present their omega-groups to the outside world. Surfaces coated with dense monolayers therefore exhibit surface characteristics not of the underlying metal, but of the functionalities present in the surfactants.

If different types of surfactants are mixed in a monolayer, or if only parts of the metal surface are covered with thiol molecules, the surface properties vary between those of the different pure monolayers or the monolayer and the underlying metal, respectively. For example, it has been shown that mixed monolayers of hydrophobic and hydrophilic molecules exhibit contact angles that span between those of the pure monolayers [7]. There is an almost linear relationship between the fraction of individual surfactant in the layer and the contact angle. Likewise, one might expect a linear change in the surface properties of sub-monolayers with increasing coverage. This simple behavior does sometimes occur, but more complexity is introduced if the sub-monolayers show structural variability in addition to chemical variability, as is seen with thiols on gold. In such layers, islands of full monolayers are formed while some thiol molecules lie down on the metal surface.

The ability to gradually tune surface properties can also be used to create chemical gradients, where one property changes with a spatial coordinate on the surface. In this case, the composition (or the density) of the monolayer has to change with a spatial coordinate. To create such a surface, we have to pattern not only the profile of the monolayer, but also its composition. Such gradients are of interest for the biological sciences, both in studies of cell adhesion and movement. They also allow

surface adsorption experiments (widely used in many fields) to be performed over a wide range of conditions on a single sample. Finally, the gradients can be used to control fluid movement, with potential applications ranging from microfluidics to self-assembly.

Various examples for the preparation of gradients have been published. A review by RUARDY et al. [153] includes methods based on diffusion in ambient air or a gel on the substrate, moving liquid menisci, as well as moving plasma sources. A particularly simple method is the slow immersion of the sample into a solution that was demonstrated by MORGENTHALER et al. [134]. Electrochemical methods based on the partial desorption of molecules depending on their position [171] have been used as well as microfluidic systems [62, 83]. CHOI and NEWBY recently showed how to use printing-time variations in μCP to create steep, stepped gradients on silicon [35]. GRZYBOWSKI's group has used printing with controlled diffusion and reaction to prepare color patterns [94] as well as surface topographies [27]. They used gels that can dissolve inorganic ions which upon printing react with other ions dissolved in the substrate.

Along these lines, we can also create surface chemistry gradients through controlled mass transfer in a solid stamp, as was shown theoretically in Section 3.2. Stamps with specific geometries influence the diffusion such that the amount of thiol brought to a point of the surface can be controlled. We will see how different stamp shapes create different gradient shapes in the following.

5.1.2 Patterning using solid diffusion

We exploit the unique capability of the silicone elastomer polydimethylsiloxane (PDMS) to dissolve certain alkanethiols and leave them mo-

bile in the bulk material. If the amount of thiol in the stamp is smaller than that in a full monolayer and the deposited amount depends on the position, we can print "analog" patterns on surfaces, i.e., surface-composition gradients with defined spatial evolution.

We printed various gradients using appropriate stamps to verify the theoretical calculations from Section 3.2 and to optimize the process. The stamps were fabricated by casting PDMS in microfabricated molds. Wedge-shaped stamps for the printing of linear gradients were removed from their mold and used on glass carriers, conical stamps were left in their metal molds.

Prior to printing, we placed the stamps on large PDMS slabs (ink pads) with defined thiol concentrations so that they equilibrated to a known thiol content (Fig. 5.1, step 1). Such slabs have a thiol content that is large compared with that of the stamps. They can be inked with high precision to a uniform thiol concentration throughout the entire slab in reasonable time [112]. Both precise concentration and uniformity are prerequisites for the gradient printing, even more so than in conventional μCP.

Upon contact with a gold surface, the stamp formed hexadecanethiol (HDT) gradients (Fig. 5.1, step 2). Immediately afterwards, we back-filled the vacant gold surface with perfluorododecanethiol (PFDDT) (Fig. 5.1, step 3). This creates a surface composition gradient at low surface-energy levels that is stable for several days at least. The fluorine content of the complementary monolayer is readily detected using XPS for the characterization.
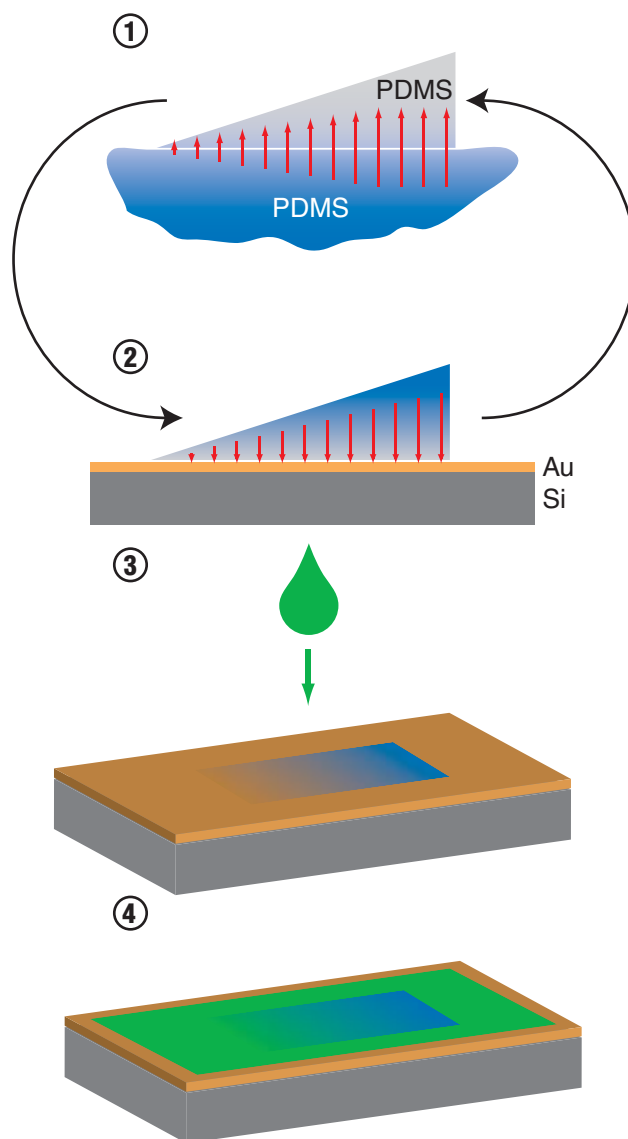
Figure 5.1: (1) Thiol diffuses into the stamp from an inkpad. (2) It leaves the stamp because of adsorption to the gold surface and creates a partially covered surface. (3) The voids can be filled with other thiols to form a two-component surface-composition gradient (4).

5.1.3 Gradient characterization

X-ray photoelectron spectroscopy, spectroscopic ellipsometry (SE) and contact angle measurements can be used to characterize the printed gradients. The fluorine contained in the PFDDT part of the monolayer causes a strong signal in XPS that is easily detected[2]. PFDDT monolayers also exhibit a distinct difference in refractive index and reduced thickness, both of which can be detected via ellipsometry. Finally, the surface energy difference between the fluorinated and the alkyl-terminated thiols can in principle be determined from the contact angle of sessile drops, although the spatial resolution is limited and the relation between surface energy and monolayer composition is not obvious. In practice, XPS provided the most efficient analytical method.

For the gradient analysis, we obtained survey spectra at a pass energy of 80 eV and high-resolution spectra of the Au 4f, the C 1s and the F 1s regions at a pass energy of 40 eV for both reference and gradient samples. Beam-induced damage was expected to be small for our monochromatized source and was not observed during the measurements. To analyze the entire length of the gradient, we repeated the analysis at 14 or 15 points spaced 1 mm apart along its length.

The fraction of PFDDT in the monolayers can be obtained from XPS spectra, either as the ratio of the measured F 1s sample peak area to that of a full PFDDT monolayer or from the splitting of the C 1s peaks that is caused by the strong chemical shift of C 1s electrons in the neighborhood of C-F bonds (Figure 5.2). The former has the advantage of yielding a strong signal, the latter providing an internal C 1s standard. However, the compound area of all C 1s peaks changes from pure HDT to pure PFDDT layers so that this standard can be only used indirectly.

---

[2]The F 1s signal is four times stronger than that of C 1s.
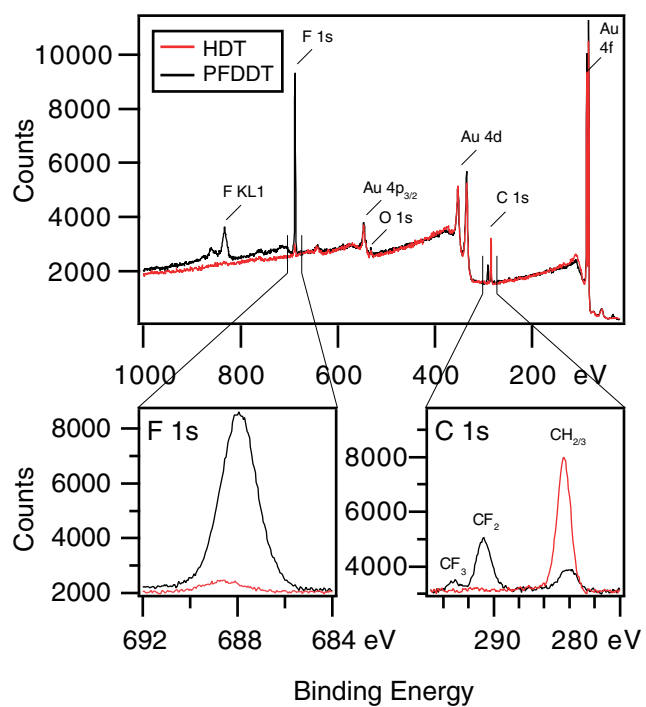
Figure 5.2: XPS signals acquired at the PFDDT end (black) and the HDT end (red) of a gradient.

Figure 5.3 shows the composition of a HDT/PFDDT gradient at different positions as obtained from the analysis of different parts of the XPS signal. Different peaks are compared directly with the peaks measured on reference samples of pure HDT (no fluorine content) and PFDDT (maximum fluorine content). The change of the unshifted C 1s signal systematically overestimates the PFDDT fraction, whereas the shifted C 1s peaks (sometimes grossly) underestimates it. The fluorine peak seems to provide the best indication of PFDDT content, and the standard error of the mean over several independent measurements was found to be low[3].

Some gradients were also analyzed using SE. Figure 5.4 shows a (non-linear) gradient composition derived from both XPS and ellipsometry data. The main difficulty in dealing with such data is that the thickness and the refractive index cannot be obtained simultaneously for such ultrathin films. This is particularly problematic because both parameters change with position in the gradient. We followed BAIN and WHITE-SIDES [8], and chose a thickness of the mixed monolayer of 1.88 nm that lies in between the measured values for HDT and PFDDT monolayers. The exact value was chosen so that the fits converged. We then created a two-component model from reference data of pure HDT and PFDDT monolayers, and used the fraction of PFDDT as the free variable for a fit. The results agree well with the composition derived from XPS, but the uncertainties connected with the fit are rather large. We therefore used XPS as our principal analytical tool.

---

[3]More detailed error analyses of the different composition values can be found in [102].
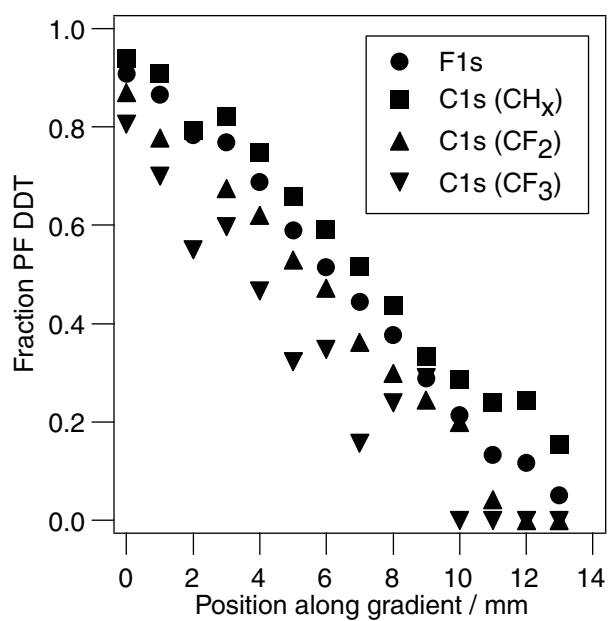
Figure 5.3: Comparison of surface composition according to different XPS peaks.
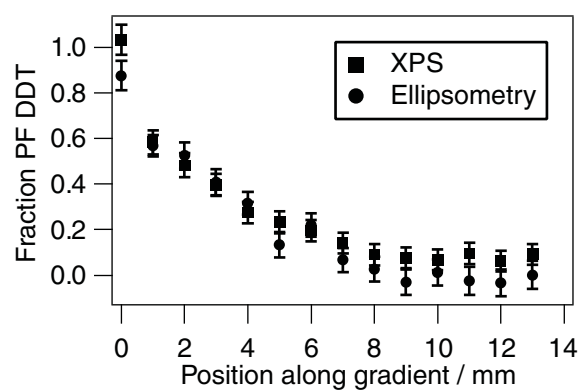
Figure 5.4: Surface composition gradient printed using a stamp with an overly high HDT concentration. The composition was analyzed using both XPS and ellipsometry. Error bars indicate the 90% confidence interval of the entire measurement for XPS data and the 90% confidence interval for the ellipsometry model fit.
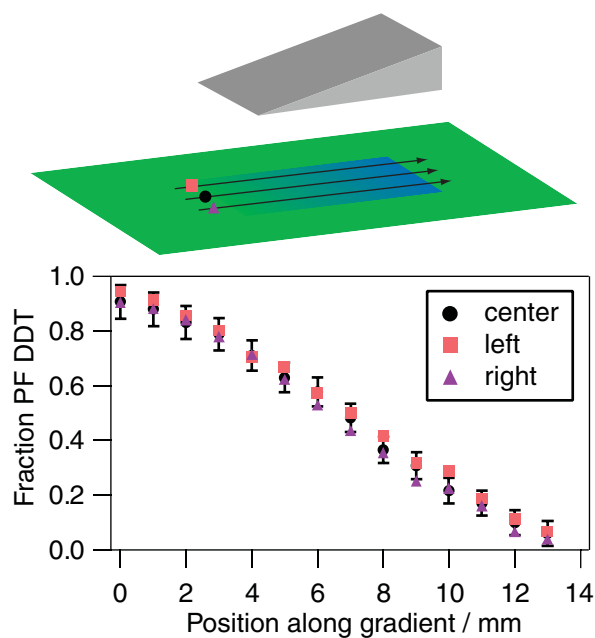
Figure 5.5: Surface composition according to XPS at three lateral positions along a single gradient.

5.1.4 Linear gradients

Highly linear gradients were fabricated reproducibly using perfectly wedge-shaped stamps. The resulting surfaces show good uniformity in the lateral direction. Figure 5.5 shows results of XPS analysis along the center line of the stamped gradient (which was 5 mm in width) and at positions two millimeters to the left and right of the center line.

As predicted in the mass-transfer analysis, the stamp shape governs the resulting gradient evolution. This also accounts for some of the typical deviations from the desired shapes: shallow gradients from stamps
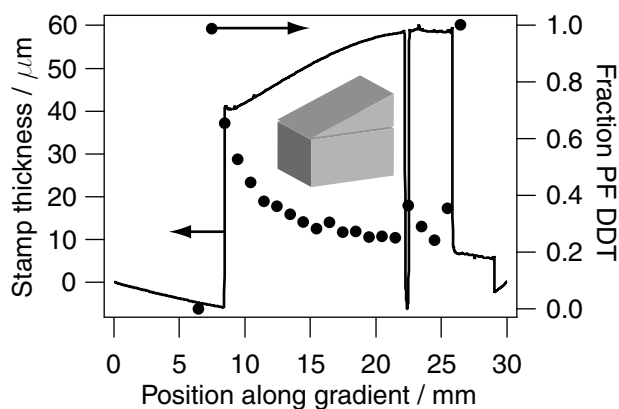
Figure 5.6: Profile of a defective stamp with little height variation. The surface composition gradient obtained is shallow.

with inadequate steepness and nonlinear gradients from stamps with bulges (Fig. 5.6). The latter occurs when too much stress builds up in the polymer layer during fabrication. The printed gradient is a faithful representation of the deformed shape as long as the deformation allows the PDMS to establish conformal contact with the gold surface. Inspection of the stamps via profilometry identified such stamps so that we could avoid undesired geometrical effects.

In addition to stamp geometry, the overall concentration of the thiol in the stamp had a profound effect. A stamp would produce a gradient that is not as steep as expected if the thiol concentration was lower than optimal. Profiles of two different gradients made using the same stamp are shown in Figure 5.7. In the second print, only part of the surface composition range is present in the gradient. This deviation also occurs when the thiol concentration inside the stamp decreases owing to oxidation or evaporation of the ink.
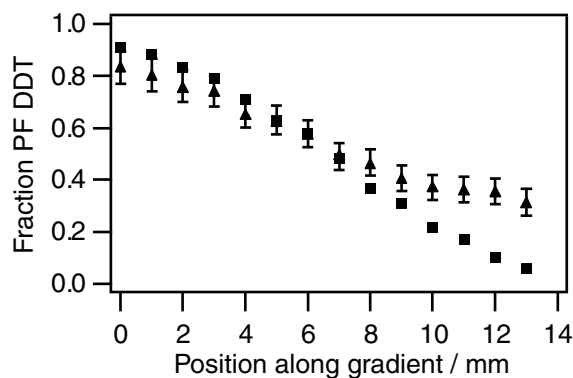
Figure 5.7: Surface composition according to XPS in two different linear gradients printed successively using the same stamp, with reinking. The thiol concentration in the second print (triangles) was slightly too low.

In contrast, excessive concentrations led to steeper gradients with a saturated region of constant HDT coverage, as shown in Fig. 5.4 (although there still is some PFDDT present, *vide infra*). Here, the PDMS stamps still contain some thiol after printing. Multiple prints using a stamp with a very large initial HDT concentration of 200 µg/mL lead to a front that moved from print to print (Fig. 5.8). The thin parts of the stamp were soon depleted, whereas the thick parts established a full monolayer and did not lose any solute thereafter. In this experiment, we kept the time in between the prints as short as possible (approximately 1 min) to limit lateral diffusion.

All concentration effects are consistent with a very simple model that only takes into account surface-normal diffusion of the thiol. Figure 5.9 shows the three possible situations: (1) Insufficient concentration where the full gradient length is preserved, but the maximum coverage is not
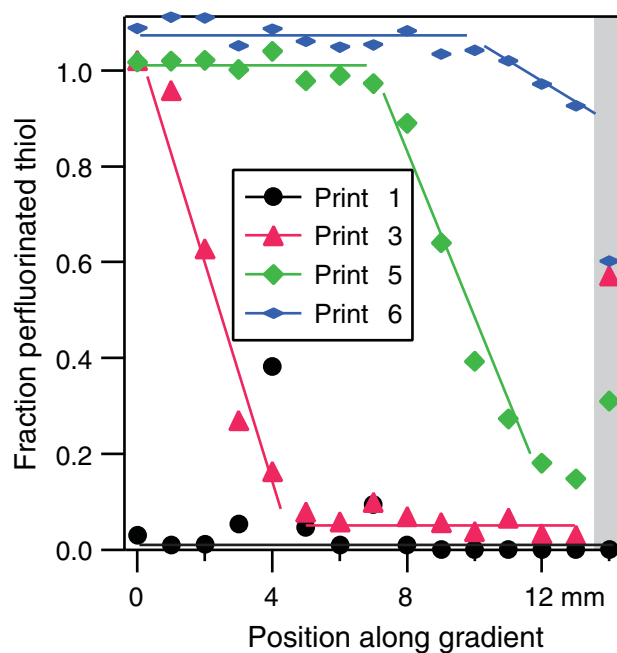
Figure 5.8: Surface-composition gradients from different prints using the same stamp without reinking, starting at an excessive concentration of 200 μg/mL. Compositional values in the last millimeter (gray background) are subject to alignment errors between the XPS analysis spot and the gradient end.
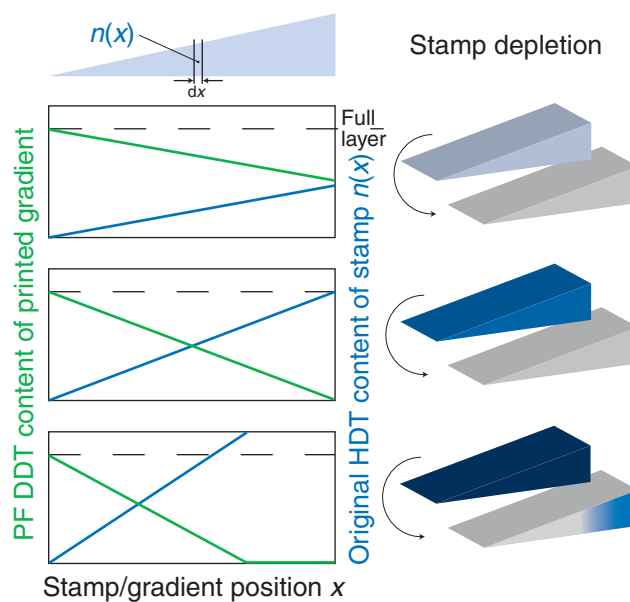
Figure 5.9: Relation between concentration and gradient shape. Low concentrations (top) lead to shallow gradients, adjusted concentrations (middle) allow full-length gradients with maximum dynamics, excessive concentrations (bottom) lead to steep gradients with saturation.

full and the dynamic range is limited; (2) adjusted concentration where the full gradient range is present and (3) excessive concentration where part of the thick stamp end contains more material than can be adsorbed on the surface.

In most cases it will be desirable to use just enough thiol so that a full monolayer is reached at the very end of the gradient. We found a concentration of 40 µg/mL to provide satisfactory gradients from our 50-µm stamps. This leads to a surface concentration of 7 µmol/m^2 on

the thick side of the stamp, slightly below the literature value [51] of 7.9 μmol/m^2 for a complete HDT monolayer.

XPS signals clearly reveal the presence of fluorinated thiol, even in regions where full coverage by HDT is expected. This is likely not due to improper stamp concentration levels. Two other effects might be responsible for this deviation. The last 20% of the monolayer formation has been reported to be considerably slower than expected from first-order Langmuir kinetics [7]. Even though our printing time of 3 min is considerably longer than required for diffusion, it might not be sufficient to form a perfect monolayer. However, the comparison of XPS data of reference monolayers[4] with that of printed gradients does not indicate enough voids to account for the entire effect. More important seems to be the replacement of adsorbed HDT molecules from the surface by PFDDT. We found that reference monolayers of HDT that were treated with PFDDT in the same way exhibited 6% of PFDDT in the monolayer. We thus optimized the second adsorption step so that it filled as large a fraction of the uncovered surface as possible while replacing as little as possible of the existing monolayer. Best results were achieved using a short treatment (about 20 s) with a solution of PFDDT (0.4 g/L) in dichloromethane. A heavily fluorinated solvent could cause contamination of the surfaces by fluorine-containing residues and disturb the analysis.

5.1.5 Radial gradients

Other stamp geometries enable both nonlinear gradient contours and profiles. We prepared radial gradients that fell off linearly from the center. The mold for the stamp used had a conical recess with a central

---

[4]Reference samples were prepared from solution with long immersion time.

protruding pin from machining. The maximum depth was 100 μm so that we had to halve the ink concentration and increase the equilibration times by a factor of four. The XPS analysis results in Fig. 5.10 reveal that there was a "plateau" in the center of the printed area, interrupted by a hole (most likely due to the above-mentioned pin in the mold). The low-fluorine plateau is probably due to a slight excess in HDT concentration inside the stamp, analogously to what has been observed for linear gradients.

Liquid droplets can move towards higher wettability regions of surface composition gradients, as demonstrated by CHAUDHURY et al. for a hydrophobic/hydrophilic gradient [30]. The gradients used in our study were all hydrophobic, but changed from oleophobic (PFDDT) to oleophilic (HDT). Droplets of hexane and heptane that were deposited on the fluorinated side should therefore move towards the other end. We performed this experiment with many of our gradients and found consistent movement when the droplets were sufficiently large and the gradient was steep (i.e., obtained from a good stamp). Smaller droplets could be moved on the gradients using vibrational excitation, as previously demonstrated by DANIEL et al. [43]. Figure 5.11 shows still images from the movement of heptane droplets on a radial gradient, excited by a vibration of the substrate. In contrast to the in-plane movement investigated by DANIEL et al. we chose a surface-normal vibration to simplify the observation of the system. It was possible to introduce sufficient energy to overcome the hysteresis at relatively low amplitudes (down to tens of micrometers) when we tuned the vibration to the eigenfrequency of the drop.
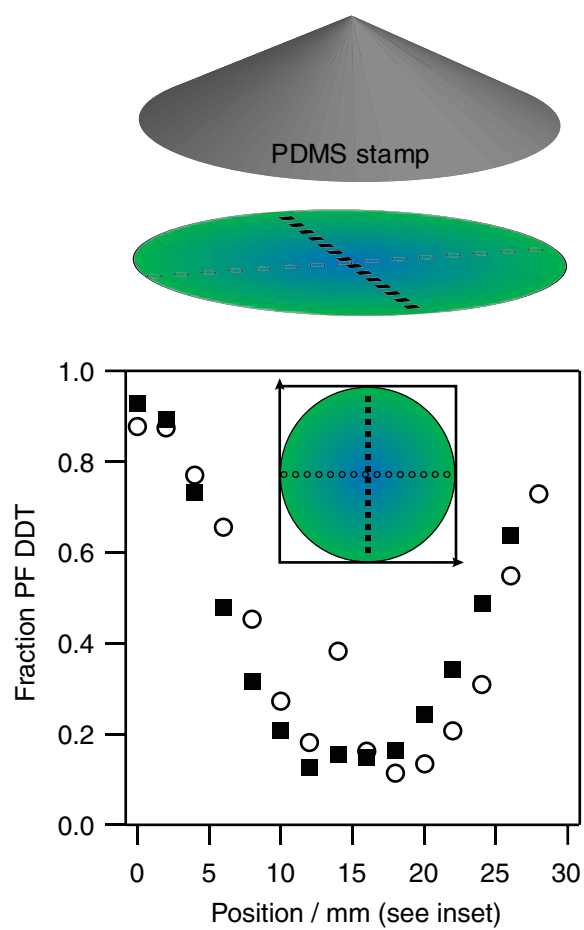
Figure 5.10: Surface-composition gradient printed using a radial stamp. Measurement positions are indicated in the inset. The coordinate origin is at the lower left hand corner.
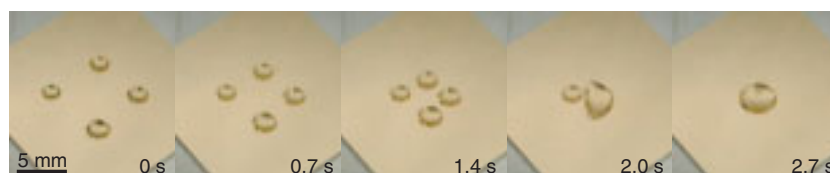
Figure 5.11: Droplets of heptane moving on radial surface energy gradient. The substrate is vibrated to excite the droplet movement.

5.1.6 Experimental details

Chemicals Used   Hexadecanethiol (Fluka, $\geq$ 95%) was used as received. Solutions of HDT in ethanol (absolute $\geq$ 99.8%, Fluka, used as received) for inking of stamps were prepared with the highest possible precision and stored at 4 °C for a maximum of one week before use. 1H,1H,2H,2H-perfluorododecanethiol $CF_3(CF_2)_9(CH_2)_2SH$ was available from previous studies. It was dissolved in dichloromethane ($\geq$ 99.8%, Fluka, used as received). Heptane (puriss. p.a. $\geq$ 99.5%, Fluka) was used as received.

Sylgard 184 (Dow Corning, Midland, MI) poly(dimethylsiloxane) prepolymer was used to prepare some of the stamps. Other stamps were made from the same mixture with an addition of extra catalyst (platinum-divinyltetramethyldisiloxane complex in xylene, Gelest, PA, USA).

Fabrication of PDMS stamps   Very thin stamps suitable for the method were fabricated with a precise thickness variation from PDMS via molding.

Ultrathick resist (SU-8 type 10, micro resist technology, Berlin, Germany) was spin-coated onto a silicon wafer to a thickness of 50 μm and patterned using standard photolithography so that rectangular areas of

10 mm by 15 mm were removed. The wafer was cut into individual pieces, mounted on a goniometer, inclined and polished until all resist was removed on one side, but none on the other. The resulting wedge-shaped mold was then fluorinated and filled with the modified PDMS prepolymer mixture. A thin glass slide was pressed onto the mold, and the polymer was left for curing at room temperature. The glass layer improves handling of the finished stamp, which strongly adheres to it.

Use of the modified PDMS instead of the standard commercial product was necessary because a component of SU-8 seems to inhibit the curing process. The diffusion properties of PDMS are likely not to be affected by the addition: full cross-linking is reached both in normal PDMS in the absence of an inhibitor and in the modified PDMS, for the latter even in the presence of an inhibitor [96].

Additional molds were made by conventional machining. A wedge-shaped mold (50 μm at its thick side) was milled from an aluminum block and a radial mold (100 μm at its center) was turned from an aluminum shaft of 30 mm in diameter. The wedge-shaped mold was polished, teflonated with spin-coatable Teflon AF or with CVD-deposited teflon, filled with PDMS and closed with a glass slide to be left for curing at 60 °C. The radial mold was treated with an adhesion promoter (Dow Corning primer 92-023), filled with PDMS, and cured. The silicone elastomer shrinks during the cross-linking and assumes a concave bow in the stamp surface. This dip was backfilled with PDMS so that the surface could make conformal contact to a substrate.

Inking of PDMS stamps The stamps were imbued with hexadecanethiol so that they contained just the right amount of thiol for our process. Three-millimeter-thick PDMS slabs (ca. 25×25 mm in size and 2 g in weight) were used as "ink pads". Ethanolic HDT solution was dis-

pensed onto one of the stamps, and a second one was placed on top so that the liquid spread at the interface. A dry nitrogen stream removed the ethanol in about 20 min. The ink pads were left in darkness under argon for at least 24 h to allow complete equilibration to an uniform concentration, as required in the PDMS stamps. The pads provide a reservoir of virtually constant concentration to the stamps placed on top of them. After at least another 12 h the stamps were ready for printing.

Printing of gradients   A freshly gold-coated wafer (40 nm gold on 3 nm titanium on a 0.5-mm silicon wafer) was cut into pieces, and particles removed with a stream of dry nitrogen. The stamp was removed from its ink pad, placed on the substrate, pressed down slightly until contact was established throughout the entire stamped area, left for 3 min and removed from the gold. Immediately afterwards, the sample was treated with a solution of the complementary thiol, washed with ethanol and dried with nitrogen.

Preparation of reference samples   Reference monolayers were prepared from HDT solutions (1 mg/mL) in ethanol and PFDDT solutions in dichloromethane (0.4 mg/mL). The same substrates as used in the printing were immersed in the corresponding solution and rinsed with the appropriate solvent after about 3 min.

X-Ray Photoelectron Spectroscopy   Spatially resolved analysis of the stamped gradients was done by x-ray photoelectron spectroscopy (XPS) using a VG Scientific Sigma Probe spectrophotometer at a base pressure of about 10^{-7} Pa with a monochromated Al Kα x-ray source ($E =$ 1486.6 eV). The x-ray was focused onto an ellipsoidal spot (the long half-axis was 1 mm, the short half-axis was 600 µm in length), the detector

was mounted at an angle of 37° to the sample. The long half-axis of the spot was always at a 45° angle to the gradient direction.

Spectroscopic Ellipsometry   Ellipsometry measurements shown here were made with a Variable Angle Spectroscopic Ellipsometre (VASE) and have been analyzed with the WVASE software (both from J.A. Wool-lam Co., Inc.). The source used is an arc-xenon lamp with a spot diameter of 1 mm. The measurements were performed using wavelengths from 400 to 1000 nm at 65, 70 and 75°. For our purpose, the incident angle of 70° turned out to be the most sensitive.

After substrate characterization, we prepared and measured pure HDT and PFDDT monolayers. A model of the references was created to find their optical indexes. In a second step, we created a gradient on the substrate and performed a mapping in millimeter steps. The data was then fitted using a BRUGGEMAN effective medium approximation model [22] (consisting of inclusions of one material dispersed in a host matrix of the other) and the composition was determined from the fit.

Profilometry   A Dektak V 200-Si profiler (Veeco, NY, USA) provided stamp profiles. The indentation force on the needle was set to 3 mg. All scans were done in the center of the stamp.

Moving droplets   Drops of heptane or hexane, typically around 2 mm in diameter, were deposited on the gradient from a capillary. In some cases, notably for the radial gradient shown here, the samples were clamped onto a home-made stage that sat on top of a commercial electromechanical vibrator (Frederiksen, Denmark). This setup allowed us to introduce vibrational movement along the surface normal of the substrate. A frequency generator and an NF-amplifier drove the vibrator

with a sine wave at around 100 Hz, manually tuned to the eigenfrequency of the drops.

5.2 Microspheres[5]

---

[5]Part of this work has been published in [100].

High-precision beads with diameters below one millimeter, often called microbeads, are well-established components in microelectronics packaging and interesting micro-optical components. Large quantities of tin microbeads are currently used in flip-chip bonding, where they provide electrical connection as well as mechanical bonds between a package and the semiconductor. In display fabrication, tin or gold-coated polymer microbeads provide precise spacing and electrical contact between planes. In much smaller numbers, glass microbeads are used to couple light into fibres.

Almost all applications of these microbeads require precise alignment with existing structures, be it the interconnects of a semiconductor, the leads on a display, or the active area of a laser diode. Industrially, microbeads are usually picked up by vacuum nozzles or in templates with strategically placed holes. This limits the minimum size of objects that can be handled. Accordingly, the smallest diameter that can currently be placed industrially is approximately 100 μm. Particles with smaller diameters exhibit strong adhesion forces and are hard to remove from vacuum nozzles.

Besides microbeads, some objects of comparable size are routinely integrated in electronics manufacturing using pick-and-place techniques. For example, unpackaged integrated circuits are often placed directly on high-volume printed circuit boards, connected electrically and encapsulated in epoxy resin. This process is limited in minimum object size, however, and it becomes uneconomical to integrate more than small numbers of these devices through pick-and-place methods.

Alternative approaches that handle objects in parallel and extend to smaller sizes have been proposed by SMITH and others at Berkeley [164] (for details and a short review, refer to Chapter 2). In effect, directed self-assembly with geometrical templates is used to arrange many small

objects rapidly. One limitation is that this requires a specialized topography in the target substrate. A common way to produce such geometrical assembly templates is to use an isotropic etch in silicon, in particular, potassium hydroxide etches that produce pyramidal holes. Both ALIEN TECHNOLOGY and ILLUMINA use such holes to trap microscale objects, as this etch is low-cost, allowing it to be performed on every single target substrate.

To completely obviate template topography, we either have to rely entirely on particle-particle interactions (which severely limits the flexibility of the assembly) or separate the assembly step from the target substrate. The SATI concept (short for Self-Assembly, Transfer and Integration, see Section 2.4) provides such separation, as shown in Figure 5.12. We discuss in this section how particles with diameters of approximately 100 µm can be integrated using the SATI approach, including both tin-coated polymer and glass spheres. An additional advantage of the SATI process is its modularity, which we demonstrate here by printing stacks of particles.

5.2.1 Particles

Two particle types are used in this section, glass and tin-coated polymer beads. Glass beads are usually produced by working pulverized glass in a hot gas jet, where it melts to spheres, which are then classified according to size [24]. Depending on the effort invested in classifying, the manufacturers can obtain powders with narrow size distributions. Here, we use spheres from Duke Scientific (Palo Alto, CL) with a standard deviation in the diameter of 3.1%. The spheres are also of good optical quality (see Fig. 5.13), although air inclusions do occur. More problematic for the assembly are small beads that adhere to the large
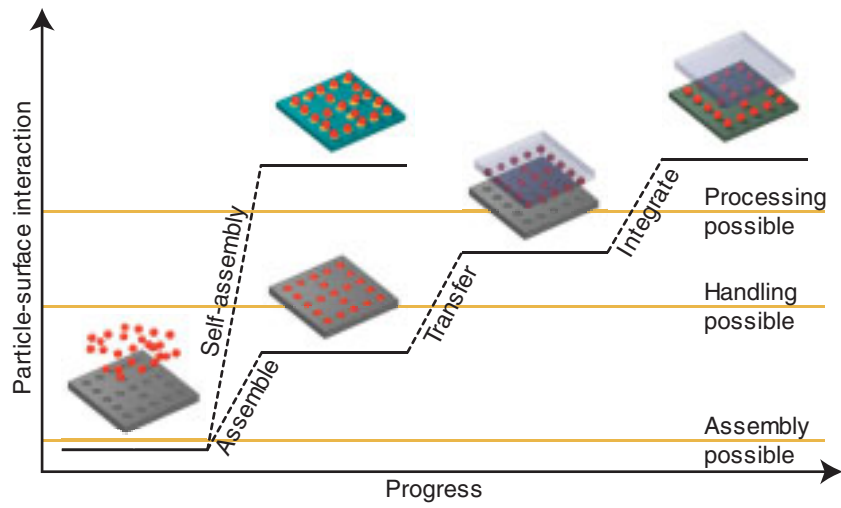
Figure 5.12: The SATI (self-assembly, transfer and integration) Process for microspheres.
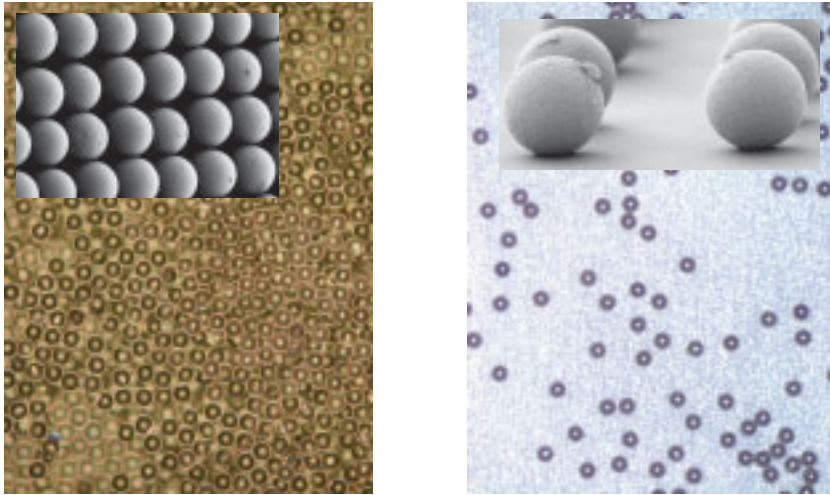
Figure 5.13: Microspheres composed of glass (left) and polymer with a tin coating (right). Both exhibit surface asperities, but only the glass beads contain smaller spheres that often adhere to the larger beads.

beads and, in general, surface asperities. Large-volume applications of such glass beads include composites and other materials that do not require alignment of the particles (for a review see [24]).

Polymer beads, on the other hand, can be produced with very smooth surfaces through emulsion polymerization [90]. They can then be coated with metals, yielding high-quality, conductive beads, as we have used here (purchased from Microbeads, Seikusi Corporation, Japan). Such beads are used industrially when the quality of solid tin beads would be insufficient, or when they should not deform, as in liquid crystal displays. Although they are highly spherical, the tin-coated polyimide beads also frequently have rough surfaces, often manifested in spherical

caps on the bead (Fig. 5.13).

5.2.2 Assembly

The conventional pick-and-place approach for the integration of micro-beads uses vacuum nozzles. An array of such nozzles is immersed in a large number of particles, and air is pumped from the nozzles until single beads close each individual nozzle. The entire array then moves onto the target substrate, where atmospheric pressure is restored, so that the particles fall on to the surface.

This scheme fails as the particle adhesion to the nozzle array increases sufficiently, usually at particle diameters $\leq$ 100 µm. Then, particles adhere to other parts of the array, and are hard to remove even when the vacuum is released. In applications that require smaller beads (such as chip bumping at higher levels of integration), the industry usually resorts to fabricating them in place through galvanic or thin-film processing.

Other placement schemes are not based on vacuum, but on vibration. Vibrational sorting has been long used to decollate electronic components and sort them depending on their geometry [15]. It can also be used to arrange particles, and there are industrial processes where structured templates are immersed into a large quantity of particles, removed by tilting under vibration, and brought into contact with an adhesive-coated target. A general class of such assembly-and-transfer processes has been patented by ALIEN TECHNOLOGY, INC [73] under the name "Web Fabrication".

We used an assembly method that employs vibration on a structured template and is often called "Gravitational Assembly" (Figure 5.14). The setup included an assembly cell that contained template and particles,
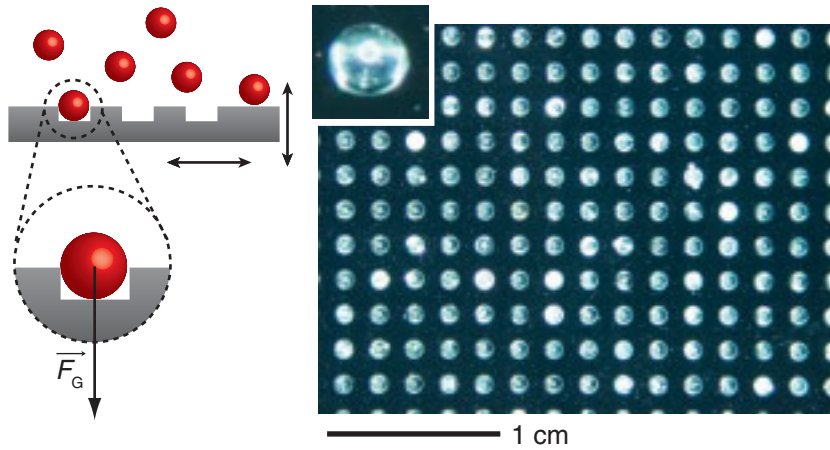
Figure 5.14: Gravitational assembly on a structured template. Dry beads are fluidized on the template through vibration, and fall into the holes, where they are trapped by gravitation.

with a top window that was coated with Indium Tin Oxide to prevent static charging. This cell was mounted on top of an electromagnetic vibrator (essentially a low-frequency loudspeaker with a rod mounted in the center, purchased from Awyco AG, Olten, Switzerland) connected to a frequency generator and an conventional audio amplifier. After the cell had been filled with template and particles, it was excited at $60 - 100$ Hz at an amplitude just sufficient to fluidize the particles.

The templates used were silicon pieces with holes defined through standard photolithography that were coated with a perfluorodecyltrichlorosilane monolayer. Figure 5.15 shows the process flow of their microfabrication, which relies on standard bulk silicon micromachining, with the structures defined by a photomask.
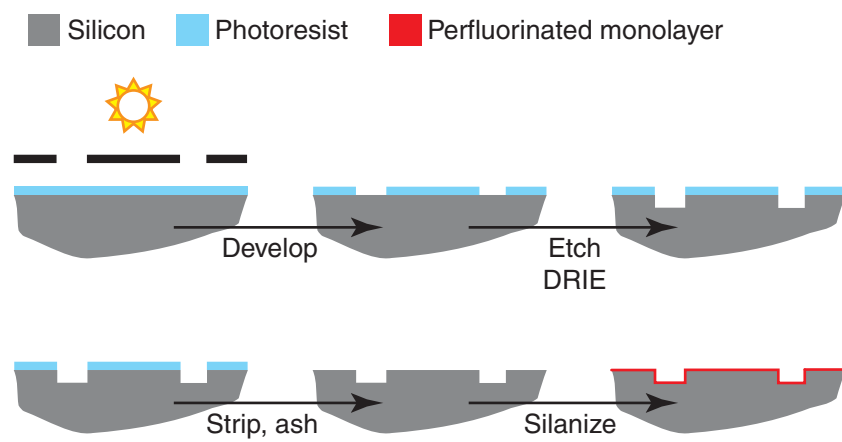
Figure 5.15: Process flow of assembly template fabrication. A conventional photoresist is patterned on a standard silicon master from a mask, holes are etched in the opened areas through Deep Reactive Ion Etching (DRIE), the template is cleaned and coated with a perfluorinated monolayer to reduce its surface energy.
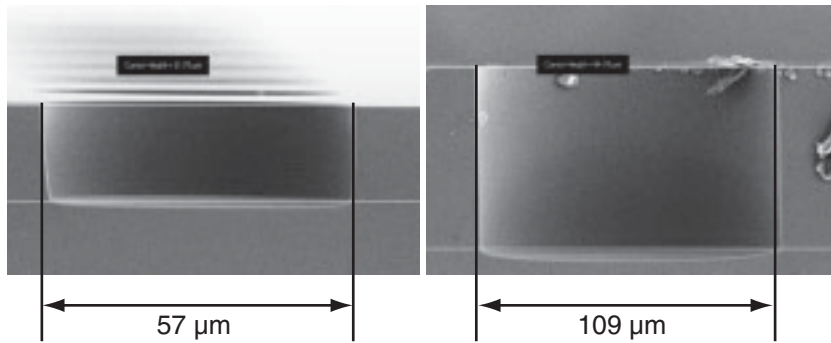
Figure 5.16: Assembly templates etched in silicon and cleaved to expose their geometry. Their accuracy is far better than the size distribution of the assembled particles. Templates for both 50 μm and 100 μm particles are shown.

At these length scales, standard microfabrication provides sufficient resolution to produce templates with a geometry and positioning accuracy that is by far better then the particles' polydispersity (see Figure 5.16). The holes in the template were chosen to be somewhat larger than the particle diameters to prevent them from getting stuck due to their geometrical imperfections. The depth used for particles with a nominal diameter of 100 μm was 60 μm. Also shown are templates for smaller particles, suitable for assembling 40-μm-diameter beads.

Gravitational assembly uses vibration to mobilize particles. Particles first adhere to the surface, but at a sufficient amplitude and frequency, the inertial force prys loose some particles, which then fly in parabolic trajectories over the template surface (the excitation amplitude was limited to minimize particles impacting the upper window of the assembly cell). These active particles can activate others when they collide with them, thus overcoming the adhesive force between quiescent particles
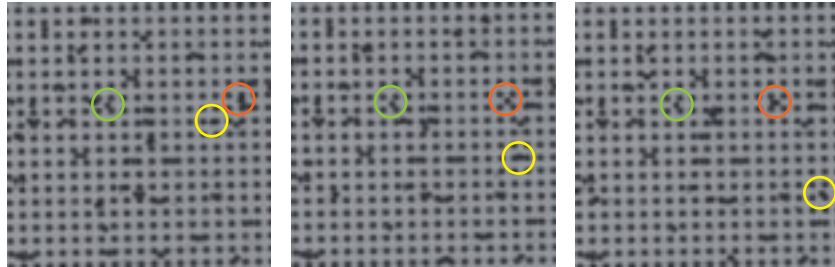
Figure 5.17: Instantaneous images of the assembly process with time intervals of 10 ms. The same three different beads are marked on each image: one (marked in green) is quiescent, one (marked in yellow) flying ballistically, one (marked in red) jumps on the surface.

and the surface.

Figure 5.17 shows three images from a high-speed video taken at a frame rate of 1000 s^{-1} with an exposure time of 40 µs, using a PHANTOM V7.1 monochrome high-speed camera. Some particles are quiescent, others are moving rapidly (the particle inside the yellow circle has an average velocity of ≈ 75 mm/s). Some particles have already been trapped in the holes, where they either sit immobile of keep jumping. The differences in behavior partially stem from differences in adhesive strength, probably mostly caused by geometrical differences of the bead surfaces. Depending on the frequency, superstructures similar to the well-known CHLADNI-figures appear; we have chosen the working frequencies such as to avoid any of those, because they can interfere with the desired arrangement.

The gravitational assembly process always requires excess particles. The particle capture in the holes is not definite — particles leave holes, in particular when they are hit by other particles in the fluidized bed. Thus,
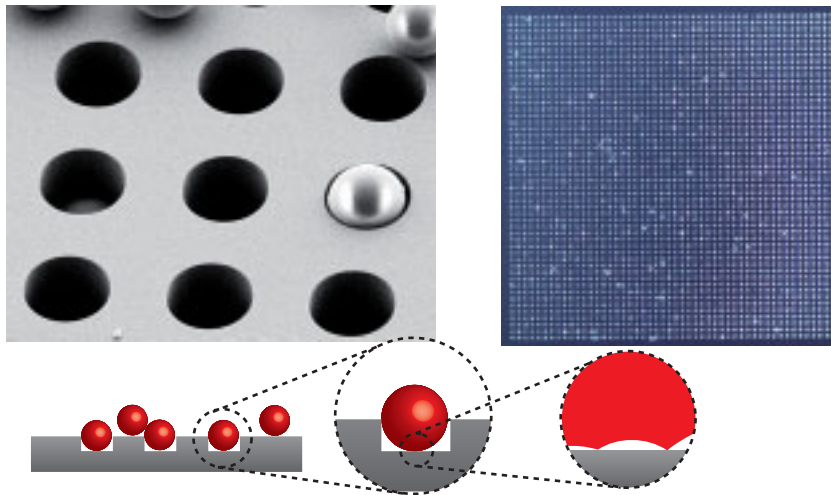
Figure 5.18: 100-µm-diameter glass beads on their master, partially assembled. The contact between the beads and the template is hard, the true contact being formed by asperities of the bead surface.

to reach sufficient yields, the number of particles filled in the assembly cell must always be larger than the number of holes, and the exciting vibration must not switched off abruptly at the end of assembly, but its amplitude must be slowly reduced until all particles are quiescent.

After short assembly times (depending on the amount of particles present and their original distribution, $20 - 60$ s suffice), all holes (or almost all, at a typical yield greater than 95%) are filled with particles. The template surface is covered with excess particles, in particular in the corners of the assembly cell (Figure 5.18).

These excess particles can be removed in a first excess removal print (Figure 5.19). A flat stamp is brought into contact with the excess layer
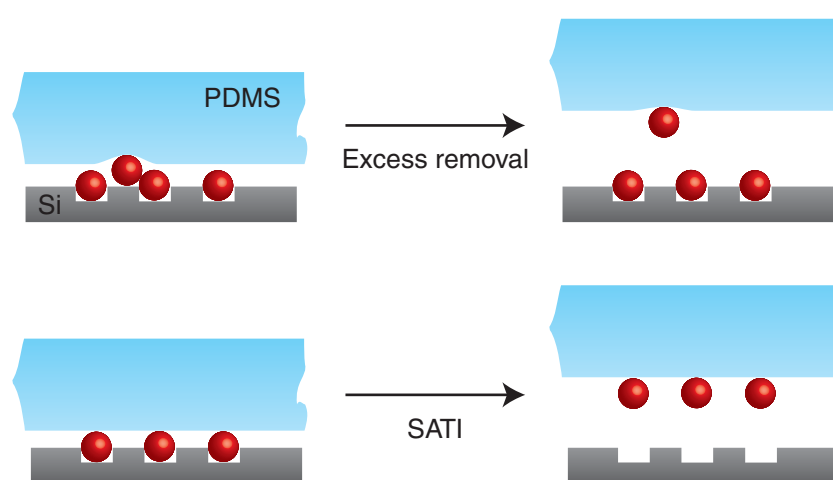
Figure 5.19: Excess removal step. A flat stamp is brought into contact with the excess particles, which adhere and can be removed from the template. This is repeated until only the particles assembled in holes are left.

of particles using the printing tool described below. When the topmost beads have come into contact, the stamp is removed, the particles are blown or scraped off the rubber surface, and the process is repeated, if necessary.

There exists a trade-off between assembly quality (accuracy and precision) and yield. The beads are relatively monodispersed, but their size distribution limits the minimum size of the template features. Even more limiting are the asperities and smaller beads on the bead surfaces, which tend to mechanically lock in the template, so that some beads become stuck. Small holes in the template enable precise particle alignment but also lead to many defects. Figure 5.20 shows three types of particles that could not be removed from the template in the transfer step. From left to right, we have one deformed bead that is too long in one axis to comfortably fit into the feature, one particle accompanied by a smaller sphere which increases adhesion and one smaller deformed particle that is blocked in between two holes. This is aggravated by the hard impacts typical for gravitational assembly: a particle might fit into a feature of the template, but its mobility reduces in a very short time upon impact on the template, so that it cannot assume a more advantageous position. Thus, particle quality is the main limitation of assembly quality in gravitational assembly.

5.2.3 Transfer

The particle handling methods described in the introduction are based on the active exertion of forces on the particles. In contrast, we use here a passive approach that takes advantage of the particle adhesion to certain surfaces. Interfacial area and surface energy are used to modulate the strength of the adhesive force, so that an adhesion cascade of the type
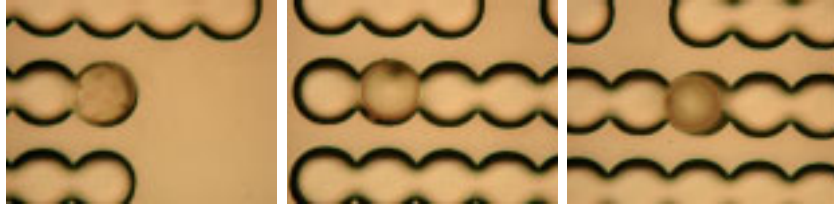
Figure 5.20: Three types of "stuck" microparticles, caused by a deformed particle (left), a secondary small particle (center) and a smaller bead (right image).

shown in Figure 5.12 is established.

Adhesion requires surfaces to be in close contact, a precondition that is often hard to meet with hard surfaces. For example, when the hard beads sit in the templates after assembly, their true contact to the template consists of a number of point contacts formed by bead asperities, totalling only a relatively small area. Soft materials can deform to create larger contact areas, even *conformal* contact, where there are no gaps in between the surfaces over the entire area (Figure 5.21).

Standard JOHNSON–KENDALL–ROBERTS theory [84] predicts a theoretical pull-off force F_A for a sphere with radius r in contact with a surface as

$$F_A = \frac{3}{2}\pi r W_A, \tag{5.1}$$

where W_A is the material-specific, areal work of adhesion. This adhesion force is usually very large. For a relatively low $W_A = 40 \text{ mJ/m}^2$ (far below typical bulk cohesion values), it already amounts to forces on the order of tens of micronewtons, whereas gravity only exerts a force on the order of tens of nanonewtons. That would indicate that a carrier could readily support relatively large and heavy particles. Practical adhesion forces, however, are usually much weaker because of imperfec-

tions in the surfaces involved. A material combination with a larger W_A poses the risk of exceeding the cohesion on one side, leading to damage of the particles or the carrier [143] during separation. A compliant material that can deform upon contact with hard surfaces can compensate for particle imperfections [17] in conformal contact with an interfacial area close to the theoretical value. Here, the carriers were made from poly(dimethylsulfoxide) (PDMS), a silicone rubber known for its mechanical compliance. Although its surface energy is relatively small [50] ($\gamma \approx 22$ mJ/m^2), the conformal contact creates a strong but reversible bond to particles. We found that a PDMS carrier can pick up comparatively heavy 100-μm-diameter glass beads and hold them with sufficient strength to allow handling of the assembly without special precautions. We use thin (typically 100 μm thick), flat PDMS layers on a thick (1–3 mm) glass piece to pick up and handle particles.

Figure 5.22 shows the entire transfer process for a 200-μm-pitch glass bead array. After they have been assembled and excess particles have been removed, beads are picked up from the template by the PDMS carrier that is brought into contact with the carrier and the particles.

To facilitate the transfer further, the surface energy of the templates was reduced as far as possible. First, all templates were fabricated from polished silicon wafers and it was ensured that the etched features did not contain rough bottom surfaces. Second, the entire template was covered with a perfluorinated monolayer, a method that has been developed for stiction reduction in microelectromechanical systems and masters for imprint lithography [163].

Besides the particle arrays shown already, this approach allows to create arbitrary patterns of particles. For example, Figure 5.23 shows particles arranged in the shape of a company logo, where the holes of the master were placed close enough for the particles to almost touch each
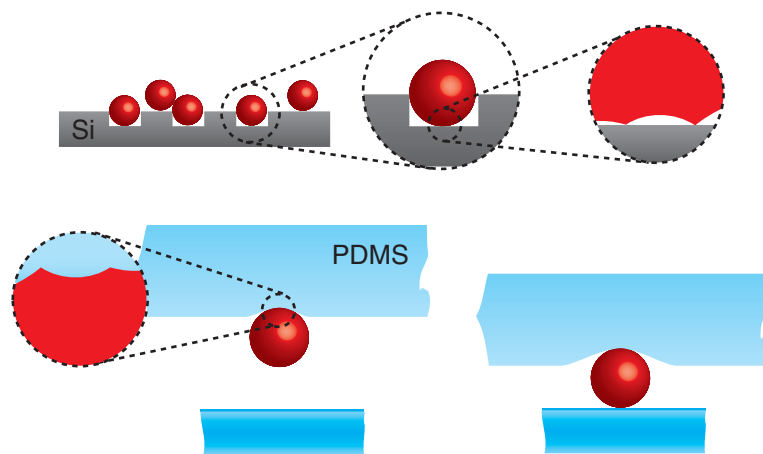
Figure 5.21: Hard and soft contacts between a surface and microbeads. Hard surfaces cannot conform to the rugged particle topography, which leads to point contacts, while soft surfaces are capable of conformal contacts, which feature large interfacial areas.
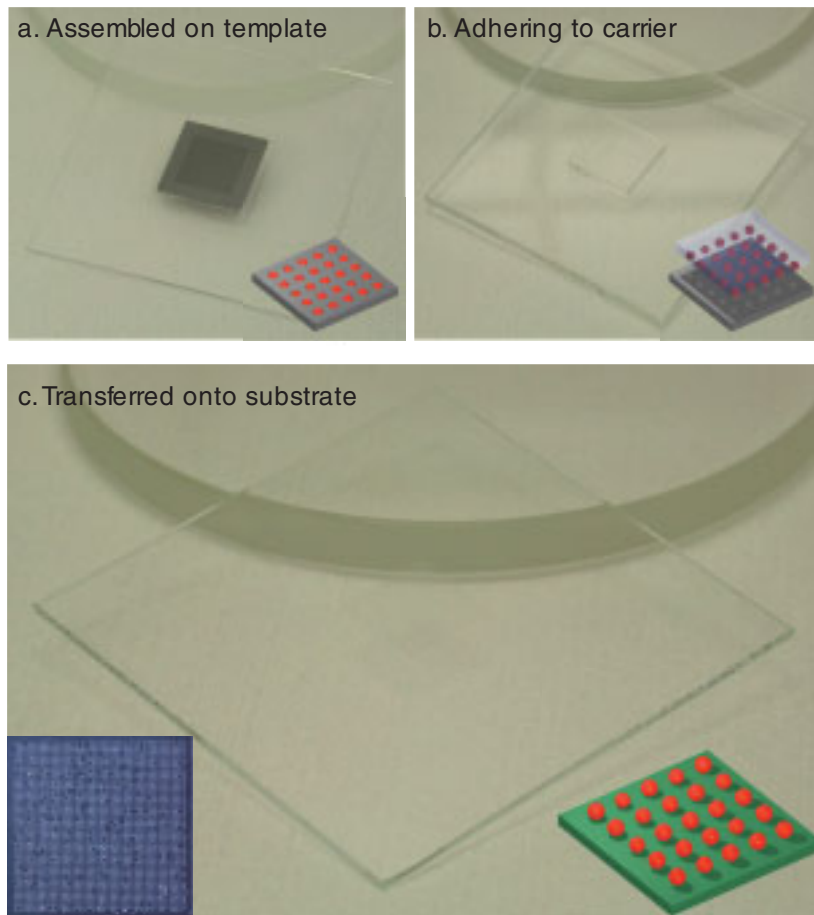
Figure 5.22: Particles adhering to different surfaces during the SATI process: First, the beads are assembled in a template, then picked up onto a PDMS carrier, to be finally printed onto a substrate.

Assembled in master
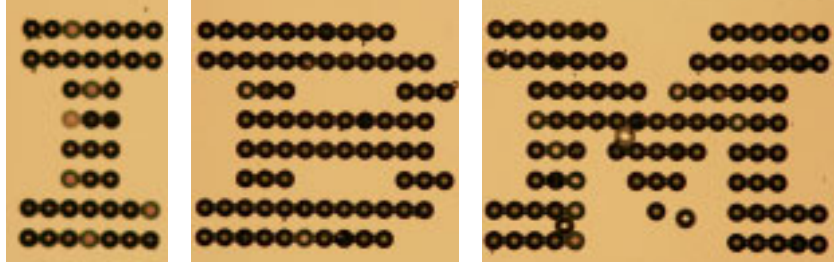
Picked up onto stamp   1 mm
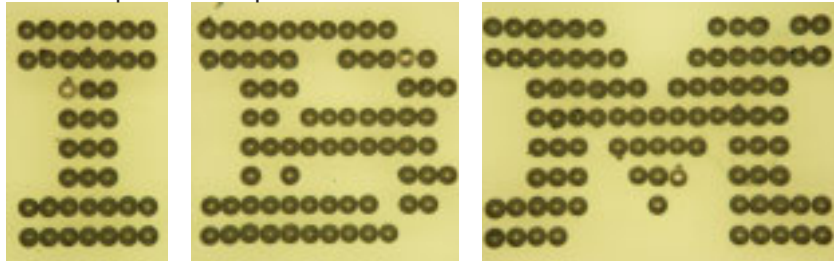
Figure 5.23: Particles assembled in the form of a logo. The top row shows the assembled beads in the template with excess particles not yet removed, while the bottom picture was taken on the PDMS stamp. Beads touch each other in the lines of the logo.

other. In a similar manner, we can assemble a dense, square particle array instead of the usually occurring hexagonal crystal. The transfer of these dense particle layers, which would be challenging for handling techniques that actively apply a force, is simple when using PDMS carriers.

5.2.4 Integration

For integration, the particles on the carrier were brought into contact with the target substrate. The flexible PDMS carrier allowed this even in the case of rough or wavy substrates. Because the particle-substrate interaction exceeded the particle-carrier interaction, all particles were printed onto the substrate.

To provide the increase in adhesive strength necessary to transfer particles from the carrier to the target, the interfacial area has to become even larger, or the interfacial energy of the created junction needs to increase. We make use of both effects through adhesion layers. These are thin, soft layers, deposited on the target by spin-coating, which flow into the crevice between particle and surface. We printed glass particles onto a spin-on-glass layer containing an organic component at 80 °C to provide conformal contact with the particles. Figure 5.24 shows the increased interfacial area formed by the flowing spin-on glass, and it shows how this high-energy liquid conforms to the surface of the microbeads. Although the layer is only 400 nm thick, is provides good mechanical stability to the integrated particles. Other possible modes of connection include the embedding of particles into a thick polymer layer and the creation of covalent bonds between substrate and particle. In case of the tin-coated polymer beads, we have formed a layer of about 5 µm polyisobutylene (PIB) via spin-coating, which is soft enough at room temperature to provide substantial adhesion.

Even in the presence of an adhesion layer, the mechanics of the integration step have to be carefully controlled to ensure complete particle transfer. Adhesion is a dynamic phenomenon, and the adhesive strength can depend greatly on the velocities of the motions involved, a fact that has itself been exploited for particle transfer [127]. Furthermore, rolling or shearing motion produces stresses in the material that can be orders
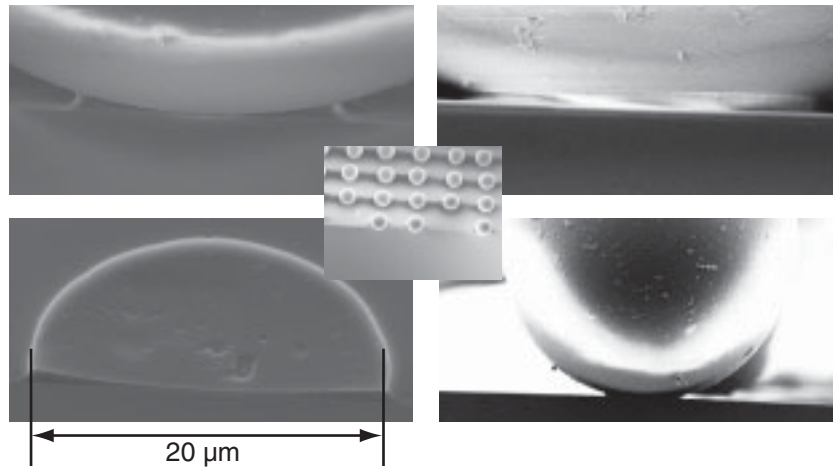
Figure 5.24: Particle-surface contacts in the presence of an adhesion layer, namely, spin-on glass.

of magnitude higher than those from normal forces and thus have to be avoided during integration. Rolling leaves rather distinct failure marks as shown in Figure 5.25, where a thin sheet of material is dragged along by the particle before it is ripped of. The most common origin of a rolling motion is a misaligned carrier that forms a wedge with the target substrate. When the carrier is removed from the target, the compressive stress is released, which can cause a sideways motion that causes the particles to roll off.

Another source of stamp deformation and, therefore, stress on the particle-surface junction are temperature differences. It is often necessary to print at elevated temperatures, where the adhesion layers are more reactive or softer. PDMS has a coefficient of thermal expansion of 3.1×10^{-4} K^{-1}, at least an order of magnitude higher than that of glass (usually smaller than 10^{-5} K^{-1}). When the carrier heats up, the defor-
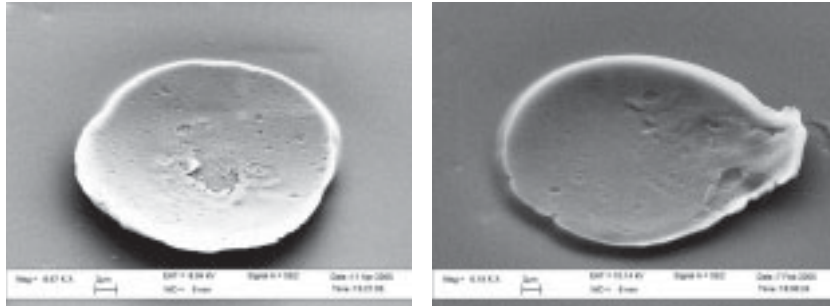
Figure 5.25: Imprints of rolling particles which failed to adhere in the integration step. The spin-on glass layer could not hold the glass beads as they rolled away due to a misaligned carrier.

mations induced are substantial, and they manifest in shear stress on the particles. Thus, in the case of glass beads, it was necessary to print the particles with short contact times (below 10 s) and to remove the carrier before the PDMS could reach high temperatures.

High-quality integration is greatly aided when using a tool that holds substrate and carrier, and we have used such tools routinely. The latest-generation printing tool is described both in Section 5.3 and in Appendix B. Briefly, a temperature-controlled vacuum chuck increases the temperature of the substrate, so that the parallel aligned substrate can be brought into contact and shear is avoided.

The particle-surface junction is often a critical part of the device: for glass beads, it might have to transmit light without distortion, for conductive particles, it might have to provide a conductive path between contact pad and bead, in any case, it has to provide sufficient mechanical stability for further processing. Reaching these targets often requires some postprocessing.

Spin-on glass, the adhesion layer used for the glass beads, can be an-
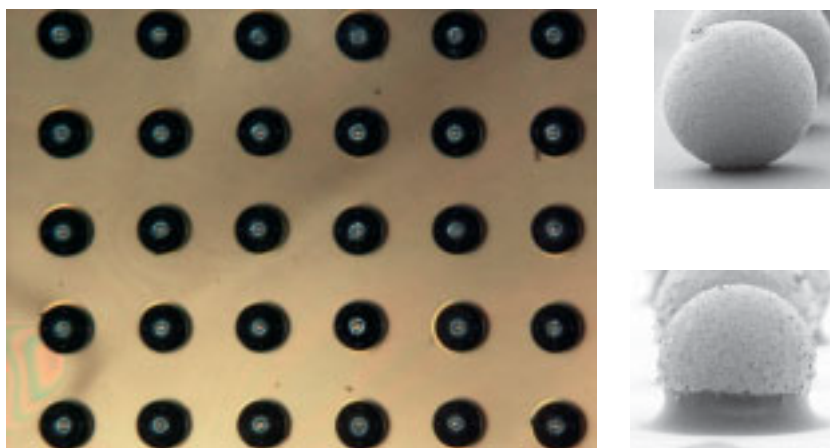
Figure 5.26: Array of tin-coated beads.

nealed to remove its organic components and only leave a compact glass layer. We have performed this annealing step at a temperature of 400 °C to produce an assembly that only consisted of glass (bead on thin film on glass substrate). In case of the conductive, tin-coated beads, no intermediate layer would be allowable which could increase the electrical resistance. The PIB adhesion layer therefore had to be removed, which we did by heating to 250 °C, where both the polymer pyrolyses and the tin from the bead starts to reflow. The result (shown in Figure 5.26) consist of particles electrically connected to the underlying gold pads.

So far we have seen spaced grids and arbitrary arrangements of particles. It might be useful, however, to also create dense monolayers of particles, possibly not with hexagonal dense packing that occurs naturally with hard spheres, but with other crystal types. This can be realized by using a master that only has thin posts in the position of the monolayer gaps, thus forcing the particles into a square grid. The adhesion-based
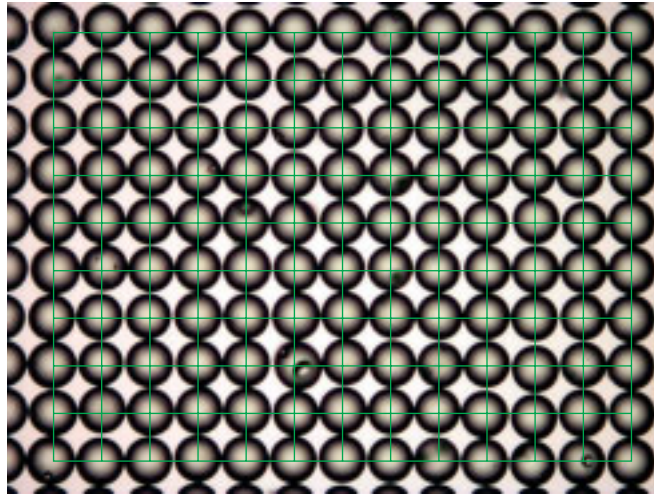
Figure 5.27: Printed, dense array of 100-μm square particle array on a
glass substrate covered with spin-on glass. The square grid
is shown as a guide to the eye.

transfer is capable of holding the dense array, even though the particle's
polydispersity causes the surface of the assembly to be exhibit consider-
able height variations (Figure 5.27).

It is again the particle polydispersity that causes defects in the assem-
bly and the transfer. Figure 5.28 has voids marked, all of which were
caused either by particles that were assembled but could not be picked
up on the carrier or by particles that blocked the neighboring position.
This reduces the yield by less than one percent, to 99.6% in the example
shown here.

This problem is alleviated when assembling in spaced arrays, where
the particles do not interact. The array in Figure 5.29 has a 200 μm pitch,
and the distortion is much smaller than that occurring in dense pack-
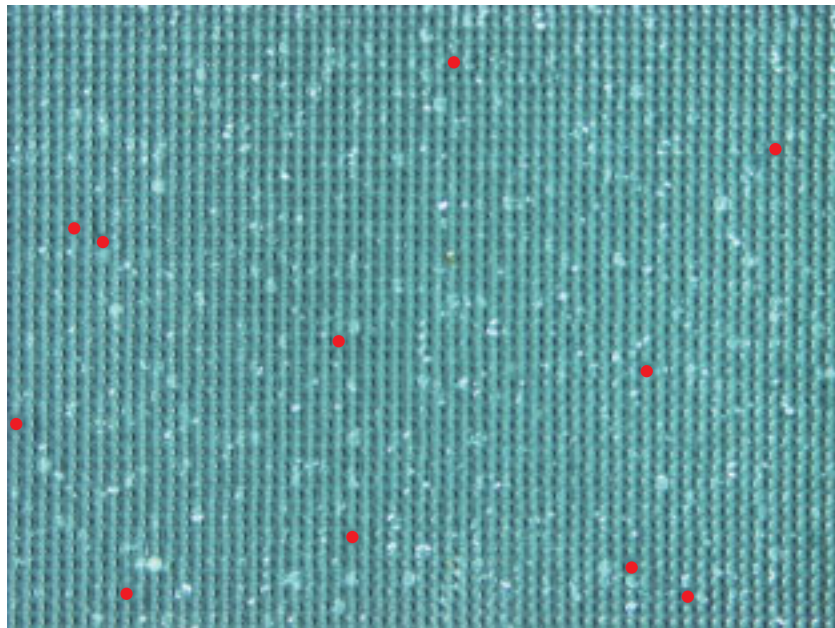
Figure 5.28: Defects in a dense, square array printed on a glass substrate covered with spin-on glass. Voids are marked by red spots for convenience. The yield in this image is at 99.6%.
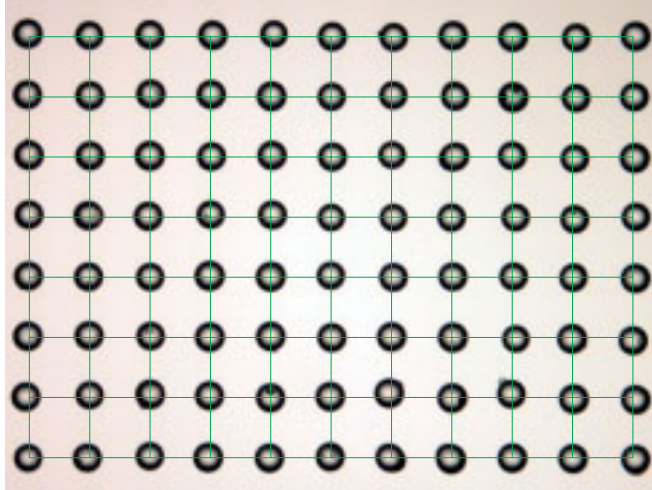
Figure 5.29: Printed, spaced array of 100-μm square particle array on a glass substrate covered with spin-on glass. The square grid is shown as a guide to the eye.

ings. This also underlines the quality of the adhesive handling, which did not introduce any long-range deformations as they may originate from bulk deformation of the soft polymer.

Defects in sparse arrays, as they are marked in Figure 5.30, generally are due to particles that were stuck in the assembly template (see above) or from particles that were too small to make contact with the carrier. The confinement of a particle sitting in a preformed hole on the template is more stringent than that of a particle in a dense array, so that particles are blocked more frequently. The yield is thus reduced by 1–5%, or 2.2% in the example shown here.

The SATI process flips the particles, so that the bottom side of the particles on the target is accessible during the transfer step. We have
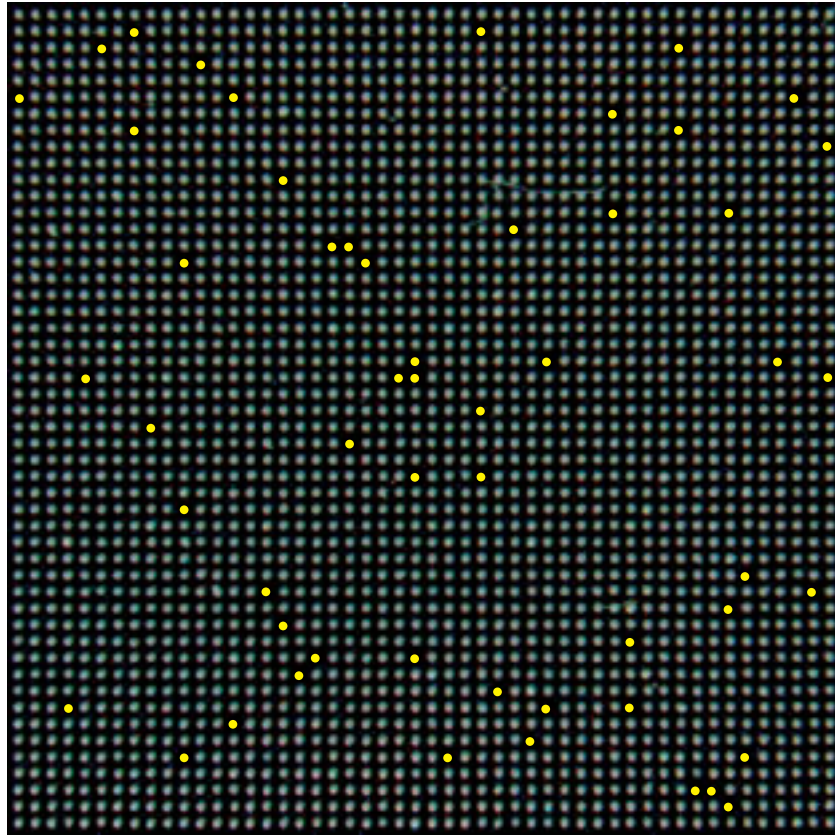
Figure 5.30: Defects in a spaced, square array printed on a glass substrate covered with spin-on glass. Voids are marked by yellow spots for convenience. The yield is at 97.8% here.

utilized this property to cover one half of an array of glass beads with thin gold films, producing microreflectors. It would also be possible to use this for the production of Janus particles that have two different chemical functionalities, depending on the side.

Finally, the entire process introduced here is modular and can be applied multiple times. In Figure 5.31, for example, an array of glass beads was printed on an existing array using a "SATI^2" double-print. Sufficient adhesion for the second print was provided by a spin-on glass layer deposited through spray-coating on the first particle layer, and the adhesive force provided by this layer proved sufficient to hold even instable particle arrangements that occurred in misaligned prints.
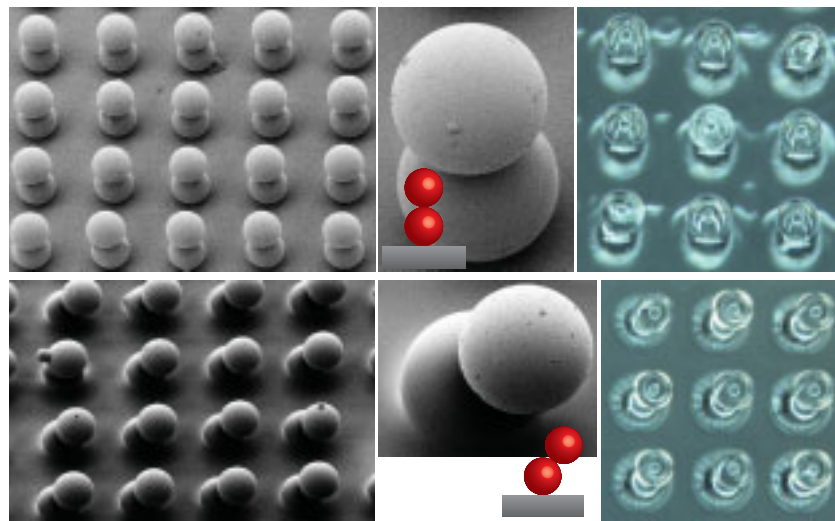
Figure 5.31: Stacks of particles fabricated using SATI². Depending on the alignment of the second printing step with the existing array, one can either produce centered stacks of beads or produce asymmetrical arrangements, both held in place solely by adhesion.

5.3 Latex beads[6]

Emulsion polymerization is a classical route producing small, spherical polymer particles in large quantities (their suspensions are called latexes). With the right choice of surfactants and process parameters, it is possible to create monodispersed particles using this method, which today are the highest-quality bottom-up nanospheres in terms of surface roughness, sphericity and size dispersion. They are frequently used as size standards for the calibration of electron microscopes or particle-size measurement instruments.

Polymer beads have been used for many years to create nanoscale structures on surfaces, first in a process termed "colloidal lithography", where hexagonal monolayers of these particles cover a surface, and a metal is evaporated only through the gaps between the particles. Depending on the evaporation angle, this produces large numbers of diverse metal objects on the surface [98]. However, their long-range order is limited by that of the particle monolayer, which always exhibits grain boundaries. More recently, XIA and others [186] have shown that polystyrene particles can also be arranged on surfaces according to topographical or chemical patterns in other arrangements than dense packings. As it is difficult or impossible to arrange sub-micron particles with pick-and-place techniques, such parallel techniques are currently the only realistic approach to the creation of complex particle arrangements.

Polymer particles also are available with a variety of different surface functionalities, including carboxylic acid, amino and active ester groups, which has made polystyrene beads the prevalent carrier particles in biology and medicine today [90]. Assays use their surfaces for DNA recognition or immunological reactions. Originally this involved a large number of particles that reacted in parallel, but single-particle assays already are in clinical use.

Dense monolayers without long-range order can be formed on unpatterned substrates, but more complex arrangements require templates, and often specialized surface chemistry for particle arrangement. In many cases, applications demand arrangements of particles on planar surfaces with simple chemistry, and it is problematic if the entire surface needs to undergo a colloidal deposition step, which commonly creates surface contamination. A simplified SATI process based on particle transfer can decouple the two steps (Figure 5.32): Assembly is performed on a patterned carrier, which provides the structures necessary for particle alignment, but the particles are transferred onto a flat surface or a preformed device only afterwards. In the following, we will show how this process can create complex particle arrangements on plain surfaces.

5.3.1 Particles

Emulsion polymerizations that yield polymer particles commonly use mixtures of surfactants to form an emulsion of the monomer, which is then polymerized using a water-soluble initiator. Through the choice of proper surfactant systems (often mixtures of ionic and non-ionic surfactants) these particles can be made monodispersed with low coefficients of variation [184]. The surfactants often remain in the latex suspension, with strong effects on the wetting properties of the system.

One popular polymer for the production of monodispersed latex particles is polystyrene and its derivatives. Polystyrene (PS) beads can be stained easily with conventional or fluorescent dyes (see Figure 5.33) by simple addition to the monomer, or functionalized on their surfaces by copolymerization of the monomer with molecules having functional groups, such as (meth)acrylic acid, glycidyl methacrylate or active-ester

197
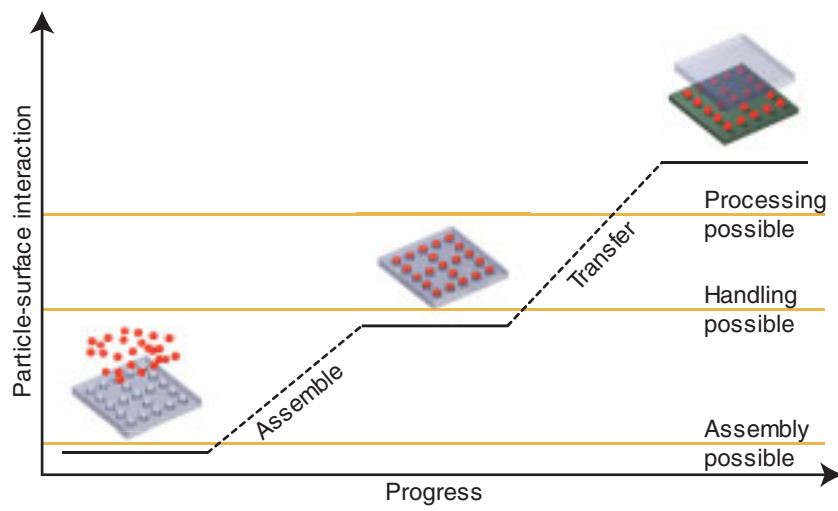
Figure 5.32: The SATI process for polystyrene spheres. The assembly
is performed directly on the (patterned) carrier, so that one
step can be skipped.
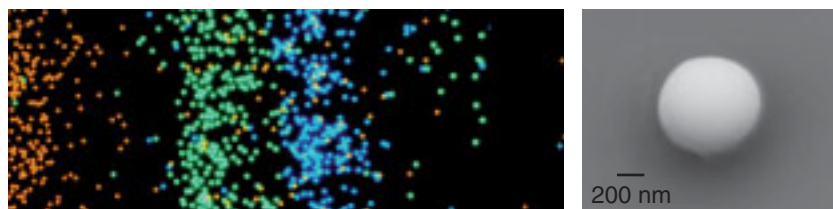
Figure 5.33: Latex beads in the optical microscope (left image) and the scanning electron microscope (right image). The dyes visible on the left are contained in the bulk polymer.

containing molecules [90].

Because of their narrow size distribution (1.3% coefficient of variation in a typical commercial system), monodispersed latexes readily form colloidal crystals, a property that has been known since their advent and was actually one of the driving forces behind the development of synthesis protocols. Already in 1968, the then-director of the Paint Research Institute, Raymond R. MYERS, wrote,

> Two decades ago uniform-sized latexes were a laboratory curiosity. In this paper you are witnessing the emergence of a third phase in the often-repeated sequence from curiosity to rare and expensive research item to readily available and useful commodity. (...) Opalescent coatings are almost a reality; and the problem now is to make them mechanically strong [184].

5.3.2 Assembly methods and tools

While it is comparatively easy to obtain dense colloidal crystals from monodispersed polymer latexes, their arrangement into sparse patterns
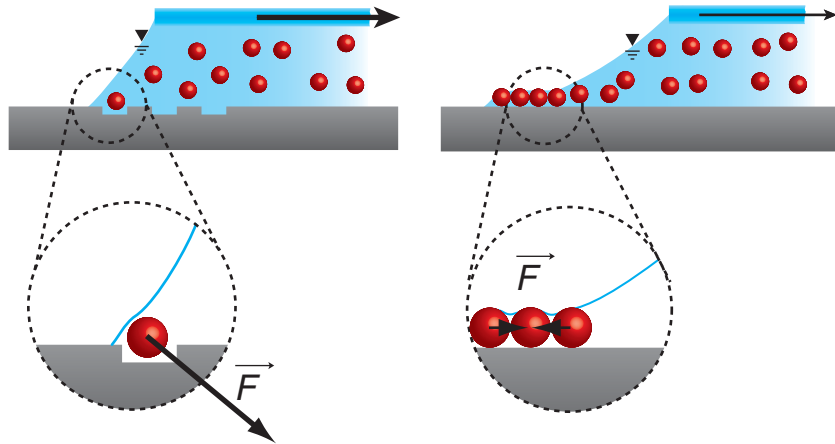
Figure 5.34: Capillary and convective particle assembly.

or dense arrangements with long-range order requires more effort. From the wide range of assembly methods for colloidal particles outlined in Section 2.3, we use two approaches based on capillary forces and convective flow here (Figure 5.34). The thin layer of liquid that forms on wetting substrates when a meniscus of colloidal suspension is moved over them provides a vertical confinement that forces particles into a dense layer, and the capillary interactions occurring between the particles in this layer while the liquid is drained help establish dense packings, most notably, hexagonal dense crystal layers [45, 144].

More confinement is necessary when particles are to be assembled into sparse structures, either into groups (be it particle lines, patches, or heaps) or individually. This local confinement can be provided by topographical structures on a hydrophobic assembly template at larger contact angles [40, 85]. The details of the possible assembly mechanisms have been discussed in Chapter 3. This method is versatile enough to

produce complex arrangements if the template geometries are chosen properly.

Experimentally, both methods require similar procedures. The meniscus of the colloidal suspension is moved over the substrate, while temperature and speed are controlled to ensure sufficient particle supply to the assembly region close to the three-phase boundary line. In convective assembly, insufficient particle supply or inappropriate process parameters lead to discontinuous assembly: instead of a full layer, narrow strips of particles are deposited. In capillary assembly, the yield drops, or the number of particles deposited at a desired position vary, if the particle flux is not controlled sufficiently. Here, we use a dedicated setup to control the particle flux via temperature and to observe the effects in-situ.

Experimental Setup. This setup (Figure 5.35) combines a translational stage with a temperature-controlled vacuum chuck that holds the template. A microscope mounted on top enables online observation of the assembly, an auxiliary microscope camera mounted at the side provides images of the meniscus itself to monitor the contact angle and amount of pinning that occurs. The colloidal suspension is injected in between the template and an inclined glass slide fixed on top of the translational stage, so that the template moves under the immobile colloid volume. All functions are controlled through a computer interface based on LabView. Two successive versions of this tool, CAPA1 and CAPA2, were used in this work. Figure 5.36 shows the second, later version, which is similar in functionality to the original tool, but provides improved microscopic observation, including fluorescence microscopy.

In a typical assembly, a volume ranging between 40 and 100 µL is placed in between template and slide with a pipette. The distance be-
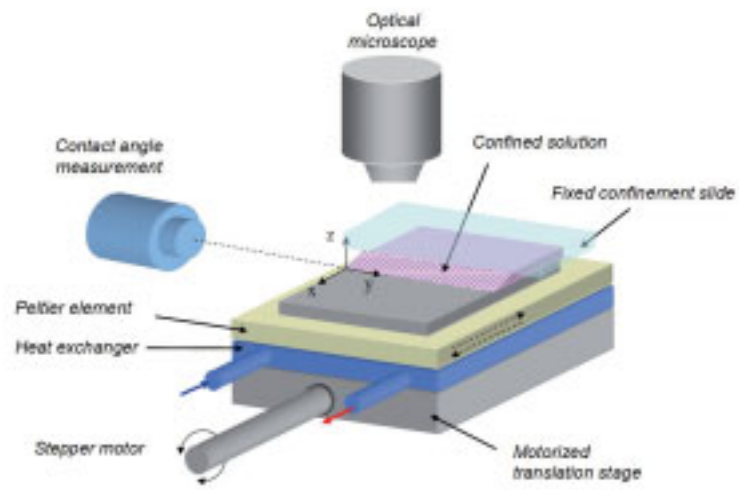
Figure 5.35: Schematic rendering of the Capillarity Assisted Particle Assembly (CAPA) Tool.
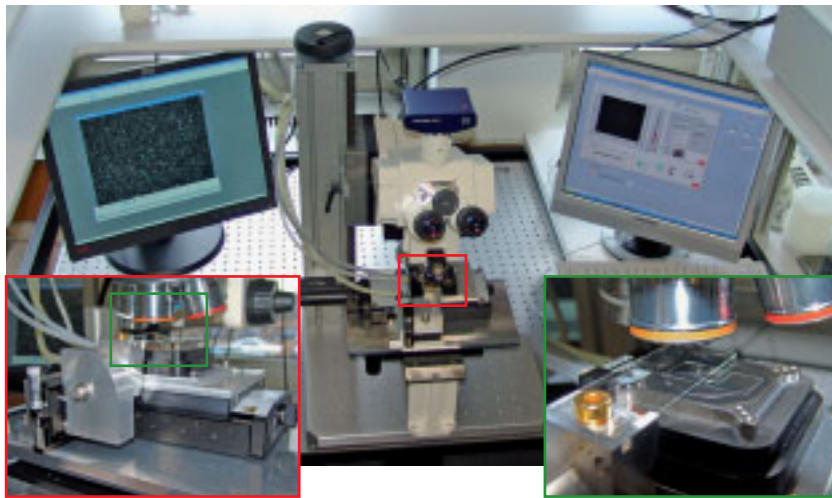
Figure 5.36: Overview of the Capillarity Assisted Assembly Tool, revi-
sion 2. The center shows the microscope for in-situ observa-
tion, insets on both sides have details of the heatable stage
underneath the microscope.

tween the moving and fixed part is adjusted to approximately 0.5 mm, and the motion of the substrate is started with velocities between 0.01–200 µm/s. The water slowly evaporates from this volume, where the rate depends on the colloid temperature and the humidity of the environment. As the liquid volume is very small, its temperature can be rapidly changed by changing the substrate temperature; to this end, the setup features a PELTIER element driven by a PID-controlled power source. Temperatures between 0 and 40 °C are thus accessible with an accuracy of ±0.1 K.

In-situ observation enables rapid analysis of the effects caused by different parameters and is provided through an optical microscope. The top-view observation in reflection or fluorescence mode reveals yields, assembly regimes, and (indirectly, through the colors) layer thicknesses. For sufficiently large particles, we can analyze particle trajectories by particle image velocimetry or track single-particle motion in movies recorded during assembly.

Monolayers and multilayers. Particle monolayers form in the thin liquid layer that wets hydrophilic substrates if the particle flux is not large enough to cause multilayers to form. This condition limits the allowable parameter space (temperature and velocity) to a rather narrow band, because insufficient particle fluxes cause discontinuous assemblies of monolayer stripes. If the flux is chosen properly, particles are continuously inserted into the monolayer and are guided on their way by the local liquid velocities that depend on the geometry of the assembled layer: a gap in the monolayer implies a reduced pressure drop acting against the evaporative flux of liquid, and a increased local flux directed at this gap, which will therefore soon be occupied. Such mechanisms have already been described for three-dimensional colloidal crystals [177] and

204

can be observed in detail here thanks to the microscopic imaging.

Monolayers created with this method are hexagonally packed, with grain sizes on the order of tens of micrometers (see Fig. 5.37). It is possible to coat areas in the square centimeter range, although it is not easy to keep the system stable for so long a time, while water evaporates and changes the bulk concentrations inside the colloid. Besides the grain boundaries, voids occasionally occur, with a density (only weakly dependent on process parameters) usually below 1%. The layers shown here were assembled from a suspension containing a 0.5% solid fraction of 500-nm polystyrene beads and at a substrate temperature of 18 °C, yielding layers with approximately 100 ppm of void defects. Regardless of the process parameters, however, it was impossible to produce continuous macroscopic crystals without grain boundaries. Decay lengths of interparticle forces are generally too short to provide longer-range order. If very large grains are required, structured templates can be used to impose order onto the assembly [190].

Figure 5.38 shows the product of convective assembly on a structured substrate. Here, the substrate had shallow (100 nm deep) lines, and while their spacing was not commensurate with the particle diameters, a superstructure with long-range order was imposed on the layer. It might even be possible to produce hexagonal layers with long-range order, as we have demonstrate for 100-μm-beads.

If the particle flux exceeds that required to form a single monolayer, and if the nucleation barrier is overcome (e.g. due to the deposition occurring while the substrate is left immobile), multilayers can be assembled in the same way as the monolayers above. In practice, we adjust substrate speed as well as colloid temperature (and, thus, rate of evaporation) to form films with the desired number of layers and distinguish the product microscopically through its characteristic color.
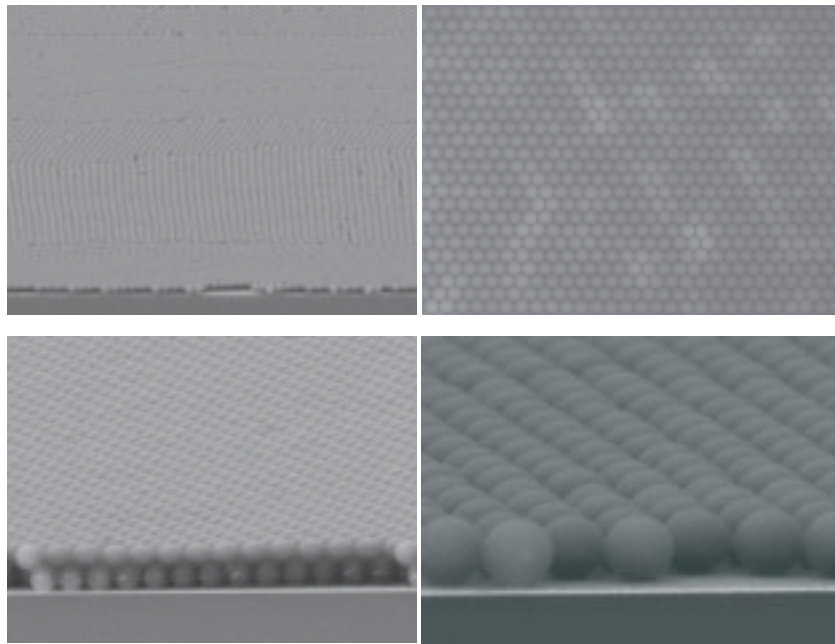
Figure 5.37: Layers of 500-nm-particles, arranged into a hexagonal dense packing on a flat, oxygen-plasma treated PDMS surface.
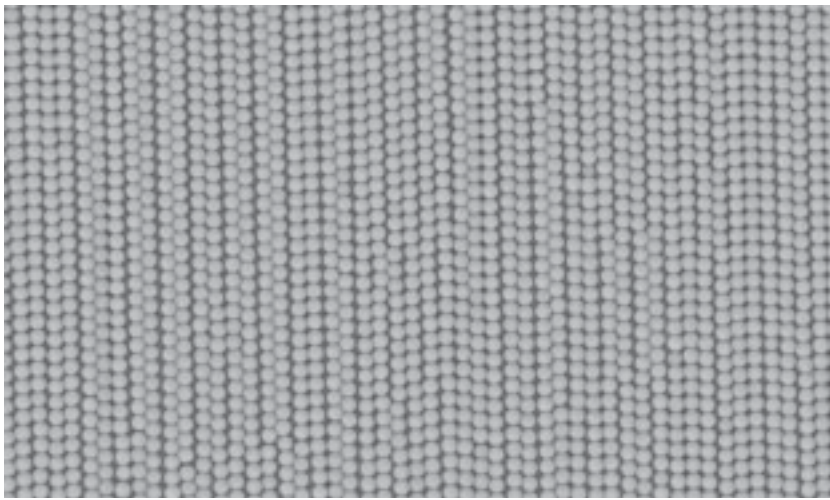
Figure 5.38: Monolayer of 500-nm-particles, arranged into a hexagonal dense packing on a patterned, oxygen-plasma treated PDMS surface. The surface featured 100-nm-deep lines to bias the assembly.

Groups of particles and single particles. When the substrate is hydrophobic and flat, no particles are deposited from the moving meniscus, because the capillary forces prevent the meniscus from breaking up, and the hydrodynamic drag moves the suspended particles along. At certain contact angles, however, the deformation of the meniscus through features on the substrate is sufficient to trap particles. In this "capillary assembly" mode, particles are deposited at positions predefined by the shape and size of the assembly sites on a template, depending on the process parameters.

We use this assembly process to place single particles and groups of particles, including lines of particles, small areas filled with particles, and three-dimensional "heaps" of particles. The assembly sites on the template can feature either convex or concave steps, where convex features generally only trap lines and small groups of particles, while concave holes and recessed areas can be entirely filled with particles. The height of the assembly sites can be smaller than one particle diameter, so that the later printing step is not hindered by the surface topography.

The motion of the three-phase boundary line is critical for this assembly method, and so is the angle of contact. This is reflected by a narrow range of contact angles between 30 and 60° that allow for successful assembly. The contact angle on a flat substrate is a function of the suspension composition and the surface properties, and while pure water has a high contact angle with PDMS of up to 107°, that of the latex suspensions is generally lower. The reason is the surfactant content from the emulsion polymerization mentioned above, which we can utilize to tune the angle in the correct range by changing the concentration of the original continuous phase.

If the contact angle is adjusted, single particles can be immobilized both by concave, square holes and convex corners (Figure 5.39). The po-
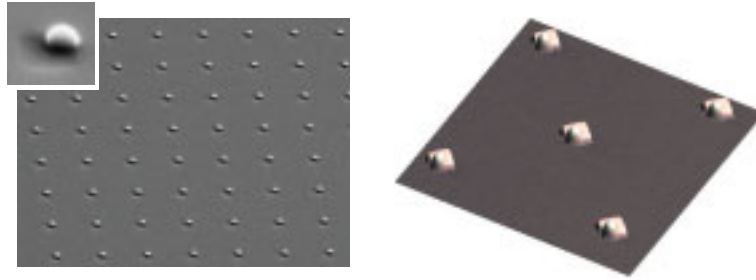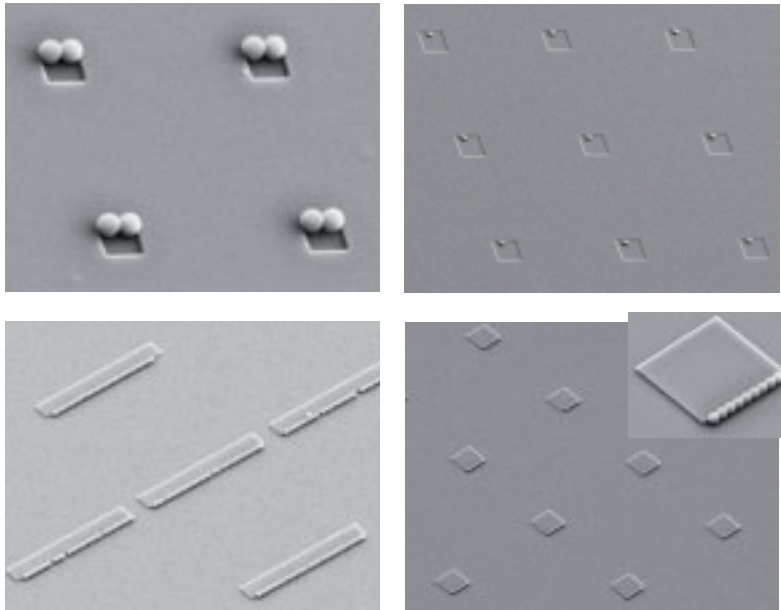
Figure 5.39: Single particles trapped in concave holes and in convex corners. The template was molded is PDMS and left hydrophobic. During assembly, the three-phase boundary line moved from the lower left to the upper right corner.

sition of the particles inside the holes is uniform over all assembly sites, depends on the assembly direction, and is preserved throughout the SATI process for these particles. Thus, we have a type of hydrodynamic focusing here that increases the resolution of the method. Small convex corners trap particles only when the assembly direction (the vector normal to the three-phase boundary line, on the substrate) goes through their open side.

In larger assembly sites that could accommodate multiple particles geometrically, the actual particle arrangement depends both on the direction of motion of the three-phase boundary line and on the process parameters used. Figure 5.40 shows concave assembly sites with two particles trapped and larger sites, where four particles per site were trapped, not filling the available space. In the micrographs below, particles sit at the step edges of convex rectangles, where they form lines. The resulting particle arrangements also give insight into the trapping

mechanisms, discussed in more detail in Section 3.3.3.

All assembly sites shown so far had height differences that were smaller than one particle diameter to facilitate particle printing in a later process step. Deeper holes can also be filled with particles using capillary assembly, as shown in Figure 5.41. The order of the particles is weaker than in many of the flat arrangements and the packing is not fully dense, both of which might be effects of the holes' geometry. It is possible to transfer even the three-dimensional arrangement in a single printing step to arrive at the structures shown in the right micrograph. The outer surfaces of the pyramidal frustra are of higher crystalline quality than the bottom that is visible before printing.

An extreme case of capillary assembly is represented by long channels, filled with particles through a boundary line that extends normal to the channel direction. The pinning becomes so strong that a part of the meniscus extends into the channel, which acts as an open microfluidic duct. Particles are then dragged into the channel by the liquid flux and form structures as they reach the assembly front, which can be tens of micrometers away from the apparent end of the meniscus. These structures can be hexagonal crystals, but we often find other structures, and oscillations between two types of order in a single channel (Figure 5.42). As noticed by Y IN et al. [193], the confined crystal deforms and assumes complex habits to fill the channel if the geometry is incompatible with a hexagonal arrangement. The driving forces are capillary interactions as the liquid is drained from the particles and dries. It is worth noticing that even during assembly, large parts of the already established crystals change color and visibly deform, so that the final structure is not only a result of the initial assembly process, but of the subsequent drying as well.

From a practical standpoint, we want to predict the particle arrange-

Figure 5.40: Groups of particles trapped in concave holes and at convex rectangles. The template was molded in PDMS and left hydrophobic. During assembly, the three-phase boundary line moved from the lower right to the upper left corner. In the upper right corner, the particles were not deposited directly at the step edge, but a heap of (usually four) particles remained close to the upper left corner of the recessed squares.
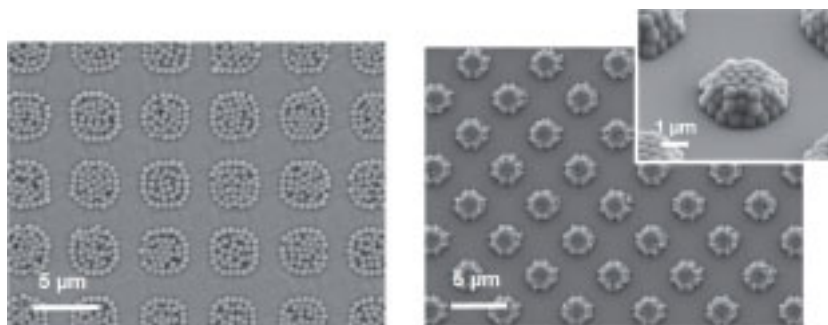
Figure 5.41: Three-dimensional arrangement of beads filling a larger hole in the template. The assembled particles were printed in a single step to allow inspection of the outside (right micrograph).

ment for a given template topography, and we want to predict the process parameters that provide the highest assembly yield and reproducibility. Two probes can give insights relevant to both interests: the influence of assembly site geometries on the final particle arrangement, as discussed above, and the dependence of the assembly on particle concentration. The relevant particle concentration is not that of the bulk colloid, but that close to the contact line, where the assembly actually takes place.

Through a mechanism discussed in Section 3, the evaporation of liquid from the colloid meniscus drives the formation of a high-concentration "accumulation zone" close to the three-phase boundary line. Its size (and probably also its structure) depends on the evaporation rate and, thus, the temperature (Figure 5.43). Reducing the colloid temperature therefore also changes accumulation zone length, until at some point there is no discernable accumulation (see Figure 5.43). We find that ac-
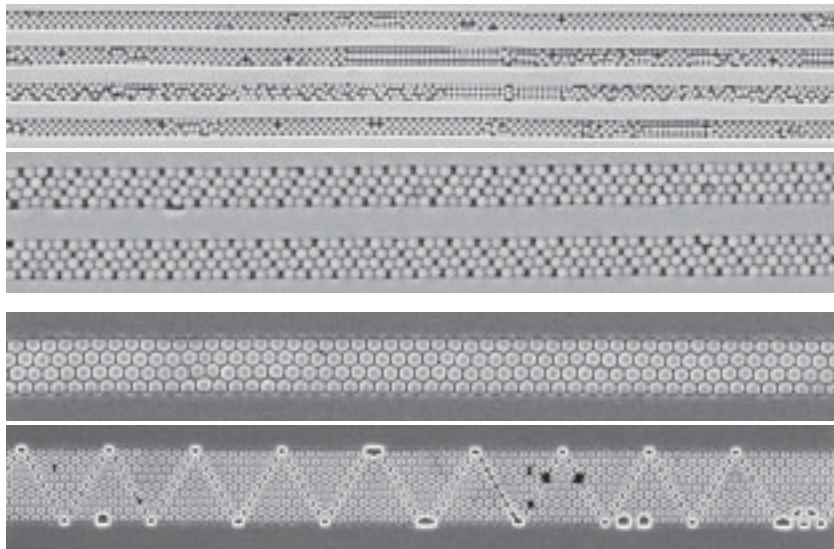
Figure 5.42: Channels filled with particles. The two micrographs on top show particles in 1-μm-deep channels, the lower two in 500-nm deep channels.
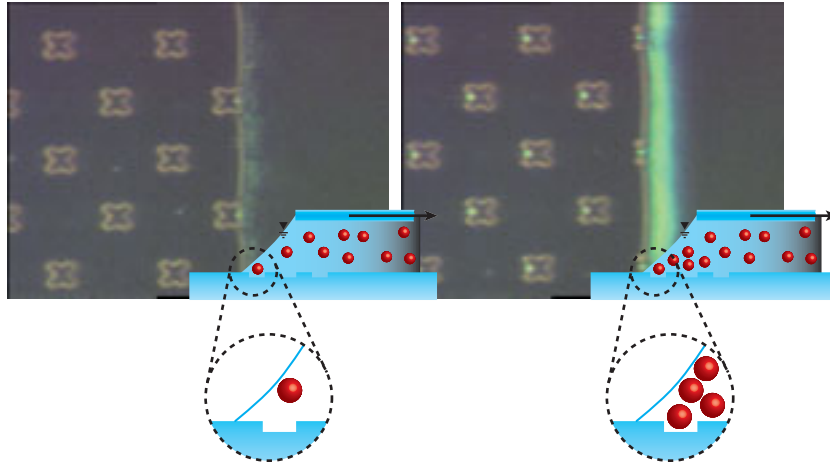
Figure 5.43: The accumulation zone at the three-phase boundary line for two different temperatures, 27 °C in the left and 32 °C in the right micrograph.

cumulation is a minimum requirement for any assembly.

While there is very little accumulation in the left micrograph in Figure 5.43 so that assembly would not be possible, an increased temperature rapidly leads to the formation of a high-concentration accumulation zone, clearly visible in the right micrograph as a bright band with opalescent colors. This band is visible even for smaller particles and provides a good feedback during the assembly process: the combination of temperature and environmental humidity can be chosen such as to provide sufficient accumulation.

The presence of an accumulation zone is necessary for assembly, but not sufficient for high-quality arrangements. Figure 5.44 shows some defects that can occur even if the assembly yield is high: grain boundaries even in small crystalline regions, variations of particle numbers in
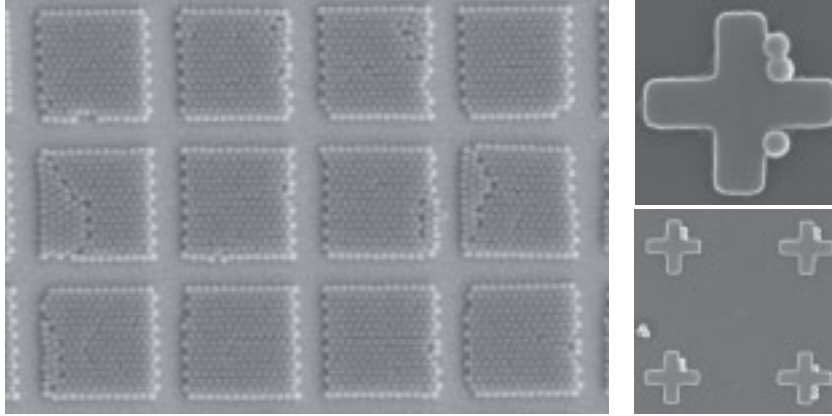
Figure 5.44: Grain boundaries, variations, and contamination during assembly.

the assembly sites, and contamination of the particle assembly. Common reasons for such defects are overly high assembly speeds, high assembly temperatures at low environmental humidity, particle-contaminated or rough templates, and excessive solute contents of the assembly colloid.

5.3.3 Transfer

Polymer beads soften at moderate temperatures (the glass transition temperature of polystyrene is around 100 °C, melting starts at 140 to 160 °C), which can be exploited for their transfer from carrier to substrate. If the beads are brought into contact with a hard surface and some force is applied, they will deform, create an increased interfacial area and gain sufficient adhesion with the substrate to provide an adhesion cascade (Figure 5.45).
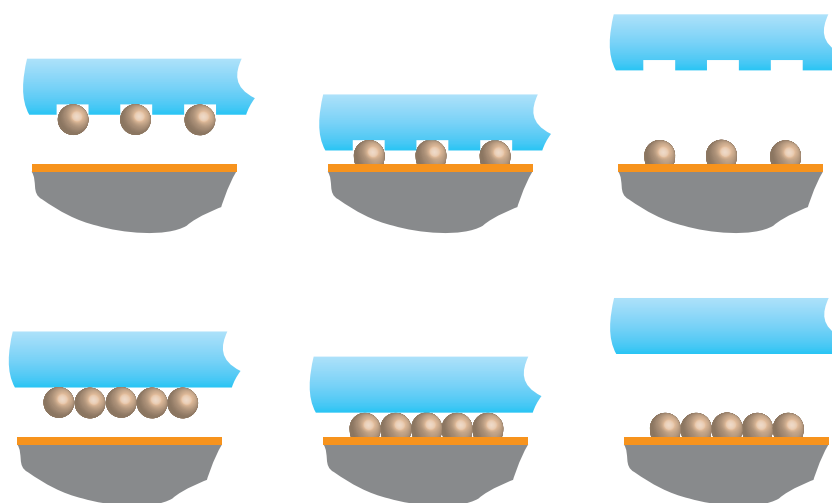
Figure 5.45: Transfer of PS particles through hot transfer. Both sparse arrangements (top) and dense lines or layers (bottom) are transferred by softening the particles on a hot substrate, which creates a large interfacial area and, thus, the last step of an adhesion cascade.

This requires, however, that the particles do not deform excessively on the other side (at the particle-carrier junction), and that the carrier does not deform excessively and distort the particle arrangement. The thin air gap between carrier and substrate and the low thermal conductivity of the beads both hinder heat transfer. It is thus important to choose both the temperature of the substrate and the force applied (which changes the gap width) properly. In particular, this requires to align the carrier and the substrate, so that the gap is uniform over the entire surface and shear forces are minimal.

We have devised a dedicated printing tool for the transfer process, shown in Figure 5.46. In the tool, the substrate is held on top of a temperature-controlled chuck by a vacuum applied through grooves on the chuck. It can be tilted in both directions and translated laterally. The carrier is held above the substrate either by clamping or by a vacuum holder. The clamping holder features three force sensors that provide both a measure of the force that is being applied during the transfer and aid the parallel alignment of the two surfaces. Vertical translation of the entire carrier is provided by a linear stage mounted vertically on a very sturdy tower. This stage can be either actuated by a manual micrometer screw or a Piezo stack, which then provides a resolution better then 100 nm. Design drawings and further details on this tool are provided in Appendix B.

To align existing structures on the substrate with objects to be printed from a carrier, a microscope is mounted on top of the tool. The operator can observe the carrier on top of the substrate through a hole in the carrier holder, because the entire stack is transparent. When the two surfaces are brought into close proximity, alignment is straightforward through the two-axes translational stage below the heatable substrate holder. In addition, there is a visible contrast between parts of the car-
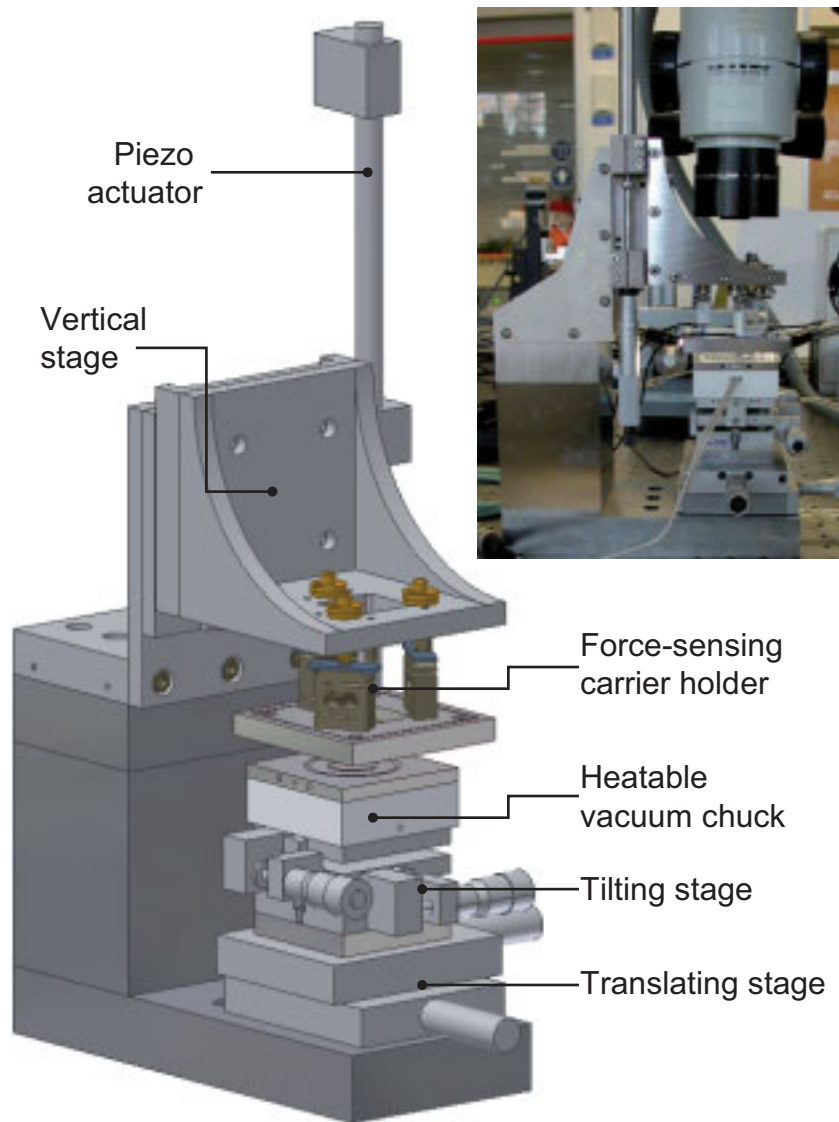
Figure 5.46: The Printing Tool. Depicted are the temperature-controlled chuck, the force-sensing holder, the alignment and the translational stages, and a stereo microscope (shown only in the picture).

rier that are in close proximity to the substrate and those that are in conformal contact. Waviness of the carrier or bad alignment thus become visible optically when parts of the stamp that come into contact long before others while the carrier is lowered on the substrate.

The tool was used by FLOREY to study particle deformations in dependence of temperature and force applied (Table 5.1) [60]. As expected, both high temperatures and high forces lead to increased deformations and a higher interfacial area. The adhesion was sufficient for transfer even at the lowest deformation observed (at around 1%), which was therefore used later unless a larger area of contact was required for other reasons. It also became clear that it is not necessary for the temperature to be above the glass transition temperature. Slight softening preserved the particle structure better and still sufficed to create a high-adhesion particle-surface junction. The lower temperature also improved the overall precision of the carrier movement and is therefore recommended for most applications.

In all experiments, the substrate was first brought to the desired temperature, the carrier was brought into contact, force was applied and the substrate was cooled to room temperature with the carrier still in contact after $60 - 90$ s printing time. At room temperature the carrier could be removed with excellent particle transfer yield.

The experiments described above were done with disordered, sparse particles layers that were directly distributed on the carriers through spin-coating. The results also hold for ordered arrays of particles, which we are ultimately interested in. Figure 5.47 shows a printed array of particles with a 10 μm spacing on a silicon substrate, transferred from a template having holes as particle binding sites.

Other, more complex geometries can be transferred equally well, for example the lines, areas and pyramidal frustra shown in Figure 5.48.

Table 5.1: Deformation of printed 500-nm PS particles in dependence of process parameters. Values from [60].

Temperature $T/^\circ\mathrm{C}$	Force F/N	Relative deformation d/d_0
115	2.5	25%
105	9	$15 - 17\%$
105	6	10%
95	8.5	3%
95	5.75	1%
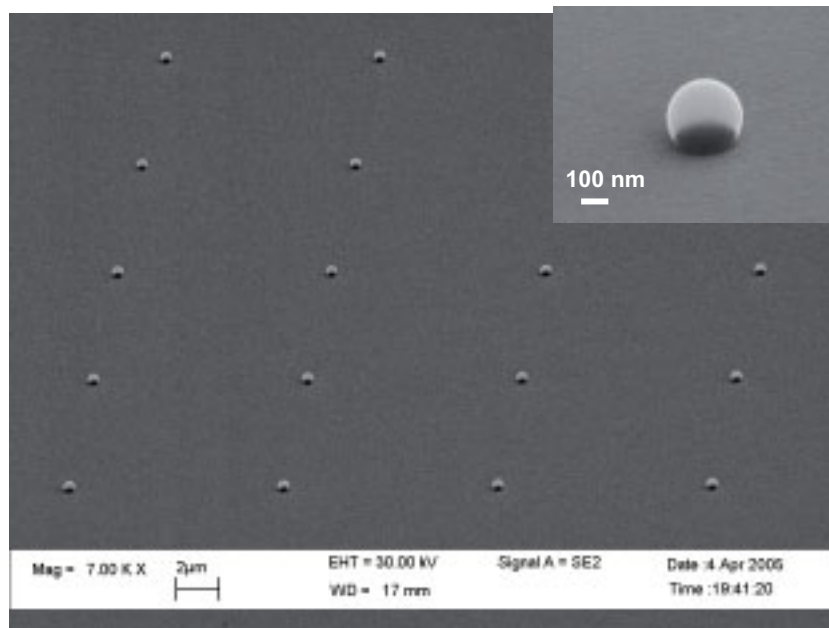
Figure 5.47: Arrays of PS beads with a 10 µm pitch printed on silicon.
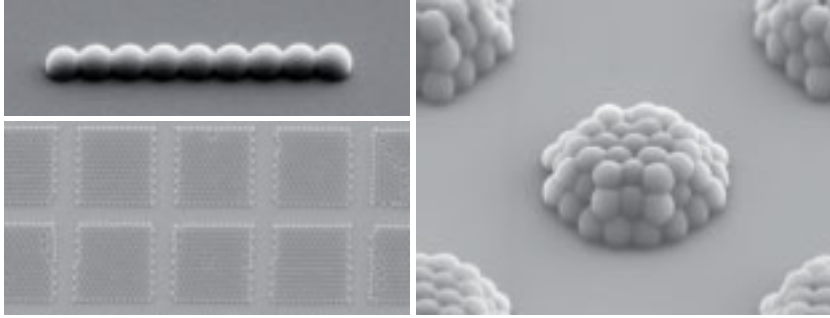
Figure 5.48: Lines, areas and pyramidal frustra assembled from PS beads in a single step and transferred onto silicon substrates. The three-dimensional frustra are held together by interparticle adhesion.

For the three-dimensional objects, the temperature and force have to be chosen such that the interparticle adhesion becomes sufficient. A temperature of $120°$ is sufficient for the particles to strongly adhere to each other while not melting together entirely.

Not only the area of the particle-substrate interface, but also the overall geometry of the printed particles depends on the printing temperature and the carrier. Figure 5.49 shows three beads with different interfacial areas, and it shows beads that have been transferred at moderate temperatures, but using a hard carrier. The hard surface changes the transfer mechanics such that a stem-like structure is formed on that side of the particles that are in contact with the hard carrier. Further details on such mechanical effects during transfer have been investigated in [60].
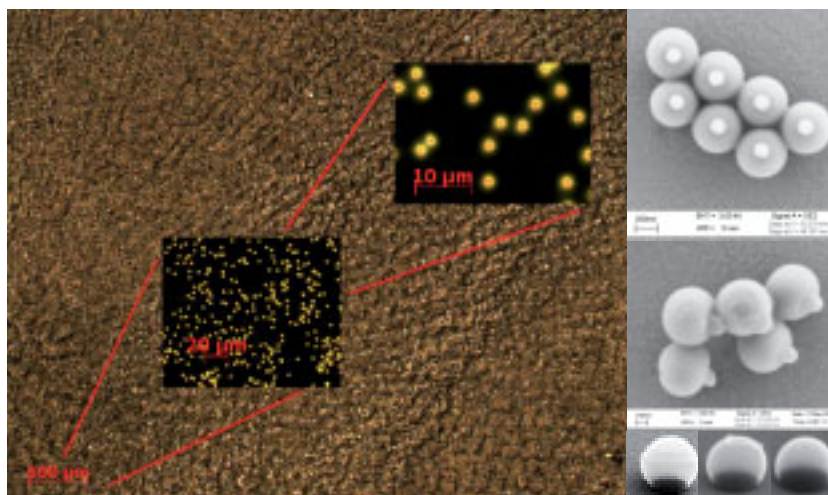
Figure 5.49: Particles with deformations and different interfacial areas.

5.3.4 Integration

With the combination of capillarity-assisted assembly and the transfer described above, we can create a variety of particle arrangements on unpatterned substrates with well-defined contact areas. Such structures allow extending the popular "colloidal lithography" approach from the exploitation of gaps in dense packings to the use of the contact areas of spaced particles. The printed beads act as resist patches and protect small circular areas of a surface, while other parts of the surface are etched.

We printed spaced arrays of 500-nm polystyrene beads on silicon wafers coated with a thin adhesion layer (Chromium or Titanium) and 30–40nm of gold. Upon immersion of the sample into a gold etch bath, the metal was removed from the entire surface except the patches under the
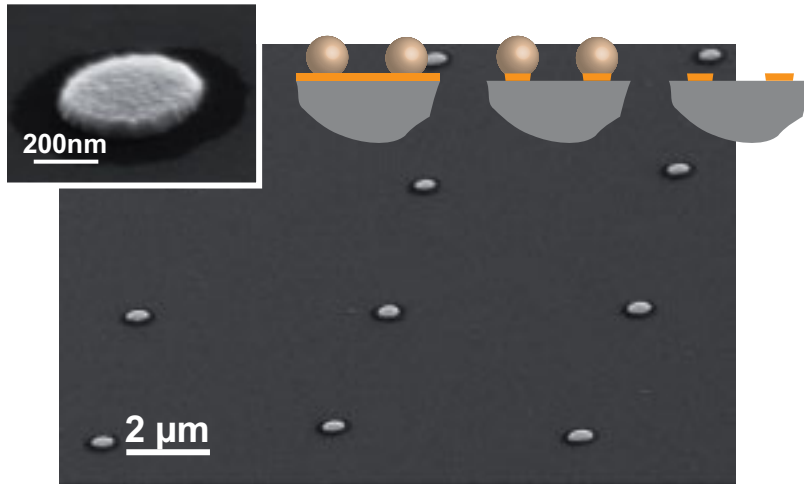
Figure 5.50: Gold patches created via sparse colloidal lithography with 500-nm PS beads. The gold was etched in a standard etch bath, while the discs were protected by the beads.

polystyrene beads. After removing the beads (in acetone and hot N-methyl-pyrrolidone, if necessary), circular gold discs remained on the surface, as shown in Figure 5.50.

Besides wet metal etches, a class of etch processes with wide applications in semiconductor technology are Reactive Ion Etches. We have tested the use of beads in such plasma etch steps by transferring them onto the oxide layer of a silicon wafer, which we then etched dryly to produce a "hard" oxide mask. This mask could be transferred into the silicon using a Deep Reactive Ion Etch to yield silicon rods as they are shown in Figure 5.51.

One target in developing the SATI method was to have a modular process that can be applied to prepatterned, complex substrates. The

Figure 5.51: Silicon rods created via sparse colloidal lithography with 500-nm PS beads. The beads' footprints were transferred into an oxide layer via RIE, and the hard mask was transferred into the bulk Silicon via DRIE.
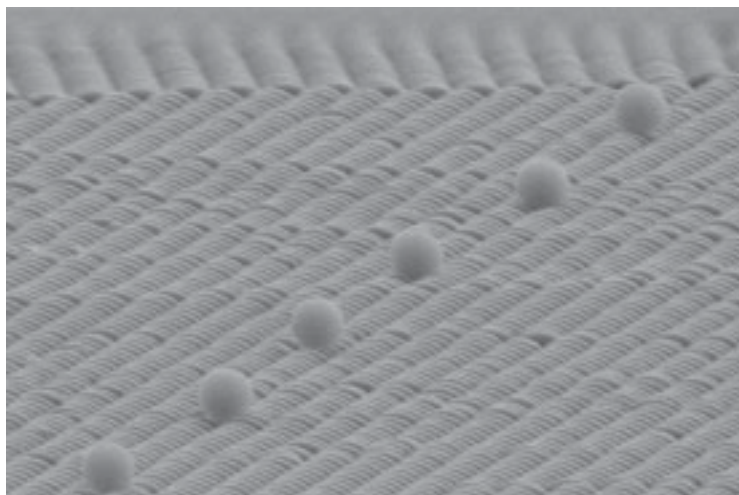
Figure 5.52: Two layers of 500-nm PS particles printed in two steps (SATI^2). Both layers were assembled independently on different carriers and combined on one silicon substrate by subsequent printing steps.

modularity of the process enables it to be applied multiple times (for example twice in the "SATI^2" process), creating structures as shown in Figure 5.52: on top of a dense monolayer of particles, we printed a sparse arrangement. In this example, the two structures were not aligned, but alignment certainly is possible utilizing the optical access through the transparent stamp.

The process also is compatible with complex surfaces, mainly because the carriers are soft and can conform to the surface topography of the substrate. It thus becomes possible to combine particles across different length scales, as shown in Figure 5.53. Here, we first integrated 100-µm glass spheres using the methods described in Section 5.2 and then
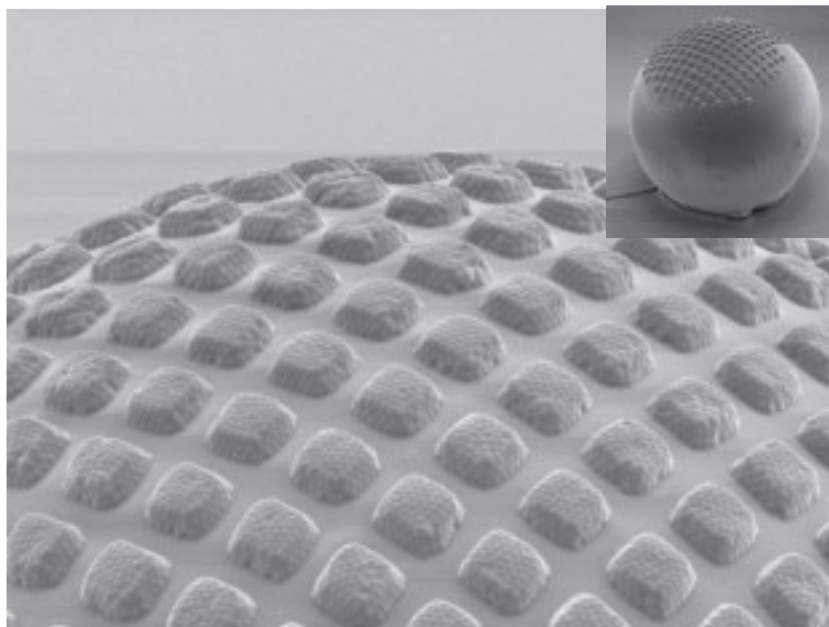
Figure 5.53: Heaps of 500-nm PS particles printed on an array of 100-µm glass beads (SATI^2 across scales).

placed a carrier with heaps of 500-nm PS spheres on top, transferring them at elevated temperature. The carrier conformed to the caps of the larger spheres, which were covered with the structures composed of the smaller spheres.

5.3.5 Experimental details

Aqueous dispersions of monodispersed polystyrene (PS) particles (499 ±5 nm, 1% of solid content) were purchased from Duke Scientific (Palo Alto, CA, USA). The particle concentration was adjusted to values rang-

ing from 0.1% to 5% of solid content by dilution with deionized water or by centrifugation (10000 rpm, 5 min). The suspensions contained a surfactant mixture, which we used to tune the angle of contact. If even lower angles of contact were necessary, we used a mixture of Triton X-45 and sodium dodecyl sulfonate, as described in the next section.

The transfer of polystyrene particles is described above and in [100]. It was performed by bringing the processed templates into contact with a 2×2 cm^2 silicon piece (covered with native oxide) or gold-coated (30–40 nm Gold on Titanium or Chromium adhesion layer) silicon wafer piece placed on a hot plate and heated to 120 °C. Pressure was applied on the carrier either manually to ensure good contact and sufficient deformation of the polystyrene particles at the interface or using the printing tool discussed above.

5.4 Nanocrystals[7]

---

[7]Part of this work has been published in [101].

Metal colloids have a long history, and many of the collective properties that such dispersions of nanocrystals exhibit have been exploited for decades. Glass staining with gold, already known in antiquity, is a favorite example; and the "soluble gold", *aurum potabilis*, was one of the favorite universal remedies of alchemists, notably PARACELSUS. The true nature of colloidal metal dispersions had long been subject of debate, and it was not until MIE published his famous treatise on the subject that the notion of finely dispersed crystals became universally accepted as the origin of their distinct colors. Even before, researchers had used this unusual form of metal to construct materials with complex properties: Michael FARADAY's dried colloids, for example, changed color when mechanical pressure was applied [57].

The idea of using metal nanoparticles as building blocks for complex structures is much more recent [42]. The first attempts in this direction were probably the studies by FRENS [64], from the PHILLIPS research laboratories, to produce monodispersed gold nanocrystals with defined sizes below 100 nm in diameter by modifying procedures of TURKEVICH and others [174]. These particles provide very good contrast in scanning electron microscopy, which made them a popular choice as contrast agent in biological applications, and have since then become one of the standard objects to be used in nanotechnology research. It has long been known that their surfaces can be functionalized with thiols, which provides a route to large numbers of surface functionalities. Very small gold particles ("clusters") were produced by SCHMIDT and others, working in the organic phase [156]. Finally, other shapes of gold particles, most notably rods, could be produced when introducing certain surfactants to the solutions. Together, these advances have made metal nanoparticles — and gold nanoparticles in particular — arguably the most general, highest-quality and best-documented class of nanoscale building blocks

available today.

It has been proposed that such nanoparticles could be the basis of more complex, designed structures, which would be manufactured, for example, by having the particles self-assemble. However, even metal nanoparticles are bad building blocks compared with the interchangeable parts that revolutionized industrial manufacturing after Eli WHITNEY had popularized them. Even the best available colloids contain particles with different shapes, often mixtures of single crystals and irregularly shaped crystal agglomerates. Their relative size distribution is considerably broader than that of macroscopic precision-machined parts. At the same time, the shape of nanometer-scale particles has a larger impact on their physical and chemical properties than that of macroscopic parts has on theirs. For example, different crystal faces have different surface energies, and different particle geometries interact with light differently.

Despite these drawbacks, small metal and semiconductor particles have attracted enormous interest in diverse fields. In electronics, optics and biology, small particles are the target of intense research and are used in a number of commercial applications [59]. Such applications exploit the particle's confined electronic systems [95], their strong interaction with light, with their matrix and with each other [120], their well-defined surface properties [54], their high catalytic activity [12] and — in sufficiently small particles — their quantum-confinement properties [109].

Using such particles as functional entities frequently requires arranging them on a surface, or integrating them between electrodes or in a device. Doing so with standard micro- and nanotechnology is difficult, and it is neither rapid nor efficient to create sparse patterns of small particles using subtractive top-down processing [142]. In this chapter,
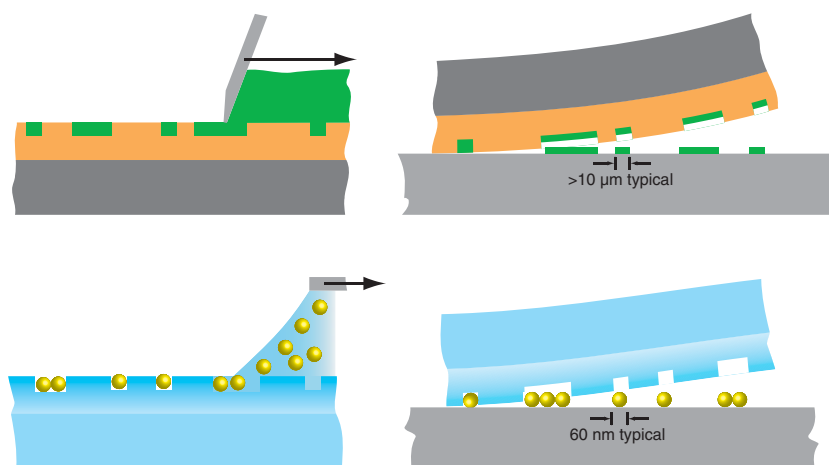
Figure 5.54: Gravure printing (top row), where a doctor blade removes excess ink, versus high-resolution particle printing (bottom row), where a meniscus removes excess particles from the printing place.

we show how the SATI process described before can be scaled down to handle nanoscale particles. The printed entities reach the size regime of pigment particles, and the resulting process is reminiscent of classical gravure printing. While standard printing methods print disordered films of particles and molecules, the process discussed in the following produces well-defined particle arrangements with single-particle resolution (see Figure 5.54).

High-resolution particle printing is based on self-assembly processes that ink nanofabricated "printing plates" with high fidelity coupled with controlled adhesion for the transfer. The process maintains the efficient, parallel nature of self-assembly without requiring specially patterned substrates or exotic surface treatments. Printing is possible on various

targets, including soft and flexible materials that are challenging to handle by other microfabrication processes.

5.4.1 Particle synthesis

Two main routes to the synthesis of gold nanocrystals exist: the "classical", water-based reduction schemes and the more recent, two-phase approaches, originally introduced by BRUST and SCHIFFRIN [23], following an original idea proposed by FARADAY [57]. In both approaches, the basic idea is to reduce a metal salt while preventing the nuclei from agglomerating. This requires protecting them either (in the aqueous phase) through electrostatic charge, as is provided by citric acid that also acts as the reduction agent in the original synthesis. In two-phase synthesis, the particles are capped with alkanethiols or other thiols as they grow in the organic phase, whereas the precursors are supplied from the aqueous phase. Electrostatically stabilized colloids are more sensitive to pH and ionic strength and are not stable in non-protic solvents, which is one of the reasons that thiol-capped colloids are now the most widespread system for particles below 10 nm if a dispersion in organic matrices is desired.

The actual reduction in the case of aqueous synthesis for gold simply is

$$n \cdot \mathrm{AuCl_4^-}\,(\mathrm{aq}) + 3n \cdot \mathrm{e^-} \longrightarrow \mathrm{Au}_n,$$
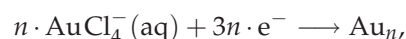
with electrons either from the oxidation of citric acid or another reducing agent, such as $\mathrm{NaBH_3}$, or phosphorus. Citric acid also adsorbs on the gold surface, thereby stabilizing the colloid, unless it is replaced by a better LEWIS base, such as oxyanions [41].

In two-phase synthesis, the situation is complicated by the presence

of a phase-transfer agent. It often starts with

$$AuCl_4^- (aq) + (C_6H_5Me)N(C_8H_{17})_4^+ \longrightarrow (C_6H_5Me)N(C_8H_{17})_4^+ AuCl_4^-$$
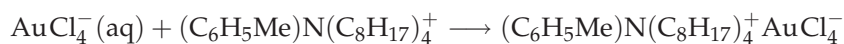
where the tetrachloroaurate ions are transferred through the toluene by tetraoctylammonium bromide as a phase-transfer agent, followed by the reduction,

$$m \cdot AuCl_4^- (C_6H_5Me) + n \cdot C_{12}H_{25}SH(C_6H_5Me) + 3m \cdot e^- \longrightarrow$$
$$4m \cdot Cl^- (aq) + [Au_m(C_{12}H_{25}SH)_n](C_6H_5Me).$$
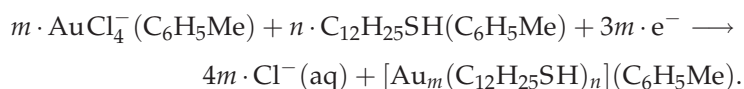
Besides the dodecanethiol used in this example, many other ligands have been used as capping agents, and the method has been combined with microemulsions and micelles, usually to improve monodispersity and allow new chemical functionalities on the particles [42].

The ultimate challenge for all approaches is a reliable synthesis of monodispersed particles having a defined size and uniform geometry, a goal that is particularly difficult to reach for particles larger than a few nanometers. In small clusters (such as the SCHMIDT clusters that contain 55 gold atoms) the atoms tend to arrange in a small set of well-defined structures, but larger particles can grow in various shapes. Gold nanocrystals (and nanocrystals from fcc metals in general) usually are either monocrystals or polycrystals, often with a pentagonal symmetry that is unique amongst all manifestations of gold. GRYAZNOV et al. [70] summarize some frequently appearing habits, their overview is reproduced in Figure 5.55.

Colloidal particles often are polydispersed, either because particles nucleate at different times, their growth rates are different or particles agglomerate during production. One strategy to reduce the polydisper-
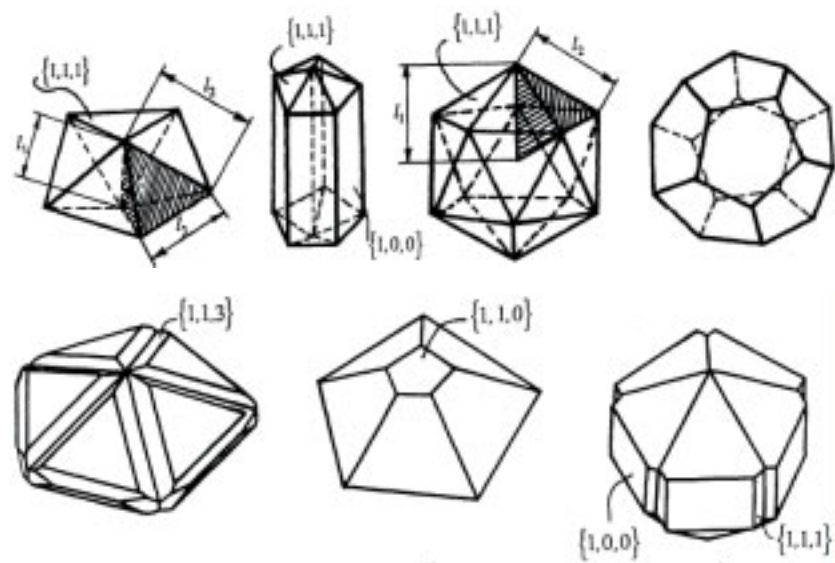
Figure 5.55: Habits of nanocrystals from fcc metals with pentagonal symmetry. From [70], copyright Wiley–VCH Verlag GmbH & Co. KGaA. Reproduced with permission.

sity is to start not from a homogeneous solution, but to introduce seed-
ing crystals. This prevents the formation of new nuclei at a later stage in
the synthesis, when larger crystals already exist, as the seeding crystals
are energetically favorable receptors for the reduced gold atoms. For
example, we use a three-step protocol to produce gold nanocrystals[8],
adapted from [21]. Seeding particles are first formed from a solution
of hexachloroauric acid by reduction with a mixture of tannic acid and
citric acid. A small amount of the product is then introduced into a
new solution of $HAuCl_4$, which is reduced with hydroxylamine that is
added to the mixture. After a third, identical growth step, the particles
have reached an average diameter of 60 nm. Their size distribution is
wider than that of some single-step procedures here, but the particles
are largely spherical. In contrast, particles which were produced in a
single-step protocol often contain a considerable concentration of plates
and tetrahedra. Even the best syntheses reported for larger nanocrystals
(above 10 nm; they cannot be synthesized in organic solvents) produce
size distributions with distribution coefficients larger than the 5% attain-
able in particles made by the thiol-based route in organic solvents.

Particle habits other than spherical ones do not only appear uninten-
tionally, they can also be provoked by the choice of process parameters
and, most notably, the addition of other surfactants. Cetyltrimethylam-
monium bromide (CTAB), for example, leads to the growth of cylindri-
cal rods under citrate gold reduction [82]. These particles often are not as
monodispersed as the spherical particles, but they can be purified more
easily thanks to their extreme aspect ratios.

A high-yield route to relatively monodispersed silver particles has
been recently reported by XIA's group [168]. Silver crystallizes in cubes
when the well-known polyol reduction of silver nitrate is performed in

---

[8]For detailed procedures refer to Appendix D.1.

the presence of the polymer polyvinylpyrollidone (PVP). The resulting crystals are remarkable as they are single crystals, so that all faces probably display {100} planes, with very low roughness. We have modified the original synthesis slightly and were able to create particles as shown in Figure 5.56. The yield of cubes as compared to other geometries, mostly wires and tetrahedra, is reported to be good, and polydispersity is reported to be low, although no quantitative measurements were provided. Of the other geometries, wires are relatively easily removed because of their very anisotropic shape, whereas tetrahedra are difficult to remove. Their occurrence is a function of the process parameters, and we will discuss some aspects of the synthesis in more detail here, as this highlights some properties that are typical for this class of particle syntheses. Detailed synthetic procedures are summarized in Appendix D.2.

Briefly, silver nanocrystals were prepared by injecting solutions (in ethylene glycol) of PVP and silver nitrate simultaneously into a larger volume of water-free ethylene glycol in the presence of hydrochloric acid. The mixture undergoes a series of color changes after $15 - 50$ h (depending on temperature) contains silver cubes with sizes ranging between about 20 nm and somewhat above 100 nm. The synthesis is sensitive to a number of different influences, most notably,

- the oxygen content of the ethylene glycol,

- reducing contaminants (metal ions), as are frequently found in ethylene glycol,

- mass transport and, thus, the geometry and fluid dynamics of vessels, and reactant addition rate, and

- cleanliness of the reaction vessels.
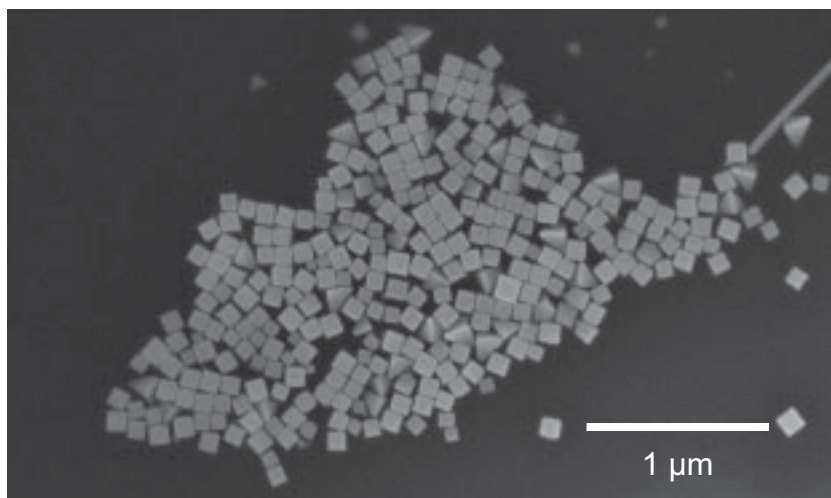
Figure 5.56: Silver nanocubes, synthesized via polyol reduction of silver nitrate in the presence of PVP. The colloid was filtered and transferred to water before this micrograph was taken. Aside from the desired cubes, the mixture contains tetrahedra.

Oxygen content is a particularly problematic aspect (and has been addressed by [182], the original authors of the synthesis), as it is not easy to exactly predict the amount of oxygen taken up by the solvent during dehydration. We have found that working under entirely oxygen-free conditions under argon does not produce cubes, but wires. IM et al. [78] suggest that oxygen is needed to etch crystal twins that occur during synthesis, because crystal twins that remain will nucleate the growth of wires.

Trace contaminations of ions are often found in solvents and cause another set of problems in silver nanocube synthesis. The original solution of silver nitrate in ethylene glycol is thermodynamically unstable, as the alcohol reduces the salt even at room temperature, but this reaction is slow in pure solutions. But already small contents of catalytically active agents can accelerate this reaction and lead to precipitation of silver, an effect we encountered in fresh ethylene glycol of p. a. quality acquired both from Fluka and J.T. Baker.

We find in our synthesis a yield of cubes (as a fraction of total particle production) of more than 90% after the removal of wires (easily possible via filtration), with a coefficient of variation around 20%. It appears, however, to be relatively hard to predict the exact size of the cubes contained in the suspension after a given period of time, even when temperature is measured inside the liquid and the other process parameters are carefully kept constant. The most reliable method to create a given particle size therefore was to take samples at two or three different points in time, measure the particle sizes, and then quench the reaction after a time calculated from the size increase of the two samples.

The silver cubes can be transferred to water without loss of stability, most likely because they are stabilized by a thin PVP layer that is still adsorbed to the walls of the cube. Highly concentrated suspensions look
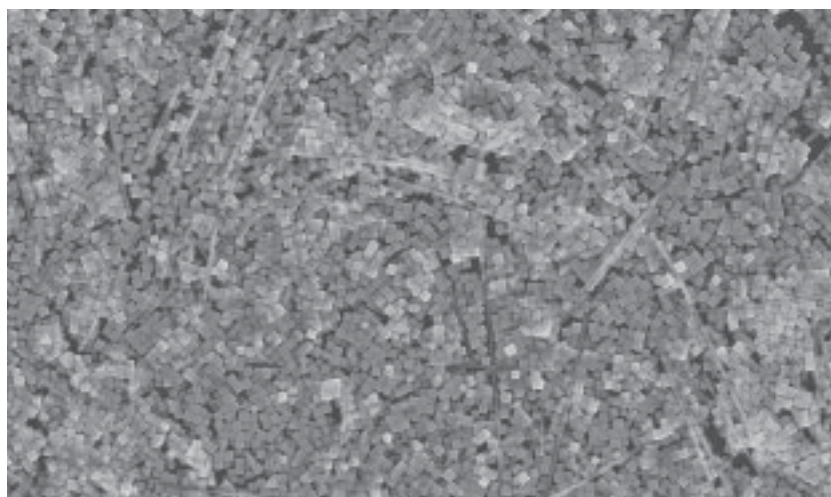
Figure 5.57: Silver nanocubes and nanowires after five weeks of storage
in an aqueous colloid at 4 °C. No signs of degradation are
visible.

opaque with a grey-brown color, and often some particle deposition oc-
curs at the walls or at the gas-liquid interface, visible as a shiny metal
layer. The bulk colloid, however, is stable even after weeks of storage
at 4 °C in water. We did not observe OSTWALD ripening or other degra-
dation mechanisms, even if the silver wires were not removed from the
aqueous suspension (Figure 5.57).

All particle syntheses are based on surfactants, and the surface of the
particles governs their behavior in many situations, in particular when
chemical bonding or particle interaction are involved. Standard meth-
ods of surface analysis such as XPS or ToF-SIMS can be applied when
the particles are immobilized on surfaces, but it is often difficult to dif-
ferentiate between the substrate's and the particle's contributions to the

239

sum signal. Moreover, these results cannot be compared to their colloidal state. A very convenient probe for the chemical matrix that can also be used in colloidal system is the surface plasmon resonance that occurs in many small metal particles and that is particularly strong in gold and silver crystals, which we use here.

The surface plasmon resonance (SPR) peak is sensitive to changes in the dielectric constant of the particle matrix. Its spectral position is a probe for adsorbed layers both in suspensions and in the dry form. KÜMIN [105] has investigated the dependence of the peak position on the thickness of alkenethiol monolayers formed on the particle surface and found that it is sufficiently sensitive to distinguish between different alkyl chain lengths. It also helps identify unintended contaminations that occur during the deposition process: adlayers from solution contents, surfactants and from the laboratory air. Figure 5.58 shows SPR spectrograms of particles with a polymer adlayer before and after treatment in a hydrogen plasma that removes the organic shell. When hexadecanethiol (HDT) adsorbs on the particles surface, it again shifts the plasmon peak to higher wavelengths.

5.4.2 Assembly

The capillarity-based particle assembly methods originally introduced for 500-nm polystyrene beads (see Section 5.3.2) scale well to smaller particles sizes, and it is possible to assemble monolayers with convective assembly and arrange single particles with capillary assembly. However, smaller particle size, stronger particle interaction, larger electrostatic field strengths and the considerably larger polydispersity (including shape dispersity) that occur in small metal particles make for new challenges. We will discuss the additional requirements for such small
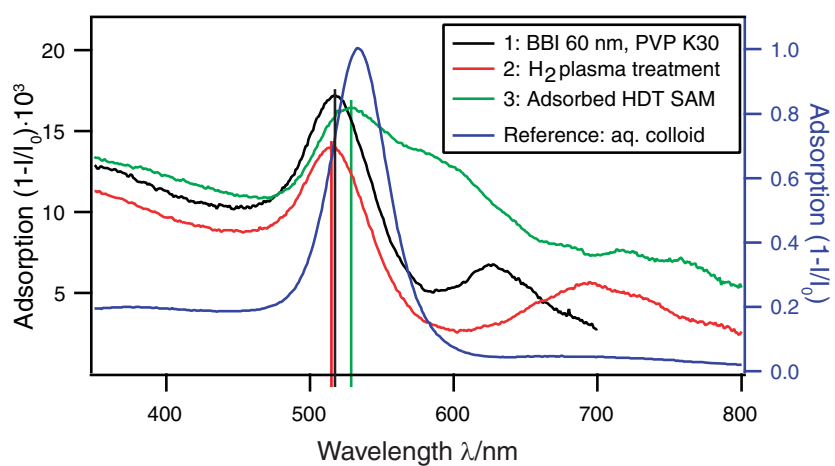
Figure 5.58: SPR spectroscopy of 60-nm gold nanocrystals on a quartz substrate. The particles were deposited with an adsorbed PVP layer, treated in a hydrogen plasma, and covered with a HDT monolayer. Spectra were recorded after every step.
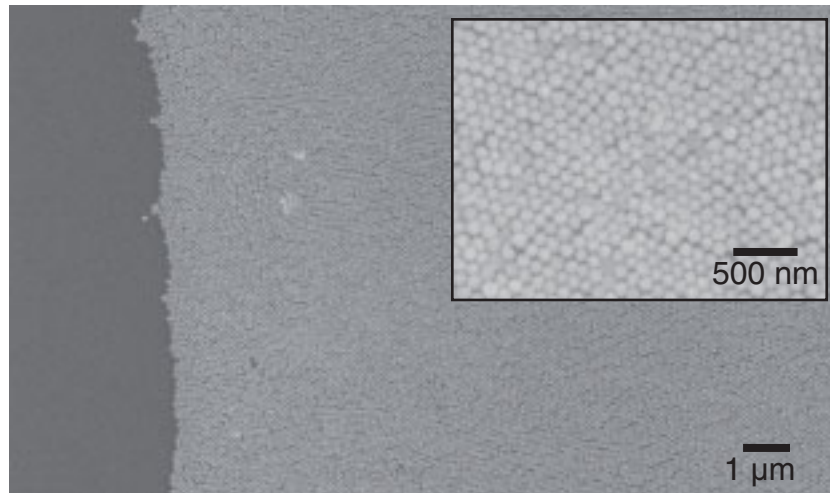
Figure 5.59: Monolayers of 100-nm gold nanocrystals, assembled with convective assembly on a hydrophilic, plasma-oxidized PDMS surface.

particles in the following.

Monolayers. Monolayer assembly using the thin wetting film that a colloid forms on a hydrophilic substrate can produce comparatively dense layers of metal nanocrystals. Figure 5.59 shows such a layer that was assembled from 100-nm gold particles on an oxidized PDMS substrate. The substrate temperature was kept relatively low, at $T_s = 18\,^{\circ}\mathrm{C}$, leading to an assembly rate (and, thus, substrate velocity) of $v_s \approx 0.3\,\mu\mathrm{m/s}$. Even at this slow velocity, the monolayer quality is not as high as that reached for larger polystyrene beads, mainly because of the lesser particle quality of the gold crystals. The domain sizes are rather limited and the lattices often deformed.

Other challenges emerge at higher assembly rates. When assembling large monolayers (with areas up to and exceeding 5×5 mm^2) at higher rates, the range of stable monolayer assembly is very narrow, with the layer easily breaking up or particles accumulating to form multilayers. This is particularly critical at substrate temperatures above 25 °C. The upper limit for simple, reliable monolayer assembly therefore is somewhere around 1 μm/s. Higher rates are possible, but will probably require an automated feedback system to keep assembly speed and substrate speed identical.

Surfactant systems for capillary assembly. Capillary assembly on hydrophobic surfaces can arrange monodispersed gold nanocrystals, too, but it requires some precautions in addition to the prerequisites known for larger polymer particles. We found for those that the contact angle of the suspension with the substrate has a strong influence on the yield and even the possibility of capillarity assembly. It is possible to modify the template surface to tune this angle. However, in a printing process, higher-energy surfaces are not an option because particles would strongly adhere to them, inhibiting the transfer step. Instead, we use surfactant systems to tune the wetting behavior with more flexibility, as is frequently done in conventional printing. It becomes necessary in the case of gold nanocrystals to carefully choose surfactant systems that provide appropriate contact angles, while we could take advantage of surfactants that are anyway present in polymer latexes for their assembly. Such surfactant systems always also influence particle-particle interactions, if only because of the change of ionic strength they cause and the resulting change in the electrostatic interaction lengths.

A surfactant system for particle inking has to change the contact angle of the colloid with the hydrophobic PDMS to an angle between 50° and

$60°$, where we find the highest assembly yield. The surfactants should not, however, destabilize the colloidal particles, not even in the accumulation zone with its high particle concentrations, and it should only leave a very thin film on the inked plate. Less obvious are the effects of the surfactant on the particle-substrate interactions. We find that some surfactants hinder the assembly, possibly by creating a repulsive force between substrate and particles, whereas others (such as polyvinylpyrrolidone) form deposits that embed the particles on the substrate. Finally, some surfactants will result in complex flow patterns in the assembly region, which are visible from the distribution of the particles and probably caused by MARANGONI flows due to local differences in surface tension. A mixture of a non-ionic, rather hydrophobic surfactant, namely, Triton X-45, an octylphenol ethoxylate having a short polyethyleneglycol chain, and the anionic sodium dodecyl sulfonate (SDS) appears to avoid all these issues, leaving the colloid stable even at high concentrations.

Other surfactants either make it hard to nucleate the assembly in lines, tend to produce discontinuous structures, or deposit large quantities of materials on the particle surfaces. A very common surfactant from the octylphenol ethoxylate class is Triton X-100, widely used in biochemical applications. When Triton X-100 is used as the only surface active component, it promotes the deposition of single particles in channels, even at particle transport rates that are sufficient to form continuous lines or at least segments with other surfactants (Figure 5.60). It is known that polymers and surfactants can stabilize colloidal suspensions, and it is conceivable that this stabilization hinders successful assembly here.

The addition of sodium dodecyl sulfonate (SDS) as a second surfactant improves the situation, although the required evaporation rate is still large, causing deposition of surfactant in the channels (and other
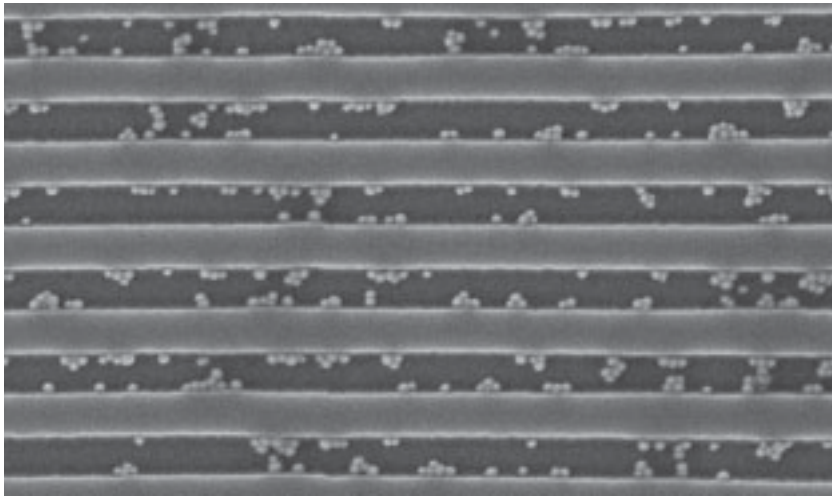
Figure 5.60: Discontinuous deposition of 60-nm gold nanocrystals in 200 nm wide channels. The sole surfactant in the colloid, Triton X-100, appears to allow for deposition, but not for the required agglomeration in the channel. This behavior even occurs at high temperatures, where the accumulation should promote packing of particles.
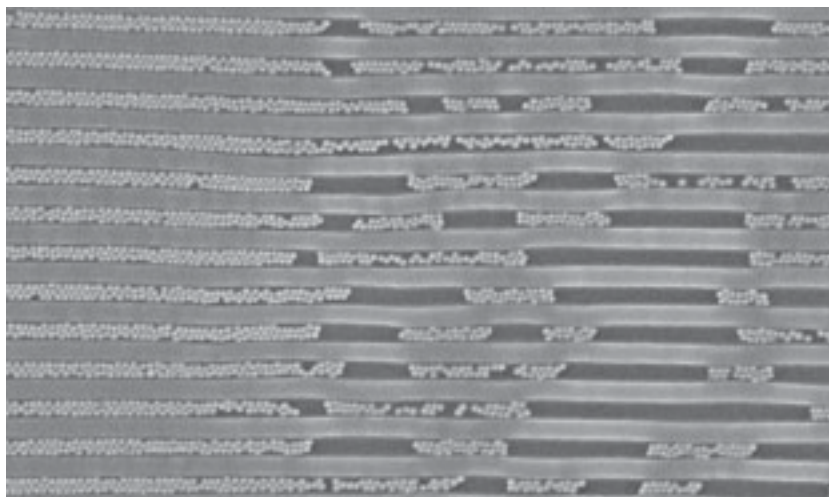
Figure 5.61: Rapid breakup of successfully nucleated lines of 60-nm gold nanocrystals in 200 nm wide channels. The surfactant mixture contained both Triton X-100 and SDS, but it still proved impossible even at high temperatures to reliably fabricate longer lines.

assembly sites). The improvement appears not to be solely an effect of ionic strength: the addition of ammonia or salts does not have the same effect as that of SDS. Even in the presence of adding SDS it is hard or impossible to sustain the assembly of nucleated lines (Figure 5.61), possibly because the required accumulation cannot be provided.

Many surfactants prove unsuitable because they cause too much deposition at the evaporation rates required to sustain assembly. Some of them embed the particles entirely, replacing the expected assembly mechanism with a deposition of bulk polymer and particles. Figure 5.62 shows particles embedded in bulk polyvinylpyrrolidone, with a spacing
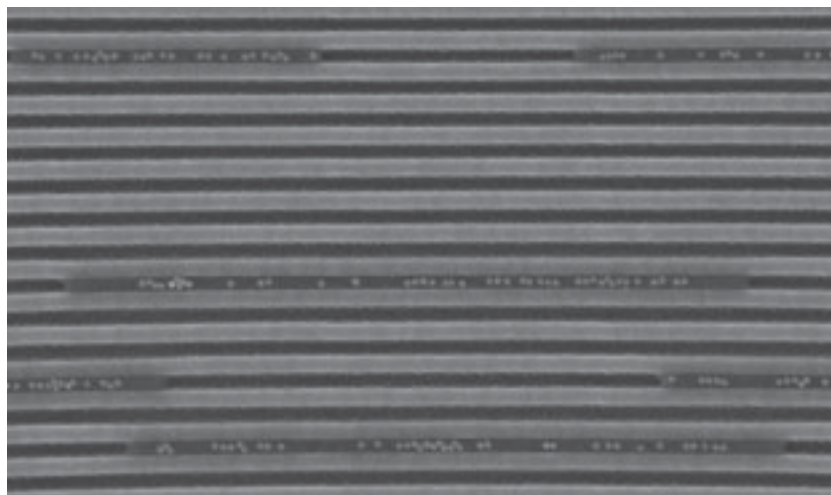
Figure 5.62: Gold nanocrystals in polyvinylpyrrolidone after assembly from a solution containing the polymer. The assembly mechanism here is likely to be not capillary-driven, but based on embedding in the deposited polymer.

and an alignment in the center of the channel that was not observed for any other surfactant. Less severe, but also unacceptable, is the deposition that occurs with ionic derivatives from the octylphenol ethoxylate family such as Triton XN-45S, Triton X-200, but also with some nonionic species such as Triton X-405.

The best combination of little deposition, slow change of contact angle with concentration (which is relevant for time-stable assembly and to avoid MARANGONI flows) and continuous assembly is provided by a mixture of Triton X-45 and sodium dodecyl sulfonate. The concentrations in this system can be chosen to be reasonably low, with 1 mmol/L SDS and 0.01 wt-% Triton X-45 in the colloidal suspension.
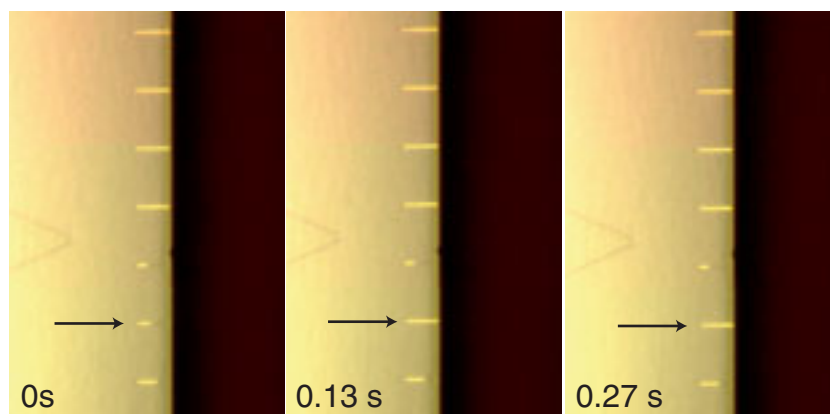
Figure 5.63: "Shooting" assembly of 60-nm gold nanocrystals. The images are captured from a video sequence, and the frame rate is almost insufficient to resolve the fast motion of the particle plug that fills the second-lowest line with particles.

Assembly mechanisms of strongly interacting particles. The surfactant system ensures a proper receding contact angle on an unstructured surface, but the local contact angle during assembly also depends on the pinning caused by the structures on the template's surface. This is particularly true for channels that are filled while moving normal to the three-phase boundary. As in the case of larger particles, the assembly does not necessarily take place directly at the boundary line. Further downstream, the channel is acting as an open microfluidic duct (Figure 5.63). Particles "shoot" into the channel and are integrated at the front of the growing crystal inside the channel. The details of this microconvective "shooting" assembly, however, appear to be different from those occurring with larger polymer beads.

The assembly of 500-nm polymer beads is often characterized by os-

cillations between different geometries of arrangement, likely explained by the confinement of the channel walls that do not accommodate a proper hexagonal packing. In contrast, smaller metal crystals tend to form dense, more or less hexagonal structures, regardless of the channel width (Figure 5.64). When they deviate from such packing, the order is lost locally and returns to the hexagonal shape. This might indicate that the order in larger polymer spheres is dictated mainly by capillary interactions, which have larger interaction lengths and can create complex patterns, while the packing for the small metal crystals is mainly a result of particle-particle interaction.

If the order formation is largely controlled by bulk attraction between the particles, this has implications for the assembly dynamics and the prerequisites of the assembly. The strength of capillary forces in a given geometry is almost only a function of the contact angle. In contrast, VAN DER WAALS interactions and other contributions to interparticle forces depend on a large number of materials properties (see Section 3.3.2). Some of them (namely electrostatic interactions) are strongly influenced by the ionic strength of the continuous medium. The ionic strength is likely to change in the channel as water evaporates, which might introduce a dependence on process parameters that exceeds the particle flux itself. Also, particle agglomeration due to VAN DER WAALS forces can appear while the particles are still entirely submerged in the colloid, while capillary forces can only occur when they are only partially immersed. Experimentally, we frequently observe that groups of particles are inserted into the crystal filling the channel. It seems likely that these groups are already densely packed and retain this packing upon integration in the channel.

This dependence on properties of the continuous phase might also explain differences in the nucleation behavior of small metal crystals when
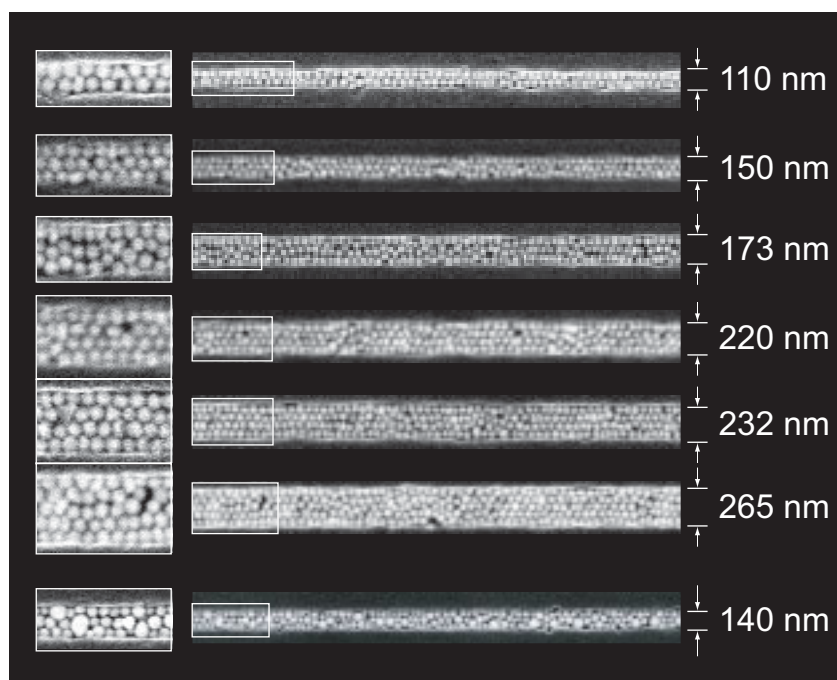
Figure 5.64: Arrangements of 60-nm gold nanocrystals in PDMS channels of different widths, all slightly deeper than the average particle diameter. Independently of the channel width, the particles tend to arrange in dense packings, even if that requires deviating from regular structures. The micrographs have been recorded in a SEM with a thin gold layer on the surface, which accounts for some of the visible distortion.

compared to that of polymer spheres. Nucleation is a relevant problem for both systems, in particular when assembling in long channels that provide additional pinning sites to start the growth. Once a line has nucleated, however, its growth will generally continue reliably if polymer spheres are involved. For the smaller metal crystals, depending on the parameters, short interruptions of the assembled line are a common occurrence. The assembly of parallel particle lines (such as shown in Figure 5.65) is therefore challenging unless the assembly parameters and surfactant concentrations are chosen properly.

Sparse arrangements.   It is not immediately obvious whether the bulk effects that affect the assembly of metal nanocrystals into lines will also affect their assembly into sparse structures. Even if the capillary forces are weaker than interparticle forces in some situations, they are the prevalent forces to drive the arrangement of single particles or small groups of particles in holes or behind obstacles. Capillary forces only act in the last stage of the assembly of a single particle, when the meniscus breaks up and moves over the assembly site. Before, geometrical confinement governs the particle motion, and forces act on the particles only through hydrodynamic drag. In this stage the particle interactions should have no major influence on the assembly mechanics if the colloid is stable.

Still, some observations do hint at an effect of interparticle forces even in the capillary assembly of metal nanocrystals. Figure 5.66 shows gold nanocrystals assembled into holes in a PDMS surface with different diameters. It is clear that only one particle will fill the hole if it is small enough, but one would expect to find two particles at least in some sites if the hole diameter is large enough to accommodate two particles. The experiments show that two particles are rarely found even in holes that are far larger than necessary. If two particles are present in a single hole,
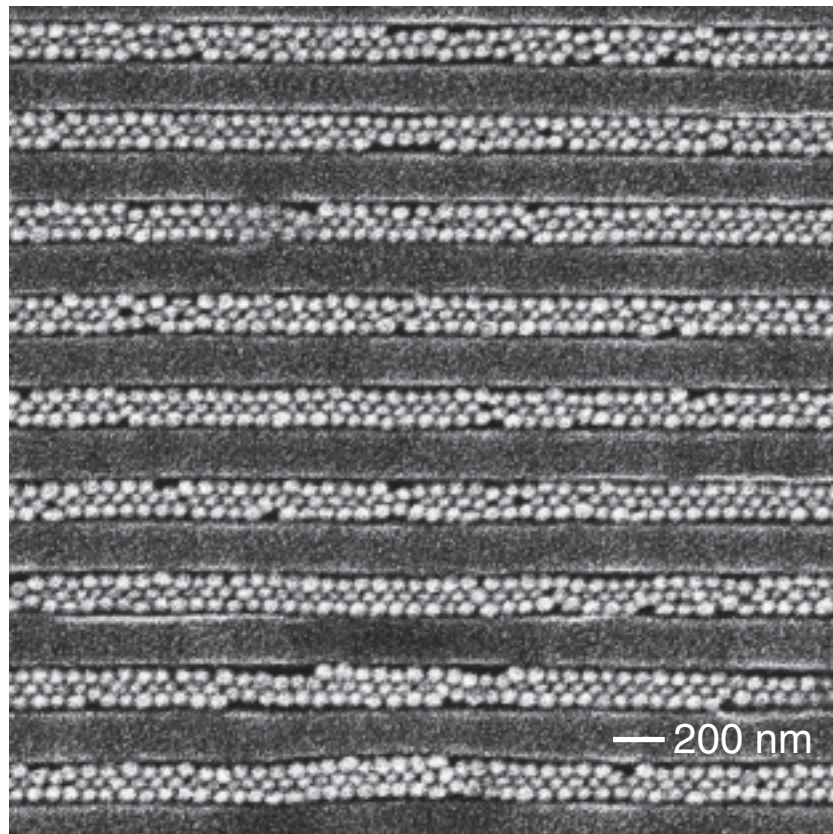
Figure 5.65: Dense lines of 60-nm gold nanocrystals assembled in parallel on a PDMS template.

they inevitably form a doublet. Those are very likely to have agglomerated before they were assembled.

For the capillary assembly of sparse particle arrangements to be reliable over a large area, the three-phase boundary line and the accumulation zone need to be uniform and stable over the entire template. Some surfactant systems introduce complex microflows into this region, probably due to MARANGONI flows that are caused by differences in local surface tensions. Even with surfactant systems that do not cause such flows, surface roughness or surface heterogeneity can cause waviness of the boundary line. In the case of PDMS templates, this commonly occurs when silicone oil accumulates at the surface, as it tends to after some storage time. We extracted templates with ethanol before use and used them immediately afterwards in order to avoid such contamination.

Template geometry. Both lines and other particle arrangements can be created with high precision if the appropriate assembly parameters are chosen, but the template geometry needs to be carefully adjusted. To achieve high yields without unspecific deposition, both an appropriate geometry and a sufficient depth of the capture sites have to be chosen. The results shown in Figure 5.64 stem from lines of particles assembled in 70- to 100-nm-deep channels, the arrays of single particles shown in Fig. 5.66 are assembled in 40- to 45-nm-deep holes. The deeper the lines, the more robust is the assembly process, at the cost of a lower transfer yield (see next section). To produce sufficiently precise templates, we use masters patterned via electron-beam or optical lithography and etched into silicon or silicon oxide. They can be used to cast many templates in a high-elastic-modulus polydimethylsiloxane rubber (for details of the template fabrication, see Appendix C).
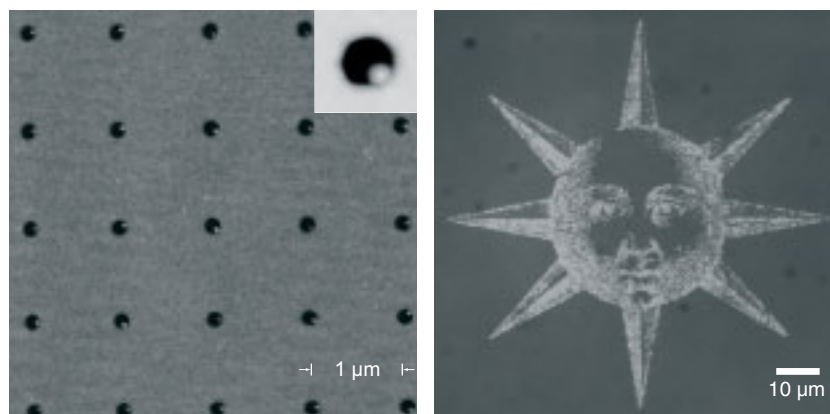
Figure 5.66: Spaced arrays and complex arrangements of 60-nm gold
nanocrystals. The AFM on the left shows particles with a
spacing of 1 µm, the darkfield micrograph on the right a 90-
µm sun formed from the same particles with a 280 nm pitch.

Sparse arrangements of particles can be assembled in almost any pat-
tern if the template is structured accordingly, even for very dense spac-
ings. We have successfully assembled 100-nm gold nanocrystals with
a 200 nm pitch (Figure 5.67). Such structures cause considerable pin-
ning and increase the risk of unspecific particle deposition, but if the
assembly parameters are chosen properly, high-yield assembly is pos-
sible. Less problematic are arrangements with large void areas, such
as the sun designed by the 17th-century alchemist Robert FLUDD [61]
shown in Figure 5.66. The pinning of the contact line in such areas is
weak, so that unspecific deposition rarely occurs. For holes that are
larger than the particle diameter, the position of the particles inside the
holes is stochastic with a strong bias in the assembly direction (compare
the AFM shown in Figure 5.66), the implications for the assembly mech-

anism are discussed in Section 3.3.4.

5.4.3 Transfer

Inking is followed by transfer in the printing process. During transfer, the printing plate and substrate are brought into conformal contact, facilitated by the elastomer layer that adjusts to the topography of the substrate surface. Upon removal of the printing plate, adhesive forces hold the particles on the substrate, thereby creating the desired arrangement. Traditional printing technologies use liquid inks, and ink transfer is based on wetting differences between the printing plate and the substrate (e.g., paper). In this work, the ink solely consists of dry nanoparticles, which are far less mobile than liquids. Particles therefore can be positioned more precisely, but they are harder to print. Their transfer is based on the different levels of particle adhesion on the printing plate and the substrate. Details on this complex adhesion problem are discussed in Chapter 4, here we will discuss the implication it has for the printing process.

Wetting differences are caused by differences in interfacial energy. Likewise, the adhesion of small particles strongly depends on the interfacial energy of the particle-surface joint. In contrast to solid-liquid interfaces, however, the particle-substrate interface is often not conformal, and its geometry can be complex. When we use surfaces with different energies to transfer particles, it is also necessary to control the interfacial area, in particular when working with individual nanocrystals. Such crystals often have irregular surfaces with sharp crystal edges. The adhesive force acting on one particle with a planar geometry can be much stronger than that acting on spherical ones. When analyzing the AFM surface topography of particles on their templates in Figure 5.67,
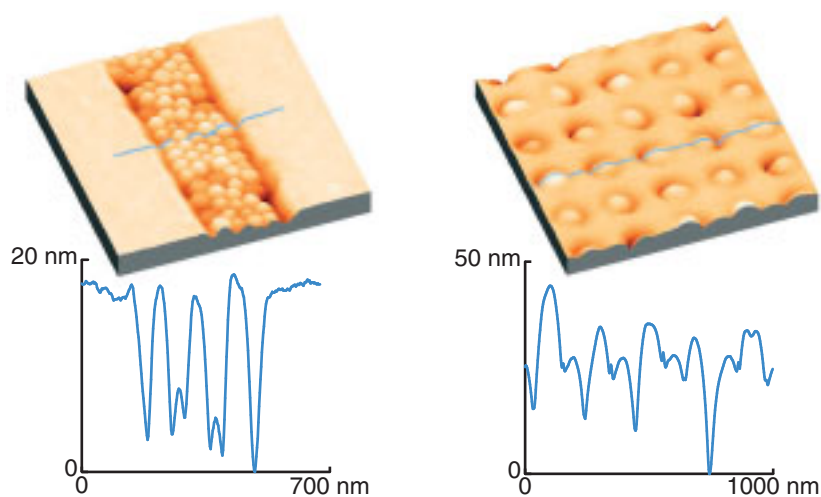
Figure 5.67: AFM profiles of 60-nm (left) and 100-nm (right image) gold
nanocrystals assembled in their PDMS templates.

it appears likely that the interface formed between particle and substrate upon conformal contact will vary considerably. To ensure high yield, even the smallest area occurring needs to provide a larger adhesive strength than that holding the particle in the PDMS template.

Moreover, solutes from the colloidal suspension frequently form adlayers on the metal surface while drying, thereby changing the chemical identity of the interface and increasing the particle-substrate distance. We describe in Chapter 4 that dry transfer of isolated, spherical gold nanoparticles with 60 nm diameter leads to very low yields on silicon, quartz, and even fresh gold layers with strong VAN DER WAALS attraction to gold particles. The transfer of cubes and plates leads to much larger yields. Likewise, lines and layers of 60-nm gold spheres could be printed with good yield onto hard silicon surface with a clean native
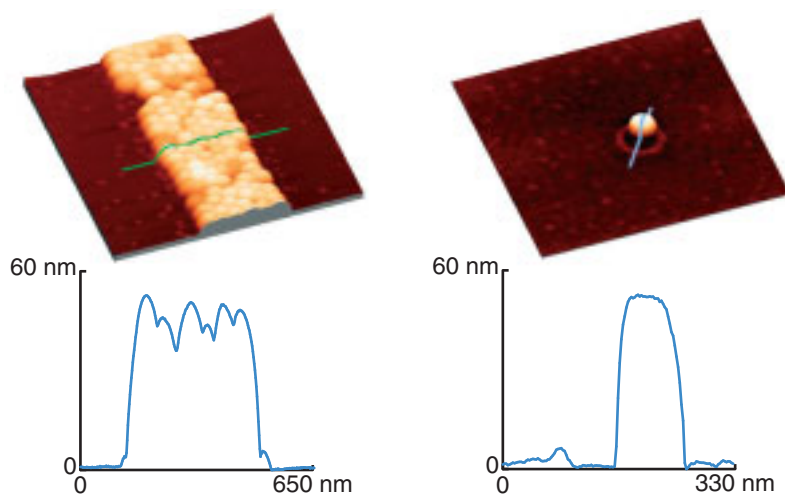
Figure 5.68: AFM profiles of 60-nm gold nanocrystals printed on bare silicon (left) and on a PMMA adhesion layer (right image).

oxide layer (see Figure 5.68). It appears that both a large crystal face in contact with the hard substrate and multiple, smaller contact points increase adhesion and transfer yield, whereas organic adlayers on the particles decrease adhesion and yield.

A reliable transfer process thus requires both surface-energy differences and defined interfacial areas. The PDMS layer on the printing plate that we use provides a low-energy surface, well-known for its capacity to release biomolecules onto more hydrophilic substrates [13]. The geometry of the PDMS layer was designed such that the particles come into contact with the substrate when the printing plate is placed on the target. This sometimes conflicts with the inking process, which for some particle arrangements (e.g., for lines) requires that the template be deeper than the particle's diameter. In such cases, the gap was kept
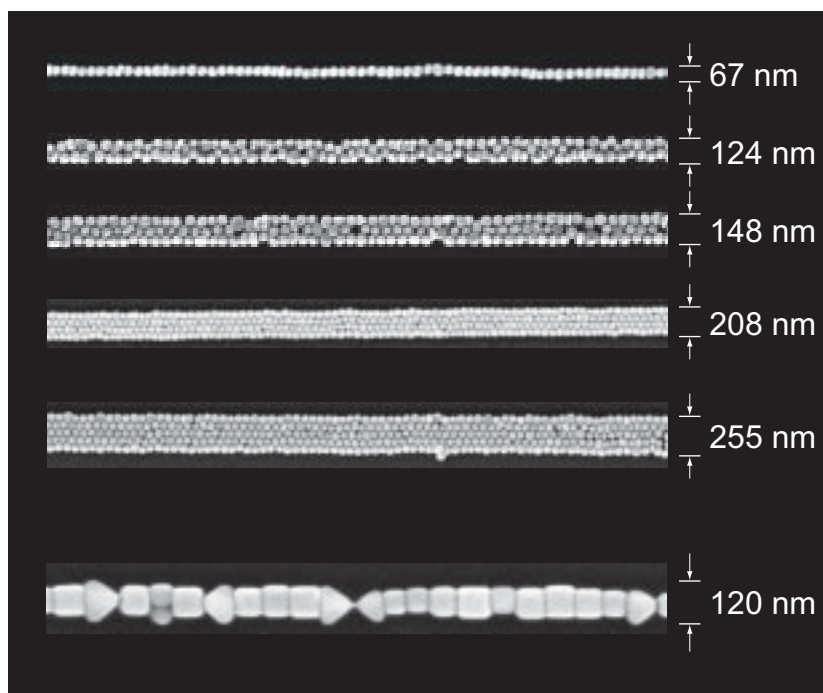
Figure 5.69: Lines of 60-nm gold nanocrystals printed on bare silicon substrates. The last line is composed of silver nanocubes.

as small as possible (almost none is present in the filled channel shown in Figure 5.67). A height difference of 5 – 10 nm can be overcome when pressure is applied on the stamp during the transfer process. Figure 5.68 shows particle lines of different widths printed on oxidized silicon using this geometry.

In contrast to lines, arrays of individual spherical nanocrystals cannot be transferred onto hard substrates, even if they protrude significantly from the template. However, transfer with high yields is possible onto
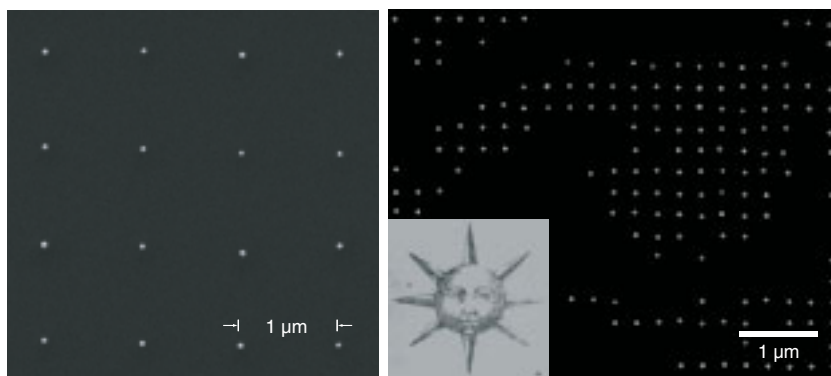
Figure 5.70: Spaced arrays and complex arrangements of 60-nm gold nanocrystals printed on silicon substrates with a PMMA adhesion layer. The SEM image on the left shows particles with a spacing of 1 μm, that on the right the eye of a 90-μm sun formed from the same particles with a 280 nm pitch. A darkfield image of the entire printed sun is included for reference.

thin polymethylmethacrylate (PMMA) layers, where a layer thickness of 10 – 30 nm is sufficient for the transfer to exceed 95% yield. Transfer takes place at a temperature of 110 – 120 °C, slightly above the glass-transition temperature of PMMA. The polymer embeds the protruding segment of the crystal (see Figure 5.68), thus providing a sufficiently large area of contact to create the adhesion necessary for transfer. Figure 5.70 shows arrays of individual nanocrystals printed on PMMA. The position of the nanocrystals is preserved during the transfer with an accuracy better than 100 nm. If necessary, the adhesion layer can be removed by thermal decomposition in a hydrogen-plasma cleaning step.

We evaluated the yield of the overall process in printed arrays of 60-nm gold nanocrystals with 1 μm spacing. Voids are easily spotted in

electron micrographs of these arrays. Upon counting different parts of arrays, each comprising approximately 1000 particles, we find yields between 97% (the highest) and 90% (the lowest) in one experiment. The yield-limiting step here was the assembly. The number of particles which remained in the template after the printing step was very low.

5.4.4 Integration

We show two surface-sensitive applications here to demonstrate that the individual gold nanocrystals still are catalytically and optically active. Figure 5.71 shows silicon nanowires (SiNW) that were grown from an array of 60-nm particles using a vapor-liquid-solid (VLS) process. The particles were printed onto a 30-nm-thick PMMA layer on top of a hydrogen-passivated silicon $\langle 111 \rangle$ substrate. The PMMA adhesion layer was removed by thermal decomposition at 300 °C in vacuum, assisted by hydrogen plasma. SiNW growth was then initiated at 460 °C in a reactor using silane as the precursor gas. Nanowires nucleated and grew from the gold particles, and their arrangement was preserved. The epitaxial relationship of the SiNW with the substrate is evident from the wires growing along both the vertical and the three inclined $\langle 111 \rangle$ growth directions. Such nanowires are regarded as novel building blocks for future transistors, memory cells and sensors, for example.

Metal nanocrystals also interact strongly with electromagnetic waves [77], a property that is exploited in applications such as glass staining, surface-enhanced Raman spectroscopy [63], and surface-plasmon-resonance-based agglomeration assays [165]. It has been noticed that the characteristics of single particles can vary considerably [103], and the printing technique adopted here can be used to study large numbers of individual particles. When they are arranged in regular arrays,
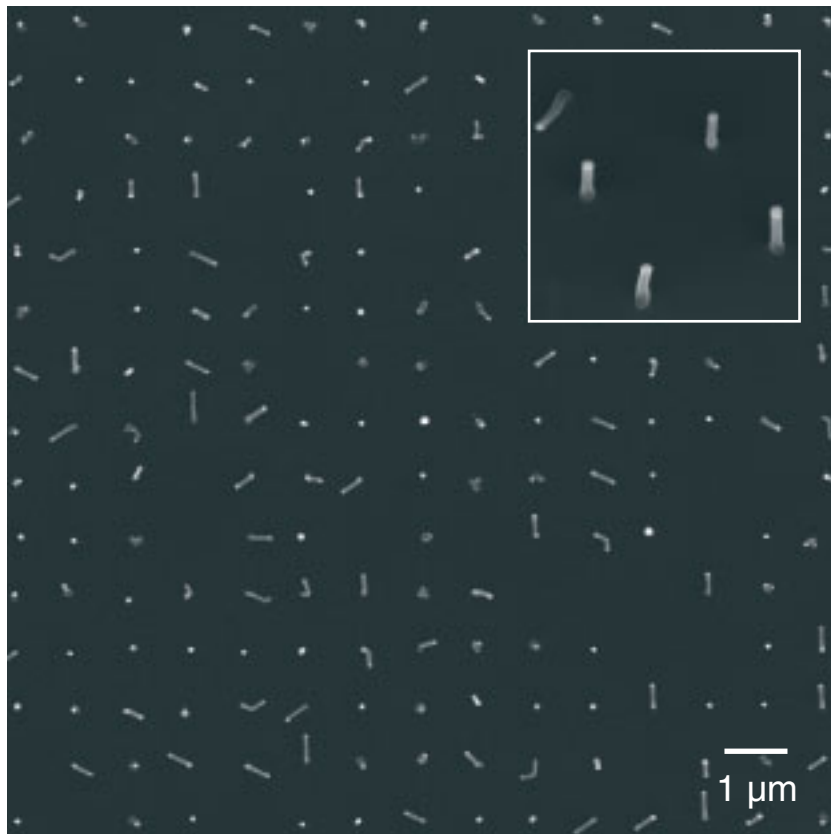
Figure 5.71: Silicon nanowires grown via a VLS process from a printed array of 60-nm gold nanocrystals (inset is tilted). The original positions of the particles are preserved in the wire positions. The wires can grow along different crystal planes.

it is easy to find "hot spot"-particles and analyze them using a variety of analytical methods. Figure 5.72 shows how some particles scatter light more strongly than others, both when immobilized in the PDMS template and when printed onto a silicon substrate. Comparison of the darkfield micrographs with the AFM and SEM images reveals that this is not simply a function of size or overall shape (although doublets of particles often scatter the light strongly), and it will be interesting to apply high-resolution electron microscopy to identify the features that characterize strongly scattering "hot spot"-particles.

5.4.5 Experimental details

High-precision inking. Colloidal suspensions of silver nanocubes and gold nanocrystals were synthesized in-house or purchased from British Biocell International, UK. Of the many surfactants we tested for their assembly in the inking step, the best results were obtained with the following mixture, which was therefore adopted for all printing experiments: an aqueous 0.1 wt-% emulsion of Triton X-45 (as received from Fluka) was mixed with a 10 mmol/L aqueous solution of sodiumdodecylsulfonate (Fluka) filtered through a PTFE 200-nm-pore syringe filter (Rotilabo, Switzerland). 50 μL of the mixture were added to 200 μL of the colloid, yielding a final particle concentration of 2×10^{14} L^{-1}.

The inking was performed in the capillarity-assisted-particle-assembly or "CAPA" tool described in detail in Appendix A, which enables control of the temperature and substrate velocity while the template is being moved under a drop of the colloidal suspension. The substrate temperature was chosen such that a clearly visible accumulation zone formed, e.g., 27 °C at the usual environmental humidity of 50%. A microscope camera recorded the contact angle of the meniscus, which was used to
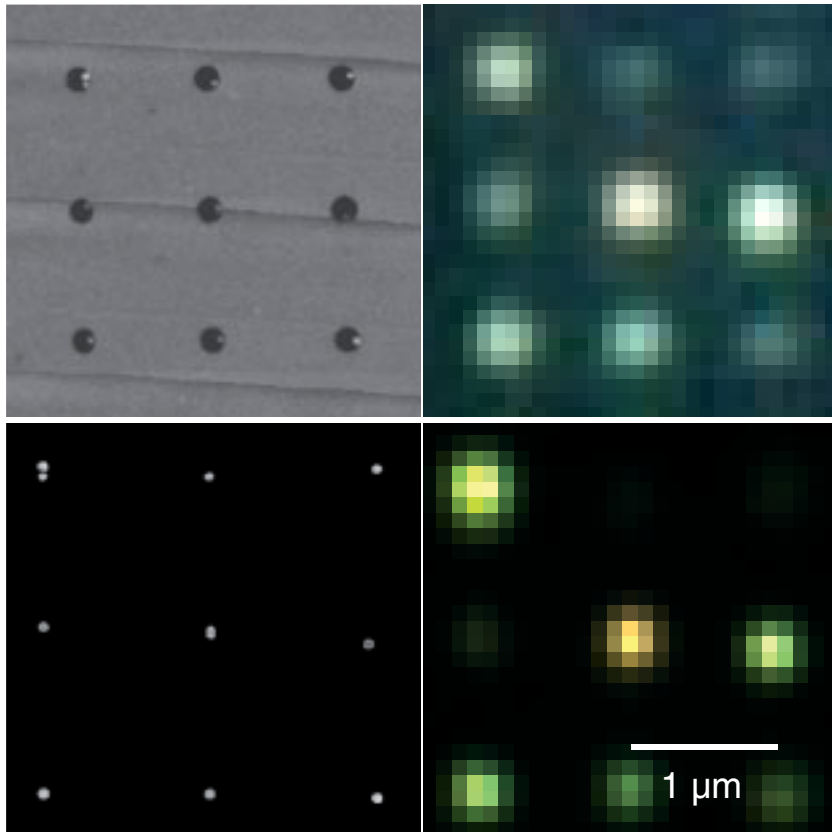
Figure 5.72: AFM topography and the corresponding darkfield image of 60-nm gold nanocrystals on their assembly template (top row) and a SEM image and the corresponding darkfield micrograph on a silicon substrate (bottom row: the images were mirrored for convenience).

ensure good quality of the substrate and the colloid, indicated by a contact angle of 50 to 60°. During the inking, a microscope mounted on top of the setup was used to monitor and record the process.

Particle transfer. Particle transfer was carried out both on bare silicon surfaces (lightly doped, p-type, polished silicon wafers, Siltronic, Germany) and on PMMA-coated silicon surfaces (spin-coated with a $10 - 30$ nm PMMA layer, having a molecular weight of 950 kDa, Microchem, Newton, MA). In both cases, the printing plates with the particles were brought into contact with the substrates either manually or in a printing tool that allows microscopic inspection and alignment with existing structures as well as force and temperature control during the transfer (see Appendix B for details on the tool). In the case of the uncoated substrates, the printing plate was firmly pressed onto the target and removed immediately after. In the case of the substrates with PMMA adhesion layers, the printing plate was placed on the target, the temperature was increased to 120 °C, pressure was applied on the backplane, the temperature was decreased, and the printing plate was removed after the temperature had dropped to 40 °C.

6 Conclusions and outlook

6 Conclusions and outlook

This thesis demonstrates that materials can be fabricated from particles with a high degree of definition and flexibility. We have assembled particles using templated self-assembly and transferred them onto target substrates. Accessible structures range from assemblies of 100-μm-diameter beads, at the lower size limit for industrially placed objects, to 500-nm-diameter spheres, at the lower end of features accessible through conventional optical lithography, to 60-nm-diameter nanoparticles, the lateral feature sizes achieved today by the best available industrial semiconductor technologies. The particle-based approach can handle a variety of materials, including glasses, polymers, and metals. Despite its extreme resolution, our approach maintains the benefits of well-established printing techniques that are known to be robust, versatile and applicable to large areas and various substrates.

To be useful in technological applications, a fabrication method needs to provide sufficient yield and create structures with high accuracy. Moreover, it has to be general enough to provide any desired useful structure (e.g., any desired particle packing) and simple enough so that structures can be defined without great effort. Depending on the application, the fabrication method may have to be compatible with earlier or later processing steps. In semiconductor fabrication, for example, no specific surface functionalities should be required, and the structures created have to be aligned with existing surface structures.

We have shown here that particle-based fabrication can meet these requirements if it is carefully optimized. As we concluded theoretically in Chapter 3, high yield and accuracy in small, fluctuating systems require high local concentrations and sharp energy differences. Experimentally, in Chapter 5, we therefore use templated self-assembly processes with topographical binding sites and strong hydrodynamic forces to confine nanoparticles. The transport of particles towards the three-phase con-

tact line, where assembly actually takes place, is engineered such that high local concentrations occur, while thermodynamic stability is maintained to prevent agglomeration and unspecific deposition. To this end, we introduce surfactants for self-assembly that enable control of contact angle, particle-particle and particle-surface interactions.

Compatibility with other fabrication methods is best provided by separating the self-assembly step with its unusual requirements on surfaces and geometries from the target substrate. The challenge is to retain the order of assembled particles while they are being transferred in parallel from the assembly template to the target substrate, and to create a functional junction between particles and target. In this thesis, controlled adhesion enabled passive handling of particles in a process called "Self-assembly, transfer and integration" (SATI). The surfaces of particle, carrier and target substrate were chosen such that the particles could be picked up on the carrier or be directly assembled on it, handled, inspected and transferred to the target substrate, where they then adhered so that the carrier could be removed. This required fine-tuning the adhesion, specifically through engineering the area of contact. We have shown that the contact area governs adhesion even in sub-100-nm-sized particles, which we can therefore attach to the target substrate by means of thin polymer adhesion layers.

The separation of assembly and integration makes SATI a modular process that can be applied, even multiple times, during device fabrication. Particles of different size ranges were combined using multi-step "SATI^2" prints. We have also created structures from chemically synthesized nanoparticles on featureless substrates, and achieved unprecedented quality. The materials fabricated were compatible with relevant technological problems, as we showed by using tin-coated beads as electrically-conducting spacers, polystyrene beads as resist layers in

etch processes, and gold nanocrystals as catalytic nucleation sites for vapor-liquid-solid growth of silicon nanowires. The yields of the overall processes routinely exceeded 90%, and reached 99% for the best-optimized nanocrystal integrations.

Particles down to 60 nm in diameter were used in this work. A very interesting class of smaller particles are quantum dots, which exhibit strong quantum confinement effects even at room temperature. Such effects usually occur for lengths below 10 nm, e.g., at about 4 nm for silicon. When particles below this size are assembled into bulk materials or surface coatings, their quantum effects might lead to qualitatively new properties that are otherwise difficult to achieve.

The techniques developed in this thesis should scale down to such extremely small particle sizes, although the thermodynamic stability of the colloid will become an issue that needs increased attention. According to the predictions made in Chapter 3, it will become more difficult to increase the concentration of such particles without causing aggregation, and it will become harder to confine them in a defined position. Finally, topographical templates will become very challenging to fabricate with critical dimensions in the sub-10-nm regime. Some of the results obtained with gold nanocrystals in this thesis suggest, however, that exclusion effects due to electrostatic interaction might occur that will allow single-particle assembly even in larger templates.

Adhesion-based transfer scales to molecular dimensions and can be combined with other self-assembly techniques if necessary. Its modularity provides additional possibilities for the fabrication of complex structures. Once particles have been assembled in a well-defined structure on a carrier, parts of them can be printed on a (protruding) surface while leaving the particle arrangement outside this area intact. Thus, the stamp can be moved (at possibly very high precision, if a piezo is

used) and another layer of particles can be printed on top of the existing one. When repeated multiple times, this "SATI^n" method can achieve complex layers on small areas.

A multi-print scheme can also introduce different particles into the printed structures if parts of the template are populated with different particles. It is thus possible to produce three-dimensional structures from a variety of different materials, providing in effect a mesoscale version of the "molecular assembler" described in Chapter 1 — a less versatile one, but much closer to realization.

6 Conclusions and outlook

A The CAPA tools

A The CAPA tools

Both capillary assembly and convective assembly of particles require the meniscus of a colloid to be moved over a substrate. The evaporative flux of liquid from the meniscus then drives the transport of particles to the accumulation zone, where they finally assemble in the binding sites of the substrate.

All effects that influence the evaporation rate can therefore influence the assembly yield and have to be carefully controlled. These parameters can include

- the temperature of the colloid,

- the environmental humidity,

- the relative velocity of the substrate,

- the contact angle.

We have designed and built a "Capillarity-Assisted Assembly" tool, or CAPA for short, to provide control of the evaporation rate. This control is achieved by tuning the substrate temperature, while the environmental humidity is kept constant. The temperature can be changed far more easily and rapidly than humidity, so that wide parameter ranges can be tested rapidly. Temperature control is provided by a heatable vacuum chuck, driven by a water-cooled Peltier element, which enables both rapid cooling and heating of the substrate that sits on its metal surface. In the latest version of the CAPA tool, this chuck was obtained from Instec (Boulder, CO, USA; a custom-designed version with the order number TC102). A PID controller provides constant closed-loop temperature control, and grooves in the chuck's surface can be connected to a vacuum pump to hold the substrate.

Figure A.1 depicts the central part of the CAPA tool in its second version. On the bottom plate, a translational stage (M405.DG, Physikinstru-

mente, Karlsruhe, Germany) is mounted, which moves the heatable vacuum chuck that sits on top of it. The stage can travel at sufficiently low speeds (below 0.1 μm/s) and introduces comparatively little vibration, because it uses a PID-controlled DC motor instead of a stepper motor. The chuck on its moving sledge is connected both electrically and with water hoses to provide heating power and cooling water. Mounted vertically on the base plate is a small, manual, linear translation stage with which the position of a microscope slide can be adjusted. This slide sits at a variable angle above the heatable stage at a distance of about 0.5 mm from the substrate. Both distance and inclination angle of the slide can be adjusted, for example to accommodate larger volumes of liquid between slide and substrate.

During assembly, a volume of liquid is held between the two surfaces to form a meniscus on the template surface. The actual assembly takes place at the front of this meniscus. In-situ observation is possible in the CAPA tool thanks to a microscope mounted above the glass slide (see Fig. A.2). Depending on the particle size, simple reflection microscopy can be sufficient to discern the accumulation zone or even the yield of the assembly; darkfield illumination is often sufficient even for very small particles. Both are provided by the microscope used in our Setup (Axiotech 100, Zeiss, Germany). If the assembly template is transparent, the surface of the underlying chuck strongly influences the quality of the microscopic imaging. We find that even microscopically rough surfaces are often problematic at lower magnification in dark-field illumination. Good results are possible with thick glass plates, but those hinder thermal conduction and increase the response time. A polished, black surface is a good compromise.

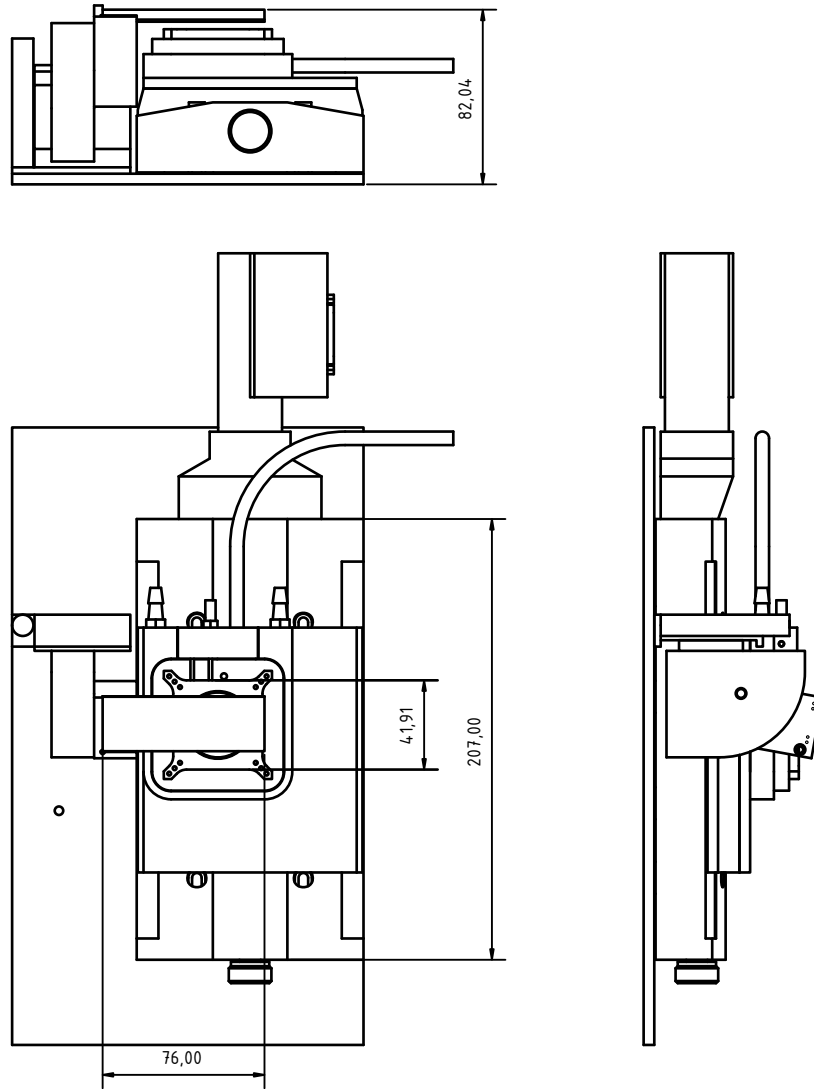Another imaging option for small particles is fluorescence. Polystyrene beads are available with fluorescent dyes and can thus be imaged

Figure A.1: Central part of the CAPA2 tool.
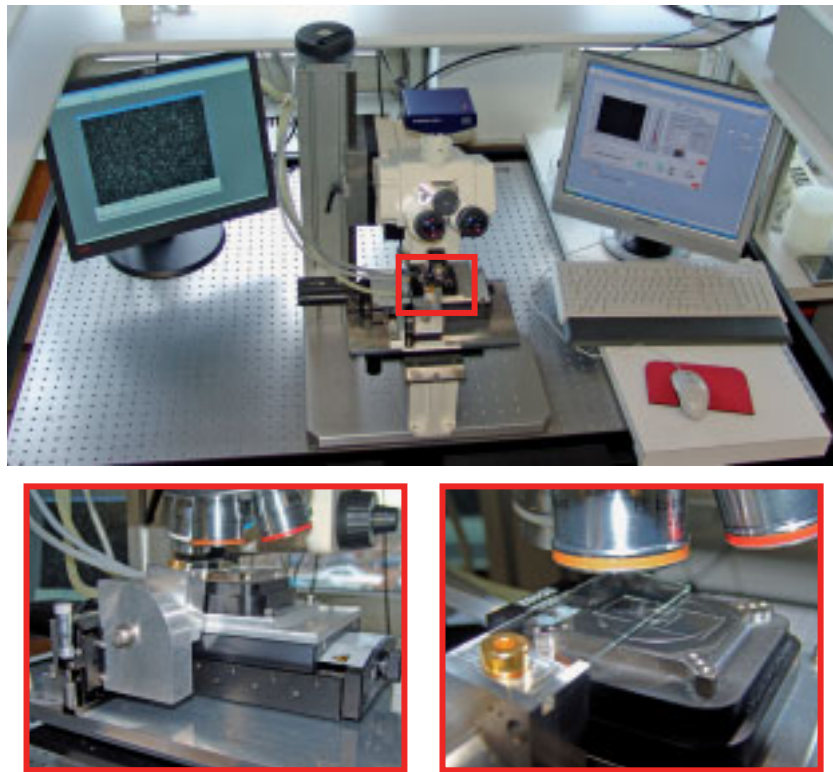
Figure A.2: The CAPA2 tool, including microscope and monitors for control and monitoring.

even if they are below the resolution limit of conventional microscopy. The fluorescence signal enables easier differentiation of particles from surface roughness than dark-field scattering does. In our setup, all images could be recorded through digital cameras for documentation or, potentially, automatic feedback control of the assembly. An additional camera was mounted at the side to observe the contact angle formed between colloid and substrate.

Vibrations are known to change pinning of the meniscus [43]. To make the assembly reproducible, the CAPA tools were therefore mounted on vibration-damping tables (standard optical equipment). The entire setups were also protected from drafts, because air flows above the surface could change the evaporation rate of the liquid.

B The printing tool

Particle transfer requires good contact between particles and target substrate. Especially if particles are large enough to prevent conformal contact, shear forces have to be avoided, as they will distort the arrangement. The printing tool (Fig. B.1) developed in this thesis provides alignment of the surfaces both through tilting (to avoid uneven contact) and laterally (to align with existing structures).

The tool is based on a sturdy steel frame that holds a substrate chuck and a movable printing arm (Fig. B.2). The printing process can be observed via an unobstructed optical path through the carrier holder using a stereo microscope.

The printing tool provides precise motion of the carrier with respect to the target substrate by means of a linear stage driven either by a manual micrometer screw or a piezo actuator with a traveling range of 100 μm (LNR50MP100S/M, Thorlabs, Germany). The carrier is either clamped or held on a vacuum chuck mounted on the printing arm that moves with the linear stage. If necessary, the carrier holder can be equipped with three force sensors (strain gauge sensors, ME Messsysteme, Germany) to measure both the overall force and its distribution across the stamp surface (Fig. B.3). The carrier holders are held on the printing arm by three strong magnets. The bearings between the printing arm and the stamp holders are formed by steel balls at the ends of three micrometer-sized screws in the arm, each of which sits on two parallel sapphire cylinders on the carrier holder.

Establishing an adhesion cascade frequently requires increased substrate temperatures, mainly to soften adhesion layers. The heatable vacuum chuck shown in Fig. B.4 provides this in the printing tool. It contains a sheet heater that can heat the surface of the chuck to at least 200 °C, controlled in a closed loop by a temperature sensor in the metal surface. Additional bores enable the introduction of pressurized air or
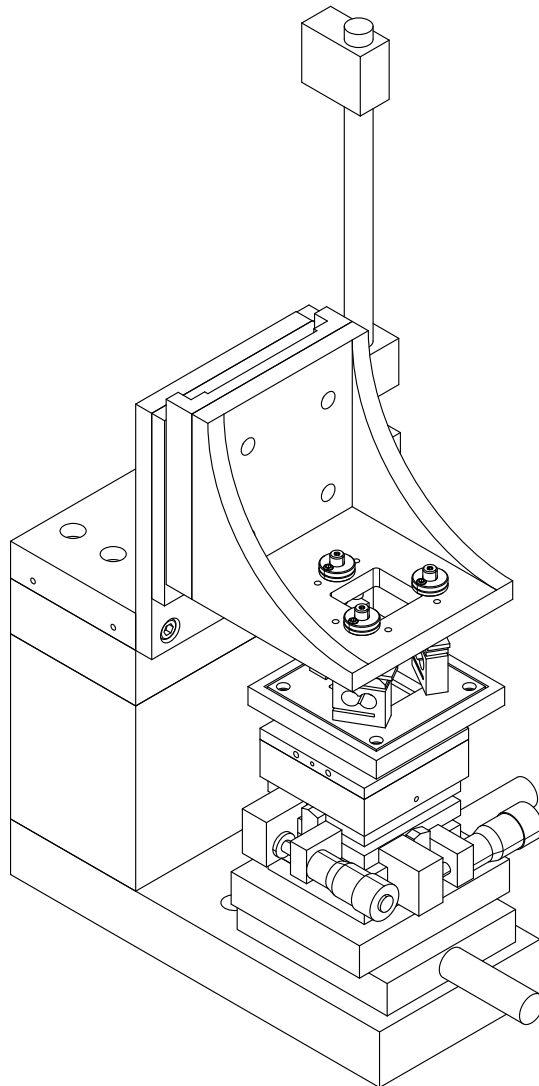
Figure B.1: The printing tool equipped with a force-sensing carrier holder.
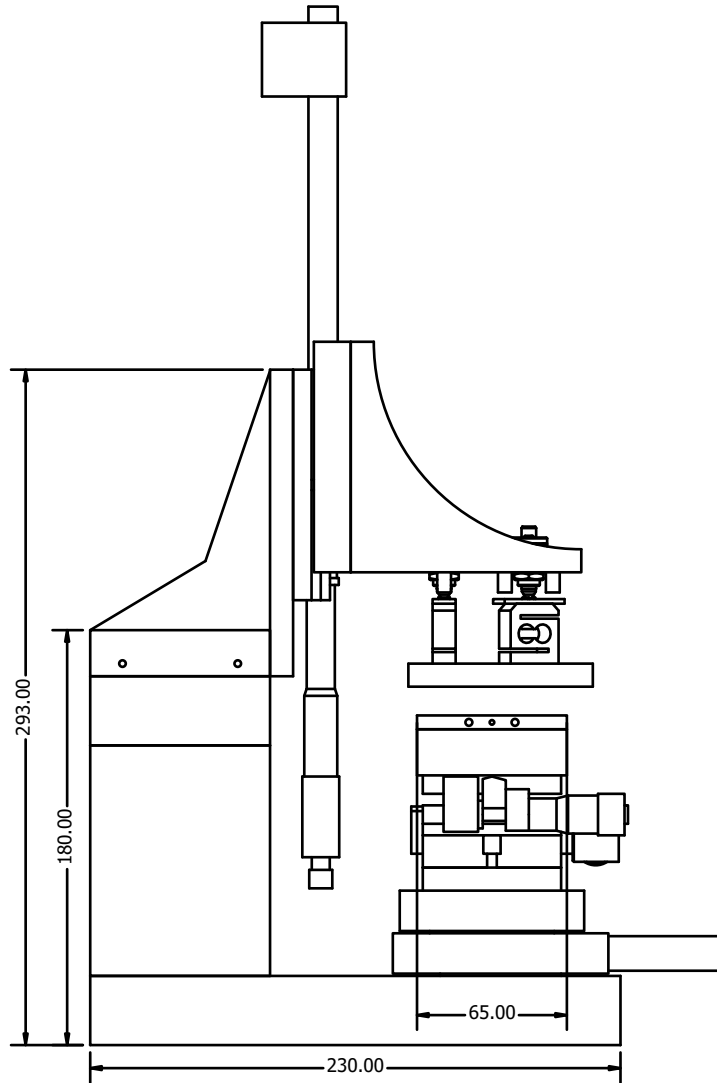
Figure B.2: Side view of the printing tool with dimensions.
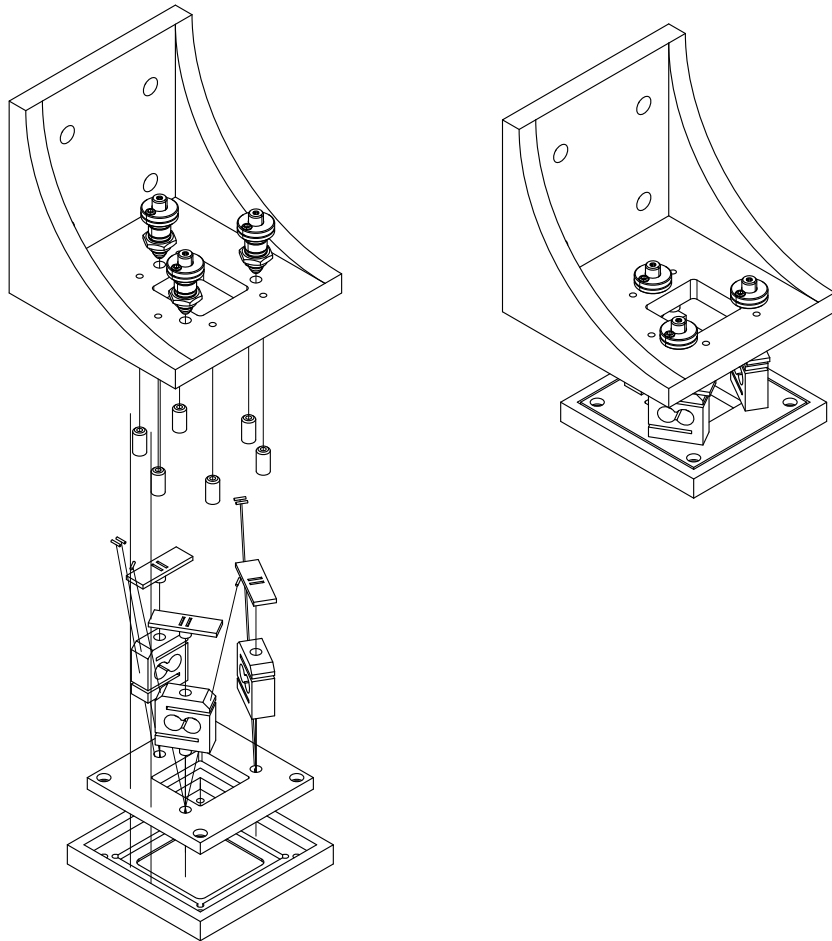
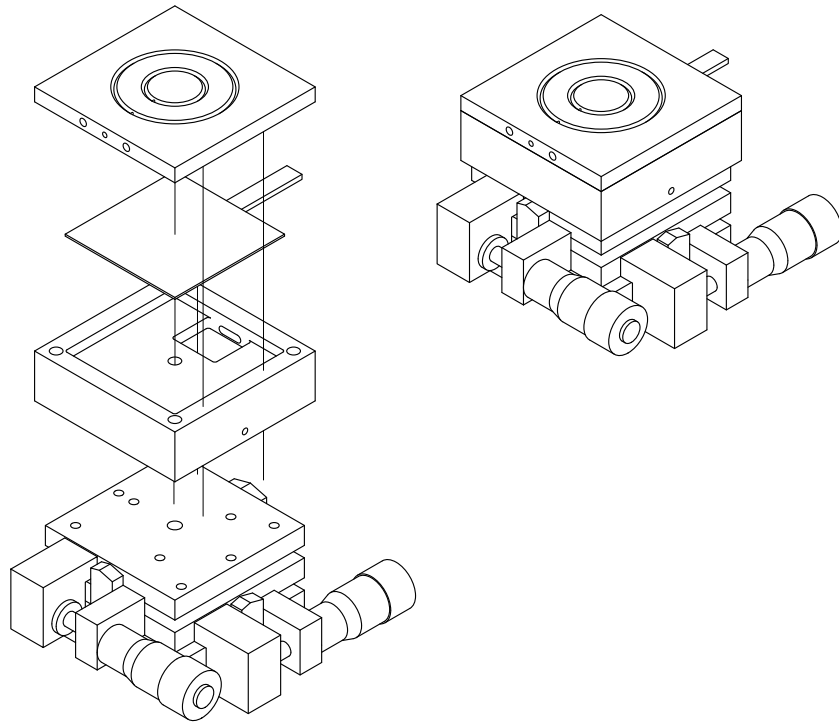Figure B.3: The force-sensing carrier holder on the arm of the printing tool.

Figure B.4: Heatable vacuum chuck for target substrates.

water to cool the surface rapidly.

The entire printing tool can be controlled via a LabView interface. Details on the program, calibration data, and verification experiments can be found in [60].

C Template fabrication

In this work, particles were assembled in topographical templates. All template patterns were initially defined using standard microfabrication. For the assembly of particles smaller than 1 μm, these templates were not used directly, but molded in silicon elastomers. This appendix gives the fabrication details for the different size ranges.

C.1 Low-resolution templates

Masters for the assembly of 100-μm-diameter glass beads were etched from standard polished silicon wafers. A computer-generated pattern was transferred via a standard chromium mask (fabricated through electron-beam writing by Photronics, Germany) into a layer of AZ 6612 resist via standard photolithography. The pattern was transferred into the wafer in a BOSCH process using an Alcatel AMS200 etcher that features a plasma with alternating flows of SF_6 (etchant) and C_4F_8 (protective layer deposition). After the etch, the resist was stripped and the surface cleaned in an oxygen plasma.

To reduce the particle adhesion to the substrate, we silanized it with a perfluorinated silane from the gas phase. Droplets of 1H,1H,2H,2H-perfluorodecyltrichlorosilane (97%, ABCR, Karlsruhe, Germany) were introduced into a desiccator together with the freshly cleaned silicon master and a droplet of acetic acid in a separate vessel. The desiccator was evacuated and left to react for about 10 min. The silicon master was then placed in an oven heated to 120 °C under nitrogen to ensure completion of the hydrolysis in the silane monolayer. Finally, the surface tension was tested by estimating the contact angle of a water droplet on the surface.

C.2 High-resolution templates

The assembly of nanoparticles was performed directly on poly(dimethyl-siloxane) (PDMS) layers that had been topographically patterned with sub-micron structures by molding on flat or patterned silicon masters using the methods and materials reported in [66]. These templates were cast in poly(dimethylsiloxane) (PDMS) using structured silicon masters. The masters were either 100 mm wafers or 10×10 mm^2 silicon pieces, patterned via electron-beam lithography. For the smallest features, a thermal oxide layer was first grown on the silicon, with a defined thickness as verified by spectroscopic ellipsometry. Then, a polymethylmethacrylate (PMMA) film (950 kDa, micro resist technology, Berlin, Germany) of 100 nm thickness was spun onto the oxide and annealed for 120 s at 160 °C on a hotplate. Masters with larger feature sizes were created on silicon wafers and SOI wafers (200 nm device layer thickness).

Some of the masters were patterned through electron-beam writing externally (by X-lith GmbH or AMO GmbH, both Germany), but the smallest features were created in-house. For the latter, the resist layer was exposed in an electron-beam lithography system (e-Line, Raith, Dortmund, Germany) which was equipped with a Gemini electron column. Exposure was performed at an acceleration voltage of 20 kV, using an aperture with a diameter of 10 μm and a beam current of $\approx$ 30 pA. After exposure, the resist was developed in a mixture of isopropanol and water (7 : 3 volume ratio) in ultrasound for 30 s, followed by an etch in a 200 W oxygen plasma for 40 s under a Faraday cage (TePla plasma reactor, TePla AG, Asslar, Germany), to remove any residual polymer at the bottom of the exposed regions.

The patterned wafers were then coated with a 30-nm-thick layer of aluminum through thermal evaporation and its unexposed regions re-

moved through lift-off first in acetone at room temperature and then in n-methylpyrrolidone at 100 °C. The aluminum provided etch protection in a subsequent reactive ion etch, in which the oxide around the features was removed entirely in a CHF_3 plasma (Plasmalab 80 plus, Oxford Instruments, Abingdon, UK). The aluminum mask was finally removed in an etch bath (85% of 85% H_3PO_4, 5% of 70% HNO_3, 10% of water), and the master was rinsed and ashed in an oxygen plasma to remove any residuals and to grow a thin oxide layer on the hydrogen-terminated silicon.

To reduce the surface energy of the master for the casting of PDMS, its surface was coated with a perfluorinated monolayer, using the CVD method described above for the low-resolution masters. For the actual casting of the polymer, a droplet of prepolymer mixture (Material C, see below) was placed on the perfluorinated master, and covered by a piece of 175-μm-thick display glass (Schott, Mainz, Germany). The display glass had been functionalized with allyltrichlorosilane from the gas phase to improve adhesion. After a minimum of 24 h in the oven at 60 °C, the glass could be peeled off the master together with the patterned silicone layer.

It was necessary to use the high-elastic-modulus PDMS instead of the softer, commercially available variants (such as Dow Corning's Sylgard 184), because the softer material did not produce faithful replication of the very small structures, deformed because of capillary action and can embed particles via strong surface deformation. The "Material C" that we used here was prepared by mixing 68 g of a purified vinylmethyl-siloxane - dimethylsiloxane trimethylsiloxy terminated copolymer containing 7 – 8 mol- % of vinylmethylsiloxane and a silica nanoparticle filler (XG 0675, custom-synthesized by ABCR, Germany) with 22 g of a (25–35% Methylhydrosiloxane) - dimethylsiloxane copolymer (HMS

301 from ABCR, Germany) and 23 µL of a platinum-divinyltetramethyl-disiloxane complex in xylene (SIP 6831.1 from ABCR, Germany). This mixture could be stored at $-70\,^\circ$C for several months in aliquots prior to use.

Silicone rubbers often contain low-molecular-weight silicone oils, and their presence on the surface can change the adhesion properties and influence the particle-assembly process. We removed these residues by placing the templates in large volumes of ethanol for at least five days, and washing and drying them directly prior to use. Templates used for convective assembly were oxidized using an O_2 plasma treatment at 200 W for 20 s in a TePla 100-E reactor (Technics Plasma GmbH, Germany).

In the fabrication of masters with larger feature sizes we often used the electron-beam patterned PMMA layer directly for etching the underlying silicon in a plasma etch with mixed SF_6 and C_4F_8 supply. The etch depth was then either defined by the etching time or by using SOI wafers with their silicon oxide etch stop.

C Template fabrication

D Particle synthesis

D.1 Gold nanocrystals

Gold nanocrystals were either obtained from British Biocell International (United Kingdom) or synthesized in a multi-step synthesis. To produce seeding particles following SLOT and GEUZE [160], 80 mL of a 0.125 mg/mL solution of $HAuCl_4$ (Fluka) were brought to 60 °C on a hot plate. A mixture of 4 mL solution containing 10 mg/mL tri-sodium citrate (Fluka), 0.03 mL solution containing 10 mg/mL tannic acid (Mallinckrodt, order number 1674) and 16 mL ultrapure water were mixed and brought to the same temperature. The mixture was then added to the gold salt solution in a single, quick injection, while the mixture was stirred vigorously. After about three minutes, the mixture was heated to the boiling point for several minutes, cooled down and stored. This yielded a colloid of seeding particles.

The seeding particles (between 3 and 6 nm in diameter) were then enlarged by the deposition of gold from its salt using the procedure of BROWN et al. [21]. A volume of 135 mL ultrapure water was stirred vigorously at room temperature. Then, 1.25 mL of a 0.2 mol/L hydroxylamine solution (Merck) and 15 mL of the seeding colloid were added. Finally, 1.5 mL of a 10 mg/mL $HAuCl_4$ solution were injected quickly, and the mixture was stirred for about 5 min.

The resulting, larger particles were enlarged in a second step. A volume of 75 mL ultrapure water was stirred vigorously at room temperature. Then, 0.56 mL of a 0.2 mol/L hydroxylamine solution and 25 mL of the first-generation colloid were added. Finally, 1.0 mL of a 10 mg/mL $HAuCl_4$ solution were injected quickly, and the mixture was stirred for about 5 min.

D.2 Silver nanocubes

Silver nanocubes were synthesized following a protocol established by Im et al. [78], which is based on the classical polyol reduction of silver nitrate in ethylene glycol, but relies on a polymer surfactant (polyvinyl-pyrrolidone) to modify the shape of the resulting crystals, and on the activity of dissolved oxygen, which probably removes twin crystals from the mixture.

We used a setup consisting of a 100-mL round-bottomed flask in a silicone oil bath, both of which contained teflon-coated stirrer bars, actuated by a magnetic stirrer at a velocity of 240 min^{-1}. Reflux was provided through a water glass chiller on top (40 cm length). The setup was gas-tight, and a current of dry synthetic air could be introduced through one of the three necks of the round-bottomed flask, exiting the chiller at its top through a silicone-oil-filled syphon. All glass pieces that came into contact with the reaction mixture were first cleaned with concentrated nitric acid, then with a saturated solution of sodium hydroxide in ethanol, rinsed with copious amounts of deionized water and finally with ultrapure water. No grease was used anywhere in the system; instead, teflon linings provided sealing of the glass connections.

In a typical synthesis, 10 mL of ethylene glycol (Merck, analytical grade) were heated to 140 °C (measured inside the solvent) under a constant stream of dry, synthetic air (PanGas, Switzerland). After 1 h, in a single shot, 2 mL of a 3 mmol/L solution of HCl were added, which had been prepared by dissolving 150 μL of 1 mol/L aqueous hydrochloric acid in 50 mL of ethylene glycol. While acid was being added, the air stream was interrupted, but resumed shortly after, and the mixture was heated for another 10 min.

An automatic syringe pump (Harvard PHD2000, Harvard Apparatus,

D Particle synthesis

Holliston, MA, USA) was used to simultaneously inject (from two different plastic syringes) 6 mL of a 147 mmol/L solution of polyvinylpyrrolidone (PVP K30, 30000 Da average molecular mass, Aldrich, order number 85656-8) and 6 mL of a 94 mmol/L solution of silver nitrate (Aldrich, analytical grade), both in ethylene glycol, at a rate of 45 mL/h. One minute after the end of the injection, the chiller was activated and the mixture was heated under reflux. About two minutes after the end of the injection, the continuously stirred mixture turned from a slightly turbid white to a clear, brown-yellow color, which intensified with time.

Samples were taken from the colloid during particle growth by removing small volumes of liquid with a clean glass pipette. The samples were then quenched by adding acetone in excess, and droplets of it were put on silicon pieces, dried, and analyzed using SEM. When the desired cube size had been reached, the entire volume of colloid was quenched by cooling it to room temperature. Three times its volume of ultrapure water was added, the mixture was centrifuged, the supernatant discarded, and the particles were washed once again with the same amount of water. We stored the (concentrated) suspension of the cubes in water in the fridge and found it to be stable for extended periods of time.

The actual growth rate of the particles not only depended on the process parameters, but also varied from synthesis to synthesis, even if all conceivable aspects were duplicated. Likewise, the exact nature of the resulting particles (in particular, the fraction of wires and other shapes contained in the product) somewhat varied. However, a reaction time of 17 h generally yielded a good fraction of cubes with a side length of between $70 - 100$ nm. Prior to use, the mixture was pressed through a 250-nm syringe filter to remove wires and other large objects.

Bibliography

[1] C. Adami. What is complexity? *Bioessays*, 24(12):1085–1094, December 2002.

[2] J. Aizenberg, P. V. Braun, and P. Wiltzius. Patterned colloidal deposition controlled by electrostatic and capillary forces. *Physical Review Letters*, 84(13):2997–3000, March 2000.

[3] F. A. Aldaye and H. F. Sleiman. Dynamic DNA templates for discrete gold nanoparticle assemblies: Control of geometry, modularity, write/erase and structural switching. *Journal of the American Chemical Society*, 129(14):4130–4131, April 2007.

[4] A. Arsenault, S. B. Fournier-Bidoz, B. Hatton, H. Miguez, N. Tetrault, E. Vekris, S. Wong, S. M. Yang, V. Kitaev, and G. A. Ozin. Towards the synthetic all-optical computer: science fiction or reality? *Journal of Materials Chemistry*, 14(5):781–794, March 2004.

[5] E. Arzt, S. Gorb, and R. Spolenak. From micro to nano contacts in biological attachment devices. *Proceedings of the National Academy of Sciences of the United States of America*, 100(19):10603–10606, September 2003.

[6] P. Bacchin, D. Si-Hassen, V. Starov, M. J. Clifton, and P. Aimar. A unifying model for concentration polarization, gel-layer formation and particle deposition in cross-flow membrane filtration of colloidal suspensions. *Chemical Engineering Science*, 57(1):77–91, January 2002.

[7] C. D. Bain, E. B. Troughton, Y. T. Tao, J. Evall, G. M. Whitesides, and R. G. Nuzzo. Formation of monolayer films by the spontaneous assembly of organic thiols form solution onto gold. *Journal of the American Chemical Society*, 111(1):321–335, 1989.

293

Bibliography

[8] C. D. Bain and G. M. Whitesides. Formation of monolayers by the coadsorption of thiols on gold—variation in the length of the alkyl chain. *Journal of the American Chemical Society*, 111(18):7164–7175, 1989.

[9] T. E. Balmer, H. Schmid, R. Stutz, E. Delamarche, B. Michel, N. D. Spencer, and H. Wolf. Diffusion of alkanethiols in PDMS and its implications on microcontact printing (muCP). *Langmuir*, 21(2):622–632, 2005.

[10] C. R. Barry, M. G. Steward, N. Z. Lwin, and H. O. Jacobs. Printing nanoparticles from the liquid and gas phases using nanoxerography. *Nanotechnology*, 14(10):1057–1063, October 2003.

[11] G. K. Batchelor. Brownian diffusion of particles with hydrodynamic interaction. *Journal of Fluid Mechanics*, 74:1–29, 1976.

[12] A. T. Bell. The impact of nanoscience on heterogeneous catalysis. *Science*, 299(5613):1688–1691, March 2003.

[13] A. Bernard, E. Delamarche, H. Schmid, B. Michel, H. R. Bosshard, and H. Biebuyck. Printing patterns of proteins. *Langmuir*, 14(9):2225–2229, April 1998.

[14] G. Böhme, P. Hohn, H. Krupp, H. Rabenhort, W. Schnabel, and G. Walter. Adhesion of gold particles to silicon and gold substrates in ultrahigh-vacuum. *Journal of Applied Physics*, 44(9):3914–3918, 1973.

[15] K. F. Böhringer, R. S. Fearing, and K. Y. Goldberg. *The Handbook of Industrial Robotics*, chapter Microassembly, pages 1045–1068. Wiley & Sons, New York, 1999.

[16] K. F. Böhringer, K. Goldberg, M. Cohn, R. Howe, and A. Pisano. Parallel microassembly with electrostatic force fields. In *Proceedings of the International Conference on Robotics and Automation (ICRA), Leuven, Belgium*, 1998.

[17] A. Bietsch and B. Michel. Conformal contact and pattern stability of stamps used for soft lithography. *Journal of Applied Physics*, 88(7):4310–4318, October 2000.

[18] W. N. Bond and H. O. Puls. The change of surface tension with time. *The London, Edinburgh, and Dublin Philosophical Magazine and Journal of Science*, 24(159):864–888, 1937.

[19] W. R. Bowen and F. Jenner. The calculation of dispersion forces for engineering applications. *Advances in Colloid and Interface Science*, 56:201–243, March 1995.

[20] W. R. Bowen and F. Jenner. Dynamic ultrafiltration model for charged colloidal dispersions—a wigner-seitz cell approach. *Chemical Engineering Science*, 50(11):1707–1736, June 1995.

[21] K. R. Brown, D. G. Walter, and M. J. Natan. Seeding of colloidal Au nanoparticle solutions. 2. improved control of particle size and shape. *Chemistry of Materials*, 12(2):306–313, February 2000.

[22] D. A. G. Bruggeman. Calculation of various physics constants in heterogenous substances. I. Dielectricity constants and conductivity of mixed bodies from isotropic substances. *Annalen der Physik*, 24(7):636–664, November 1935.

[23] M. Brust, M. Walker, D. Bethell, D. J. Schiffrin, and R. Whyman. Synthesis of thiol-derivatized gold nanoparticles in a 2-phase liquid-liquid system. *Journal of the Chemical Society—Chemical Communications*, (7):801–802, April 1994.

[24] V. V. Budov and L. S. Egorova. Glass microbeads, application, properties, and technology. *Glass and Ceramics*, 50(7):275–279, July 1993.

[25] M. Bäumle, D. Stamou, J. M. Segura, R. Hovius, and H. Vogel. Highly fluorescent streptavidin-coated CdSe nanoparticles: Preparation in water, characterization, and micropatterning. *Langmuir*, 20(10):3828–3831, May 2004.

[26] N. Camillone. Diffusion-limited thiol adsorption on the gold(111) surface. *Langmuir*, 20(4):1199–1206, 2004.

[27] C. J. Campbell, E. Baker, M. Fialkowski, and B. A. Grzybowski. Arrays of microlenses of complex shapes prepared by reaction-diffusion in thin films of ionically doped gels. *Applied Physics Letters*, 85(11):1871–1873, 2004.

Bibliography

[28] B. Cappella and G. Dietler. Force-distance curves by atomic force microscopy. *Surface Science Reports*, 34(1-3):1–104, 1999.

[29] S. Chandrasekhar. Stochastic problems in physics and astronomy. *Reviews of Modern Physics*, 15(1):1–89, January 1943.

[30] M. K. Chaudhury and G. M. Whitesides. How to make water run uphill. *Science*, 256(5063):1539–1541, 1992.

[31] G. Chen, M. S. Dresselhaus, G. Dresselhaus, J. P. Fleurial, and T. Caillat. Recent developments in thermoelectric materials. *International Materials Reviews*, 48(1):45–66, February 2003.

[32] J. Y. Cheng, A. M. Mayes, and C. A. Ross. Nanostructure engineering by templated self-assembly of block copolymers. *Nature Materials*, 3(11):823–828, November 2004.

[33] O. Cherniavskaya, A. Adzic, C. Knutson, B. J. Gross, L. Zang, R. Liu, and D. M. Adams. Edge transfer lithography of molecular and nanoparticle materials. *Langmuir*, 18(18):7029–7034, September 2002.

[34] P. Y. Chiou, A. T. Ohta, and M. C. Wu. Massively parallel manipulation of single cells and microparticles using optical images. *Nature*, 436(7049):370–372, July 2005.

[35] S. H. Choi and B. M. Z. Newby. Micrometer-scaled gradient surfaces generated using contact printing of octadecyltrichlorosilane. *Langmuir*, 19(18):7427–7435, 2003.

[36] Michael B. Cohn. Method and apparatus for the assembly of microfabricated devices. U.S. Patent 5355577, 1994.

[37] International Roadmap Committee. *International Technology Roadmap for Semiconductors 2005 Edition*. International Roadmap Committee, 2005.

[38] J. Crank. *The Mathematics of Diffusion*. Oxford University Press, 1964.

[39] T. L. Credelle, O. Alvarado, G. S. W. Craig, M. A. Hadley, and K. D. Schatz. Method and apparatus for transferring blocks. U.S. Patent 6731353, 2004.

[40] Y. Cui, M. T. Bjork, J. A. Liddle, C. Sonnichsen, B. Boussert, and A. P. Alivisatos. Integration of colloidal nanocrystals into lithographically patterned devices. *Nano Letters*, 4(6):1093–1098, June 2004.

[41] S. L. Cumberland and G. F. Strouse. Analysis of the nature of oxyanion adsorption on gold nanomaterial surfaces. *Langmuir*, 18(1):269–276, January 2002.

[42] M. C. Daniel and D. Astruc. Gold nanoparticles: Assembly, supramolecular chemistry, quantum-size-related properties, and applications toward biology, catalysis, and nanotechnology. *Chemical Reviews*, 104(1):293–346, January 2004.

[43] S. Daniel and M. K. Chaudhury. Rectified motion of liquid drops on gradient surfaces induced by vibration. *Langmuir*, 18(9):3404–3407, 2002.

[44] F. den Hollander and G. H. Weiss. *Contemporary problems in statistical physics*, chapter Aspects of Trapping in Transport Processes, pages 147–197. Society for Industrial and Applied Mathematics, Philadelphia, 1994.

[45] N. D. Denkov, O. D. Velev, P. A. Kralchevsky, I. B. Ivanov, H. Yoshimura, and K. Nagayama. Mechanism of formation of 2-dimensional crystals from latex-particles on substrates. *Langmuir*, 8(12):3183–3190, December 1992.

[46] J. K. G. Dhont. *An Introduction to Dynamics of Colloids*. Elsevier Science, 1996.

[47] A. S. Dimitrov and K. Nagayama. Continuous convective assembling of fine particles into two-dimensional arrays on solid surfaces. *Langmuir*, 12(5):1303–1311, March 1996.

[48] B Doris, M. Ieong, R. Kanarsky, Y. Zhang, R. A. Roy, O. Dokumaci, Z. Ren, F.-F. Jamin, L. Shi, W. Natzle, H.-J. Huang, J. Mezzapelle,

A. Mocuta, S. Wornack, M. Gribelyuk, E. C. Jones, R. J. Miller, H.-S. P. Wong, and W. Haensch. Extreme scaling with ultra-thin si channel mosfets. In *Proceedings of the IEDM*, pages 267–270, 2002.

[49] K. Eric Drexler. *Engines of creation*. Anchor Press/Doubleday, 1986.

[50] C. J. Drummond and D. Y. C. Chan. van der waals interaction, surface free energies, and contact angles: Dispersive polymers and liquids. *Langmuir*, 13(14):3890–3895, July 1997.

[51] L. H. Dubois and R. G. Nuzzo. Synthesis, structure, and properties of model organic-surfaces. *Annual Review of Physical Chemistry*, 43:437–463, 1992.

[52] N. V. Dziomkina and G. J. Vancso. Colloidal crystal assembly on topologically patterned templates. *Soft Matter*, 1(4):265–279, October 2005.

[53] A. Einstein. The motion of elements suspended in static liquids as claimed in the molecular kinetic theory of heat. *Annalen der Physik*, 17(8):549–560, July 1905.

[54] P. Englebienne. Use of colloidal gold surface plasmon resonance peak shift to infer affinity constants from the interactions between protein antigens and antibodies specific for single or multiple epitopes. *Analyst*, 123(7):1599–1603, July 1998.

[55] R. Evans and D. H. Napper. Disjoining pressures in colloidal dispersions. *Journal of Colloid and Interface Science*, 63(1):43–48, 1978.

[56] F. Q. Fan and K. J. Stebe. Assembly of colloidal particles by evaporation on surfaces with patterned hydrophobicity. *Langmuir*, 20(8):3062–3067, April 2004.

[57] M. Faraday. The Bakerian lecture: Experimental relations of gold (and other metals) to light. *Philosophical Transactions of the Royal Society of London*, 147:145–181, 1857.

[58] D. L. Feldheim and C. D. Keating. Self-assembly of single electron transistors and related devices. *Chemical Society Reviews*, 27(1):1–12, January 1998.

[59] J. H. Fendler and F. C. Meldrum. The colloid-chemical approach to nanostructured materials. *Advanced Materials*, 7(7):607–632, July 1995.

[60] Guillaume Florey. Contact mechanics in a particle transfer tool. Master's thesis, ETH Zurich, 2006.

[61] Robert Fludd and Johann Theodor de Bry. *Utriusque cosmi maioris scilicet et minoris metaphysica, physica atque technica historia, in duo volumina secundum cosmi differentiam diuisa*. Aere J. T. de Bry, typis H. Galleri, Oppenhemii, 1617.

[62] K. A. Fosser and R. G. Nuzzo. Fabrication of patterned multicomponent protein gradients and gradient arrays using microfluidic depletion. *Analytical Chemistry*, 75(21):5775–5782, 2003.

[63] R. G. Freeman, K. C. Graba, K. J. Allison, R. M. Bright, J. A. Davis, A. P. Guthrie, M. B. Hommer, M. A. Jackson, P. C. Smith, D. G. Walter, and M. J. Natan. Self-assembled metal colloid monolayers — an approach to SERS substrates. *Science*, 267(5204):1629–1632, March 1995.

[64] G. Frens. Controlled nucleation for regulation of particle-size in monodisperse gold suspensions. *Nature-Physical Science*, 241(105):20–22, 1973.

[65] F. Garcia-Santamaria, H. T. Miyazaki, A. Urquia, M. Ibisate, M. Belmonte, N. Shinya, F. Meseguer, and C. Lopez. Nanorobotic manipulation of microspheres for on-chip diamond architectures. *Advanced Materials*, 14(16):1144–1147, August 2002.

[66] M. Geissler, H. Wolf, R. Stutz, E. Delamarche, U. W. Grummt, B. Michel, and A. Bietsch. Fabrication of metal nanowires using microcontact printing. *Langmuir*, 19(15):6301–6311, July 2003.

[67] M. J. Gordon and D. Peyrade. Separation of colloidal nanoparticles using capillary immersion forces. *Applied Physics Letters*, 89(5):053112, July 2006.

[68] K. V. Gothelf and T. H. LaBean. DNA-programmed assembly of nanostructures. *Organic & Biomolecular Chemistry*, 3(22):4023–4037, November 2005.

Bibliography

[69] A. N. Grigorenko, A. K. Geim, H. F. Gleeson, Y. Zhang, A. A. Firsov, I. Y. Khrushchev, and J. Petrovic. Nanofabricated media with negative permeability at visible frequencies. *Nature*, 438(7066):335–338, November 2005.

[70] V. G. Gryaznov, J. Heydenreich, A. M. Kaprelov, S. A. Nepijko, A. E. Romanov, and J. Urban. Pentagonal symmetry and disclinations in small particles. *Crystal Research and Technology*, 34(9):1091–1119, 1999.

[71] V. G. Gryaznov, M. Y. Tanakov, and L. I. Trusov. Plasticity and mass-transfer in contacting nanoparticles. *Journal of Materials Science*, 27(18):4829–4841, September 1992.

[72] K. W. Guarini, C. T. Black, and S. H. I. Yeuing. Optimization of diblock copolymer thin film self assembly. *Advanced Materials*, 14(18):1290–1294, September 2002.

[73] M. A. Hadley, A. Chiand, G. S. W. Craig, J. J. Jacobsen, J. S. Smith, J. Tu, and R. G. Stewart. Web fabrication of devices. U.S. Patent 7172910, 2007.

[74] A. J. Haes, D. A. Stuart, S. M. Nie, and R. P. Van Duyne. Using solution-phase nanoparticles, surface-confined nanoparticle arrays and single nanoparticles as biological sensing platforms. *Journal of Fluorescence*, 14(4):355–367, July 2004.

[75] K. R. Hall. Another hard-sphere equation of state. *Journal of Chemical Physics*, 57(6):2252–2254, 1972.

[76] Barry D. Hughes. *Random Walks and Random Enviroments. Volume 1: Random Walks*. Oxford Science Publications, London, 1995.

[77] E. Hutter and J. H. Fendler. Exploitation of localized surface plasmon resonance. *Advanced Materials*, 16(19):1685–1706, October 2004.

[78] S. H. Im, Y. T. Lee, B. Wiley, and Y. N. Xia. Large-scale synthesis of silver nanocubes: The role of HCl in promoting cube perfection and monodispersity. *Angewandte Chemie—International Edition*, 44(14):2154–2157, 2005.

300

[79] Jacob N. Israelachvilii. *Intermolecular and Surface Forces*. Academic Press, 1991.

[80] J. J. Jacobsen, G. W. Gengel, and J. S. Smith. Apparatuses and methods used in forming assemblies. U.S. Patent 6274508, 2001.

[81] J. J. Jacobsen, M. A. Hadley, and J. S. Smith. Methods for transferring elements from a template to a substrate. U.S. Patent 6555408, 2003.

[82] N. R. Jana, L. Gearheart, and C. J. Murphy. Wet chemical synthesis of high aspect ratio cylindrical gold nanorods. *Journal of Physical Chemistry B*, 105(19):4065–4067, May 2001.

[83] N. L. Jeon, S. K. W. Dertinger, D. T. Chiu, I. S. Choi, A. D. Stroock, and G. M. Whitesides. Generation of solution and surface gradients using microfluidic systems. *Langmuir*, 16(22):8311–8316, 2000.

[84] K. L. Johnson, K. Kendall, and A. D. Roberts. Surface energy and contact of elastic solids. *Proceedings of the Royal Society of London Series A—Mathematical and Physical Sciences*, 324(1558):301–313, 1971.

[85] F. Juillerat, H. H. Solak, P. Bowen, and H. Hofmann. Fabrication of large-area ordered arrays of nanoparticles on patterned substrates. *Nanotechnology*, 16(8):1311–1316, August 2005.

[86] Y. W. Jun, J. H. Lee, J. S. Choi, and J. Cheon. Symmetry-controlled colloidal nanocrystals: Nonhydrolytic chemical synthesis and shape determining parameters. *Journal of Physical Chemistry B*, 109(31):14795–14806, August 2005.

[87] L. S. Jung and C. T. Campbell. Sticking probabilities in adsorption from liquid solutions: Alkylthiols on gold. *Physical Review Letters*, 84(22):5164–5167, 2000.

[88] L. S. Jung and C. T. Campbell. Sticking probabilities in adsorption of alkanethiols from liquid ethanol solution onto gold. *Journal of Physical Chemistry B*, 104(47):11168–11178, 2000.

[89] S. Jung and C. Livermore. Achieving selective assembly with template topography and ultrasonically induced fluid forces. *Nano Letters*, 5(11):2188–2194, November 2005.

Bibliography

[90] H. Kawaguchi. Functional polymer microspheres. *Progress in Polymer Science*, 25(8):1171–1210, October 2000.

[91] Kevin Kendall. *Molecular Adhesion and its Applications. The Sticky Universe.* Kluwer Academic/Plenum Publishers, New York, 2001.

[92] E. Kim, Y. N. Xia, and G. M. Whitesides. Micromolding in capillaries: Applications in materials science. *Journal of the American Chemical Society*, 118(24):5722–5731, June 1996.

[93] Helmut Kipphan. *Handbook of Print Media*. Springer, 2004.

[94] R. Klajn, M. Fialkowski, I. T. Bensemann, A. Bitner, C. J. Campbell, K. Bishop, S. Smoukov, and B. A. Grzybowski. Multicolour micropatterning of thin films of dry gels. *Nature Materials*, 3(10):729–735, 2004.

[95] D. L. Klein, P. L. McEuen, J. E. B. Katari, R. Roth, and A. P. Alivisatos. An approach to electrical studies of single nanocrystals. *Applied Physics Letters*, 68(18):2574–2576, April 1996.

[96] U. Kloter, H. Schmid, H. Wolf, B. Michel, and D. Juncker. High-resolution patterning and transfer of thin PDMS films: fabrication of hybrid self-sealing 3D microfluidic systems. In *Proceedings of the 17th IEEE International Conference on Micro Electro Mechanical Systems. Maastricht MEMS 2004 Technical Digest, IEEE Cat. No. 04CH37517.*, 2004.

[97] Manuela Kobas. Transfer behavior of colloidal nanoparticles. Master's thesis, ETH Zurich, 2006.

[98] A. Kosiorek, W. Kandulski, P. Chudzinski, K. Kempa, and M. Giersig. Shadow nanosphere lithography: Simulation and experiment. *Nano Letters*, 4(7):1359–1363, July 2004.

[99] H. A. Kramers. Brownian motion in a field of force and the diffusion model of chemical reactions. *Physica*, 7:284–304, 1940.

[100] T. Kraus, L. Malaquin, E. Delamarche, H. Schmid, N. D. Spencer, and H. Wolf. Closing the gap between self-assembly and microsystems using self-assembly, transfer, and integration of particles. *Advanced Materials*, 17(20):2438–2442, October 2005.

[101] T. Kraus, L. Malaquin, H. Schmid, W. Riess, N. D. Spencer, and H. Wolf. Nanoparticle printing with single-particle resolution. *Nature Nanotechnology*, 2:570–576, 2007.

[102] T. Kraus, R. Stutz, T. E. Balmer, H. Schmid, L. Malaquin, N. D. Spencer, and H. Wolf. Printing chemical gradients. *Langmuir*, 21(17):7796–7804, August 2005.

[103] J. T. Krug, G. D. Wang, S. R. Emory, and S. M. Nie. Efficient raman enhancement and intermittent light emission observed in single gold nanocrystals. *Journal of The American Chemical Society*, 121(39):9208–9214, October 1999.

[104] H. Krupp. Particle adhesion. theory and experiment. *Advances in Colloid and Interface Science*, 1:111–239, 1967.

[105] Cyrill Kümin. Matrix effects on the surface plasmon resonance of dry, supported gold nanocrystals. Master's thesis, ETH Zurich, 2007.

[106] I. Langmuir. The evaporation, condensation and reflection of molecules and the mechanism of adsorption. *Physical Review*, 8(2):149–176, August 1916.

[107] N. B. Larsen, H. Biebuyck, E. Delamarche, and B. Michel. Order in microcontact printed self-assembled monolayers. *Journal of the American Chemical Society*, 119(13):3017–3026, 1997.

[108] S. W. Lee and R. Bashir. Dielectrophoresis and electrohydrodynamics-mediated fluidic assembly of silicon resistors. *Applied Physics Letters*, 83(18):3833–3835, November 2003.

[109] T. H. Lee and R. M. Dickson. Discrete two-terminal single nanocluster quantum optoelectronic logic operations at room temperature. *Proceedings of the National Academy of Sciences of the United States of America*, 100(6):3043–3046, March 2003.

[110] J. Liao, L. Bernard, M. Langer, C. Schonenberger, and M. Calame. Reversible formation of molecular junctions in 2D nanoparticle arrays. *Advanced Materials*, 18(18):2444–2447, September 2006.

Bibliography

[111] Y. C. Liao, E. I. Franses, and O. A. Basaran. Computation of dynamic adsorption with adaptive integral, finite difference, and finite element methods. *Journal of Colloid and Interface Science*, 258(2):310–321, 2003.

[112] L. Libioulle, A. Bietsch, H. Schmid, B. Michel, and E. Delamarche. Contact-inking stamps for microcontact printing of alkanethiols on gold. *Langmuir*, 15(2):300–304, 1999.

[113] J. F. Liu, L. G. Zhang, N. Gu, J. Y. Ren, Y. P. Wu, Z. H. Lu, P. S. Mao, and D. Y. Chen. Fabrication of colloidal gold micro-patterns using photolithographed self-assembled monolayers as templates. *Thin Solid Films*, 329:176–179, August 1998.

[114] S. T. Liu, R. Maoz, G. Schmid, and J. Sagiv. Template guided self-assembly of $[Au_{55}]$ clusters on nanolithographically defined monolayer patterns. *Nano Letters*, 2(10):1055–1060, October 2002.

[115] Z. T. Liu, C. Lee, V. Narayanan, G. Pei, and E. C. Kan. Metal nanocrystal memories — Part I: Device design and fabrication. *IEEE Transactions on Electron Devices*, 49(9):1606–1613, September 2002.

[116] C. Lopez. Materials aspects of photonic crystals. *Advanced Materials*, 15(20):1679–1704, October 2003.

[117] Y. Lu, Y. D. Yin, B. Gates, and Y. N. Xia. Growth of large crystals of monodispersed spherical colloids in fluidic cells fabricated using non-photolithographic methods. *Langmuir*, 17(20):6344–6350, October 2001.

[118] V. Mahalingam, S. Onclin, M. Peter, B. J. Ravoo, J. Huskens, and D. N. Reinhoudt. Directed self-assembly of functionalized silica nanoparticles on molecular printboards through multivalent supramolecular interactions. *Langmuir*, 20(26):11756–11762, December 2004.

[119] S. A. Maier, M. L. Brongersma, P. G. Kik, S. Meltzer, A. A. G. Requicha, and H. A. Atwater. Plasmonics — a route to nanoscale optical devices. *Advanced Materials*, 13(19):1501–1505, October 2001.

304

[120] S. A. Maier, P. G. Kik, H. A. Atwater, S. Meltzer, E. Harel, B. E. Koel, and A. A. G. Requicha. Local detection of electromagnetic energy transport below the diffraction limit in metal nanoparticle plasmon waveguides. *Nature Materials*, 2(4):229–232, April 2003.

[121] L. Malaquin, T. Kraus, H. Schmid, E. Delamarche, and H. Wolf. Controlled particle placement through convective and capillary assembly. *Langmuir, in press*, 2007.

[122] C. B. Mao, D. J. Solis, B. D. Reiss, S. T. Kottmann, R. Y. Sweeney, A. Hayhurst, G. Georgiou, B. Iverson, and A. M. Belcher. Virus-based toolkit for the directed synthesis of magnetic and semiconducting nanowires. *Science*, 303(5655):213–217, January 2004.

[123] O. Masala and R. Seshadri. Synthesis routes for large volumes of nanoparticles. *Annual Review of Materials Research*, 34:41–81, 2004.

[124] D. Maugis. Adherence of solids. In *Microscopic Aspects of Adhesion and Lubrication. Proceedings of the 34th International Meeting of the Société de Chimie Physique*, pages 221–252, 1981.

[125] Robert M. Mazo. *Brownian Motion. Fluctuations, Dynamics, and Applications*. Clarendon Press, Oxford, 2002.

[126] R. A. McMillan, C. D. Paavola, J. Howard, S. L. Chan, N. J. Zaluzec, and J. D. Trent. Ordered nanoparticle arrays formed on engineered chaperonin protein templates. *Nature Materials*, 1(4):247–252, December 2002.

[127] M. A. Meitl, Z. T. Zhu, V. Kumar, K. J. Lee, X. Feng, Y. Y. Huang, I. Adesida, R. G. Nuzzo, and J. A. Rogers. Transfer printing by kinetic control of adhesion to an elastomeric stamp. *Nature Materials*, 5(1):33–38, January 2006.

[128] E. Menard, K. J. Lee, D. Y. Khang, R. G. Nuzzo, and J. A. Rogers. A printable form of silicon for high performance thin film transistors on plastic substrates. *Applied Physics Letters*, 84(26):5398–5400, June 2004.

Bibliography

[129] P. Mesquida and A. Stemmer. Attaching silica nanoparticles from suspension onto surface charge patterns generated by a conductive atomic force microscope tip. *Advanced Materials*, 13(18):1395–1398, September 2001.

[130] P. Mesquida and A. Stemmer. Guiding self-assembly with the tip of an atomic force microscope. *Scanning*, 24(3):117–120, May 2002.

[131] A. S. Michaels. New separation technique for CPI. *Chemical Engineering Progress*, 64(12):31–43, 1968.

[132] C. W. Ming and G. E. Uhlenbeck. On the theory of the brownian motion—II. *Reviews of Modern Physics*, 17(2-3):323–342, 1945.

[133] K. Molhave, T. M. Hansen, D. N. Madsen, and P. Boggild. Towards pick-and-place assembly of nanostructures. *Journal of Nanoscience and Nanotechnology*, 4(3):279–282, March 2004.

[134] S. Morgenthaler, S. W. Lee, S. Zürcher, and N. D. Spencer. A simple, reproducible approach to the preparation of surface-chemical gradients. *Langmuir*, 19(25):10459–10462, 2003.

[135] C. B. Murray, C. R. Kagan, and M. G. Bawendi. Synthesis and characterization of monodisperse nanocrystals and close-packed nanocrystal assemblies. *Annual Review of Materials Science*, 30:545–610, 2000.

[136] M. Nirmal and L. Brus. Luminescence photophysics in semiconductor nanocrystals. *Accounts of Chemical Research*, 32(5):407–414, May 1999.

[137] M. Ohtsu, K. Kobayashi, T. Kawazoe, S. Sangu, and T. Yatsui. Nanophotonics: Design, fabrication, and operation of nanometric devices using optical near fields. *IEEE Journal of Selected Topics in Quantum Electronics*, 8(4):839–862, July 2002.

[138] B. O'Regan and M. Grätzel. A low-cost, high-efficiency solar-cell based on dye-sensitized colloidal TiO_2 films. *Nature*, 353(6346):737–740, October 1991.

[139] A. O'Riordan, P. Delaney, and G. Redmond. Field configured assembly: Programmed manipulation and self-assembly at the mesoscale. *Nano Letters*, 4(5):761–765, May 2004.

[140] A. O. Orlov, I. Amlani, G. H. Bernstein, C. S. Lent, and G. L. Snider. Realization of a functional cell for quantum-dot cellular automata. *Science*, 277(5328):928–930, August 1997.

[141] V. Adrian Parsegian. *Van der Waals Forces*. Cambridge University Press, 2006.

[142] B. A. Parviz, D. Ryan, and G. M. Whitesides. Using self-assembly for the fabrication of nano-scale electronic and photonic devices. *IEEE Transactions on Advanced Packaging*, 26(3):233–241, August 2003.

[143] Alphonsus V. Poccius. *Adhesion and Adhesives Technology*. Hanser Publishers, 1997.

[144] B. G. Prevo and O. D. Velev. Controlled, rapid deposition of structured coatings from micro- and nanoparticle suspensions. *Langmuir*, 20(6):2099–2107, March 2004.

[145] Philippe Réfrégier. *Noise Theory and Application to Physics*. Springer-Verlag Berlin Heidelberg New York, 2004.

[146] F. Remacle, C. P. Collier, J. R. Heath, and R. D. Levine. The transition from localized to collective electronic states in a silver quantum dots monolayer examined by nonlinear optical response. *Chemical Physics Letters*, 291(3-4):453–458, July 1998.

[147] D. S. Rimai, D. J. Quesnel, and A. A. Busnaina. The adhesion of dry particles in the nanometer to micrometer-size range. *Colloids and Surfaces A—Physicochemical and Engineering Aspects*, 165(1-3):3–10, May 2000.

[148] Hannes Risken. *The Fokker-Planck Equation*. Springer-Verlag Berlin Heidelberg New York, 1989.

[149] V. I. Roldughin. Self-assembly of nanoparticles at interfaces. *Uspekhi Khimii*, 73(2):123–156, 2004.

Bibliography

[150] H. B. Rosenstock. Luminescent emission from an organic solid with traps. *Physical Review*, 187(3):1166–&, 1969.

[151] P. W. K. Rothemund. Folding DNA to create nanoscale shapes and patterns. *Nature*, 440(7082):297–302, March 2006.

[152] P. W. K. Rothemund, N. Papadakis, and E. Winfree. Algorithmic self-assembly of DNA Sierpinski triangles. *PLoS Biology*, 2(12):2041–2053, December 2004.

[153] T. G. Ruardy, J. M. Schakenraad, H. C. van der Mei, and H. J. Busscher. Preparation and characterization of chemical gradient surfaces and their application for the study of cellular interaction phenomena. *Surface Science Reports*, 29(1):3–30, 1997.

[154] W. R. Russel, D. A. Saville, and W. R. Schowalter. *Colloidal Dispersions*. Cambridge University Press, 1989.

[155] V. Santhanam and R. P. Andres. Microcontact printing of uniform nanoparticle arrays. *Nano Letters*, 4(1):41–44, January 2004.

[156] G. Schmid, R. Pfeil, R. Boese, F. Bandermann, S. Meyer, G. H. M. Calis, and W. A. Vanderwelden. $Au_{55}[P(C_6H_5)_3]_{12}Cl_6$—a gold cluster of an exceptional size. *Chemische Berichte—Recueil*, 114(11):3634–3642, 1981.

[157] J. M. Schurr. Role of diffusion in bimolecular solution kinetics. *Biophysical Journal*, 10(8):700–716, 1970.

[158] E. V. Shevchenko, D. V. Talapin, N. A. Kotov, S. O'Brien, and C. B. Murray. Structural diversity in binary nanoparticle superlattices. *Nature*, 439(7072):55–59, January 2006.

[159] A. N. Shipway, E. Katz, and I. Willner. Nanoparticle arrays on surfaces for electronic, optical, and sensor applications. *Chemphyschem*, 1(1):18–52, August 2000.

[160] J. W. Slot and H. J. Geuze. A method to prepare isodisperse colloidal gold sols in the size range 3–17 nm. *Ultramicroscopy*, 15(4):383–383, 1984.

[161] Richard E. Smalley. Of chemistry, love and nanobots. *Scientific American Magazine*, pages 76–77, 2001.

[162] P. A. Smith, C. D. Nordquist, T. N. Jackson, T. S. Mayer, B. R. Martin, J. Mbindyo, and T. E. Mallouk. Electric-field assisted assembly and alignment of metallic nanowires. *Applied Physics Letters*, 77(9):1399–1401, August 2000.

[163] U. Srinivasan, M. R. Houston, R. T. Howe, and R. Maboudian. Alkyltrichlorosilane-based self-assembled monolayer films for stiction reduction in silicon micromachines. *Journal of Microelectromechanical Systems*, 7(2):252–260, June 1998.

[164] U. Srinivasan, D. Liepmann, and R. T. Howe. Microstructure to substrate self-assembly using capillary forces. *Journal of Microelectromechanical Systems*, 10(1):17–24, March 2001.

[165] J. J. Storhoff, A. A. Lazarides, R. C. Mucic, C. A. Mirkin, R. L. Letsinger, and G. C. Schatz. What controls the optical properties of DNA-linked gold nanoparticle assemblies? *Journal of The American Chemical Society*, 122(19):4640–4650, May 2000.

[166] S. H. Sun, C. B. Murray, D. Weller, L. Folks, and A. Moser. Monodisperse FePt nanoparticles and ferromagnetic FePt nanocrystal superlattices. *Science*, 287(5460):1989–1992, March 2000.

[167] Y. G. Sun and J. A. Rogers. Fabricating semiconductor nano/microwires and transfer printing ordered arrays of them onto plastic substrates. *Nano Letters*, 4(10):1953–1959, October 2004.

[168] Y. G. Sun and Y. N. Xia. Shape-controlled synthesis of gold and silver nanoparticles. *Science*, 298(5601):2176–2179, December 2002.

[169] R. R. A. Syms, E. M. Yeatman, V. M. Bright, and G. M. Whitesides. Surface tension-powered self-assembly of micro structures—the state-of-the-art. *Journal of Microelectromechanical Systems*, 12(4):387–417, August 2003.

Bibliography

[170] J. J. Talghader, J. K. Tu, and J. S. Smith. Integration of fluidically self-assembled optoelectronic devices using a silicon-based process. *IEEE Photonics Technology Letters*, 7(11):1321–1323, November 1995.

[171] R. H. Terrill, K. M. Balss, Y. M. Zhang, and P. W. Bohn. Dynamic monolayer gradients: Active spatiotemporal control of alkanethiol coatings on thin gold films. *Journal of the American Chemical Society*, 122(5):988–989, 2000.

[172] J. Tien, A. Terfort, and G. M. Whitesides. Microfabrication through electrostatic self-assembly. *Langmuir*, 13(20):5349–5355, October 1997.

[173] A. M. Turing. The chemical basis of morphogenesis. *Philosophical Transactions of the Royal Society of London Series B—Biological Sciences*, 237(641):37–72, 1952.

[174] J. Turkevich, P. C. Stevenson, and J. Hillier. A study of the nucleation and growth processes in the synthesis of colloidal gold. *Discussions of the Faraday Society*, (11):55–75, 1951.

[175] Abraham Ulman. *An Introduction to Ultrathin Organic Films: From Langmuir-Blodgett to Self-Assembly*. Academic Press, 1991.

[176] M. v. Smoluchowski. Drei Vorträge über Diffusion, Brownsche Molekularbewegung und Koagulation von Kolloidteilchen. I. Diffusion im unbegrenzten Raum. *Physik. Zeitschr.*, XVII:557–571, 1916.

[177] J. Vermant and M. J. Solomon. Flow-induced structure in colloidal suspensions. *Journal of Physics—Condensed Matter*, 17(4):R187–R216, February 2005.

[178] J. Y. Walz. The effect of surface heterogeneities on colloidal forces. *Advances in Colloida and Interface Science*, 74:119–168, February 1998.

[179] C. J. Wang, M. Shim, and P. Guyot-Sionnest. Electrochromic nanocrystal quantum dots. *Science*, 291(5512):2390–2392, March 2001.

[180] D. Y. Wang and H. Möhwald. Template-directed colloidal self-assembly — the route to 'top-down' nanochemical engineering. *Journal of Materials Chemistry*, 14(4):459–468, February 2004.

[181] G. M. Whitesides and B. Grzybowski. Self-assembly at all scales. *Science*, 295(5564):2418–2421, March 2002.

[182] B. Wiley, T. Herricks, Y. G. Sun, and Y. N. Xia. Polyol synthesis of silver nanoparticles: Use of chloride and oxygen to promote the formation of single-crystal, truncated cubes and tetrahedrons. *Nano Letters*, 4(9):1733–1739, September 2004.

[183] E. Winfree. Algorithmic self-assembly of DNA: Theoretical motivations and 2D assembly experiments. *Journal of Biomolecular Structure and Dynamics*, 11:263–270, 2000.

[184] M. E. Woods, J. S. Dodge, I. M. Krieger, and Pierce P. E. Monodisperse latices .i. emulsion polymerization with mixtures of anionic and nonionic surfactants. *Journal of Paint Technology*, 40(527):541–&, 1968.

[185] X. C. Wu, A. M. Bittner, and K. Kern. Microcontact printing of CdS/dendrimer nanocomposite patterns on silicon wafers. *Advanced Materials*, 16(5):413–417, March 2004.

[186] Y. N. Xia, Y. D. Yin, Y. Lu, and J. McLellan. Template-assisted self-assembly of spherical colloids into complex and controllable structures. *Advanced Functional Materials*, 13(12):907–918, December 2003.

[187] X. R. Xiong, Y. Hanein, J. D. Fang, Y. B. Wang, W. H. Wang, D. T. Schwartz, and K. F. Böhringer. Controlled multibatch self-assembly of microdevices. *Journal of Microelectromechanical Systems*, 12(2):117–127, April 2003.

[188] X. Yan, J. M. Yao, G. Lu, X. Li, J. H. Zhang, K. Han, and B. Yang. Fabrication of non-close-packed arrays of colloidal spheres by soft lithography. *Journal of the American Chemical Society*, 127(21):7688–7689, June 2005.

Bibliography

[189] X. Yan, J. M. Yao, G. A. Lu, X. Chen, K. Zhang, and B. Yang. Microcontact printing of colloidal crystals. *Journal of the American Chemical Society*, 126(34):10510–10511, September 2004.

[190] S. M. Yang and G. A. Ozin. Opal chips: vectorial growth of colloidal crystal patterns inside silicon wafers. *Chemical Communications*, (24):2507–2508, 2000.

[191] M. Yeadon, M. Ghaly, J. C. Yang, R. S. Averback, and J. M. Gibson. "contact epitaxy" observed in supported nanoparticles. *Applied Physics Letters*, 73(22):3208–3210, November 1998.

[192] Y. D. Yin, Y. Lu, B. Gates, and Y. N. Xia. Template-assisted self-assembly: A practical route to complex aggregates of monodispersed colloids with well-defined sizes, shapes, and structures. *Journal of the American Chemical Society*, 123(36):8718–8729, September 2001.

[193] Y. D. Yin, Y. Lu, and Y. N. Xia. Assembly of monodispersed spherical colloids into one-dimensional aggregates characterized by well-controlled structures and lengths. *Journal of Materials Chemistry*, 11(4):987–989, 2001.

[194] Z. L. Zhang and S. C. Glotzer. Self-assembly of patchy particles. *Nano Letters*, 4(8):1407–1413, August 2004.

312

Acknowledgements

314

quick, and not afraid to tell you what you should know. He is also reliable, positive, and always ready for a joke. He was a great manager to have; kudos to him.

This thesis is about technology, even if it is somewhat unconventional technology. I would not have come far without conventional technology. Thus, I would not have come far without Ute Drechsler, who not only does technology on a research level, but also taught me how to remain in a good mood while doing it. Whoever has done microfabrication knows what that takes. May she forever reign in the cleanroom!

The Science & Technology department at IBM is managed by Paul Seidler, the asker of good questions. He also knows how to answer questions without saying too much. He somehow manages to keep ZRL the unique place that it still is. The whole place owes him a lot for that, and I certainly do.

Three diploma students worked full-time on various aspects of this project: Manuela Kobas, Guillaume Florey, and Cyrill Kümin. Manuela was the one to prove, in an extensive and exhausting series of experiments, that geometry often outweighs chemistry in particle adhesion. I am grateful to her for going through it all. Guillaume found, amongst other things, that he could create ears on polystyrene beads, which seem to have made great impressions on some in his audience. I, for my part, am more grateful to him for taming LabView to operate the printing tool. Cyrill seemed like a jolly guy when I first met him, so we gave him the tricky task of analyzing the surface state of nanocrystals. They get dirty immediately, even in Switzerland. Cyrill prevailed and, to my great relief, remained jolly.

The second PostDoc to join the self-assembly project was Andrea Decker. She is the best-organized of us all, and if anyone can handle the myriads of samples I leave behind, it will be her. I should already apologize and thank here for not complaining.

We built a number of gorgeous gadgets and marvelous machines in this project, and it was the ZRL technicians who actually did the work there. My gratitude goes to Richard Stutz, who has done all kinds of things for the advancement of science, to Meinrad Tschudy, who diced and welded and drilled to make us happy, and to the entire ZRL machine shop, who actually built the printing tool and many parts of the CAPA tools. Thanks also to Bruno Mazenauer for not despairing over my orders of arcane chemicals with unknown toxicity.

Curriculum vitae

Curriculum vitae

Personal Data

Name	Tobias Kraus
E-Mail	tobias@kraus.net
Born	February 2nd, 1979 in Wertingen, Germany
Nationality	German

School Education

1985–1988	Grundschule Meitingen (elementary school)
1989–1998	Paul-Klee-Gymnasium, Gersthofen (high school)
1998	Abitur (high school diploma), grade average 1.3 (i.e., "very good")

Civil Service

1998–1999	Civil service at the "Ökumenische Sozialstation Meitingen", supporting a blind girl attending a regular high school

Internships

3/2000–4/2000	Clariant AG, Gersthofen: Mechanical machining
1/2001–4/2001	Kernkraftwerke (nuclear power plant) Gundremmingen, project work: "Influences of tubing materials on the microbiology of the cooling circuits in a boiling water reactor"

University Education

1999-2004	Student of **Chemical Engineering** at the Technical University of Munich (**TU München**)
2001	Pre-degree ("Vordiplom") of Chemical Engineering, grade "very good"

4/2001–9/2002	Research project at **Prof. Sten Vepřek's group at TU Munich**, "*Nanocomposite Coatings from Materials of the Ti-B-Ni-System*", grade "very good"
10/2002–5/2003	Research project at **Prof. Klavs Jensen's group at MIT** (Cambridge), "*Sensing in Two Phase Microflows*", grade "very good"
9/2003–3/2004	**Diploma thesis** at **Prof. de Rooij's group** at the Institute of Microtechnology, University of **Neuchâtel**, "*A microfluidic dispensing system for localized stimulation of cellular networks*", grade "very good"
5/2004	**Graduation** from the Technical University of Munich, degree "Diplom-Ingenieur Univ.", overall grade "very good"
5/2004–6/2007	**PhD student at ETH Zurich** (Laboratory of Surface Science and Technology, **Prof. Nicholas D. Spencer**) and the **IBM Zurich Research Laboratory**

Scholarships and Awards

1999-2004	Scholarship of the "Studienstiftung des deutschen Volkes" (German National Merit Foundation)
2002	Scholarship of the Ernest Solvay Foundation for the visit to MIT
2005	1st price, Student Mobility Award of the European Federation of Chemical Engineering
2006	IBM predoctoral fellowship
2007	SSOM Award of the Swiss Society for Microcopy and Microtechnology

Zürich, July 10th, 2007